State of the art constraints on black hole formation

The story of black holes told with high-precision kinematics

By

Cordelia Dashwood Brown

0009-0000-2064-3810

A thesis submitted in partial fulfilment for the degree of Doctor of Philosophy

School of Physics and Astronomy
Faculty of Engineering and Physical Sciences
University of Southampton

With Prof. Poshak Gandhi

September 2025

Abstract

State of the art constraints on black hole formation

by Cordelia Dashwood Brown

Black holes have been the subject of study by mathematicians and physicists alike for over 100 years, though the challenges associated with observing them mean they remain the most enigmatic objects in the Universe. This is an era of astronomy defined by unprecedented access to data, including groundbreaking astrometric surveys and advanced spectrographs. Such high-precision kinematic measurements offer insight into the most fundamental characteristics of black holes: their masses, through the orbital motion of companion stars; and their velocities, through analysis of their motion with respect to the Galactic potential. These observations act as keystones, around which to build and develop theory, enabling a deeper understanding of physics in the most extreme environments.

Taking advantage of groundbreaking astrometric surveys, this thesis presents the most extensive study of X-ray binary natal kicks to date, analysing 68 X-ray binaries including both neutron stars and black holes. This investigation finds that, contrary to theoretical predictions, the natal kicks applied to neutron stars and black holes are formally indistinguishable. This suggests that natal kicks are governed by similar physics irrespective of remnant type, and necessitates a revision of supernova hydrodynamic theory. With these results comes an observationally motivated distribution for implementation in future models: a Gamma distribution with mean $147\,\mathrm{km\,s^{-1}}$. This prescription is agnostic to the drivers of these natal kicks, thereby removing a key degeneracy in population synthesis studies.

The biggest caveat to this study, and to much of the research on compact objects, is that the vast majority of confirmed black holes exist in X-ray binaries, meaning they are actively accreting matter from a stellar companion. In light of this, high-precision astrometry and dynamical observations were used to identify and characterise a small sample of black hole candidates. These putative black holes were identified as ordinary stellar binaries, highlighting the complexities of astrometric studies of two-component systems. Nevertheless, the number of confirmed non-interacting black holes is growing, providing further constraints on black hole evolution beyond the X-ray binary population.

An additional issue in the study of black holes is the difficulty of observing their luminous companions (and, consequently, determining the mass of the compact object) in the heavily extincted regions within the Galactic plane. The development of microcalorimeters marks a significant step forward in X-ray astronomy and presents an opportunity to study new high-precision observations in the X-ray waveband, offering the potential to probe regions that are significantly obscured in the optical. The narrow component of the iron fluorescent line, originating from the X-ray irradiated companion, provides a potential means to further constrain the binary system properties, including the mass of the compact object. Modelling the geometry of the binary system and considering the composition of the stellar surface

indicates the equivalent width of this narrow iron line should be 2-40 eV (dependent on the binary mass ratio). The precision of cutting-edge X-ray spectrographs means velocity deviations can be measured within $< 40\,\mathrm{km\,s^{-1}}$ (depending on X-ray flux), enabling dynamical mass measurements of systems which are inaccessible with optical and infrared observations.

State of the art observing instruments and techniques provide exceptionally precise measurements of the kinematics of black holes, which in turn offer insight into their velocities and provide dynamical measurements of their masses. The mass and velocity distributions of black holes are intrinsically linked to their formation processes and subsequent evolution, many aspects of which remain uncertain, and have appreciable implications for gravitational wave astronomy. This thesis aims to highlight the interconnection of observation and theory, with the ultimate goal of understanding the genesis of black holes.

And where other animals walk on all fours and look to the ground, man was given towering head and commanded to stand, his face uplifted towards the skies to gaze upon the stars.

OVID, *METAMORPHOSES*

Table of Contents

List of Tables

List of Figures

Publication List

Published

C. Dashwood Brown, P. Gandhi, and Y. Zhao. "On the natal kick of the black hole X-ray binary H 1705-250". In: Monthly Notices of the Royal Astronomical Society 527.1 (Jan. 2024), pp. L82–L87. doi: 10.1093/mnrasl/slad151. arXiv: 2310.11492 [astro-ph.HE].

Y. Zhao, P. Gandhi, C. Dashwood Brown, C. Knigge, P. A. Charles, T. J. Maccarone, and P. Nuchvanichakul. "Evidence for mass-dependent peculiar velocities in compact object binaries: towards better constraints on natal kicks". In: Monthly Notices of the Royal Astronomical Society 525.1 (Oct. 2023), pp. 1498–1519. doi:10.1093/mnras/stad2226. arXiv: 2307.06430 [astro-ph.HE].

P. Gandhi, C. Dashwood Brown, Y. Zhao, K. El-Badry, T. J. Maccarone, C. Knigge, J. Anderson, M. Middle- ton, and J. C. A. Miller-Jones. "New Compact Object Binary Populations with Precision Astrometry (Roman White Paper)". In: arXiv e-prints, doi: 10.48550/arXiv. 2306.16479. arXiv: 2306.16479 [astro-ph.IM].

C. Dashwood Brown, P. Gandhi, and P. A. Charles. Measuring interacting binary mass functions with X-ray fluorescence". In: Monthly Notices of the Royal Astronomical Society 517.2 (Dec. 2022), pp. 2426–2435. doi: 10.1093/mnras/stac2725. arXiv: 2209.09920 [astro-ph.HE].

In prep

C. Dashwood Brown, P. Gandhi, Y. Zhao, C. Knigge, P. Charles, and P. Nuchvanichakul. "Black Holes and Neutron Stars Share Similar Natal Kick Distributions". In: Nature (Feb. 2025). Submitted for review.

P. Nuchvanichakul, P. Gandhi, C. Knigge, Y. Zhao, P. Irawati, S. Wanawichian, and C. Dashwood Brown. "Further evidence for natal kick segregation by spectral type in high-mass X-ray binaries". In: Monthly Notices of the Royal Astronomical Society (Nov. 2024). Submitted for review.

M. Middleton, G. Wiktorowicz, and C. Dashwood Brown. "Self-lensing binaries as probes of supernova physics". In: Monthly Notices of the Royal Astronomical Society (2025). Expected.

Acknowledgements

Dedicated to my grandfather, Ivan Woodhouse, for his unwavering support for me and my whole family. We owe you so much and love you even more. I hope I can continue to make you proud.

First and foremost, I must thank my supervisor, Poshak, for his constant support, academic and otherwise. I am so appreciative of your time, and I thank you for demonstrating a dedication to my research and career beyond that which is expected. Thank you for tolerating my mistakes, answering my questions and, more importantly, teaching me how to ask the important questions. I am a far better scientist than I ever thought possible and I will always be grateful.

Similar thanks must go to Professor Christian Knigge for the time and insight he has offered me throughout my four years here (despite not knowing he was my co-supervisor for the first 18 months). Hearing your perspective on my work has been invaluable, and I am grateful for all your work toward this thesis and much else.

I thank Professor Matt Middleton, who, despite not being my supervisor, always had time for me and provided me with fantastic opportunities to further my career, as well as much-needed chit-chat. I thank Professor Phil Charles for his contributions, kindness, and encyclopedic knowledge of our Universe. I am sincerely grateful for all other academics, both at the University of Southampton, the University of Leicester, and beyond, who have supported me over the years, with particular thanks directed toward Dr Yue Zhao, Dr Itumeleng Monageng, Dr Darren Wright, Dr Jonathan Nichols, & Dr Tom Stallard.

I must also thank my family, particularly my siblings, for their love, support, and the many lessons they have taught me. Hugh, Patience, and Ludo: you are my whole world, and I love you more than I can say. Thank you for standing with me for all these years. Additionally, I must thank my mother and father for all their help along the way.

To my very best friend, Emily, thank you. You mean more to me than you know, and I couldn't have done any of it without you. I thank those I've studied alongside, particularly Amy, Judith, and Maddie, for putting up with my ramblings and idiosyncrasies in the office. Thank you to Anna, Emily, Jack, Mark, Millie, and Ruth for all your love, support, and encouragement - the past four years have been the best of my life, and I owe much of my happiness to you. Additionally, thank you Emma, for providing much-valued love,

insight, and perspective, and thank you Charli, for always encouraging me to keep moving forward.

I must also acknowledge all the women who came before: the women who paved the way for my success in science. I stand on the shoulders of generations of women who fought for my right to do what I love. Their successes and sacrifices are not lost on me. I will always be grateful for the opportunities they created for me, and strive to hold the door open so our daughters may go even further.

Finally, I want to thank Tottenham Hotspur Football Club for reassuring me that there will always be people who love you, even when your performance is, unequivocally, dreadful.

This work was made possible by financial support from the Science and Technology Facilities Council (STFC). This research has made use of data and/or software provided by the High Energy Astrophysics Science Archive Research Center (HEASARC), which is a service of the Astrophysics Science Division at NASA/GSFC. Additional thanks go to Dr K. Breivik and the team behind `cosmic` for their work in developing & maintaining the code, and making it open access for the benefit of the community.

With the oversight of my main supervisor, editorial advice has been sought. No changes in intellectual content were made as a result of this advice.

Declaration of Authorship

I, Cordelia Dashwood Brown, declare that this thesis, titled "State of the art constraints on black hole formation" and the work presented in it are my own and have been generated by me as the result of my own original research.

I confirm that:

- This work was done wholly or mainly while in candidature for a research degree at this University.
- Where any part of this thesis has previously been submitted for a degree or any other qualification at this University or any other institution, this has been clearly stated.
- Where I have consulted the published work of others, this is always clearly attributed.
- Where I have quoted from the work of others, the source is always given. With the exception of such quotations, this thesis is entirely my own work.
- I have acknowledged all main sources of help.
- Where the thesis is based on work done by myself jointly with others, I have made clear exactly what was done by others and what I have contributed myself.

SIGNED:

DATE:

Chapter 1

Introduction

1.1 Overview

As the most fundamental science, physics has a head start on many other disciplines. Yet a complete understanding of the world around us remains out of reach. The twin pillars that govern modern physics are general relativity and quantum field theory, describing the laws of nature on the astronomical and atomic scales respectively.

In the vast majority of cases, one is purely academic. We can discard the effects of the former and favour the gospel of the latter, or vice versa, depending on what aspect of the world we are studying. Galactic evolution is untroubled by the effects of quantum tunnelling, and nuclear power stations need not worry about the precession of Mercury's orbit around the sun. This is not the case for black holes.

The behaviour around black holes is dominated by their immense gravity, creating an event horizon beyond which nothing can escape, yet a cornerstone of quantum field theory is that everything is conserved and retainable. The two Titans meet, and what happens next remains a mystery.

It is reasonable to suggest that the holy grail of modern physics is a complete model of quantum gravity, a framework in which all elements of physics can coexist. Physical black holes provide the perfect laboratory. While this all-encompassing theory remains elusive, understanding black holes in the context of astrophysics is a valuable endeavour, promising to shed further light on the mechanisms that drive the Universe and complementing numerous other areas of astronomy and physics.

Regrettably, the timescales of the Universe in comparison to our lifespan are unforgiving. While a biologist can study the life of a mayfly in a single day, we are unable to watch the complex cycles of collapsing nebulae, stellar evolution, black hole formation,

and black hole death. The solution: gather all the evidence available to us, and attempt to fill in the blanks. To be an astronomer is to be an archaeologist, to look back in time and across the Universe in an attempt to understand how everything happened, and continues to happen, and will go on happening.

1.1.1 A consequence of general relativity

Despite often being referred to as a science, mathematics is, in fact, the language of the Universe, capable of describing anything and everything. Typically, we observe and interact with the physical world, then search for the mathematics that describes it. Black holes are a rare instance of the process acting in reverse, having been a purely theoretical (i.e. mathematical) phenomenon for over 50 years (though a hypothetical one for much longer).

In 1915, Einstein's Theory of General Relativity demonstrated the importance of gravity beyond Newtonian physics, presenting the Einstein Field Equations [76]. Shortly thereafter Schwarzschild [258] (and, soon after, Droste [74]) presented a solution exhibiting apparently unphysical behaviour (and, unknowingly, providing a mathematical description of English astronomer John Michell's idea that a star could be so massive that the surface velocity would exceed the speed of light [254]).

Schwarzschild's solution to the Einstein Field Equations expressed the line element ds (an infinitesimal small line describing the geometry of a space) in the form:

$$ds^2 = \left(1 - \frac{2GM}{c^2 r}\right) dt^2 - \left(1 - \frac{2GM}{c^2 r}\right)^{-1} dr^2 - r^2 d\theta^2 - r^2 \sin^2(\theta) d\phi^2 \qquad (1.1)$$

with M denoting mass, and (t, r, θ, ϕ) describing the spacetime coordinates. The result of this is a singularity existing at $r = 0$ and an event horizon at $r_s = \frac{2GM}{c^2}$ (known as the Schwarzschild radius), beyond which the escape velocity surpasses the speed of light, marking the point of no return.

The possibility of this exotic surface existing in physical form remained dubious (though theoretical study continued), until the 1960s, when Jocelyn Bell's discovery of pulsars (a subclass of neutron stars) provided some evidence that the curiosities evoked by general relativity may be physical after all [130]. Just a few years later, the X-ray source Cygnus X-1 became the first identified black hole [27; 299], launching a new era of astronomy and the possibility of understanding the Universe beyond conventional physics.

1.1.2 Classifications

Black holes exist in many forms and are mainly differentiated based on their mass.

Stellar-mass black holes: The subject of this thesis, stellar-mass black holes are the most numerous, with around 100 million expected to exist in our Galaxy alone [262]. They represent the final stage of stellar evolution, formed by the collapse of a massive star ($\geq 8\,\mathrm{M}_\odot$) into a supernova. Their masses are dependent on the stellar progenitor mass and their evolution (e.g. if they have accreted mass from another star) and typically span $5 \leq M_{\mathrm{BH}} \leq 50\,\mathrm{M}_\odot$, although the growing field of gravitational wave astronomy suggests this may extend up to $\geq 100\mathrm{M}_\odot$ [185].

Super-massive black holes: These black holes range $10^6 \leq M_{\mathrm{BH}} \leq 10^{10}\,\mathrm{M}_\odot$; they exist at the centre of galaxies, including our own (Sgr A*). These behemoths remain poorly understood, with many unanswerables related to their formation and growth [e.g. 238; 193].

Intermediate-mass black holes: Observational evidence for black holes spanning $10^2 \leq M_{\mathrm{BH}} \leq 10^5\,\mathrm{M}_\odot$ is sparse; the most promising candidates are ultra-luminous sources (ULXs), though for the time being they evade extensive study [64; 167].

For brevity's sake, stellar-mass black holes are hereafter referred to simply as black holes.

1.2 Black hole formation

Black holes are the product of the death of a massive star, and the conclusion to its evolution. The onset of stellar evolution occurs when nebulae (molecular clouds of hydrogen and helium, referred to as stellar nurseries) experience small density fluctuations, leading to their collapse. The density and temperature of the material increase, and the mass begins to rotate as it forms a protostar. Once the temperature exceeds 10 million Kelvin, nuclear fusion erupts, and lighter elements (initially, hydrogen) combine to form heavier elements (in the first stages, helium). Nuclear fusion releases tremendous amounts of energy (of order 10^{26} joules per second), and is the mechanism that drives the universe.

Despite generating immense power, fusion processes are counter-balanced by the star's own gravity. It is the precise balance between thermonuclear and gravitational forces

that defines a star; a steady equilibrium that lasts millions of years. In its final stages, the star forms an iron core. As an element, iron marks the cut-off between exothermic and endothermic fusion processes. The star is unable to overcome the iron's gravitational binding energy, and nuclear fusion ceases. The lack of internal radiative pressure can no longer mediate the immense gravity. The result: the delicate harmony of the star collapses, and with it, the star itself.

1.2.1 Supernovae

The core collapses inward, reaching nuclear densities, in which nuclei are broken down into nucleons, and ionisation processes emit highly energetic neutrinos [1; 25]. At this density, the equation of state stiffens, the core becomes all but incompressible, and the collapse halts. The collapsing matter rebounds, forming an outgoing shock wave, which itself is stalled due to energy loss via photo-disintegration, meaning the wave can no longer compete with the ram pressure from the infalling outer core. Core-collapse supernovae are accompanied by an explosion in the event of this shock wave being re-energised (for a review, see Burrows and Vartanyan [41]).

There are a variety of mechanisms by which this may occur; the most commonly cited being neutrino heating first invoked by Wilson [305]. There forms a region behind the shock wave in which neutrinos decouple from matter, and the associated heating deposits energy into the shock wave, allowing it to overcome external pressures and leading to an explosion. Simulations investigating the neutrino transport within supernovae suggest that this process alone may be insufficient to re-energise the stalled shock and therefore does not cause an explosion, although this is contingent on the neutrino flux & heating efficiency, among other parameters [236; 279; 37; 210; 218; 123].

Alternatives to neutrino-driven explosions include magneto-rotational instabilities that result from differential rotation of the stellar core and seed magnitude fields [269], or acoustic mechanisms, in which excitation of low-frequency oscillations within the stellar interior propagate sound waves that reinvigorate the shock [43; 223].

In the event of insufficient re-energising of the shock (plausibly more likely in the event of high mass-infall rates), the collapse continues, forming a black hole, with very little stellar material ejected [45]. This is referred to as a 'failed supernova'. There may exist an intermediate scenario in which some stellar material is initially ejected but has insufficient energy to escape the system, so accretes back onto the newly formed black hole (referred to as 'fallback') [95; 96].

Whilst core-collapse is considered the most common channel for compact object formation, at least in the stellar mass regime, there exist alternatives. Pair-instability collapse, resulting from electron-positron pair production may result in a very massive black hole (50-100 $M_\odot$) or no stellar remnant whatsoever [11]. It has also been argued that some black holes may form due to accretion onto a neutron star, causing it to exceed 3 $M_\odot$ [49].

Black holes are the ghosts of dead stars, but their story does not begin after the formative supernova. One must look further back in time to understand their characteristics, particularly their masses. Thus arises the importance of stellar binaries. A binary system is made up of two components, dynamically coupled and orbiting a common centre of mass. These binaries may host two ordinary stars, a companion star and a compact object, or two compact objects. It is widely agreed upon that most massive stars exist in binaries [163]. Given that it is the more massive stars that form black holes, it naturally follows that black holes will preferentially exist in binaries in the earlier stages - although these binaries may become disrupted (i.e. the star and compact object become unbound) due to the supernova explosion, or a stellar companion may be completely swallowed by the compact object.

The next section gives a brief overview of our current understanding of binary evolution, specifically isolated field formation. In this case, the stars existed in their binary system from birth, likely forming from a common cloud. The alternative is the dynamical capture scenario, in which two isolated stars pass close enough to become gravitationally coupled to one another. The latter scenario is thought to be sub-dominant [281], although the exact proportion is unclear. The formation of X-ray binaries is identified as a crucial means of understanding black holes and acting as test beds for related physics.

1.3 The evolution of stellar binaries

The binary fraction of our Galaxy is estimated to be dependent on Galactic location and stellar mass [174; 200; 29]; in the high mass regime, the binary fraction increases to ≥ 0.7 [163; 103]. This is partially responsible for the interconnection between binary stars and black holes.

Unlike single stars, binary evolution is often governed by interactions such as mass transfer, tidal forces, and mergers, leading to a diverse range of astrophysical phenomena. Long-period binaries (wide binaries) often evolve similarly to isolated stars, with no interaction between the two components [157] - other systems, particularly compact

object progenitors, undergo episodes of mass transfer and other interactions. For in-depth reviews of binary evolution, including the specific scenarios involving black holes, see [231; 300; 59; 198] or, most recently, Marchant and Bodensteiner [199].

At first, both stars evolve independently, following standard stellar evolution channels relying on the nucleosynthesis of progressively heavier elements in their core. When the most massive star expands (the primary), it begins interacting and impinging on the development of the other star (the secondary). This may involve Roche lobe overflow, in which the gravitational influence of the binary results in the transfer of mass and stellar material onto the secondary [289; 18] (for a detailed discussion of the Roche lobe and its geometry, see Section 4.5). This mass transfer may be stable, or lead to a common envelope phase [132].

The common envelope phase describes the scenario in which mass transfer from the primary to the secondary occurs rapidly - the transfer of matter results in changing orbital energy and the binary separation decreases [230; 275; 18]. This phase may end in the ejection of the common envelope from the system, or the total merger of the two stellar components. Regardless, the more massive star reaches the end of its life, culminating in a supernova. If the remnant exceeds the Chandrasekhar limit (the maximum mass of a stable white dwarf, $\sim 1.4\,\mathrm{M}_\odot$ [57]) it will form a compact object; either a neutron star or a black hole.

Whilst the above provides an overview, the subject of binary evolution is extensive - an example evolutionary pathway is shown in Figure 1.1. Mass transfer mechanisms, including stellar winds and common envelope scenarios, are subject to much speculation with a variety of different theories [e.g. 231; 18; 33]. As well as the complex and often ill-defined supernova physics, the evolution of a binary system is governed by a variety of other processes and parameters, which include the following:

Magnetic braking: Magnetic braking is the process by which binary orbits shrink (and may eventually merge), where stellar magnetic fields increase the specific angular momentum of stellar winds, which is then counteracted by the loss of orbital angular momentum. The rate at which this occurs is uncertain, related to the component masses, radii, orbital period, and magnetic field strength [137; 141]; it is mainly relevant for older stars with stronger magnetic fields. Recent evidence of a flat distribution of orbital periods below 10 days in low mass binaries suggests the effects of magnetic braking may asymptote, which is in tension with established models [77].

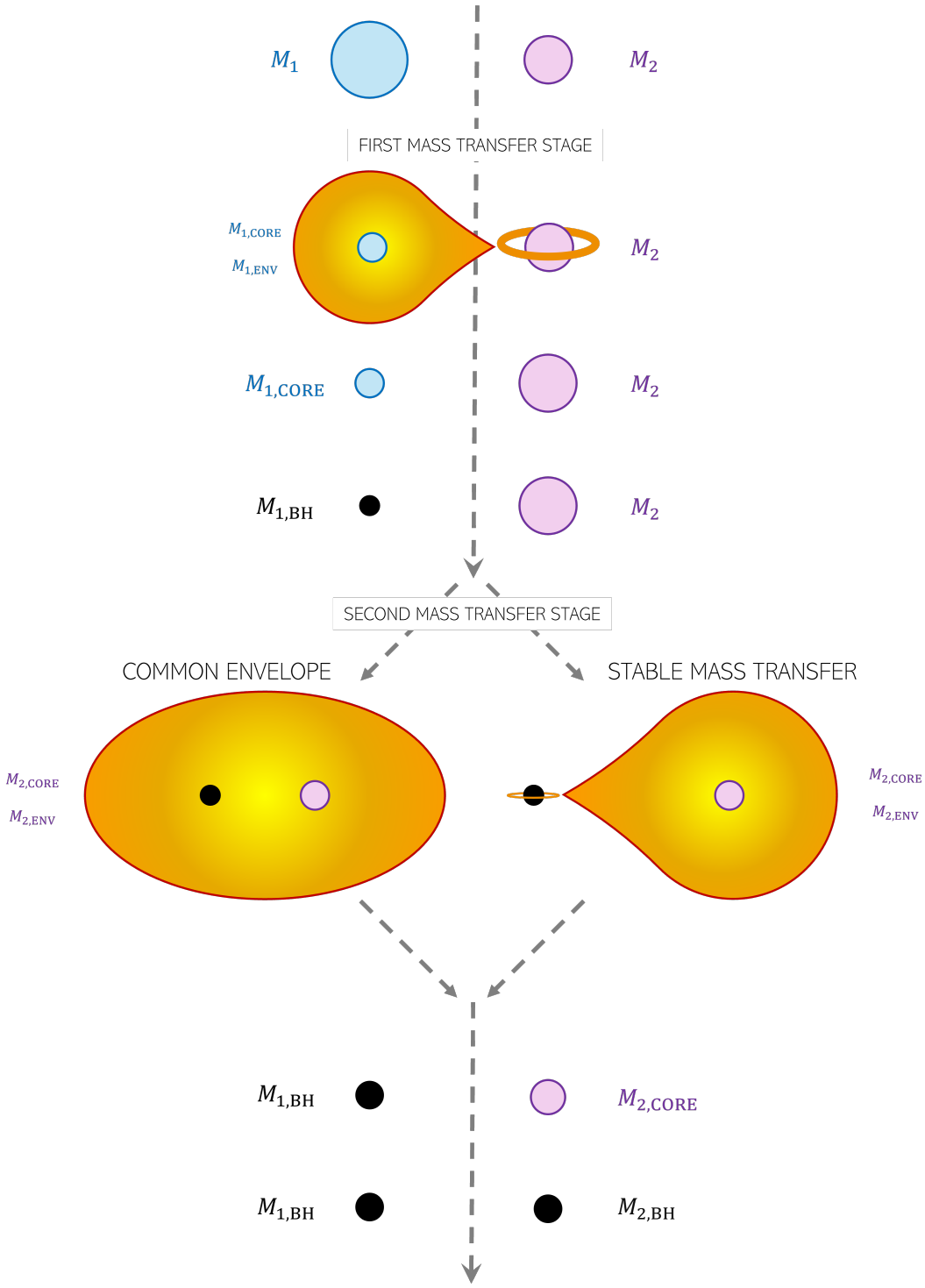

Figure 1.1: **Schematic of Binary Evolution**: One potential channel of binary evolution. The primary mass expands to fill its Roche lobe, initiating mass transfer onto the secondary. Eventually, it undergoes a core-collapse supernova forming a black hole. The second stage of mass transfer occurs as mass from the stellar companion is accreted by the black hole; this may be stable or result in a common envelope phase (as could be the case in the first stage of mass transfer). The secondary star may also evolve into a black hole, leaving a double black hole (BH-BH) binary, which will eventually merge and emit gravitational waves.

Gravitational wave radiation: Gravitational radiation serves as a key mechanism for angular momentum loss, significantly impacting the orbital evolution over time. In short orbits, gravitational wave emission can dominate over other mechanisms (e.g. magnetic braking, tidal synchronisation, etc.). This shrinks the orbit, enhancing the rates of mass transfer which increases the X-ray luminosity of the system and can result in a merger.

1.3.1 Mass transfer

Periods of mass transfer (also referred to as accretion) are instrumental in determining the evolution of a binary system and may be related by various processes. Historically, it is only through accretion processes that we have been able to identify black holes (although this is changing).

1.3.1.1 Roche lobe overflow

The motion of fluid is governed by the Euler equation:

$$\rho\frac{\partial\vec{v}}{\partial t} + \rho\vec{v}\cdot\nabla\,\vec{v} = -\nabla P + \vec{f} \tag{1.2}$$

where ρ is the density, t: time; $\vec{v}$: velocity; P: pressure; and $\vec{f}$: any external forces. In the case of a binary system, the presence of centrifugal and Coriolis forces leads to the definition of the Roche potential:

$$\Phi_{\mathrm{R}}(\vec{r}) = -\frac{\mathrm{G}M_1}{|\vec{r}-\vec{r_1}|} - \frac{\mathrm{G}M_2}{|\vec{r}-\vec{r_2}|} - \frac{(\vec{\omega}\wedge\vec{r})^2}{2} \tag{1.3}$$

in which M_1 & M_2 are the masses of each star, $\vec{r_1}$ & $\vec{r_2}$ are the positions of the two stars, and $\vec{\omega}$ is the angular velocity of the whole binary. The size and shape of binary stars are defined by this surface and must lie on one of the equipotentials (see Figure 1.2). The Roche lobe is the figure-of-eight region in which the potentials around each of the component stars come into contact. The size of this may be approximated by considering a sphere of the same volume, the radius of which is given by Equation 1.4 [75] (where q is $\frac{M_2}{M_1}$, and R_2 is normalised to the orbital separation of the two components - e.g., $R_2 = 0.5$ indicates the point in the centre of the binary system) and ranges 0.1-0.75 for $0.01 \leq q \leq 100$.

$$R_2 = \frac{0.49q^{2/3}}{0.5q^{2/3} + \ln(1+q^{1/3})} \tag{1.4}$$

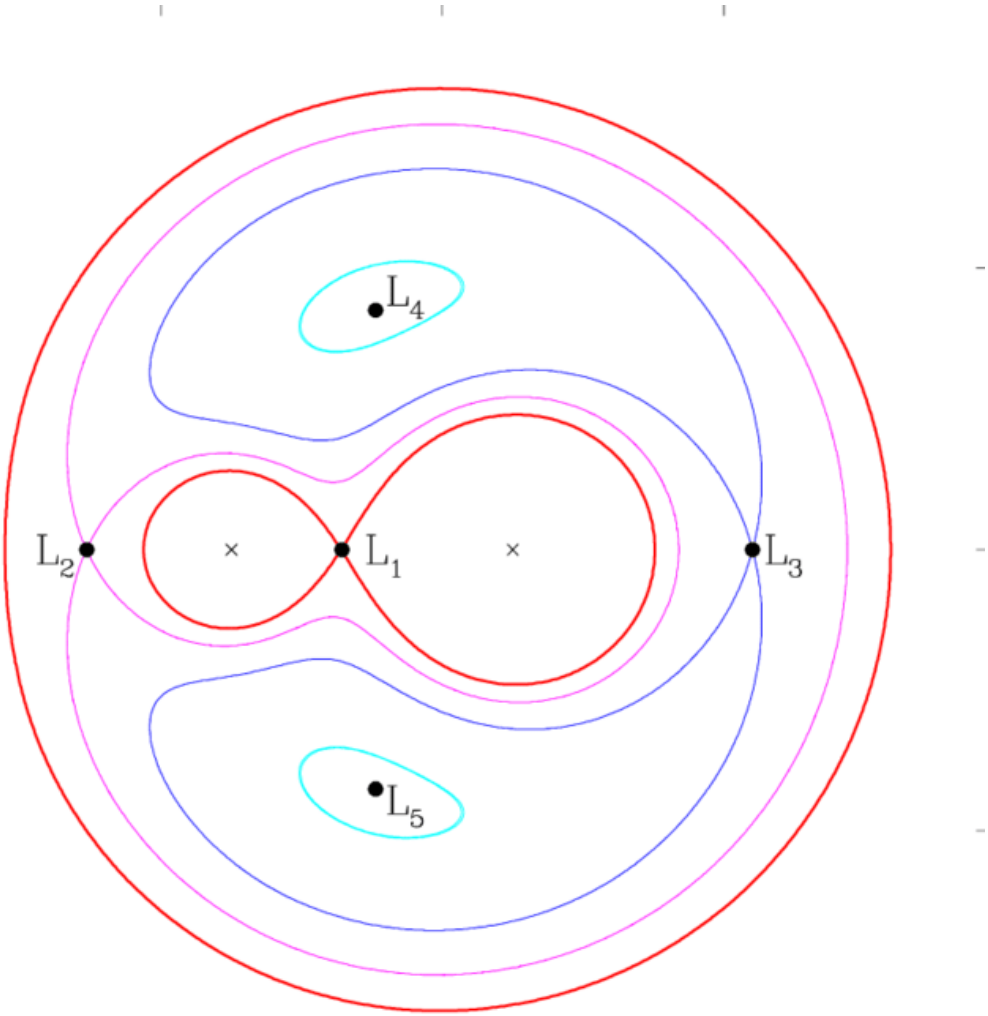

Figure 1.2: **Roche Potential**: Equipotentials of the Roche surface, with the L_1 Lagrangian Point (through which mass transfer may occur) indicated [27]. This system has a mass ratio q = 3, the point masses indicated with an 'x'. [Image credit: Boffin [26].]

The L_1 Lagrangian point indicates the point at which matter will pass from the gravitational potential of one system to the other, rather than be lost from the system. If a star expands as it evolves, it may fill its Roche lobe, resulting in the transfer of matter onto the other star, at a rate governed by their relative masses and the rate of expansion (i.e. the nuclear timescale of hydrogen, t_n), expressed as:

$$\dot{M}_2 = \frac{M_2}{(5/3 - 2q)t_n} \tag{1.5}$$

Mass transfer often leads to the formation of an accretion disc. The 'ejected' mass has to rid itself of the orbital angular momentum it held while bound to its star, and an accretion disc provides a means of liberating momentum and energy, resulting in the emission of electromagnetic radiation (see Figure 1.3). In some cases, as mass transfer shrinks the orbital separation, the two stars may completely merge.

The stability of Roche lobe overflow mass transfer is determined by the 'critical mass ratio'; if the mass of the accreting star relative to the donor star exceeds this, the system will undergo a common-envelope phase. The critical mass ratio may be directly related to stellar radii [298] or spectral type [60].

1.3.1.2 Common Envelope

The common envelope phase is often associated with two constants, α being the common-envelope efficiency parameter (describing the transfer of orbital energy to the common envelope, and, consequentially, the likelihood that the system will eject the envelope) and λ being the binding energy of the common envelope [285; 138]. $\alpha = 1$ indicates that all the orbital energy has gone into ejecting the envelope, where $\alpha < 1$ means only some of the energy has been transferred, and $\alpha > 1$ requires an additional source of energy. The quoted values of α vary (indeed, it is likely that α is not constant [239]); $\alpha = 1$ is fairly typical in the literature [e.g. 215], although may be as low as 0.2 [321], or as high as 5 [91].

Determining whether the common envelope phase ends in the merger of the two components typically considers two scenarios; the 'pessimistic' scenario suggests that, in the event of an ill-defined core-envelope boundary the system will merge [142; 18]. The 'optimistic' scenario, where this is not the case, predicts fewer merging systems (ergo more surviving binaries).

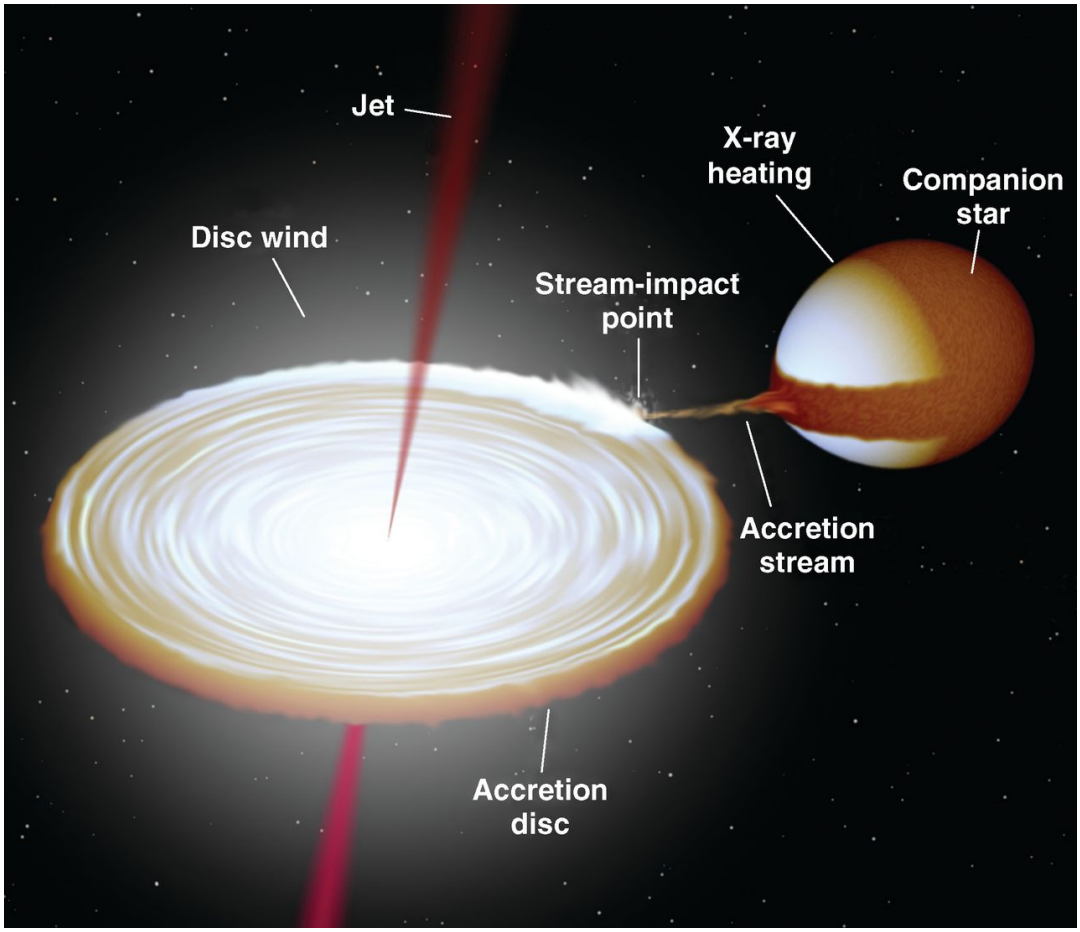

Figure 1.3: **Roche lobe overflow accretion**: Schematic showing a black hole accreting matter from a stellar companion via Roche lobe overflow, resulting in an accretion disc and X-ray emission.[Image credit: produced with BinSim by Rob Hynes [139].]

1.3.1.3 Stellar winds

In the case of closely separated binaries, stellar winds may result in the ejection of mass from one component which may then be accreted by the other. This is likely more relevant for binaries containing larger and younger O- and B- type stars (these are the massive, hot stars with shorter lifespans than other main sequence stars).

The velocity of this wind is related to its mass and radius by:

$$v_w(r)^2 \propto \frac{2\mathrm{G}M}{R} \tag{1.6}$$

with the proportionality constant depending on stellar type [138].

The rate of accretion is often described by:

$$\dot{M} = \frac{2\pi \mathrm{G}^2 M^2 \rho}{v_w^2} \tag{1.7}$$

in which M is the mass of the accretor and ρ is the density of the surrounding medium [28], and can range $10^{-6} - 10^{-5}\,\mathrm{M}_{\odot}$ per year [92].

Metallicity is cited as a crucial parameter in determining the effectiveness of stellar wind mass transfer [296; 294]; the specific dependencies are a function of effective temperature of the star in question. The role of metallicity may be diminished in the event of near Eddington accretion [114; 293].

The mass-accretion rate is interconnected with the system's luminosity. Evidence of a 'kink' in the luminosity-accretion rate relation was presented by Vink [293] & Yang et al. [316] and parametrised by Vink and Sabhahit [295], but the mass-accretion rate of binaries remains the subject of debate.

1.3.2 X-ray binaries

X-ray binaries (XRBs) consist of a compact object (a neutron star (NS) or black hole (BH)) and another ordinary star. These binaries are sufficiently close that mass transfer occurs, with the compact object accreting material from its companion via Roche lobe overflow, or strong stellar winds. The relative contribution of each of these channels is typically dependent on the mass of the companion. In either scenario, the liberation of gravitational potential energy from the accreting matter leads to highly energetic radiation, typically in the form of X-rays ($\sim$0.1-100 keV). Consequentally, these systems are highly luminous in X-rays and represent among the most extreme objects in the universe.

Much of what is known about compact objects comes from studies of X-ray binaries. This is *not* necessarily attributable to these being the dominant population of compact objects, but rather reflective of the challenges associated with observing compact objects which inherently emit no radiation themselves (as outlined in Section 1.6).

X-ray binaries are broadly distinguished by a) the nature of the compact object (i.e. BH-XRBs or NS-XRBs) and b) the characteristics of the companion star. The nature of the X-ray emission (i.e. variability and hardness) provides another means of differentiation - see Table 1.1.

Low-mass X-ray binaries (LMXBs) host smaller companions (typically $< 1\,\mathrm{M}_{\odot}$). These are often later-type main-sequence stars, and accretion is primarily governed by Roche lobe overflow. A sub-population of older LMXBs may have been 'spun up', and consequently are rapidly rotating; these are known as millisecond pulsars (or, simply, pulsars) [196]. For a review of LMXBs, see Bahramian and Degenaar [7].

	HMXBs	LMXBs
X-ray spectra	Hard, $\geq 15\,\mathrm{keV}$	Soft, $\leq 10\,\mathrm{keV}$
Variability	X-ray pulses, rarely outburst	X-ray outbursts, rarely pulses
Accretion	Stellar winds	Roche lobe overflow
Companion	Larger & brighter, O- B-type	Smaller & fainter

Table 1.1: **Characteristics of X-ray Binaries**: Typical (though not universal) properties of high-mass and low-mass X-ray binaries, adapted from Tan [276].

High-mass X-ray binaries (HMXBs) host more massive stars (often defined as $M_2 \geq 10\,\mathrm{M}_\odot$). These stars are often O- or B-type stars (e.g. OB supergiants or Be stars). The accretion of the high-mass companion onto the compact object is dominated by strong stellar winds. For a review of HMXBs, see Tan [276].

There exists a small population of 'intermediate-mass' X-ray binaries, where $1.5 \leq M_2 \leq 5\,\mathrm{M}_\odot$ [228]. In this thesis, these systems are included as low-mass X-ray binaries, and the cut-off mass between low- and high-mass systems is $M_2 = 5\,\mathrm{M}_\odot$).

1.3.3 Open questions

The above descriptions only scratch the surface of the range of processes which govern binary and black hole evolution. Given such complexity, population synthesis codes such as `cosmic` [33] and `StarTrack` [19] have been developed, allowing the user to investigate the role of each of these different channels, with the aim of explaining the observed patterns and characteristics of compact objects, such as those existing in X-ray binaries. These codes, including their advantages and limitations, are discussed extensively in Chapter 2.

However, in spite of these advanced codes and the development of detailed theories motivated by fundamental physics, questions regarding the characteristics of black holes remain. The different evolutionary processes and mechanisms which may be responsible are numerous and arguably the most fundamental parameters remain enigmatic. These are the mass distribution and velocity distribution.

1.4 The masses of black holes

1.4.1 Measuring black hole masses

The masses of compact objects cannot be measured directly, however, they can be constrained through observations of the radial velocity curves of the companion star [92; 53] - this method is not dependent on the interaction between the companion star and the black hole, so whilst most examples concern X-ray binaries, astrometrically identified non-interacting black holes may also be characterised in this way [e.g. 78; 79; 99].

Consider a binary system, comprising a compact object (M_1) and a companion star (M_2), orbiting a centre of mass (defined by $M_1 a_1 = M_2 a_2$). Assuming circular orbits (a reasonable assumption, given that tidal effects typically circularize orbits on comparatively short timescales [16]), the radial velocity amplitude (K_2) of the companion star is given by:

$$K_2 = \frac{2\pi}{P} a_2 \sin i \tag{1.8}$$

Using the centre of mass definition and Kepler's third law, the 'mass function' can be derived:

$$f(M_1) = \frac{M_1^3 \sin^3 i}{(M_1 + M_2)^2} = \frac{P_{\rm orb}\ K_2^3}{2\pi G}, \tag{1.9}$$

where M_1 is the mass of the compact object, M_2 is the observed mass of the companion, K_2 is the peak Keplerian velocity of the companion, $P_{\rm orb}$ is the orbital period, and i is the inclination. By reducing the assumed companion mass to 0, $f(M_1)$ provides the minimum mass for the compact object, and combining this with observations of the companion star's mass (e.g. through spectral type) provides more stringent constraints.

In the 1970s, observations of Cygnus X-1 (among the first X-ray sources identified) established the presence of a massive dark companion, making it the first dynamically confirmed black hole [299; 27], although the uncertainty in the mass of the luminous companion means the compact object mass is still debated. Casares et al. [54] presented the mass function of V404 Cyg, providing evidence for a $\sim 6\,\mathrm{M}_\odot$ black hole, with a much higher precision[1] (Figure 1.4). Since then, around 50 black holes have been identified and measured, [e.g. 54; 220; 202; 270; 191; 53; 127; 205].

When determining mass functions, it is important to consider the caveat of the 'K-correction'. Given that some spectral features arise from the irradiated 'half' of the companion, this is offset from the donor's centre of mass, and therefore a small correction

[1]The estimated mass of the black hole continues to be updated/revised [e.g. 260], and was recently posited to be part of a hierarchical triple [38].

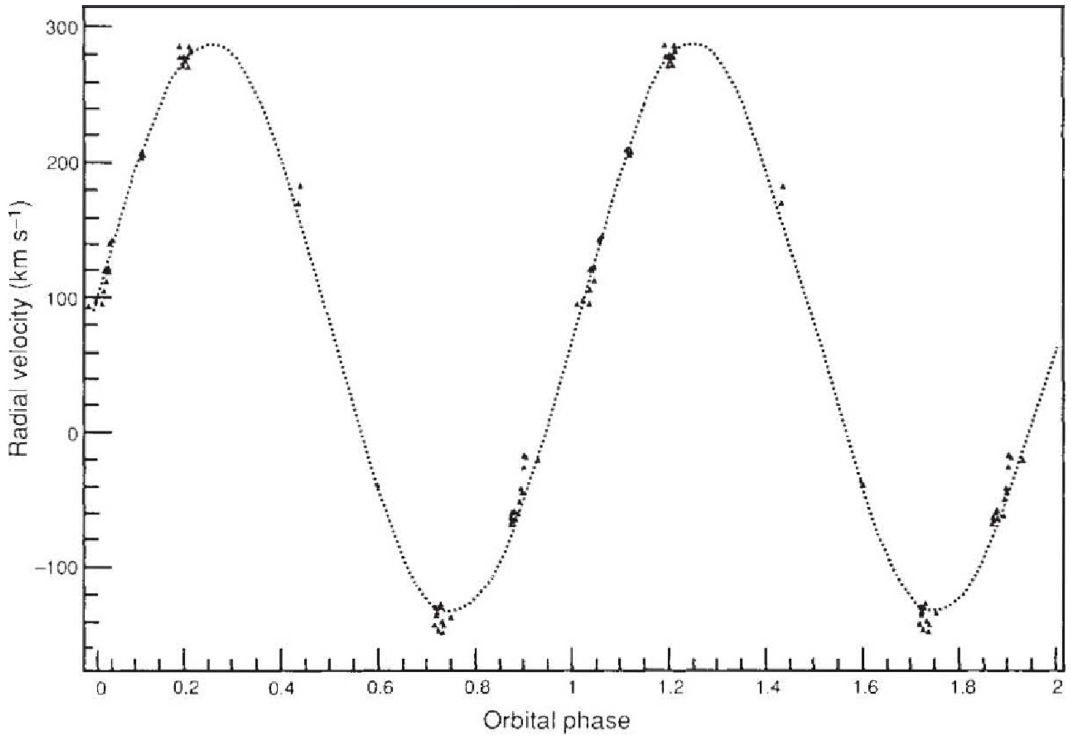

Figure 1.4: **Radial velocity curve of the black hole in V404 Cygni**: In 1992 Casares et al. [54] presented the radial velocity curve for the luminous component of the system V404 Cygni which indicated the presence of a $6.2M_{\odot}$. [Image credit: Casares et al. [54].]

needs to be accounted for when calculating mass functions [209]. This factor is typically small, and, without it, the masses are slightly underestimated.

1.4.2 Mass distribution

The distribution of stellar mass black holes is linked to their origin & evolution (including interactions with companion stars); supernova physics [93; 95; 18]; and the rates of gravitational wave predictions [182] (amongst numerous other phenomena). Despite a growing catalogue of black holes with well-measured masses, a complete description of the mass distribution is still out of reach. At its centre is the debate surrounding the so-called 'lower mass gap' - the phenomenon that most compact objects are less than $3\,M_{\odot}$ (neutron stars) or greater than $4.5\,M_{\odot}$ (black holes).

1.4.3 Lower mass gap

First proposed by Bailyn et al. [10], the lower mass gap describes the apparent absence of compact objects between 3-5 $M_{\odot}$ - this lies above the established threshold for the

most massive neutron stars [158], but below the smallest observed black holes. Bayesian analysis of mass measurements of black holes in transients suggested a peak at $7\,M_\odot$, and noted a dearth of sources below $4\,M_\odot$. More than a decade later, coincident studies by Özel et al. [224] and Farr et al. [83] independently reaffirmed both the clustering of observed masses between 6-10 $M_\odot$ and the absence of sources in the lower regime (e.g. Farr et al. [83] determined the minimum black hole mass, $M_{1\%} > 4.3M_\odot$ at 90% confidence interval).

1.4.4 Selection biases

As a discipline, astronomy is at the mercy of observational capabilities, meaning selection and observation biases are frequently troublesome. With that in mind, each of the previous papers ([10; 83; 224]) investigated the likelihood of the mass gap being non-physical but rather an artefact. Among the biases considered were: incomplete inclination measurements leading to different mass precisions; limiting the sample to primarily LMXBs; flux limitations; and the requirement of a stellar companion.

Testing the influence of inclination, Özel et al. [224] applied their Bayesian analysis of 16 LMXBs, both including and *excluding* measurements of inclination, which are present for fewer than half the systems in their sample. These inclination estimates are primarily derived from the ellipsoidal modulations in the light curves of X-ray binaries [51]. Whilst adjusting the distribution of masses for each system had some effect on the overall distribution, the lower mass gap remained robust to these changes, indicating incomplete analysis of inclinations is unlikely to be responsible. However, the importance of inclination is highlighted in another study of stellar mass distributions by Kreidberg et al. [173]. Contrary to the previous studies, revising mass estimates based on assuming an underestimation of inclinations by previous studies suggests the mass gap is likely populated after all. The total sample in this work comprises 16 sources, but one source, GRO J0422+32, has mastery over the rebuttal of the mass gap. Kreidberg et al. [173] proposed its inclination is substantially higher than previous estimates of the stellar mass population would predict, being heavily influenced by the X-ray activity (as is perhaps the case with A0620-00, another BH-LMXB). If this is the case, the proposed mass decreases to 2-3 $M_\odot$, thus populating in the mass gap. However, if the inclination is more moderate, as is consistent with other systems, the mass gap prevails.

Whilst the sample sizes used by both Özel et al. [224] & Farr et al. [83] exceed the initial study of seven LMXBs, (comprising 16 and 20 sources respectively), each sample was dominated by LMXBs and, more specifically, transient X-ray sources. This was not

a deliberate choice by either author; the transient nature of most LMXBs (and a handful of HMXBs) make dynamical mass measurements both easier and more reliable, as there are periods when the source is not dominated by X-ray emission (quiescence) and the spectrum of the companion star may be more easily interpreted [242]. One may then consider that, whilst the transient nature of these systems is primarily due to orbital periods [162], there may be a class of lower-mass black holes existing as *persistent* X-ray sources. However, as outlined by Özel et al. [224], of 72 persistent X-ray sources, 46 are confidently identified as neutron stars, and only two of the remainder exhibit behaviour that could be associated with the presence of a black hole - in short, there is not room in the observed persistent X-ray sources for a significant population of low-mass black holes.

There is a case to be made for the luminosity of sources introducing inherent bias in the numbers and characteristics of the sources that are observed. Özel et al. [224] demonstrated that, somewhat intuitively, more luminous LMXBs (based on peak X-ray fluxes) have been subject to sufficient observation for dynamical mass measurements. In an attempt to quantify this bias, they considered whether a mass-luminosity relation could result in fewer low-mass black holes being identified and studied, but found that the sample of 16 luminous LMXBs would be accompanied by 4 fainter (i.e. less massive) LMXBs.

In fact, Jonker et al. [154] posited that selection effects result in a bias against *higher* mass black holes. Jonker et al. [154] noted that, despite the general consensus that most black holes form within the Galactic plane, the majority of dynamically confirmed black holes (in LMXBs) exist further from the plane (two-thirds lie more than half a kiloparsec above (or below) the Galactic plane, with only two lying within 100 pc). There is an anti-correlation between black hole mass and Galactic scale height, indicating the more massive black holes in LMXBs exist within the Galactic plane; extinction levels are significantly higher in this region and are therefore less likely to be identified or well-characterised. [2]

The influence of selection effects was further investigated by Siegel et al. [266]; the population synthesis code `cosmic` was used to generate populations of compact objects with a continuous mass distribution (this was done by assuming a delayed supernova mechanism, as is explained herein). They found a substantial population of black holes existing in the lower mass gap (∼40%) - a large fraction of which formed via accretion-induced collapse (AIC) of higher mass neutron stars. These populations demonstrated

[2] Jonker et al. [154] cites the influence of natal kicks as responsible for these spatial distributions; this is discussed further in Chapter 2.

that the selection biases associated with the transient nature of most observed black holes could plausibly be responsible for the apparent dearth of low-mass black holes.

Whilst specific observational constraints provide food for thought on the selection biases, what is more difficult to counter is the fact that, by definition, electromagnetic dynamical mass measurements require the black hole to be coupled to a stellar companion. That most large stars exist in binaries is uncontroversial, but the survival of these binaries during the formative supernova is more complex and largely dependent on the supernova channels and related natal kicks. Any relation between survival likelihood and remnant compact object mass is not straightforward, meaning the bias introduced by the binary requirement is not easily accounted for or corrected.

The limitations introduced by relying on dynamical mass measurements are slowly being mediated by the growing field of gravitational wave astronomy, which has provided some evidence of the lowest mass black holes [184; 186]. LIGO/Virgo is becoming a useful tool in testing the lower mass gap [280; 68; 149] but for now, electromagnetic observations dominate.

It is also worth noting that the most recently identified black hole (at the time of writing), Swift J1727.8-1613, is theorised to host a black hole with mass $M_1 \geq 3.1 \pm 0.1$, which sits within the mass gap [252] - further observations are necessary to refine this measurement.

1.4.5 Theoretical predictions

Given that observational evidence of the mass gap is inconclusive, one can consider whether current theoretical expectations, particularly in the context of supernova physics, are consistent with such a gap [93; 95; 96; 164]. Fryer [93] conduct simulations of supernovae to determine the black hole mass function, relying on the initial stellar mass function for massive stars and the relation between compact progenitor and remnant mass. The latter relies upon the magnitude of the explosion energy relative to the gravitational binding mass of the star. According to this approximation, a gap between 3-5 $M_\odot$ is **not** expected.

On the contrary, Belczynski et al. [20] propose that a rapidly exploding supernova (i.e. within 100-200 ms after the collapse of the core) could result in scarcity of low-mass black holes, as opposed to the delayed mechanism (where the explosion occurs >200 ms after initial collapse) (this delayed-supernova theory was implemented in the study conducted by Siegel et al. [266], as mentioned earlier).

The distribution of stellar mass black holes and the legitimacy of the mass gap is contingent on available data; to that end, further measurements of the mass of black holes, particularly those not subject to the biases described above, will be vital. Whilst dynamical mass measurements have historically relied on the optical and infrared wavelengths, Chapter 4 discusses the potential to use X-ray emission features. This method may not be subject to some of the biases described above; for instance, where optical and infrared spectroscopy favours transient LMXBs, X-ray spectroscopy is most viable for more active HMXBs.

1.5 The kinematics of black holes

1.5.1 Peculiar velocity

Peculiar velocity ($\upsilon_{\rm pec}$) describes the motion of a system beyond that which is predicted by the Galactic potential (and, at a higher level, the Hubble flow[3]). The peculiar velocities of Galactic objects (such as stars, stellar clusters, and compact objects) have been observed for decades [e.g. 304; 263], with pulsars in particular being subject to intensive study [e.g. 189; 66; 125; 284; 133]. Since then, a number of other neutron stars and black holes have also been identified as having high peculiar velocities [e.g. 303; 90; 308; 197].

These peculiar velocities can be measured using astrometry (see Section 1.6.3). As laid out by Reid et al. [240], the Galactocentric 3D velocity is calculated from the distance to the star, its position in the Galaxy, and its observed its motion through the Galaxy (and various constants, such as the distance between the Sun and the Galactic centre, Galactic rotational speed, etc.).

Gaia observatory is an astrometric mission designed to create a precise map of the positions and movements of the Galaxy - for further details see Section 1.6.3. Zhao et al. [318] present a catalogue of the 89 compact objects that have well-measured astrometry, including the results of the *Gaia* mission, as well as individual studies of distances and radial velocities (Figure 1.5 shows the *Gaia* measured positions and proper motions of all the neutron stars and black holes in this study). This sample demonstrated anti-correlations of $\upsilon_{\rm pec}$ with both total system mass and orbital period ($\upsilon_{\rm pec} \propto M_{\rm tot}^{-0.5}$ and $\upsilon_{\rm pec} \propto P_{\rm orb}^{-0.2}$). This is not the first statistical study of high-peculiar velocity systems [e.g.

[3]The Hubble flow describes the velocity of galaxies due to the expansion of the Universe; any deviation from this may be observed as redshift/blueshift and indicative of influences outside this expansion. For example, the Andromeda galaxy is hurtling towards us with a peculiar velocity $\upsilon_{\rm pec} \sim 300\,{\rm km\,s^{-1}}$ [268].

206; 133] and serves to reaffirm the presence of additional drivers of motion beyond that which is expected due to the Galactic potential.

1.5.2 The importance of natal kicks

The deaths of massive stars can impart additional acceleration to compact objects at the instant of supernova (SN), an impulse referred to as a natal kick. The high peculiar velocity of many XRBs supports the hypothesis that non-negligible natal kicks occurred at the instant of supernova [206; 133; 100; 5; 87; 221], although this is only a proxy for kick velocity. There remains uncertainty in the role of natal kicks in the evolution of black hole systems. Previous literature has made a distinction between kicks associated with neutron stars [e.g., 119; 286; 190; 189; 31; 133; 292] versus black holes [e.g., 152; 117; 245; 143; 197], with the former being more extensively studied. Whilst there exists evidence for neutron star kicks with both high and low velocities, evidence of black holes receiving natal kicks is less clear.

These kick velocities have a profound effect on the remnant's subsequent dynamical evolution [156; 159; 214; 133]; its spin [48; 65; 89; 45; 8]; the rate of gravitational wave merger events in binary systems [21]; the rate of lensing events they may give rise to [169]; remnant retention fraction in stellar clusters [227; 272; 109]; and the evolution and characteristics of these clusters [267; 247]. Natal kicks may disrupt the binary, resulting in isolated black holes (and neutron stars) and a population of high-velocity 'run-away' (or, perhaps, 'walk-away') stars [243]. These isolated black holes are all but impossible to find, and being able to quantify their contribution to the Galactic population would be valuable in determining the degree to which inferences based on X-ray binaries apply to the entire population. Conversely, natal kicks may be responsible for systems merging. In the case of surviving binaries, the natal kicks impact not only the velocity but also the eccentricity and orbital separation, which in turn govern whether there will be periods of accretion and mass transfer, and have a hand in determining how likely we are to observe these systems using the techniques outlined in Section 1.6.

Kicks have been put forward to explain binary population features beyond peculiar velocities; namely the anti-correlation between period and distance from the Galactic plane (Z height) [100]. If black hole X-ray binaries are formed within the Galactic disc, then the current Z distribution may be the result of kicks (both asymmetric progenitor kicks and 'Blaauw' kicks [24] - for further detail see Chapter 2), which either displace the binary to somewhere further from its natal site or, if the binary is more widely

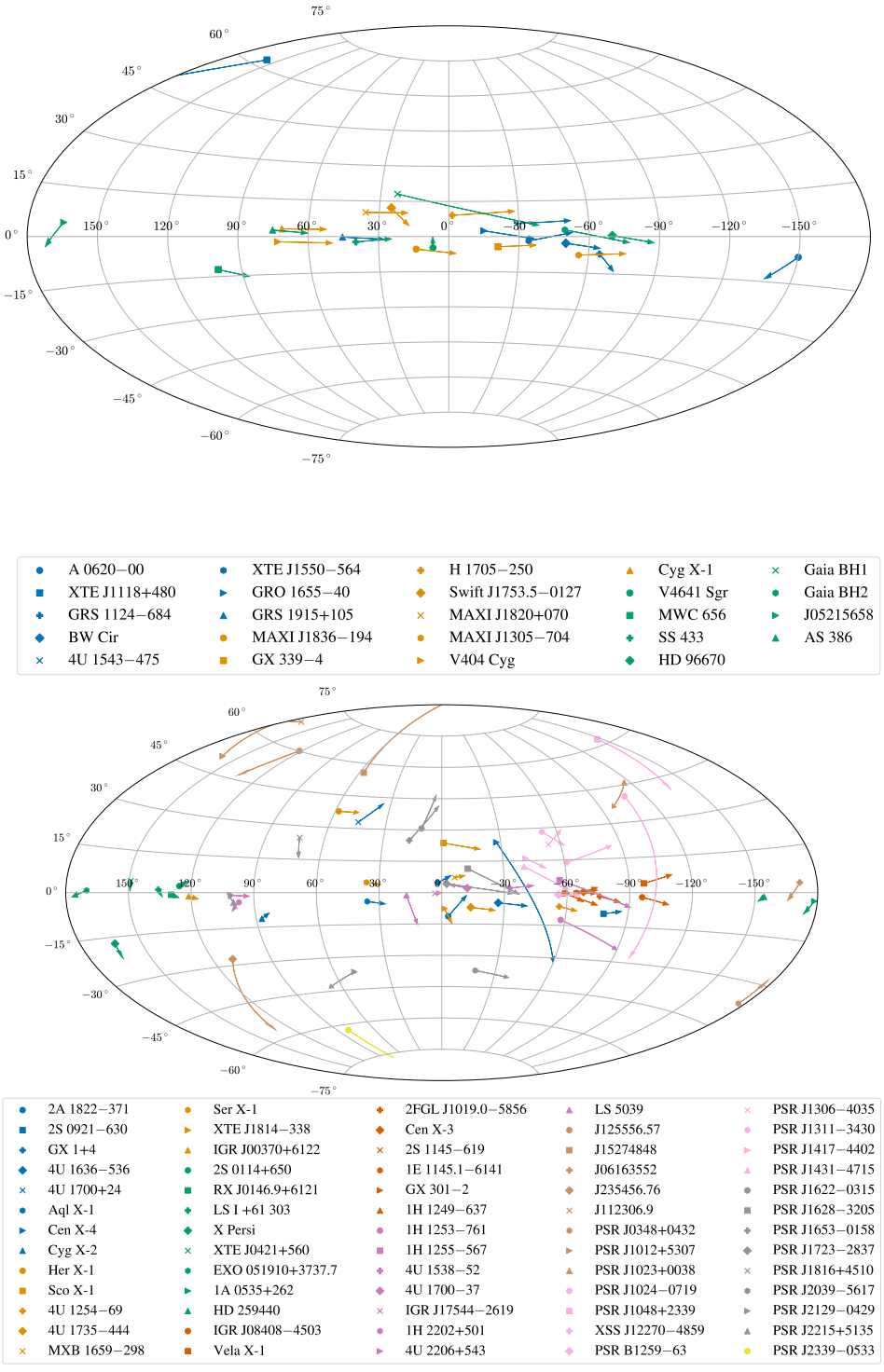

Figure 1.5: **Proper Motions of Galactic compact objects**: The *Gaia* observed positions and proper motions of 24 black holes (upper) and 65 neutron stars (lower) in Galactic coordinates. [Image credit: Zhang et al. [317].]

separated, disrupt it entirely, hence the lack of observed long period binaries at high Galactic latitudes.

These kicks may be associated with any number of physical processes - many of which invoke asymmetries as an intuitive explanation for a recoiling compact object (recalling Newton's ubiquitous Third Law). These may be associated with ejected matter (baryonic) or neutrinos [126; 145; 40; 94; 255; 256; 165]. Inhomogeneities likely exist in both the density of the stellar progenitor [265; 40], the neutrino heated region behind the shock wave [40; 176], and the shock wave itself [255]; Rayleigh-Taylor instabilities, for instance, are a well-established feature of supernova hydrodynamics [42; 129; 146]. These non-negligible perturbations likely grow with time - it is for this reason that a slower onset of explosion is conducive to larger asymmetries and therefore larger recoils imparted to the newly formed compact object [94; 255][4].

Whilst extensive, multidimensional hydrodynamic simulations provide examples of natal kick velocities, one may predict the magnitude of a recoil kick under the assumption it is proportional to the degree of asymmetry within the star. Janka and Müller [146] propose recoil velocities may be expressed as follows:

$$\upsilon_{\rm NS} = \alpha \, \frac{M_{\rm ej}}{M_{\rm NS}} \, \upsilon_{\rm ej} \tag{1.10}$$

where $M_{\rm ej}$ is the mass of ejected material and $M_{\rm NS}$ is the mass of the remnant neutron star. $\alpha = \langle \upsilon_z \rangle / \langle |\upsilon| \rangle$ indicates the deviation from spherical symmetry. Under this assumption, even slight asymmetries (of order a few per cent or less) would be conducive to natal kicks consistent with observations [42; 146; 217; 219]. This may be elaborated upon to consider the recoil velocities associated with specific mechanisms (i.e. convective instability within the newly formed neutron star, turbulence in post-shock material, and anisotropic neutrino emission).

Nordhaus et al. [219] present:

$$a_c = \int_{r>r_c} \frac{G\vec{r}}{r^3} {\rm d}m - \frac{1}{M_c} \left[\int_{r=r_c} P \, d\vec{S} + \int_{r=r_c} \rho \upsilon_r \vec{v} \, {\rm d}S \right] \tag{1.11}$$

where a_c and M_c are the acceleration and mass of the core; P is the gas pressure; ρ indicates the fluid density; and $\vec{v}$ denotes the fluid velocity (with υ_r being the radial component). Each of the three terms corresponds to the contribution from a) gravity of matter external to the core, b) anisotropic gas pressure, and c) momentum flux, respectively. Here, perfect isotropy results in each term vanishing, and zero recoil kick,

[4]Yamada and Sato [314] report that prompt explosions are hindered by rotation of the stellar core - the link between progenitor rotation and natal kick strength requires further research.

whereas asymmetric explosions yield recoil velocities of $10 < v_{\rm NS} < 1000\,{\rm km\,s^{-1}}$. Equation 1.11 may appear to provide a simple analytical prediction of recoil velocities; however, the interconnection between pressure and momentum flux, coupled with the fact that each of these terms evolves over different time scales, means predicting recoil velocities remains complex and highly model-dependent.

A thorough review of the hydrodynamic & radiative processes within supernovae and their associated kinematics is beyond this thesis' jurisdiction. Whilst the exact mechanisms and their associated kick magnitudes remain subject to debate, one comment remains strikingly consistent among hydrodynamical studies; that is, that natal kicks are considerable for neutron stars and inconsequential for black holes. Observational evidence for non-negligible natal kicks applied to black holes is growing (as is described in Chapter 2) but a description of natal kick mechanisms that fully describes all observations is, for now, out of reach.

That neither the mass nor the velocity of compact objects is fully explained is curious; the key characteristic of black holes is their mass, and the key characteristic of the Universe is arguably its restlessness. That the both mass distribution and velocity distribution of black holes evade explanation highlights that the marriage between theory and observation is a quarrelsome one.

Whilst fundamental physics can aid in the development of theoretical models and prescriptions, science is separated from mathematics by the presence of data. Fortunately, this is an era in which data from black holes is more accessible than ever before.

1.6 Observations of black holes

As a discipline, astronomy dates back as far as the dawn of humanity itself. To become an astronomer, one need only step outside and look up. All that separates us now from early humankind is the development of technologies allowing us to look beyond that which we can observe by eye.

One could imagine returning to Mesolithic Scotland, explaining to the makers of the world's oldest lunar calendar that not only do we still look to the Moon, but we can now see each mountain and crater as clearly as the ground we walk on. It is plausible that our ancestors could come to terms with the idea of using a ground-based optical telescope as a glorified magnifying glass, allowing us to effectively zoom in on the skies. What is more difficult to explain is our ability to see the invisible; the most fundamental feature of black holes is that they absorb everything and emit nothing, no electromagnetic

radiation, no light of any kind. And yet, in this era of astronomy, observing black holes is discussed in the same context as observing exoplanets or solar flares. Advancements in space technology and the development of strategies to circumvent the problem of observing the unobservable have made black holes visible - though they remain shrouded in mystery.

Observations of black holes began in the 1960s[5], with the discovery of the first non-stellar X-ray source in the Galaxy Scorpius X-1 (Sco X-1) - though at the time the nature of this source was unknown [107]. The first evidence of a black hole was presented independently by Webster and Murdin [299] and Trimble [286], relying on dynamical mass measurements (as described in Section 1.4 & Chapters 3 & 4). Since then black holes have been studied with a range of techniques, each with its own advantages. A thorough review of black hole observations could be a thesis in itself - this section provides an outline of the main techniques and missions and highlights those used in this work.

1.6.1 X-ray emission

Despite coming more than 500 years after the optical, X-ray astronomy is now intrinsic to studies of black holes and other compact objects. X-ray binaries are the best candidates with which to observe and characterize black holes. Their X-ray luminosities range over $10^{36} - 10^{40}\,\mathrm{ergs\,s^{-1}}$, depending on the specific system, and whether it is experiencing X-ray outburst active or is in quiescence [92][6]. Outburst activity can be associated with a number of processes, the most commonly cited of which is the accretion disc instability mechanism, where thermal instabilities within the accretion disc increase its viscosity, allowing for more efficient mass transfer and greater emission of X-rays [288; 162].

The *Chandra X-ray Observatory*, *XMM-Newton*, and *eROSITA* have been able to identify and characterise hundreds of X-ray binaries, including both neutron stars and black holes [e.g. 153; 120; 85] (see Figure 1.6). In their wake, a new era of X-ray astronomy has been enabled by the development of microcalorimeters. The latest X-ray mission, *XRISM* includes a microcalorimeter, *Resolve*, which can measure X-ray energies to a resolution of 5-10eV (more than a factor of 10 greater than *Chandra*, for instance) [313; 312]. The future of X-ray astronomy is promising; high energy resolution translates

[5]Whilst this discussion is focused on stellar mass black holes, observations of super-massive black holes began with Seyfert galaxies [259].

[6]Quiescence here is a relative term, since even faint LMXBs are some of the most luminous X-ray sources in the Galaxy.

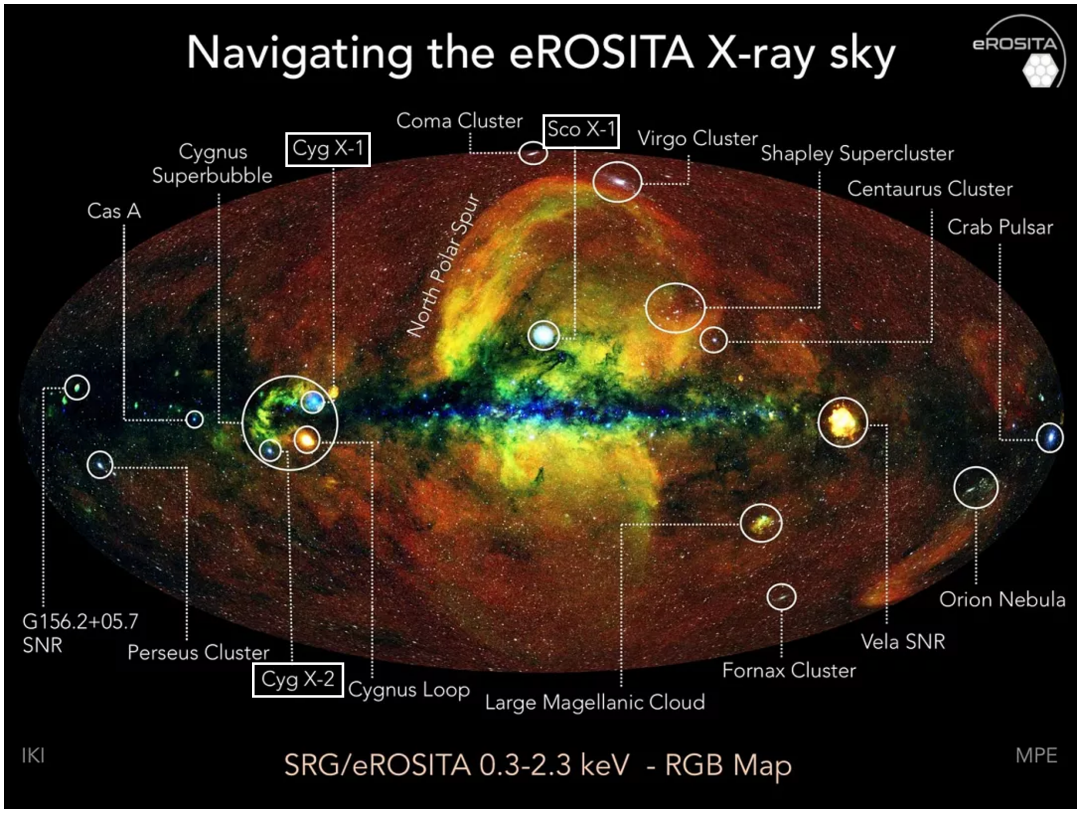

Figure 1.6: **The X-ray Universe, as seen by *eROSITA***: *eROSITA* (extended ROentgen Survey with an Imaging Telescope Array) is the primary instrument on the Spectrum-Roentgen-Gamma (SRG) mission (0.1-10 keV). This image (from eROSITA All-Sky Survey DR1 [203]) shows the number of X-ray sources within the universe; the X-ray binaries Cyg X-1 (BH), Cyg X-2 (NS), and Sco X-1 (NS) are highlighted with white boxes.[Image credit: Jeremy Sanders, Hermann Brunner, Andrea Merloni, and the eSASS team (MPE); Eugene Churazov, Marat Gilfanov (on behalf of IKI)].

to high velocity resolution and, in our dynamic universe, this is sure to unearth a plethora of information on the nature of black holes.

1.6.2 Optical surveys and spectroscopy

If black holes remain coupled to an ordinary luminous star, the latter may be used to infer the existence and properties of the black hole. Stellar spectra carry the signatures of the orbital motion of the companion star around the black hole, observed as variations in the wavelength of known emission and absorption features (à la the Doppler effect). These orbital motions provide constraints on the mass of the black hole, and other characteristics of the binary (e.g. orbital period) (see Equation 1.9 & Figure 1.4) [e.g. 54]. Observations of these luminous stars are typically conducted in the optical or infrared

wavebands, as these have the advantage of penetrating the Earth's atmosphere and being visible from ground-based observatories.

Relying on spectra from the luminous companion means these techniques are viable for non-interacting systems (i.e. where there is no mass transfer between a black hole and its companion star and the system is, therefore, quiet in X-ray). Leading observatories include the Very Large Telescope (VLT - Chile) and The Keck Observatory (Hawaii).

Additionally, photometric data (e.g. in the ASAS-SN Catalogue [166]), can be a useful tool in identifying binaries, particularly those with high inclinations, due to elliptical variations in the light curves. Optical surveys such as LAMOST [69] may be used in tandem with photometric surveys to identify binaries hosting compact objects [319].

1.6.3 Astrometric measurements

First carried out in the radio waveband [67], astrometry is the science of measuring the positions and motions of astronomical objects. The key parameters are: parallax, ω, (the angular shift in position due to the motion of an observer (i.e. the Earth), from which one can derive distance ($d = 1/\omega$, where d is measured in parsecs and ω is measured in arcseconds)); position, defined by right ascension α (RA) and declination δ (Dec); proper motions, both the RA & Dec components, μ_α & μ_δ; and systemic radial velocity γ (along the line of sight).

The standard model of stellar motion [80; 47] described the trajectory of a star travelling through our Galaxy, expressed linearly as:

$$\vec{b}(t) = \vec{b}_0 + t\vec{v} - t_0\vec{v} \tag{1.12}$$

where $\vec{b}$ is the star's barycentric position and $\vec{v}$ is the constant space velocity. t is, of course, time and $\vec{b}_0$ and t_0 are the reference position and time respectively. The peculiar velocities of compact objects are best constrained through astrometry (e.g. Figure 1.5 shows the proper motions of 89 Galactic X-ray binaries, from which one may calculate their peculiar velocity), and the spatial distribution of X-ray binaries has been deemed the result of natal kicks [100; 154] (and also cited as a potential bias when understanding the mass distribution of black holes [154]). Additionally, the motion of luminous stars can be tracked using astrometry, and any deviations from the expected behaviour of isolated stars can act as a smoke signal for a more exotic system, perhaps those containing a compact object which is not interacting with its associated star.

The *Hipparcos* mission provided the first major catalogue of astrometrically measured stars, with over a million sources [80; 188; 134]. The success of optical astrometry over radio led to the development of the renowned *Gaia* mission (for further details, see Section 3.2).

1.6.4 Microlensing

Whilst still in its infancy, microlensing is expected to become a powerful means of identifying black holes. Microlensing occurs due to the occultation of a luminous star by a black hole (the lens) resulting in a characteristic increase in luminosity [113]. Microlensing as a technique is best suited to long-term observations; upcoming optical missions, including the ongoing surveys using TESS [246] and LSST [287], will provide a wealth of information on Galactic transients and variable objects. These surveys are expected to uncover hundreds to potentially thousands of black holes, many of which may be viable for additional follow-up with other techniques [302; 322].

The Nancy Grace Roman Telescope [115], scheduled for launch in 2027, aims to use microlensing to identify exoplanets, but is also well-suited for searches for black holes in widely separated binaries [102]

1.6.5 Gravitational waves

Beyond the electromagnetic spectrum, gravitational wave astronomy has become a hugely powerful means of studying black holes. This September (2025) marks 10 years since the first observation of a binary black hole merger by LIGO/Virgo [183], and the field has developed rapidly since. LIGO/Virgo/Kagra have since detected dozens of gravitational waves associated with compact objects [187]. Relying on laser interferometry (where imperceivable changes in the gravitational field result in the length contraction of the interferometers, measurable by a reflecting light beam) [180], observed gravitational waveforms can be used to determine the masses and spins of the associated black holes, and there is a great deal of research into what other information that may be encoded in the waveforms

In the 2030s, the Laser Interferometer Space Antenna (LISA) [181] promises to further revolutionise the field, able to study hundreds more black holes, including populations that are as yet undetectable. Gravitational waves provide a unique opportunity to study black holes at later stages of their evolution and act as a laboratory for tests of General Relativity.

1.6.6 Union of theory and observation

Access to such a rich wealth of data means theoretical studies of black holes are now supported (or limited, depending on your point of view) by observational evidence. There are of order 300 Galactic X-ray binaries that have been identified, a few dozen of which harbour black holes [87; 88], and a growing sample of non-interacting black holes. Compared to the complexity and variability of these systems, these populations are relatively small. Consequently, there remains much to be understood about the characteristics, evolution, and populations of black holes, within our Galaxy and beyond.

1.7 Thesis Outline

In this thesis, I will describe how the most cutting-edge data may be used to further develop and constrain our understanding of black hole evolution.

Given the importance of natal kicks in determining various aspects of black hole evolution, Chapter 2 uses state of the art astrometry to investigate the natal kicks applied to Galactic X-ray binaries. It has long been assumed that black holes receive smaller/negligible kicks compared to neutron stars, with typical magnitudes for each class differing by more than an order of magnitude. To test whether this theory prevails and given the updated astrometric measurements of compact objects, I determine the possible natal kicks for 68 Galactic X-ray binaries, comprising both neutron stars and black holes. I detail the comprehensive binary population synthesis used in tandem with ab initio descriptions of the influence of natal kicks on a system's parameters to understand its history and formation. This methodology improves upon previous studies in various ways, notably that the work does not rely solely on present-day space velocities.

The results show that the natal kick distributions of black holes and neutron stars are extremely similar and formally indistinguishable, at least for Galactic compact accreting binary systems. I propose that black holes can receive large natal kicks and that kicks for all remnant types are consistent with being drawn from a common distribution, with no strong dependence on remnant mass.

These results demonstrate that similar physics drives kicks, irrespective of remnant type and suggest an as yet unidentified evolutionary channel in which both classes of system receive moderate natal kicks. I discuss the implications of this result in the context of supernova physics and the inferences that can be made regarding the physical drivers of these natal kicks. Additionally, the consequences of strong natal kicks being applied to

black holes are investigated in the context of gravitational wave astronomy. If double compact objects suffer similar kicks, these results will improve merger rate predictions for gravitational wave detectors. I find that, perhaps counterintuitively, merger rates do not scale down monotonically with natal kick, likely due to enhanced mergers in highly perturbed and eccentric systems.

Chapter 3 concerns the newly emerging field of non-interacting black holes; I outline the discovery (and controversy) surrounding Gaia BH1, the first astrometrically identified non-interacting black hole, and give an overview of the plausible evolutionary pathways (and the associated inconsistencies with observations). Thereafter, I searched the *Gaia* catalogue for systems that resemble Gaia BH1 in order to identify other non-interacting black holes. Deriving the radial velocity curves of 6 candidate black holes, using high-resolution optical spectra, show that these systems are better characterised as ordinary stellar binaries. The astrometric solutions presented in *Gaia* DR3 are inconsistent with observations, and I discuss the repercussions of this, in terms of systems which have already been identified, and those which remain undetected.

In Chapter 4 I explore the potential of advanced X-ray spectrometers to constrain the mass function of the compact object in X-ray binaries. Fe K line fluorescence is a common feature in the spectra of luminous X-ray binaries, with a Doppler-broadened component from the inner accretion disc extensively studied. If a corresponding narrow line from the X-ray irradiated companion can be isolated, this provides an opportunity to further constrain the binary system properties. Here, I model binary geometry to determine the companion star's solid angle and deduce the iron line's equivalent width, finding that for systems with a mass ratio $q > 0.1$, the expected Kα equivalent width is 2–40 eV. Simulations using `XSPEC` indicate that new microcalorimeters, such as *XRISM*'s *Resolve* will have sufficient resolution to be able to produce Kα emission line radial velocity measurements with precision of 5–40 $\mathrm{km\,s^{-1}}$. The caveats to this are identified and explained, the primary one being that this method is dependent on the successful isolation of the narrow line from the broad component, and the observation of clear changes in velocity independent of scatter arising from complex wind and disc behaviour.

Despite this method remaining untested, there is huge potential to apply it to bright X-ray sources, thereby expanding the sample of well-measured black hole masses to include binaries for which optical and infrared measurements are not viable.

Finally, Chapter 5 provides a summary, detailing the progress that has been made, and areas suitable for further research.

Chapter 2

Interpreting the velocities of compact objects

Despite sometimes appearing as a great and dark void, our Galaxy is a dynamic, ever-changing entity. This constant motion is the result of innumerable complex and multi-layered mechanisms, which, if understood, offer insight into the fundamental physics that drives the universe.

In this Chapter, the high-precision astrometry provided by *Gaia* (see Section 1.6.3 and, for further detail, Section 3.2) is used in tandem with the most up-to-date system parameters for Galactic compact objects (specifically those in X-ray binaries) to infer the natal kicks imparted at formation. Applying the same methodology, including detailed population synthesis and a thorough description of the impact of natal kicks on a system, to both neutron stars and black holes means any discrepancies are likely to be genuine, rather than the result of different analytical approaches.

There appears to be no statistically significant difference in the distributions of natal kicks applied to black holes compared to neutron stars. The natal kicks applied to each type of compact object span similar ranges, and can be well-described with a gamma distribution with mean $147\,\mathrm{km\,s^{-1}}$. The distribution of natal kicks applied to compact objects provides crucial information on the plausibility of formation mechanisms, and the implications of the results presented here are discussed in Section 2.2. Crucially, there is evidence for a formation channel resulting in moderate to large natal kicks being applied to black holes, which is currently at odds with hydrodynamic simulations.

2.1 Constraining natal kicks

2.1.1 The sample of compact objects

As outlined in Section 1.5, the peculiar velocity of astronomical objects has been studied for decades. Pulsars have been identified as a class of objects that often have high peculiar velocities, of order hundreds $\mathrm{km\,s^{-1}}$. This has been cited as evidence that neutron stars are subject to strong natal kicks (an additional impulse imparted to the compact object upon its formation). Whether black holes experience the same natal kicks, however, is more contentious. Whilst studies of high velocity pulsars (and other neutron stars) are numerous [e.g. 189; 66; 125; 284; 133], investigations into the peculiar velocity of black holes are less extensive; a handful of studies have been conducted for individual systems [e.g. 303; 90; 308; 161; 70], and only a few studies consider samples of black holes [e.g. 245; 211].

Each of these studies employs a range of methodologies to examine and explain the peculiar velocities of compact objects, meaning a thorough comparison between neutron stars and black holes is subject to extensive caveats. Additionally, the present-day peculiar velocity of a compact object is often used as a proxy for the velocity of any natal kick, neglecting the influence of mass-loss during the supernova (SN) and the varying characteristics of each system. For example, it is elementary that a more massive system will achieve a smaller velocity when subject to the same force (i.e. natal kick) as a smaller system.

Zhao et al. [318] (hereafter referred to as Zhao23) compiled a catalogue of 89 Galactic compact objects (both neutron stars and black holes) and their peculiar velocities, derived from the most up-to-date astrometry from *Gaia* DR3. Present-day peculiar velocities were calculated following the method presented by Reid et al [240]. Additionally, estimates of birth peculiar velocity were calculated by tracing the systems motion through the Galaxy and identifying the peculiar velocity of the system when it crossed the Galactic plane - the idea being that, if systems were formed in the Galactic plane, this provides a better estimate of birth peculiar velocity, as they have not been subject to deceleration due to the Galactic potential [72]. However, given that this is subject to the assumption of formation within the Galactic plane[1], and the fact that older LMXBs may have experienced multiple plane crossings over their history, the peculiar velocities used in this study are those from

[1]Although, Brandt and Podsiadlowski [30] report that the spatial distribution of X-ray binaries is in good agreement with models assuming formation in the Galactic plane, and does not require a population of progenitors existing at greater scale heights.

the present day. These values are, in all cases, lower than estimates from Galactic plane crossings, meaning inferences on natal kicks are, broadly speaking, more conservative. Presenting evidence for an anti-correlation between the peculiar velocity and total system mass, Zhao23 proposed that peculiar velocities are consistent with a two-component Maxwellian distribution ($\sigma_1 = 23 \pm 3\,\mathrm{km\,s^{-1}}$ & $\sigma_2 = 107 \pm 10\,\mathrm{km\,s^{-1}}$)

One source of post-SN velocity is symmetric mass-loss [214], where mass is instantly ejected from the compact progenitor by the supernova, resulting in a recoil kick to the system. Considering this in tandem with Kepler's laws, one can derive an expression for the velocity imparted to the binary system:

$$\upsilon_{\mathrm{MLK}} = 213 \times \frac{m}{M_\odot}\frac{\Delta M}{M_\odot}\left(\frac{P_{\mathrm{circ}}}{\mathrm{day}}\right)^{-\frac{1}{3}}\left(\frac{M_{\mathrm{tot}}}{M_\odot}\right)^{-\frac{5}{3}}\mathrm{km\,s^{-1}}, \tag{2.1}$$

where m and M_{tot} are the luminous companion and post-SN total system masses, ΔM is the mass lost from the compact object progenitor due to SN, and P_{circ} is the post-SN circularised orbital period (see Appendix A for derivation).

Equation 2.1 yields an estimate of the post-SN velocity of a system purely perturbed by symmetric mass loss, subsequently referred to as the mass-loss kick velocity (υ_{MLK}). These are sometimes referred to as Blaauw kicks [24]. Comparing these to the peculiar velocities yields an estimate of the natal kicks (or, the very least, provides an inference on the extent to which an additional source of momentum is necessary).

Using the calculations presented by Nelemans et al. [214], one can estimate the magnitude of the systemic velocity that would result from the mass-loss kick for each of their systems, and compare this to the observed peculiar velocity, in order to identify systems for which mass-loss alone was insufficient to explain the systemic velocity. These systems may therefore have received a non-zero natal kick (though the mechanisms associated with these kicks remain ambiguous).

High natal kick candidates can be identified as follows. For each binary, the maximum velocity associated solely with mass-loss (υ_{MLK}) can be estimated and compared to the calculated υ_{pec}. From the virial theorem, it follows that a system that loses more than half its total mass due to the supernova will be disrupted; therefore the present-day M_{tot} of the system provides an upper limit of ΔM. Provided there has been no significant change in P_{orb} due to mass transfer, magnetic braking, etc., P_{circ} may be substituted by P_{orb}.

Where systems have a υ_{pec} higher than υ_{MLK}, it can be inferred that an additional source of momentum may have been imparted — an additional kick related to mechanisms

other than instantaneous mass ejection. Figure 2.1 shows the estimated $v_{\rm MLK}$ compared to the measured $v_{\rm pec}$ for the Zhao23 sample.

However, the above calculation provides only *estimates*, based on broad assumptions about supernovae progenitors. Whilst these estimates are a good litmus test for systems that may require additional kicks, they are far from rigorous. In practice, there are usually many viable progenitors for any particular combination of present-day peculiar velocity and binary parameters. That is, the observed properties of a compact binary system permit a *range* of kick velocities. In order to infer the true kick velocity distribution, it is necessary to determine this range for each observed system. This requires the combination of accurate and precise observations with theoretical binary evolution models.

Here, detailed population synthesis is carried out to identify evolutionary channels and progenitor properties of all interacting objects included in the Zhao23 catalogue (with the addition of the newly dynamically confirmed black hole system Swift J1727.8–162 [252]). The aim is to use the observational constraints of known compact object systems, including their peculiar velocities, to constrain their evolutionary histories and the magnitude of any natal kicks they may have received. Whilst a number of previous studies have studied the natal kicks of individual systems or populations of pulsars, this is the first study of a large sample of compact object binaries *including both neutron stars and black holes*.

There are 89 compact object binaries presented in Zhao23; of these, 9 are non-interacting systems & 8 do not have well-constrained companion masses or orbital periods. There are 4 pulsars and 1 NS-LMXB for which constraints on their formation history are indeterminate; J1431–4715; J1622–0315; J1628–3205; J2039–5617; & Ser X–1. These systems have the lowest total mass within the sample; each hosts a neutron star and a sub-solar companion, $0.1 \leq M_2 \leq 0.2\,{\rm M}_\odot$, with orbital periods 2–12 hours. These systems proved difficult to replicate through standard population synthesis channels - likely due to their low system mass and low mass ratio (0.05–0.15) making it more difficult for them to survive mass-transfer & common envelope intervals without merging.

Population synthesis identifies the likely evolutionary history of the 67 remaining interacting compact objects, alongside the newly characterised black hole LMXB, Swift J1727.8–0127 [252]. The final sample comprises: 20 black holes in X-ray binaries (15 BH-LMXB & 5 BH-HMXB); 33 neutron stars in X-ray binaries (14 NS-LMXB & 19 BH-HMXB); and 15 neutron star pulsars (14 NS-LM-PSR & 1 NS-HM-PSR) (see Table 2.1). For a detailed discussion of the sample, observational and astrometric measurements, selection effects, and peculiar velocity calculations, see Zhao23. With a total sample

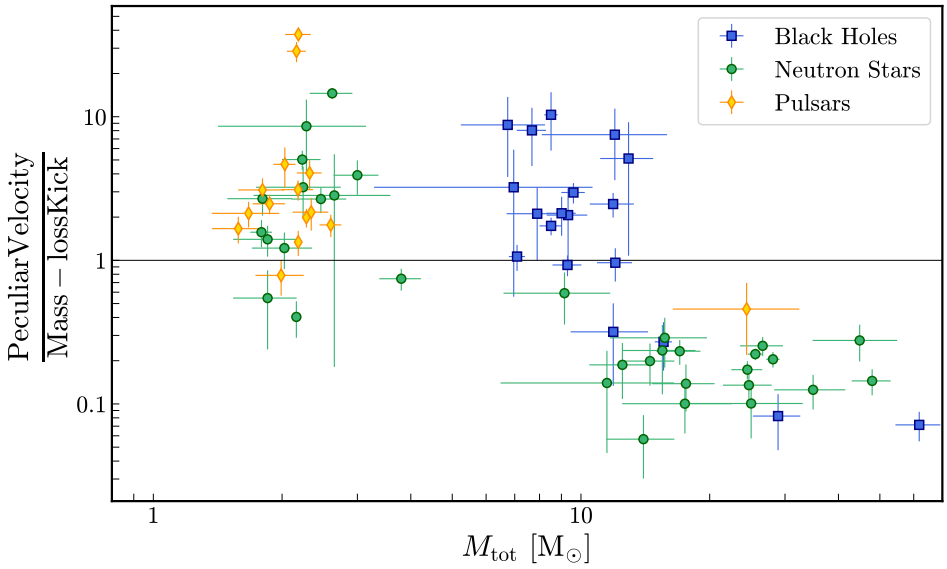

Figure 2.1: **Observed peculiar velocity compared to estimated mass loss kick**: Ratio between present-day system velocity and estimated mass-loss kick velocity as a function of total system mass for Zhao23 sample. Coloured markers indicate 68 systems for which there are synthesised populations, their types distinguished by marker shape and colour (blue circles: black holes, green squares: neutron stars, orange diamonds: pulsars).

	High mass	Low Mass	Total
Black Holes	5	15	20
Neutron Stars	19	14	33
Pulsars	1	14	15
Total	40	28	

Table 2.1: **System types:** Summary of the compact object systems used in this study, differentiated based on compact object type and the nature of the companion star.

size of 68 systems, this study is the largest of its kind and the first to apply the same methodology, including detailed population synthesis, to neutron stars and black holes.

Comparing the characteristics of the black hole, pulsar, and neutron star populations within the sample shows no obvious systematic bias - i.e. each population spans a range of distances, orbital periods, companion mass, apparent magnitudes, and Galactic scale heights, with no evidence of populations being distinguished by anything other than their system classification (see Figure 2.2).

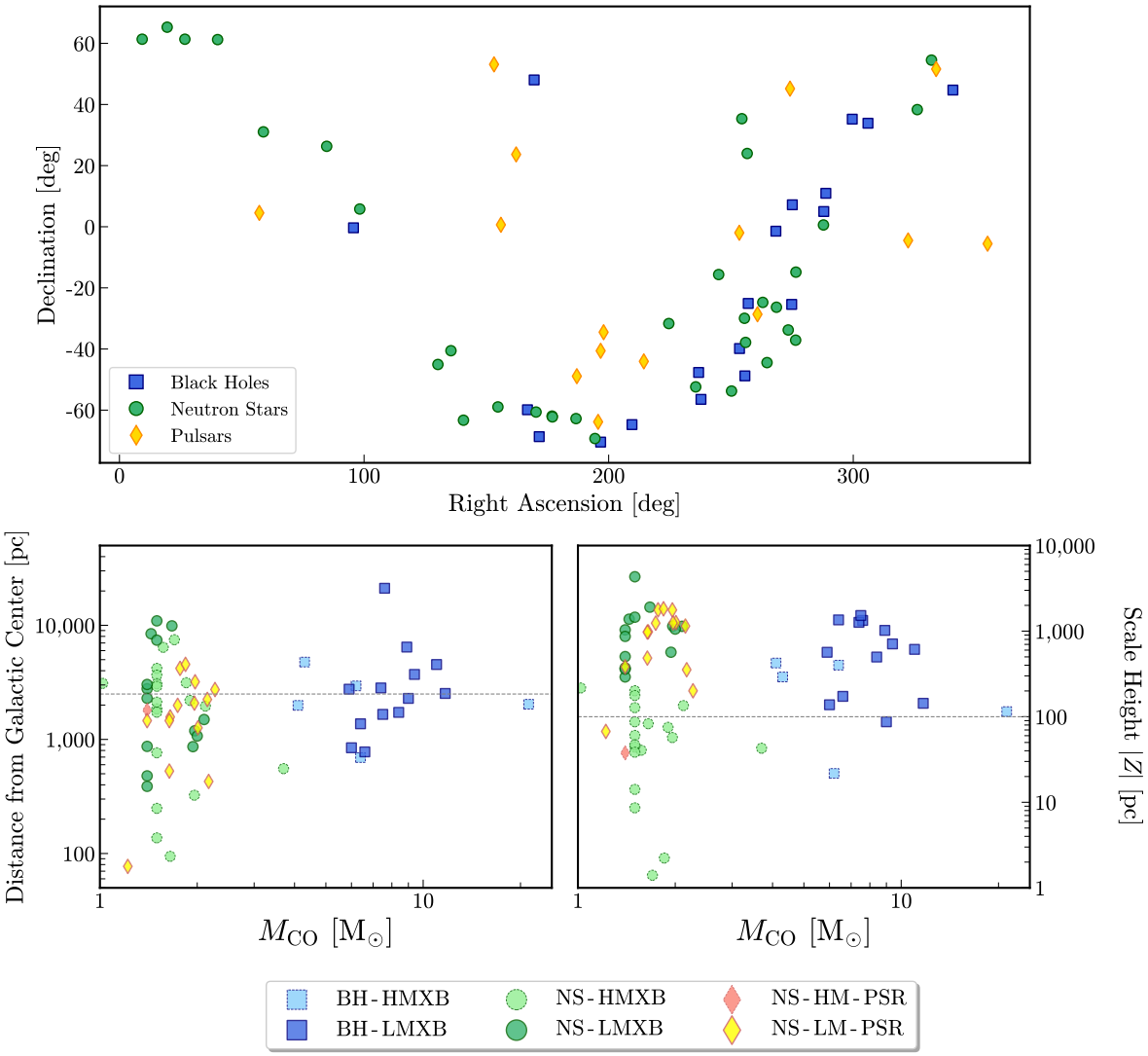

Figure 2.2: **Galactic locations of sample**: The sky position of each system (upper); the distance of each system from the Galactic centre (left); and its height above the Galactic plane (right). System types are distinguished by marker shape and colour (blue circles: black holes, green squares: neutron stars, orange diamonds: pulsars). No obvious distinction between neutron star and black hole populations - potential selection bias due to obscuration close to the Galactic plane is discussed in Section 2.1.8.

2.1.2 Population synthesis

Binary population synthesis provides a powerful means to understand the evolution and formation of compact objects within binaries. This relies on the assumption that isolated evolution is the dominant channel through which binaries form (i.e. systems were born in stellar binaries as opposed to existing for an undetermined amount of time as single stars before becoming coupled as the result of dynamical interaction (referred to as dynamical capture). However, the simulations are independent of the Galactic position, meaning formation outside of the Galactic plane (in a globular cluster for example) does not affect the results of simulations (although may affect inferences on natal kick velocities, as is discussed later in Section 2.1.8).

Compact Object Synthesis and Monte Carlo Investigation Code (`cosmic`) is a binary population synthesis code adapted from Binary Stellar Evolution code (`BSE`) to include modified and updated evolution prescriptions and parameters [34]. Synthesised populations were generated and analysed, to generate populations of binaries that evolve to resemble each system following the first supernova (i.e. with masses and orbital periods consistent with the observed values within 1-σ), referred to henceforth as 'system analogues' (for examples, see Table 2.2).

2.1.2.1 Assumptions & Prescriptions

The initial parameter space covered in the search for analogous systems is as follows: $0.5 \leq M_1 \leq 80\,\mathrm{M}_\odot$; $0.05 \leq M_2 \leq 80\,\mathrm{M}_\odot$; $10^{-3} \leq P_{\mathrm{orb}} \leq 10^4$ days. Factors such as differing descriptions of common envelopes & magnetic braking were kept constant in all simulations, using canonical estimates common in binary population synthesis. Given the complexity and uncertainty surrounding binary evolution, simulations for this study do not explore all possible evolutionary scenarios and formation channels.

Initial eccentricities for all systems were set at zero; this is a fair assumption given that tidal forces will act to circularise binaries quickly (within a few million years), particularly closely separated binaries such as these. Note that whilst evolutionary uncertainties such as common envelope efficiency, rates of mass-loss from stellar wind, and changes in P_{orb} associated with magnetic braking may all impact the evolution of simulated binaries, the focus of this study is the effect of kicks.

Stellar winds are modelled based on theoretical predictions of radiation-driven mass loss (where mass-loss rates scale with metallicity depending on temperature) and Luminous Blue Variable mass loss [296; 294]. Wind velocities and accretion rates are kept

consistent with those employed by `StarTrack`, as described in Belczynski et al.[18], and accretion rates are Eddington limited.

Descriptions of mass transfer are motivated according to the process used by Hurley et al. [138]. The critical mass ratio determining the onset of unstable mass transfer is consistent with standard BSE (Binary Stellar Evolution) codes and includes distinct conditions in the case of giant stars [138; 132].

The common envelope phase is based on the standard $\alpha\lambda$ model (as described in Section 1.2), characterised by an ejection efficiency parameter $\alpha = 1.0$. The binding energy factor, λ, is calculated following the method presented by Pols et al. [232]. Simulations consider mergers unavoidable in the case of unstable mass transfer, in which the core-envelope boundary is ill-defined (this is often considered a 'pessimistic' CE scenario). Magnetic braking (the loss of angular momentum due to the interaction between stellar material and magnetic fields) adheres to the prescription of Ivanova and Taam [141].

For comparative purposes, further simulations were carried out under different assumptions. Two other descriptions of stellar winds were employed: 1) the standard model used in BSE, presented in Hurley et al. [138], where winds are a function of stellar spectral type; 2) the prescription used in `StarTrack`, where mass-loss is a function of temperature & metallicity [18]. In additional sets of simulations, stellar metallicities were drawn randomly from 0.01–10 times solar metallicity, and eccentricities adhere to the distributions proposed by Sana et al. [251], where the the probability of a given eccentricity is $\mathrm{P}(e) \sim e^{-0.42}$.

The results of these simulations are largely consistent with the primary investigation. The main differences concern the likelihood of producing given systems, as well as the evolutionary timescales. The inferences made on natal kicks are robust to these changes, given that the properties of each system at the instant of supernova are similar across all simulations, as is the ejected mass.

For example: The ratio between a system's peculiar velocity and the estimated velocity due to the mass-loss kick indicates that H 1705-250 (amongst other systems) was likely subject to a strong kick upon formation - although as discussed, this is merely conjecture. Population synthesis supports a 'standard' binary evolution channel for H1705-250. The more massive component of the initial binary evolves, eventually breaching its Roche lobe and resulting in mass transfer; it then undergoes a core-collapse supernova, leaving behind a black hole. At SN, the black hole progenitor (a stripped Helium star) likely had

a mass of 9.25 – 11.5 $M_\odot$, and the companion had a mass of 0.25 – 0.45 $M_\odot$.

Simulations indicate that the compact progenitor loses $\sim 4\,M_\odot$ as a consequence of the supernova - 40% of its initial mass. Substituting this value into Equation 2.1 yields an improved estimate of the mass-loss kick, at $\upsilon_{\rm MLK} \approx 16\,{\rm km\,s^{-1}}$ (though the momentum imparted by mass-loss is treated fully when considering plausible natal kicks, see Section 2.1.8). It is apparent that the momentum imparted to the surviving system from the mass ejection in the H 1705-250 system cannot explain the high system velocity observed in isolation. An additional source of momentum, due to natal kick related to mechanisms other than mass ejection, is required.

On the other hand, in the case of IGR J00370+6122, an NS-HMXB, the magnitude of the estimated mass-loss kick is comparable to the observed peculiar velocity, and there is little reason to assume a natal kick *must* have been imparted upon formation. With a progenitor mass $M_{1,\rm i} \leq 2M_\odot$, the ejected mass lies in the range $0.14 \leq \Delta M \leq 0.73\,M_\odot$, and is unlikely to invoke a systemic velocity of more than $10\,{\rm km\,s^{-1}}$. Whilst this is smaller than initial estimates (as well as the nominal peculiar velocity), a natal kick is not required if one attributes the small discrepancy to an intrinsic Galactic dispersion.

Table 2.2: **Examples of the output of population synthesis**: The expected progenitor parameters and mass loss for 5 X-ray binaries within this sample. The estimated kick velocity associated purely with mass loss based on broad assumptions is indicated in comparison to those calculated from detailed population synthesis.

Name	Type	$\upsilon_{\rm pec}$ [$\rm km\,s^{-1}$]	$\upsilon_{\rm MLK,est}$ [$\rm km\,s^{-1}$]	$\frac{\upsilon_{\rm pec}}{\upsilon_{\rm MLK,est}}$	$M_{1,\rm i}$ [$M_\odot$]	$\mathrm{d}M$ [$M_\odot$]	$\langle\upsilon_{\rm MLK,sim}\rangle$ [$\rm km\,s^{-1}$]
Cyg X-1	BH-HMXB	22.3 ± 2.9	107 ± 5.1	0.2	19-25.9	0.5-2.9	3
H 1705-250	BH-LMXB	221.2 ± 109	24 ± 6.1	9.2	9.5-11.3	3.6-4.4	8
Her X-1	NS-LMXB	125.5 ± 10.9	66.5 ± 4.6	1.9	1.4-5.1	0.14-3.3	61
J00370	NS-HMXB	23.4 ± 8.1	21.8 ± 6.7	1.1	1.4-2	0.14-0.73	7
J1417-4402	NS-LM-PSR	98.5 ± 19	20.6 ± 1.9	4.8	2.3-3.7	0.6-1.6	6

2.1.3 Natal kick MCMC algorithm

The influence of a given natal kick on the binary system parameters is described as follows [30; 156; 138]:

$$\upsilon_{\rm sys}^2 = \left(\upsilon_{\rm NK}\,\frac{M_{\rm CO}}{M_{\rm CO}+M_2}\right)^2 + \left(\upsilon_{\rm r}\,\frac{M_2\,(M_1-M_{\rm CO})}{(M_1+M_2)\,(M_{\rm CO}+M_2)}\right)^2 \left(\alpha_S^2+\alpha_C^2\right) + 2\,\upsilon_{\rm NK}\,\upsilon_{\rm r}\,\frac{M_{\rm CO}M_2\,(M_1-M_{\rm CO})}{(M_1+M_2)\,(M_{\rm CO}+M_2)^2}\,(P+Q) \tag{2.2}$$

$$a_{\rm post-SN} = \left(\frac{2}{r} - \frac{\upsilon_{\rm NK}^2+\upsilon_{\rm r}^2-2\,\upsilon_{\rm NK}\,\upsilon_{\rm r}\,(P+Q)}{\rm G(M_{CO}+M_2)}\right)^{-1} \tag{2.3}$$

$$e_{\rm post-SN} = \sqrt{1-\frac{r^2\left((\upsilon_{\rm NK}{\rm sin}(\theta))^2+\upsilon_{\rm NK}{\rm cos}(\phi){\rm sin}(\theta)-(\upsilon_{\rm r}\,\alpha_S)^2\right)}{{\rm G}\,a_{\rm new}(M_{\rm CO}+M_2)}} \tag{2.4}$$

Here, $\upsilon_{\rm NK}$ and $\upsilon_{\rm r}$ are the natal kick vector and initial orbital velocity vector; $\alpha_S = \sqrt{\frac{a^2(1-e^2)}{r(2a-r)}}$; $\alpha_c = -\frac{e\,{\rm sin}(M)}{\sqrt{1-e^2\,{\rm cos}(M)^2}}$; $P = {\rm cos}(\phi)\,{\rm cos}(\theta)\alpha_s$; $Q = {\rm sin}(\phi)\,{\rm cos}(\theta)\alpha_c$. The polar angle θ refers to the angle between the natal kick and the orbital plane, and the azimuthal angle ϕ denotes the angle between the direction of motion of the progenitor star and the natal kick vector. M_1, $M_{\rm CO}$ & M_2 denote the masses of the compact object progenitor, the compact object, and the companion star, respectively. a refers to the semi-major axis at the instant of supernova, r refers to the binary separation at the instant of supernova (i.e. $r = a\,[1-e\,{\rm cos}(M)]$), e and M are the initial eccentricity and eccentric anomaly, θ and ϕ describe the direction of the kick. For full derivation, see Appendix B.

For each of the 68 simulated systems, 2000 simulated analogues were drawn (specifically focusing on their binary parameters at the time of the supernova). Each of these simulated binaries is then subject to various kicks, encompassing a range of magnitudes and directions, and the resultant systemic velocity, orbital separation, and eccentricity are calculated. By comparing these values to those observed, one can determine if a given natal kick is plausible. When considering the observed peculiar velocity, an assumed intrinsic Galactic dispersion velocity of $40\,{\rm km\,s^{-1}}$, (based on observations of late type stars) is subtracted in quadrature from the nominal value, to account for system velocities not associated with natal kicks (e.g. perhaps due to interactions with other celestial bodies, or perturbations in the Galactic potential).

Each of the 2000 binaries drawn from these simulations is subject to 2500 kicks, uniformly spaced between $0 \leq \upsilon_{\rm NK} \leq 1000\,{\rm km\,s^{-1}}$, and for each of these magnitudes, a natal kick is directed in 50 random directions (i.e. random configurations of θ & ϕ drawn from a uniform distribution between $-1 \leq {\rm cos}(\theta) \leq 1$ and $0 \leq \phi \leq 2\pi$). This means each simulated binary undergoes 125,000 different kicks, and each of the 68 systems is subject

to 250 million test runs. These kicks are agnostic to the underlying physical mechanisms and are intended to maximise coverage of parameter space.

A kick is determined to be plausible if; 1) the system survives supernova (i.e. is neither disrupted nor merged); 2) the resultant systemic velocity is consistent with the observed peculiar velocity (once Galactic dispersion velocity is subtracted) within the errors quoted in Zhao23; 3) the resultant masses and orbital period are consistent with those observed, within 10%. Consistent errors for masses and orbital periods are used to avoid potential bias introduced by differing observational uncertainties between systems (for example, errors in compact object mass range $0.01 \leq \frac{\sigma_{M_1}}{M_1} \leq 0.6$).

Subtracting an assumed intrinsic Galactic dispersion velocity ensures that any scatter in stellar velocities not associated with natal kicks is accounted for (for example, the velocity of systems that formed within stellar clusters may be partially attributed to the peculiar velocity associated with those clusters, as is seemingly the case for Cyg X–1 [237]). These natal kicks are, in general, lower limits - for example, the minimum natal kick Cyg X–1 could have received is calculated as $36\,\mathrm{km\,s^{-1}}$ when considering its nominal peculiar velocity of $22^{+4.6}_{-2.9}\,\mathrm{km\,s^{-1}}$, but the system could have formed without a natal kick if its systemic velocity is due to an intrinsic velocity dispersion of objects within the Galactic disc.

In practice, the stellar dispersion velocity is a function of Galactic location. Where the velocity dispersion of the Galactic disc is $\sim 40\,\mathrm{km\,s^{-1}}$ [52], the dispersion in the Galactic halo is larger: 50–$120\,\mathrm{km\,s^{-1}}$ [14; 35]. When examining evidence for natal kicks in a sample of black holes, Nagarajan et al.[211] use the local stellar dispersion velocity for each system, quoting values from $40 < \mathrm{V_{68\%}} < 125\,\mathrm{km\,s^{-1}}$. Here, the Galactic dispersion velocity is the same for each system. This choice is justified given that the primary focus here is on the comparison between the kicks applied to black holes vs neutron stars - applying the same corrections to each system makes for a more meaningful direct comparison, however, it must acknowledged that the natal kick estimates for individual systems are subject to error based on this assumption. Within this sample, there is no obvious difference in Galactic location or scale height between the neutron star and black hole populations (see Figure 2.2), and, therefore, consistency between each system, whilst technically erroneous, is arguably more appropriate for the nature of this study. Additionally, whilst $40\,\mathrm{km\,s^{-1}}$ describes the velocity distribution of late-type stars, this may be an over-estimate for the velocity dispersion for compact objects, which may have been slowed due to interactions with other celestial bodies and the interstellar medium.

Table 2.3 summarises the results for 63 out of 68 systems.

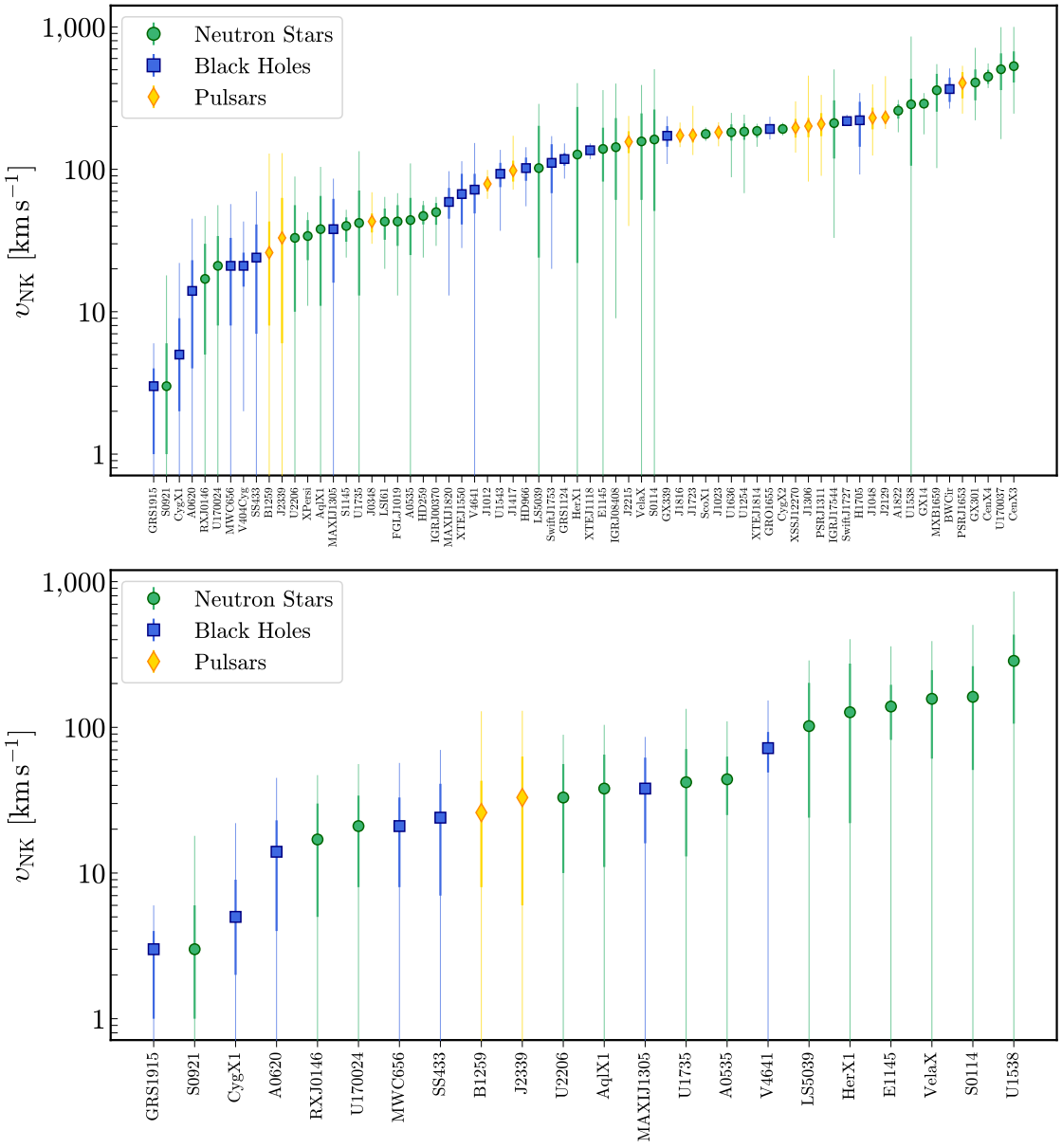

Figure 2.3: **Individual natal kick constraints**: Natal kick magnitudes for all 68 systems (upper panel) and those that can form without a natal kick (lower panel). Marker indicates mean value, solid error bars indicate 68% confidence intervals (ETI), pale errorbars indicate minimum & maximum values. The nature of the compact object is indicated by the colour & marker shape (blue squares: black holes, green circles: neutron stars, orange diamonds: pulsars).

2.1.4 Systems with irreproducible systemic velocities

The results for the remaining 5 systems are presented in Table 2.4. The evolutionary pathways for each of these systems have been successfully identified, as well as the natal kicks which would result in the observed masses, orbital period, and eccentricity; however, no natal kicks could replicate the observed peculiar velocity (corrected for Galactic dispersion). Therefore, plausible natal kicks are defined as those that would result in the observed orbital period, eccentricity, and a systemic velocity $v_{\rm sys} \leq 40\,{\rm km\,s^{-1}}$.

These systems are; HD 97760; IGR J08408–450; MWC 656; 2S 0114+650; 4U 1700+24. Given that this group includes both black holes & neutron stars, high-mass & low-mass systems, their inclusion is unlikely to significantly affect inferences on populations and the primary findings of this work. The fact that these systems prove difficult to explain may be attributed to the fact that the present-day observed peculiar velocity (or indeed, the inferred peculiar velocity when the system crossed the Galactic disc) may not be equivalent to the systemic velocity imparted upon formation.

It should be noted that the mass of MWC 656 is controversial; whilst this sample is based on an unseen companion mass of $4.1\,{\rm M_\odot}$ [56] it has been suggested this system does not host a black hole, but rather a neutron star or white dwarf, with mass $< 2.4\,{\rm M_\odot}$ [147] - this may explain the difficulties in successfully explaining the evolutionary history.

Table 2.3: **Natal Kick Constraints:** Natal kick constraints for 63 compact objects based on uniform priors, including the mean mass-loss-kick, the minimum and mean allowed natal kick magnitudes, and the 68% confidence intervals (ETI). All velocities are in $\rm km\,s^{-1}$.

Name	Type	$v_{\rm pec}$	$v_{\rm MLK}$	$v_{\rm NK}$		
				Min	Mean	68%
1A 0535+262	NS-HMXB	45 ± 4	18	0	44	25 - 63
1E 1145.1–6141	NS-HMXB	56 ± 10	33	0	139	82 - 196
2A 1822–371	NS-LMXB	254 ± 33	32	182	258	227 - 286
2FGL J1019.0-5856	NS-HMXB	31 ± 3	3	13	43	29 - 56
2S 0921–630	NS-LMXB	38 ± 7	4	0	3	1 - 6
2S 1145–619	NS-HMXB	16 ± 4	1	24	40	31 - 46
4U 1254–69	NS-LMXB	155 ± 18	36	68	184	161 - 210
4U 1538–52	NS-HMXB	77 ± 10	45	0	286	106 - 433

4U 1543–475	BH-LMXB	99 ± 15	28	37	93	75 - 111
4U 1636–536	NS-LMXB	165 ± 13	35	88	182	159 - 207
4U 1700–37	NS-HMXB	71 ± 11	43	163	504	360 - 652
4U 1735–444	NS-LMXB	60 ± 31	32	0	42	13 - 71
4U 2206+543	NS-HMXB	28 ± 4	4	0	33	10 - 56
A 0620–00	BH-LMXB	44 ± 7	15	0	14	4 - 23
Aql X–1	NS-LMXB	42 ± 12	8	0	38	11 - 65
B1259–63	NS-HM-PSR	25 ± 8	2	0	26	8 - 43
BW Cir	BH-LMXB	352 ± 99	11	267	366	297 - 442
Cen X–3	NS-HMXB	102 ± 4	54	246	530	407 - 673
Cen X–4	NS-LMXB	419 ± 69	15	372	447	398 - 500
Cyg X–1	BH-HMXB	22 ± 3	3	0	5	2 - 9
Cyg X–2	NS-LMXB	164 ± 9	13	173	192	185 - 200
GRO 1655–40	BH-LMXB	162 ± 6	35	162	192	182 - 201
GRS 1124–684	BH-LMXB	119 ± 15	7	86	118	106 - 130
GRS 1915+105	BH-LMXB	32 ± 15	0	0	3	1 - 4
GX 1+4	NS-LMXB	189 ± 8	22	176	289	272 - 310
GX 301–2	NS-HMXB	58 ± 4	23	221	407	305 - 503
GX 339–4	BH-LMXB	166 ± 35	22	109	172	144 - 201
H 1705–250	BH-LMXB	221 ± 109	8	92	221	144 - 298
HD 259440	NS-HMXB	10 ± 3	1	24	47	41 - 56
Her X–1	NS-LMXB	125 ± 11	61	0	127	22 - 274
IGR J00370+6122	NS-HMXB	23 ± 8	7	29	50	40.76 - 58
IGR J17544–2619	NS-HMXB	44 ± 4	10	33	211	119 - 305
J0348+0432	NS-LM-PSR	62 ± 12	14	30	43	36 - 49
J1012+5307	NS-LM-PSR	84 ± 12	3	62	79	70 - 89
J1023+0038	NS-LM-PSR	131 ± 6	25	145	182	169 - 194
J1048+2339	NS-LM-PSR	158 ± 35	26	125	230	191 - 271
J1306–4035	NS-LM-PSR	121 ± 17	24	82	201	168 - 230
J1311–3430	NS-LM-PSR	109 ± 16	27	90	208	171 - 248
J1417–4402	NS-LM-PSR	99 ± 19	6	72	98	82 - 115
J1653–0158	NS-LM-PSR	178 ± 9	49	246	404	315 - 481
J1723–2837	NS-LM-PSR	110 ± 11	18	126	174	154 - 192

J1816+4510	NS-LM-PSR	165 ± 26	3	143	173	154 - 193
J2129–0429	NS-LM-PSR	201 ± 24	12	192	232	209 - 252
J2215+5135	NS-LM-PSR	118 ± 17	26	40	156	130 - 185
J2339–0533	NS-LM-PSR	64 ± 13	23	0	33	6 - 63
LS 5039	NS-HMXB	88 ± 3	64	0	102	24 - 202
LS I +61 303	NS-HMXB	9 ± 4	3	20	43	32 - 53
MAXI J1305–704	BH-LMXB	58 ± 22	8	0	38	16 - 62
MAXI J1820+070	BH-LMXB	72 ± 16	10	13	59	45 - 74
MXB 1659–298	NS-LMXB	260 ± 204	30	102	359	254 - 468
RX J0146.9+6121	NS-HMXB	12 ± 4	1	0	17	5 - 30
Sco X–1	NS-LMXB	168 ± 10	16	158	177	168 - 186
SS 433	BH-HMXB?	44 ± 16	40	0	24	7 - 41
Swift J1727.8–1613	BH-LMXB	207 ± 7	21	201	218	211 - 224
Swift J1753.5–0127	BH-LMXB	110 ± 57	16	20	111	68 - 150
V404 Cyg	BH-LMXB	45 ± 3	4	2	21	15 - 26
V4641 Sgr	BH-HMXB	92 ± 7	37	0	72	49 - 93
Vela X–1	NS-HMXB	59 ± 7	39	0	157	61 - 247
X Persi	NS-HMXB	18 ± 8	1	11	34	23 - 44
XSS J12270–4859	NS-LM-PSR	131 ± 21	21	131	196	167 - 226
XTE J1118+480	BH-LMXB	143 ± 11	5	118	136	128 - 144
XTE J1550–564	BH-LMXB	79 ± 32	1	28	67	41 - 93
XTE J1814–338	NS-LMXB	171 ± 51	26	144	186	167 - 200

2.1.5 Natal kick constraints

The output of modelling for each system, including the mean & minimum natal kick for each of the 68 systems (20 black holes [BH] & 48 neutron stars [NS]; 25 high-mass [HM] & 43 low-mass [LM]), are summarised in Tables 2.3 & 2.4 and Figure 2.3. These summarise plausible kicks for each system. Together with scatter in these estimates, these form the distribution of kicks as a whole (see Section 2.1.6).

Name	Type	$v_{\rm pec}$	$v_{\rm MLK}$	$v_{\rm NK}$		
				Min	Mean	68%
2S 0114+650	NS-HMXB	22 ± 2	11	0	98	26 - 172
4U 1700+24	NS-LMXB	39 ± 9	21	0	18	3 - 34
HD 96670	BH-HMXB?	24 ± 9	49	55	102	83 - 121
IGR J08408–4503	NS-HMXB	39 ± 5	33	9	143	61 - 229
MWC 656	BH-HMXB?	26 ± 13	25	0	18	6 - 30

Table 2.4: **Natal Kick Constraints:** Kick constraints for 5 compact objects based on uniform priors, including the mean mass-loss-kick, the minimum and mean allowed natal kick magnitudes, and the 68% confidence intervals (ETI). These values are based on scenarios in which the post-supernova systemic velocity does not exceed $v_{\rm sys} \leq 40\,{\rm km\,s^{-1}}$ (rather than using the observed peculiar velocity to provide constraints). All velocities are in $\rm km\,s^{-1}$.

Figures 2.3, 2.4, 2.5, & 2.6 show the natal kick constraints for all 68 objects in the sample. There is no identifiable correlation between the masses of the system (compact, companion, or total) and the magnitude of its natal kick (see Figure 2.7). That the magnitude of the natal kick does not appear to be related to the total system mass may raise suspicion, given that there is a correlation between observed peculiar velocity and total system mass [318], however, this is to be expected. The systemic velocity obtained by a system from a given natal kick has a strong dependence on both component masses (particularly the ratio between the companion mass and the total system mass - it is for this reason that many NS-HMXBs appear to be consistent with a broad range of natal kicks, spanning $> 100\,{\rm km\,s^{-1}}$ in some cases). This further highlights the limitations in using present-day peculiar velocity as a proxy for natal kick velocity (see Figure 2.8).

It is possible to constrain the direction of the natal kicks, with respect to the exploding progenitor star (see Figures 2.5 & 2.6). Here, the polar angle θ refers to the angle between the natal kick and the orbital plane, and the azimuthal angle ϕ denotes the angle between the direction of motion of the progenitor star and the natal kick vector (projected onto the orbital plane). In the case of black hole systems, both the azimuthal and polar angles of the natal kicks are uniformly distributed (i.e. there appears to be no strong preference for particular kick directions), however, neutron star systems show a strong preference for kicks aligned with the orbital plane. The preference for natal kicks to be closely aligned with a binary's orbital plane was also demonstrated by Kotko et al. [170]. 60% of neutron star systems have $|\cos\phi| \geq 0.75$, compared to just 35% for black holes. Given that these natal kicks span a range of magnitudes, this cannot be explained by the relationship between kick direction and magnitude. The relative impact of the direction of a natal

kick is related to the component masses and is greater for systems with lower compact object and progenitor mass. Whether this is sufficient to explain the stark contrast in the distribution of natal kick angles is unclear - it may be that the *direction* of natal kicks is substantially different for black hole systems vs neutron star systems (i.e. higher mass vs lower mass progenitors).

2.1.5.1 Negligible natal kicks

At least 23 Galactic X-ray binaries may have formed without a natal kick: 8 black holes and 15 neutron stars - a substantial fraction of each population. The mean peculiar velocities of these systems range from 12–92 $\mathrm{km\,s^{-1}}$, but simulations show that their kinematics can be accounted for, or at least moderated, by the known Galactic velocity dispersion of 40 $\mathrm{km\,s^{-1}}$ for field stars [52] and their mass-loss kicks ('Blaauw' kicks). These mass-loss kicks have magnitudes up to 60 $\mathrm{km\,s^{-1}}$, and their properties are described individually in Table 2.5 at the end of this chapter.

Whilst neutron star formation is often associated with significant natal kicks, that some neutron stars may have formed without any meaningful kick has been demonstrated in previous studies [e.g. 140; 221]. Additionally, evidence of neutron star-neutron star mergers in stellar clusters may imply small natal kicks, as larger kicks are more likely to have ejected the neutron stars from the cluster. The findings of this study reinforce the argument that strong natal kicks are not inherent to neutron star formation, and serve to further reduce evidence of dichotomous kick distributions between black holes and neutron stars.

A larger fraction of high-mass systems may have formed without a natal kick, as was proposed in Zhao23 - however, the mean natal kicks for many of these systems are still substantial. Only two pulsars, B1259–63 (PSR J1302–6350) and J2339–053, may have been formed without a natal kick - this is primarily due to the fact that their peculiar velocities are uncharacteristically low for pulsars (45 $\mathrm{km\,s^{-1}}$ & 64 $\mathrm{km\,s^{-1}}$ respectively). Furthermore, these statements are ultimately conservative assessments of the simulations, considering only the *minimum* natal kick required and do not necessarily indicate the most probable scenario (i.e. for 7 of these 24 systems (2 black holes and 5 neutron stars), fewer than 5% of kicks are less than 10 $\mathrm{km\,s^{-1}}$).

Despite the lack of any statistically significant correlation between natal kick magnitude and system mass, it is worth noting that the two most massive black holes in the sample (Cyg X-1 & GRS 1915+105) are subject to the smallest natal kicks of the black holes, and only rivalled by the NS-LMXB 2S 0921–630 when considering all compact

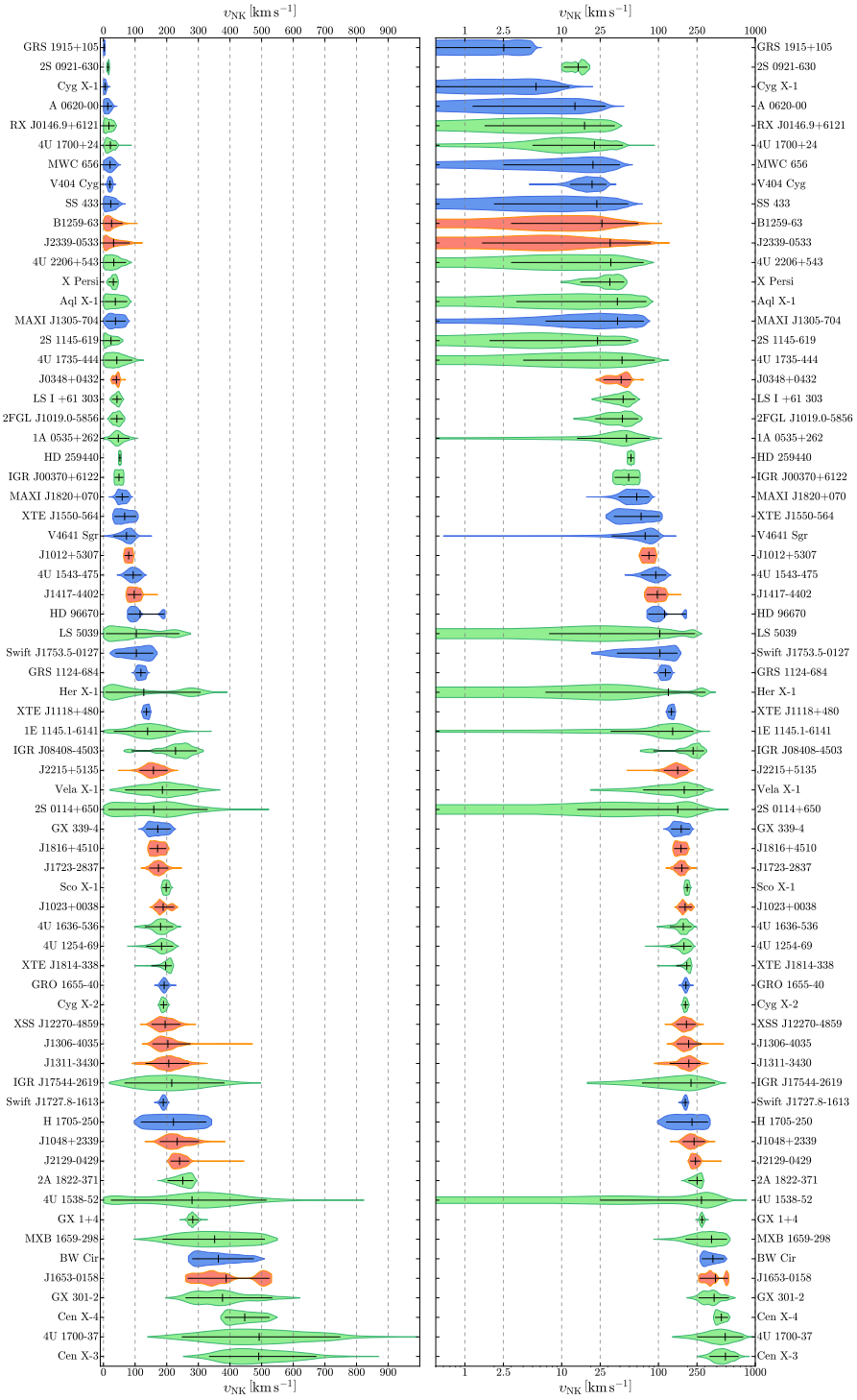

Figure 2.4: **Density plots for all systems**: Mirrored density plots of natal kick distributions for individual sources in both linear (L) and logarithmic (R) scales. The nature of the compact object is indicated by colour (blue: black holes, green: neutron stars, orange: pulsars).

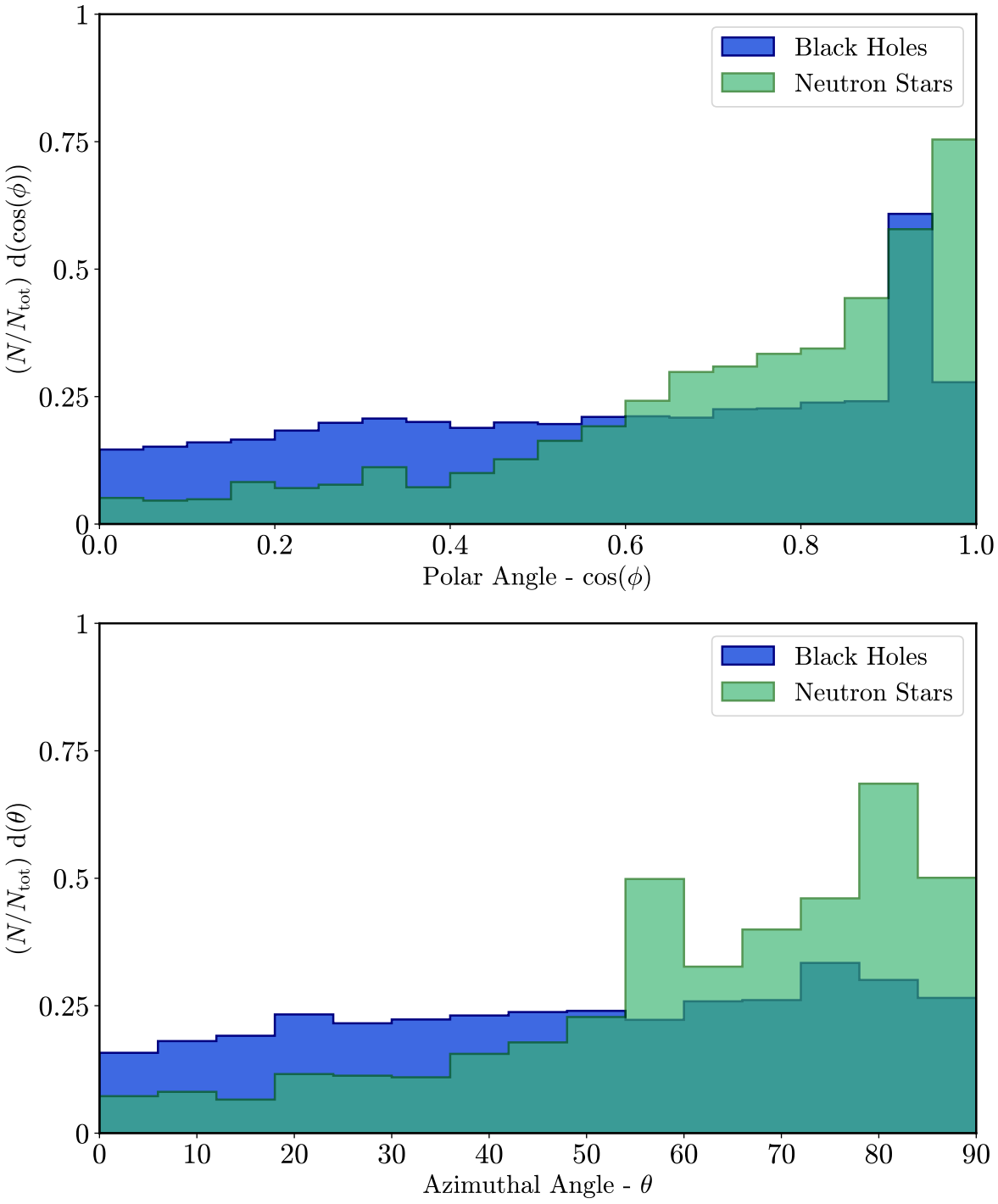

Figure 2.5: **Distribution of natal kick angles**: Distribution of explosion angles for black holes compared to neutron stars (blue & green respectively). Black hole systems appear to have uniformly distributed natal kick directions whereas neutron stars show a preference for kicks to be directed within the orbital plane and with minimal components in the direction of orbital motion.

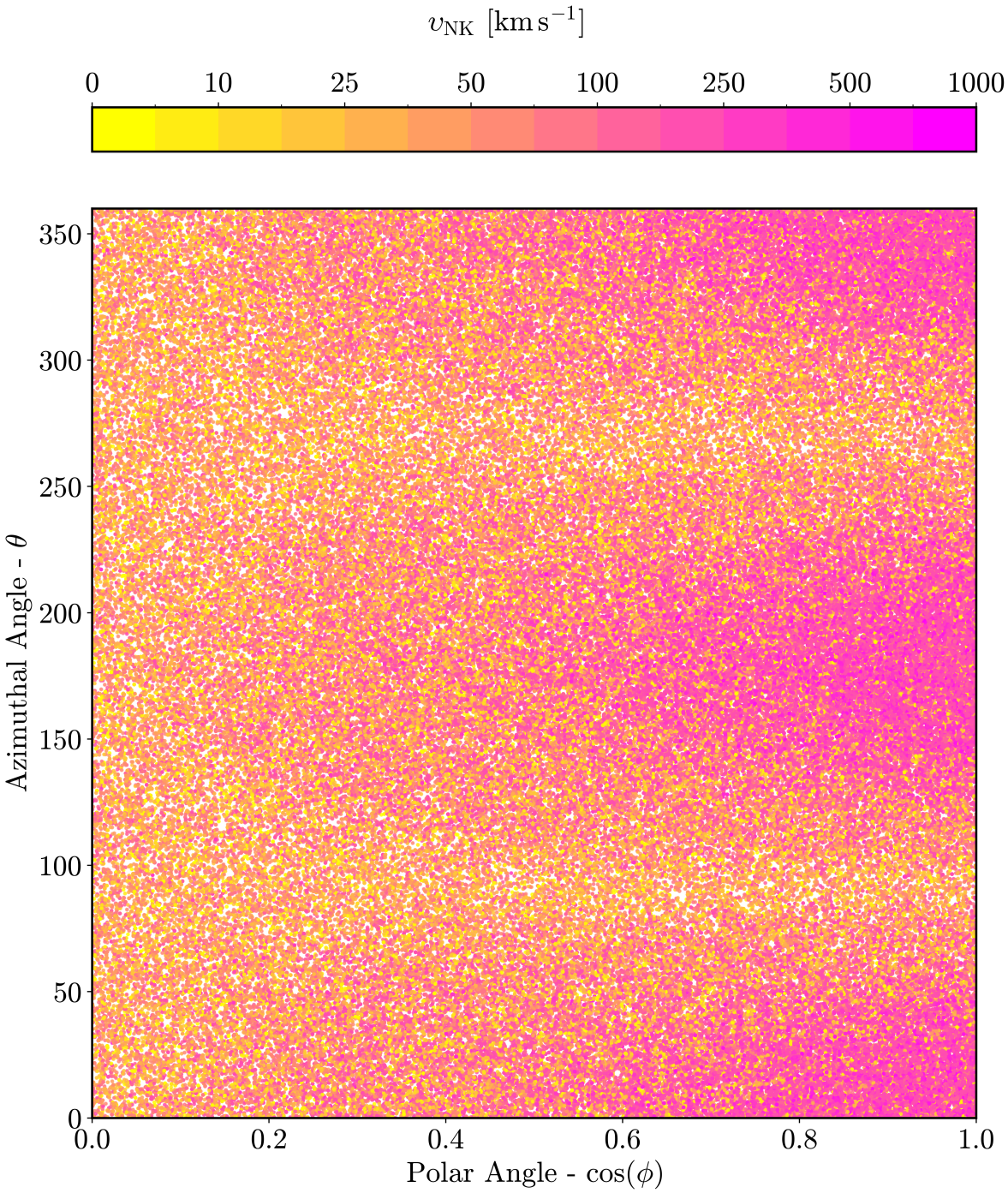

Figure 2.6: **Natal kick angles compared to magnitude**: Angles of supernova explosion compared to natal kick magnitude. Strong natal kicks must be directed in the orbital plane, whereas weaker natal kicks may result in successful binaries regardless of kick direction.

objects. Whether this is coincidental, or evidence of a mass dependence beyond current detection capabilities is uncertain; further studies of natal kicks and observations of higher mass black holes (such as Gaia BH3, and those expected to be astrometrically identified by *Gaia* in DR4 and beyond) may be able to address this.

2.1.5.2 Large natal kicks

5 out of 20 black holes require kicks $\upsilon_{\rm NK} \geq 100\,{\rm km\,s^{-1}}$, compared to 17 out of 48 neutron stars, and for an additional two black holes, the natal kicks exceed $100\,{\rm km\,s^{-1}}$ at 95% confidence. Their properties are described individually in Table 2.6 at the end of this chapter. They appear to show no commonality in primary or companion mass, orbital period; the requirement for a large natal kick is dominated by their peculiar velocities. That these systems require substantial kicks contradicts the idea that black holes may only form with low kicks. Conversely, the fact that a number of neutron stars can form *without* strong kicks provides a counterpoint to the view that such systems are always associated with substantial kicks.

2.1.5.3 Relation to peculiar velocity

Whilst a system's peculiar velocity is heavily influenced by the magnitude of the natal kick imparted following the supernova, the relationship is not strictly linear, with substantial scatter between the two (Figure 2.8). System mass scales inversely with peculiar velocity [318], but there appears to be no significant dependence between mass and natal kick.

These findings demonstrate that peculiar velocity, whilst providing some insight into the kinematic history of a system, is not a suitable proxy for natal kick magnitude. Aspects such as the mass lost from the progenitor, the direction in which the kick is applied, and the orbital separation & mass ratio of the initial binary, play a substantial role in determining the characteristics & velocity of the system post-supernova. These inferences are not obviously changed under different baseline assumptions regarding physical processes that may impact binary evolution, including progenitor metallicity, common envelope prescriptions, and various descriptions of mass transfer via stellar winds.

2.1.5.4 Neutron star kicks vs black hole kicks

To compare the distributions of natal kicks for black holes and neutron stars, 10 million tests are carried out, in which one possible natal kick from the kick distribution for each

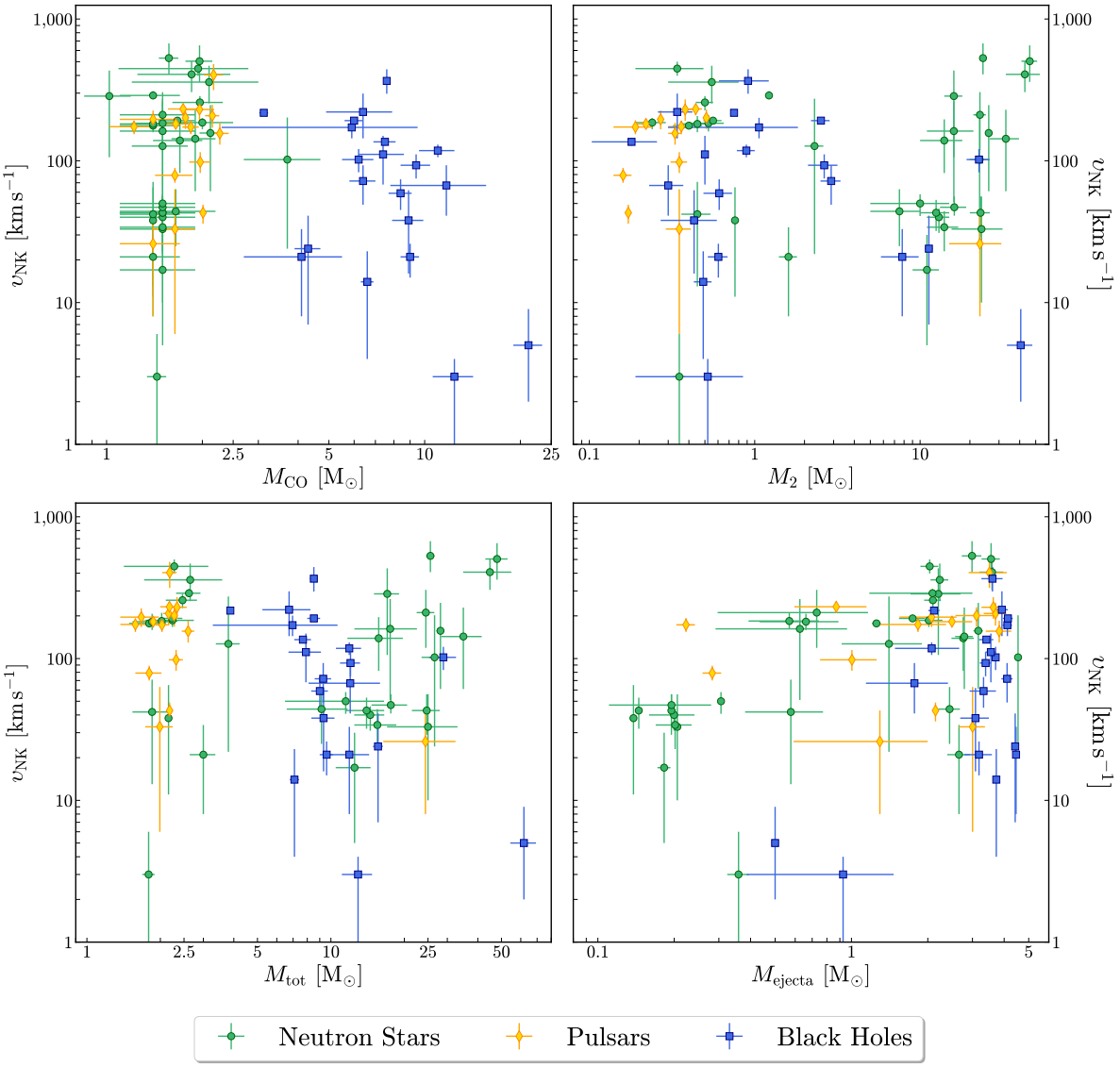

Figure 2.7: **Natal kick against mass**: Mean natal kick velocity against: compact object mass (upper left); companion mass (upper right); total system mass (lower left); and ejecta mass (lower right). The errors in natal kick show the 68% confidence intervals (ETI), and the errors in component masses indicate the standard deviation (see Zhao23 for further details). The nature of the compact object is indicated by the colour & marker shape (see inner box).

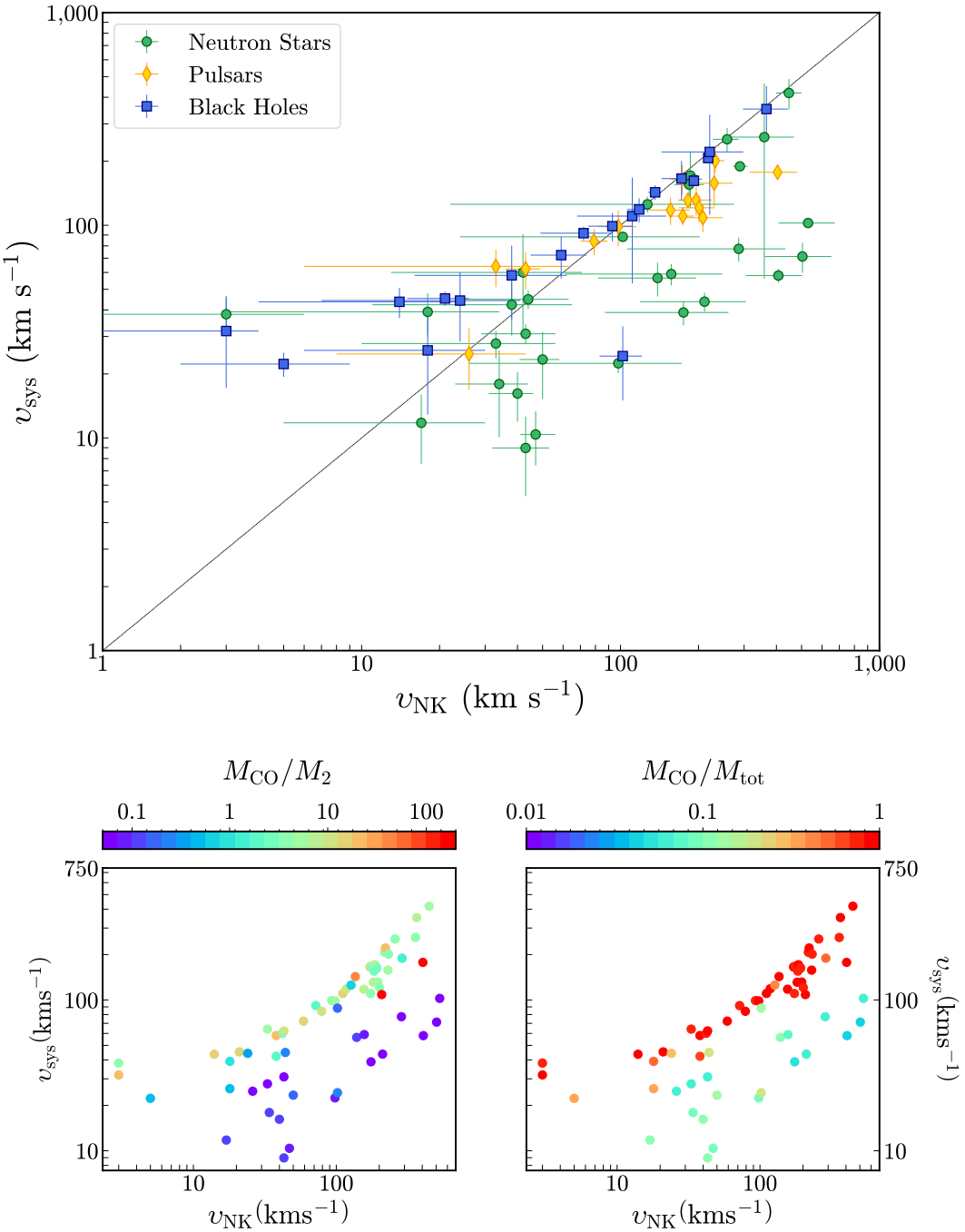

Figure 2.8: **Natal kick against system velocity**: System velocity as a function of mean natal kick for each of the 68 systems. The errors in natal kick and peculiar velocity show the 68% confidence intervals (ETI). Upper panel: The nature of the compact object is indicated by the colour & marker shape (blue circles: black holes, green squares: neutron stars, orange diamonds: pulsars). Lower panels: Systems are differentiated based on the ratio between compact object mass and companion mass (L) and total mass (R) (see colourbars).

of 68 systems is randomly sampled. These are then subject to two-sample Kolmogorov-Smirnov testing between the 20 natal kicks associated with black holes and the 48 natal kicks associated with neutron stars. They appear to be entirely consistent with one another (i.e. p-value $\geq$ 0.05, $\geq$ 95 % of the time). In other words, there exists no statistically significant evidence that black hole and neutron star natal kicks are inherently different in magnitude.

The salient result is that kicks applied to black holes are entirely consistent with those applied to neutron stars; i.e. there is no statistically significant evidence for an intrinsically different kick distribution between the two populations. Both types of systems can receive large ($\upsilon_{\rm NK} > 200\,{\rm km\,s^{-1}}$) or very small ($\upsilon_{\rm NK} < 5\,{\rm km\,s^{-1}}$) kicks. The distribution of kicks applied to neutron stars vs black holes share many qualitative, as well as quantitative, similarities (see Figure 2.9); both range from 0 to several hundred ${\rm km\,s^{-1}}$; the mean values for natal kick are 102 & 146 ${\rm km\,s^{-1}}$ for black holes and neutron stars respectively; and the 90% confidence intervals are 2–300 ${\rm km\,s^{-1}}$, 6–400 ${\rm km\,s^{-1}}$. Standard statistical tests show that the natal kick distributions for both samples are entirely consistent with each other; therein lies the verdict that the natal kicks imparted to neutron stars and black holes are drawn from the same distribution.

2.1.6 Parameterisation of the natal kick distribution

The probability density (PDF) of a Gamma distribution is given by Equation 2.5:

$$PDF(\upsilon_{\rm NK}) = \frac{1}{\Gamma(\alpha)}\beta^{\alpha}\,(\upsilon_{\rm NK})^{\alpha-1}\,e^{-\beta\,(\upsilon_{\rm NK})} \tag{2.5}$$

Here, the distribution is parameterised by its mean $\langle\upsilon_{\rm NK}\rangle = \alpha/\beta$ and its skewness $s = 2/\sqrt{\alpha}$. $\Gamma(\alpha)$ is the Gamma function; $\Gamma(n) = \int_0^\infty e^{-t}t^{n-1}dt$.

α & β can be fit using Maximum Likelihood Estimation and using KS-tests to quantify goodness of fit.

The results can be described with a Gamma distribution, with mean $\langle\upsilon_{\rm NK}\rangle = 147^{+29}_{-26}\,{\rm km\,s^{-1}}$ and skew $s = 1.01^{+0.04}_{-0.04}$ (see Figure 2.10). Though this is far from a thorough statistical description of the data, it describes the magnitude of the natal kicks $>95\%$ of the time and is well-suited for implementation in future population synthesis models.

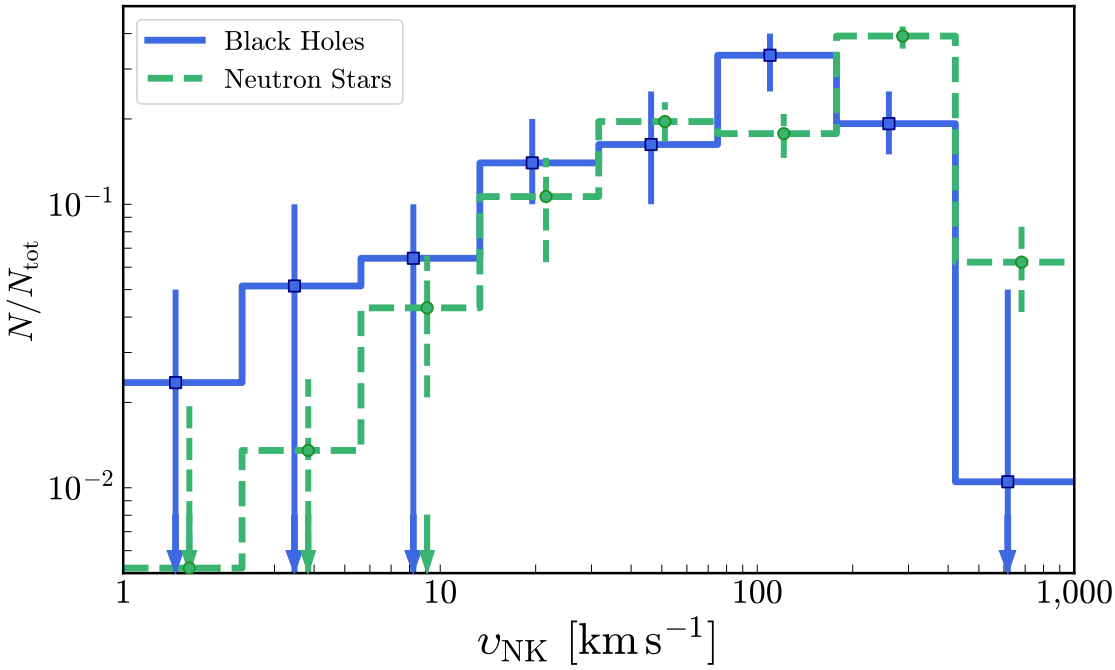

Figure 2.9: **Inferred distribution functions of natal kicks for black holes vs. neutron stars**: Ensembles of natal kicks are simulated from each of the distributions for individual sources, each iteration corresponding to a possible physical scenario. The histograms here denote the mean and one standard deviation amongst these ensembles. The blue solid line indicates the distribution of natal kicks for black holes, and the green dashed line represents neutron stars. Arrows denote bins consistent with being upper limits.

2.1.6.1 Statistical Sensitivity

Given the small number statistics on which these distributions are based, one might assume the number of systems is insufficient to distinguish different distributions between black holes and neutron stars.

First, suppose that the natal kick distributions for both neutron stars and black holes are characterised by the same shape, but with divergence in a single parameter: i.e. a single Maxwellian with mean σ ranging from 0–500 km s^{-1}, or a Gamma distribution with mean $\langle v_{\rm NK} \rangle$ ranging from 0–500 km s^{-1}. KS testing can be used to quantify the similarity (or lack thereof), by repeatedly drawing 20 and 48 random numbers from two distributions and determining the number of instances in which they would appear consistent with one another ($N_{(\rm p-value > 0.05)}$). These results are summarised in Figure 2.11.

Even with the small number of systems, different underlying distributions would be

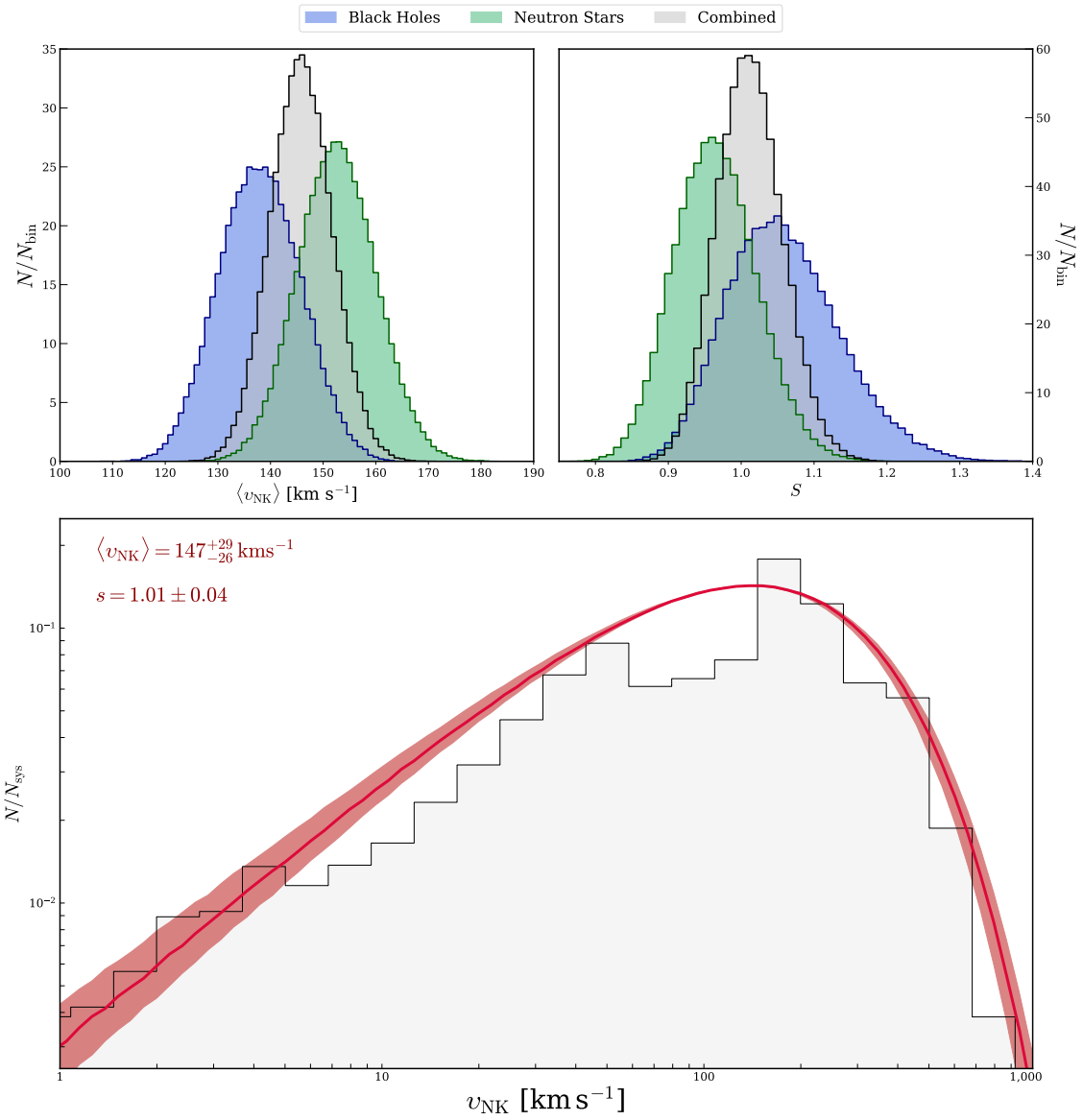

Figure 2.10: **Proposed natal kick distribution**: Upper: Distribution of mean $\langle v_{\rm NK}\rangle$ [L] and skew s [R] values when fitting samples of: 20 kicks (for black holes, blue); 48 kicks (for neutron stars, green); and 68 kicks (combined, grey) 1 million times. Lower: Gamma distribution of mean $\langle v_{\rm NK}\rangle = 147^{+29}_{-26}\,{\rm km\,s^{-1}}$ and skew $s = 1.01 \pm 0.04$ compared to mean histogram - solid red line indicates mean fits, shaded red region indicates 68% confidence interval.

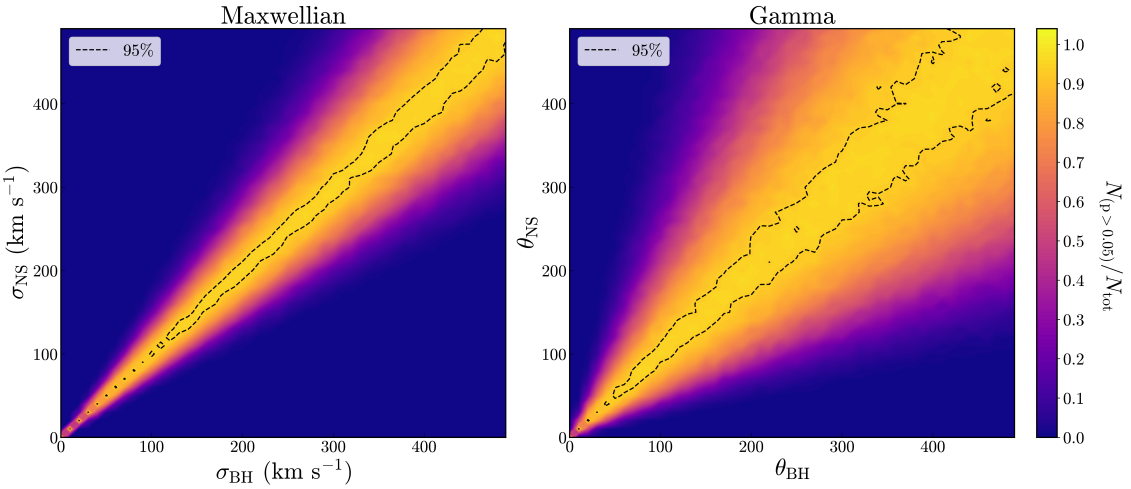

Figure 2.11: Fraction of scenarios in which the distributions of black holes and neutron stars would be observed to be consistent with one another (according to standard KS tests), assuming both neutron star and black hole kick distributions can be described by a single component Maxwellian (left) or a single component Gamma distributions (right) with two different means (σ & θ respectively).

distinguishable, provided that both rms σ be $\geq 10\,\%$ of each other if both distributions are Maxwellian, or θ be $\geq 15\,\%$ of each other in the case of two Gamma distributions. This supports the notion that both neutron star and black hole natal kicks are drawn from similar distributions and that the magnitude of natal kicks does not vary drastically between the two populations.

2.1.7 Comparison to previous studies

2.1.7.1 Individual Systems

Past studies have investigated specific systems to determine the magnitudes of their natal kicks [303; 90; 308; 21; 161; 70], or samples of particular types of systems (e.g. BH-LMXBs [244]; NS-HMXBs [86]; black holes located in the Galactic disc [211]). The results for individual systems in comparison to those presented in other studies are summarised at the end of this chapter in Table 2.7 (and Figures 2.12 & 2.13). The results are consistent with predictions for previous studies in the majority of cases, with a reasonable scatter associated with different methodologies.

One of the most recent comprehensive studies of natal kicks was conducted by Fortin et al. [86]. They used a similar MCMC algorithm, based on uniform priors, to determine plausible natal kicks for 35 NS-HMXBs; 14 of those systems are included in this study.

While the results are comparable, there do exist some discrepancies. For a handful of systems, the mean natal kick estimated by Fortin et al. [86] lies outside the range calculated using the methods described earlier.

The largest difference is the result for the NS-HMXB 4U 1700–37. Fortin et al. [86] predict a natal kick velocity of $\upsilon_{\rm NK} = 79^{+113}_{-56}\,{\rm km\,s^{-1}}$ for 4U 1700–37, which is significantly smaller than the values quoted here ($163 \leq \upsilon_{\rm NK} \leq 964\,{\rm km\,s^{-1}}$). The maximum kick determined in that study ($\sim 190\,{\rm km\,s^{-1}}$) is only just coincident with the lowest estimates presented here - only 0.5% of natal kicks are below $200\,{\rm km\,s^{-1}}$. This can be attributed to differences in $M_{1,{\rm pre-SN}}$ & $P_{\rm orb,pre-SN}$ between both studies. The quoted values for initial mass and initial orbital period are $7.5^{+1.4}_{-1.6}\,{\rm M_\odot}$ and $2.9^{+0.9}_{-0.7}\,$days in the study conducted by Fortin et al., whereas targeted simulations predict a progenitor mass of $\sim 5.5\,{\rm M_\odot}$ and a pre-supernova orbital period of 1.5 days. Whilst these differences may seem small, they are significant enough to result in different system evolution, notably systemic velocity (see Equation 2.2) - indeed, the second term in Equation 2.2 describes the contribution of mass loss from the progenitor (and is the driving influence in determining the systemic velocity for NS-HMXB, where $M_{\rm CO}/(M_{\rm CO}+M_2)$ is small) and varies by almost a factor of two when considering the different parameters[2].

The story is similar for other systems: 2FGL J1019.0-5856; 4U 2206+543; GX 301–2; IGR J00370+6122; and LS I +61 303. In all cases, differing estimates for the initial primary mass and orbital period result in varying contributions from mass loss and therefore different constraints on natal kicks. Whilst the mean natal velocities are not consistent it should be noted that, for many of these systems, the range of plausible natal kicks determined by each study overlap.

2.1.7.2 Distributions

In addition to estimates of natal kicks for individual systems, there exist a variety of theoretical distributions of natal kicks, many of which are used in population synthesis codes such as `cosmic` or `StarTrack`. Here, each prescription is briefly discussed in comparison to these results (see Figure 2.14).

Hobbs et al. [133] provide the most common kick prescription quoted and used in many population synthesis models. They assume kicks are drawn from a Maxwellian distribution with $\sigma = 265\,{\rm km\,s^{-1}}$. No similarity between this distribution and those derived

[2]4U1700-37 is not without controversy; accurate K-velocities are unknown and the mass presented by Falanga et al. [82] is determined from the eclipse duration and studies of the donor star and differs starkly from the previous estimates [61] ($1.96\,{\rm M_\odot}$ vs $2.44\,{\rm M_\odot}$). This means there is a high level of uncertainty, and it may be argued that the neutron star is more reminiscent of the smaller Cen X-3.

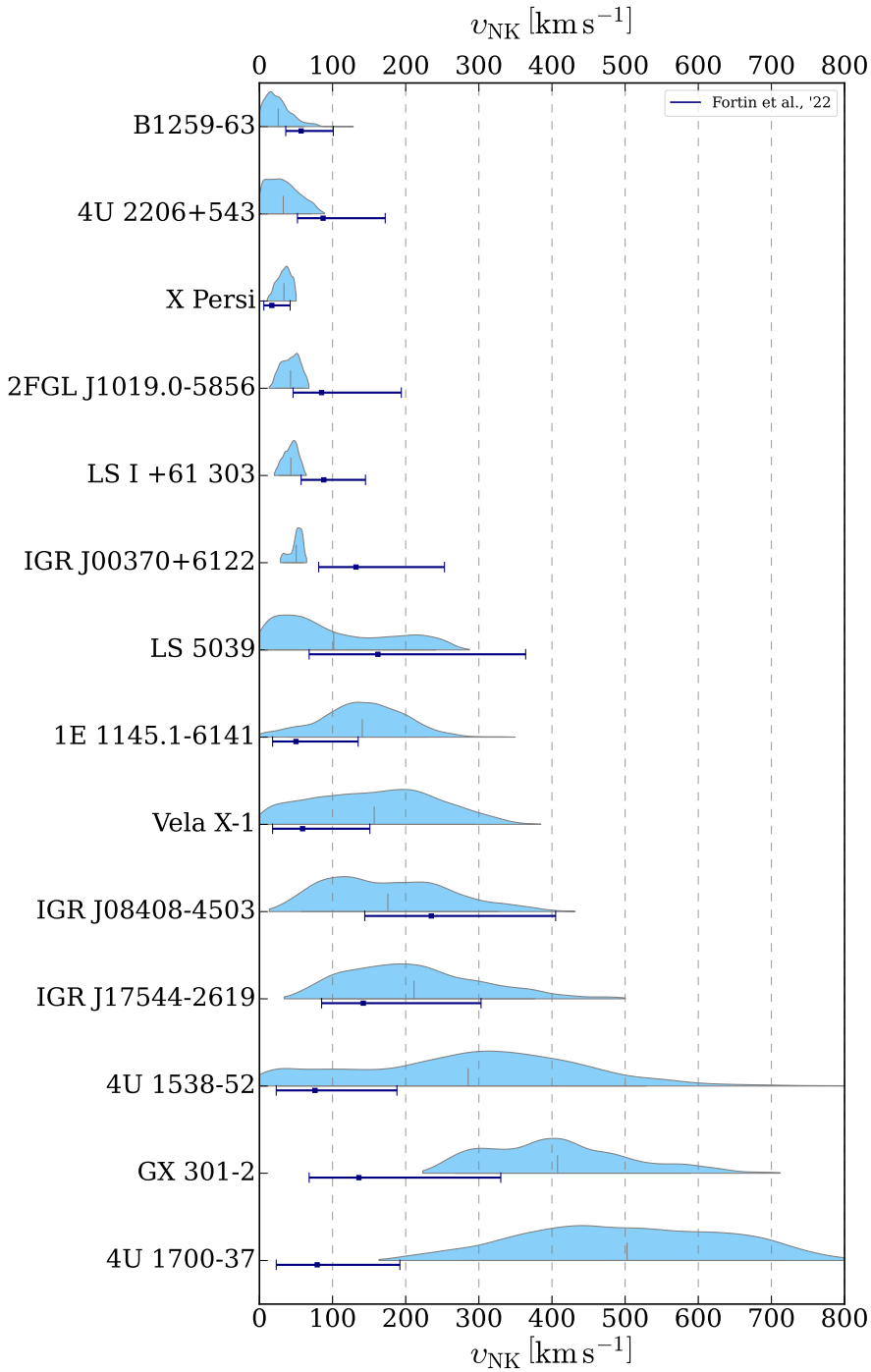

Figure 2.12: **Comparison between the new results and Fortin et al. [86]**: Density plots of plausible natal kicks for 14 NS-HMXB systems in order of mean natal kick magnitude, compared with previous estimates (solid navy blue lines).

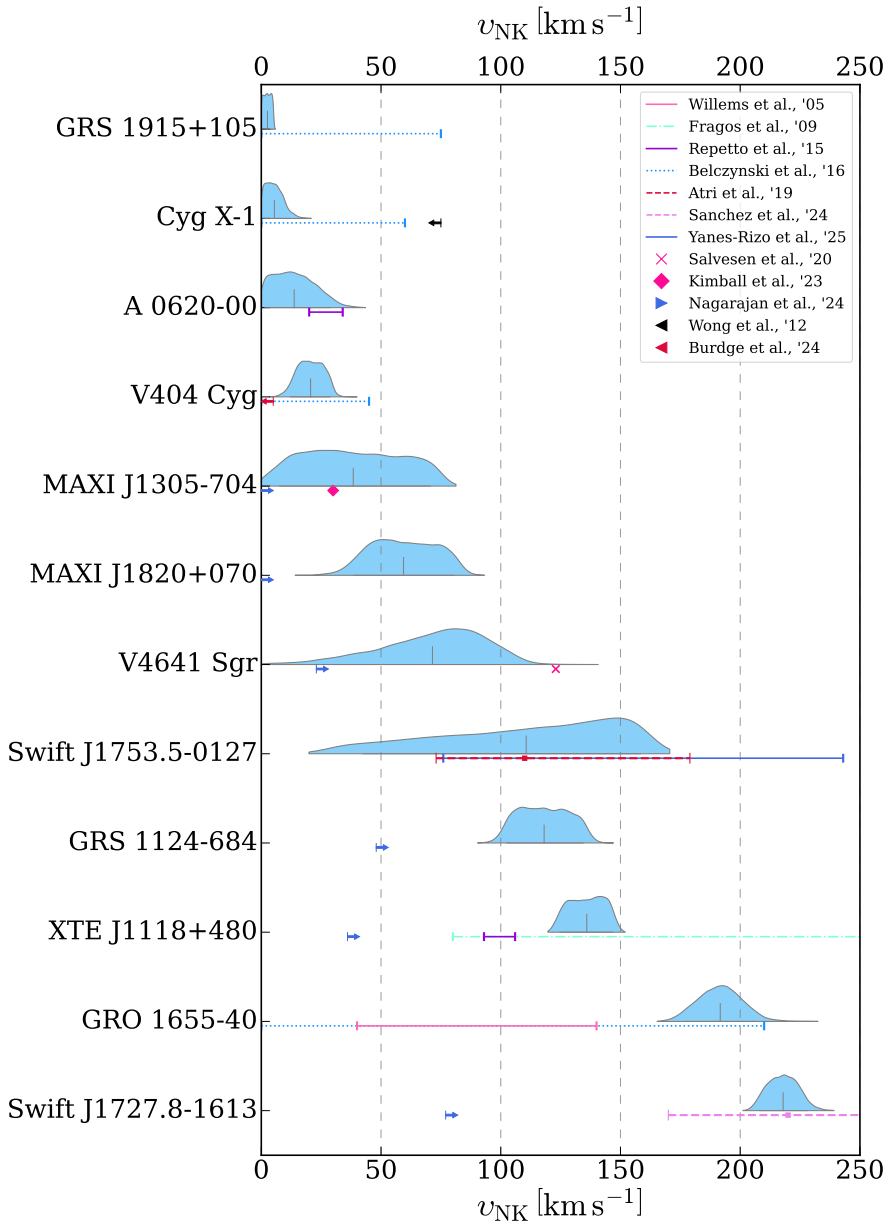

Figure 2.13: **Comparison between the new results and previous studies [303; 90; 244; 21; 5; 252; 315; 250; 161; 211; 308; 38]**: Density plots of plausible natal kicks for 12 X-ray binaries in order of mean natal kick magnitude, compared with previous estimates (coloured lines, markers, and arrows - see inset box).

(distribution of neutron star kicks, black hole kicks, and combined) can be recovered. Therefore, this study suggests this case is unlikely, at least in the context of the types of Galactic systems used in this study (i.e. interacting binaries). This prescription is often adapted to account for different supernova mechanisms, with mean $\sigma = 265\,\mathrm{km\,s^{-1}}$ for core-collapse supernova, but being lower for electron-capture supernova (ECSN) ($\sigma = 30\,\mathrm{km\,s^{-1}}$). Neither the single component Maxwellian nor a double component accounting for variation according to supernova type is a suitable description of these results.

Bray and Eldridge [32] present a simple linear relation, depending on the ratio of ejecta to remnant mass, with varying constants - each of these relations is inconsistent with these updated findings, with a particular mismatch arising due to the fact that the linear relation assumes a non-zero minimum natal kick. However, it should be noted that their study focused on neutron stars, and may still be relevant for isolated neutron stars & pulsars.

Giacobbo and Mapelli [108] offer two kick prescriptions, also using a Maxwellian distribution & scaling with a) ejecta and final mass, and b) purely ejecta mass. Whilst the former is statistically inconsistent with these results, the latter is deemed more plausible; KS-testing (following the method described above) evinces a statistically significant (p-value $\geq$ 0.05) similarity can be recovered $\simeq 50\%$ of the time.

Fortin et al. [86] study the peculiar velocities of 44 neutron stars, and propose that natal kicks (at least in the case of neutron stars) are drawn from a Gamma distribution, with mean $116\,\mathrm{km\,s^{-1}}$. This relationship is generally consistent with the above findings; statistically similar $\simeq 60\%$ of the time.

2.1.8 Caveats

The primary limitation of this study is that it only considers compact objects that exist within interacting binaries. The number of observed quiescent compact objects (black holes) is growing [249; 78; 79; 99], largely due to the success of astrometric missions like *Gaia* (additionally, microlensing is expected to become a useful method of detecting such black holes) - however, numbers remain small for the time being. The best constrained compact object systems involve interaction between the compact object and a companion star - this observational constraint introduces an inherent bias. Certain types of systems are more likely to be interacting (i.e. particular orbital periods/separations, companion mass & nature etc.) and so one cannot assume these inferences apply to the full spectrum of compact objects in the Galaxy.

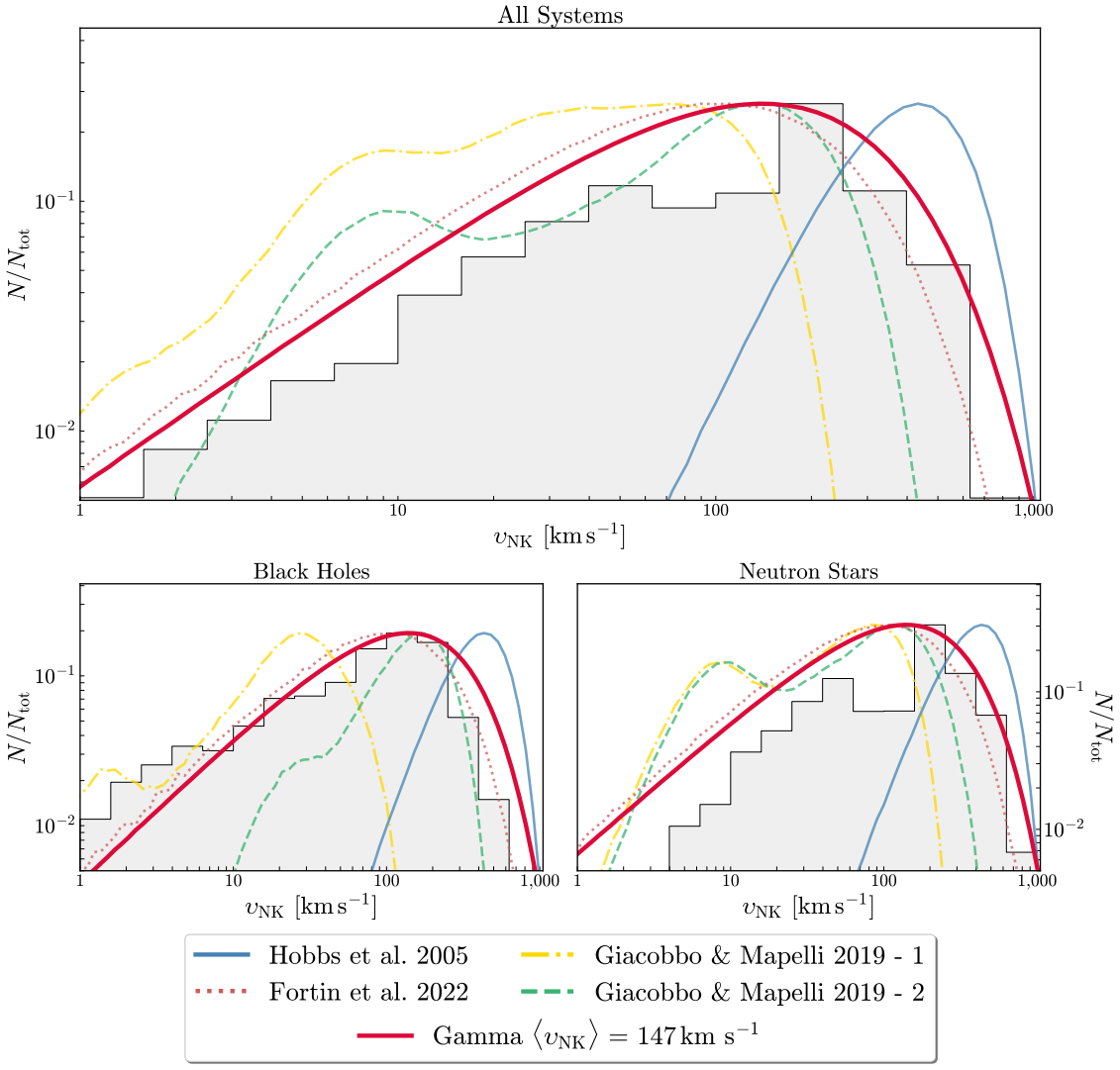

Figure 2.14: **Natal kick prescriptions**: Distribution of natal kicks determined in this study compared to proposed distributions from various literature. Upper panel: Mean histogram for all 68 sources (grey), compared to the distributions proposed by; Hobbs 2005 [133] (solid blue); Giacobbo & Mapelli 2019 [108] (dashed yellow and dashed green); & Fortin et al. [86] (dotted red). Red bold line shows the proposed distribution (a Gamma distribution with mean $147\,{\rm km\,s^{-1}}$). Lower panels: The same as above but for all black holes (L) and all neutron stars (including pulsars) (R).

Estimates of the natal kicks involved in non-interacting systems are becoming more viable; it is generally agreed that Gaia BH1 & Gaia BH2 received low-moderate kicks ($\sim$0–50 km s^{-1})[78; 79; 170; 211]. Whilst the sample size remains too small to draw any meaningful conclusions, these results are consistent with the general distribution seen in interacting compact object binaries. However, the nature of these systems remains contentious and the small number which have been identified are controversial (for further discussion, see Chapter 3); it is currently unknown whether they represent a small subset or substantial fraction of Galactic black holes. One might assume that given these systems are more widely separated, they are likely to have received higher kicks. However, the relationship between kick velocity and post-supernova separation is not strictly linear - factors such as the initial configuration of the binary, the component masses, initial eccentricity, and the mass lost during the supernova all contribute to the evolution of the system. It is therefore difficult to make inferences on how these non-interacting systems contribute to the overall distribution of natal kicks and to quantify the bias induced by considering only interacting binaries.

Given that current data are limited to systems that must remain bound following the supernova of the primary, it is entirely possible the sample is missing a population of (likely fast-moving) isolated compact objects that could be the result of high natal kicks. The existence of high-velocity (runaway) stars may be suggestive of companion stars that were ejected from the binary due to the supernova, though this is far from categorical.

This sample is also limited to the lower-mass regime of black holes, where $M_{\rm BH} < 30\,{\rm M}_{\odot}$. At higher masses, including the higher end of systems identified with LIGO/Virgo, black holes may undergo different formation channels and supernovae mechanisms, including direct collapse and pair-instability supernovae [235]. That being said, the purpose of this study is not to to create a *complete* sampling of compact objects in binaries, but rather to present a more representative comparison between neutron star and black hole systems.

Another potential concern is that X-ray binary observations are biased against higher-mass black holes. Jonker et al. [154] argue that these heavier black holes are more likely to lie closer to the Galactic plane, and are therefore more obscured than their counterparts at greater scale heights. This effect is expected to be significant for LMXBs with smaller and fainter companion stars. It is a fair assessment that systems in the Galactic disc are more difficult to identify - there is, in fact, a slight dearth of black holes at scale heights $|{\rm Z}| \leq 0.1$ kpc. However, this is not exclusive to the black holes. Of the 18 systems that exist within 0.1 kpc of the Galactic plane, 2 are black holes and the remaining 16

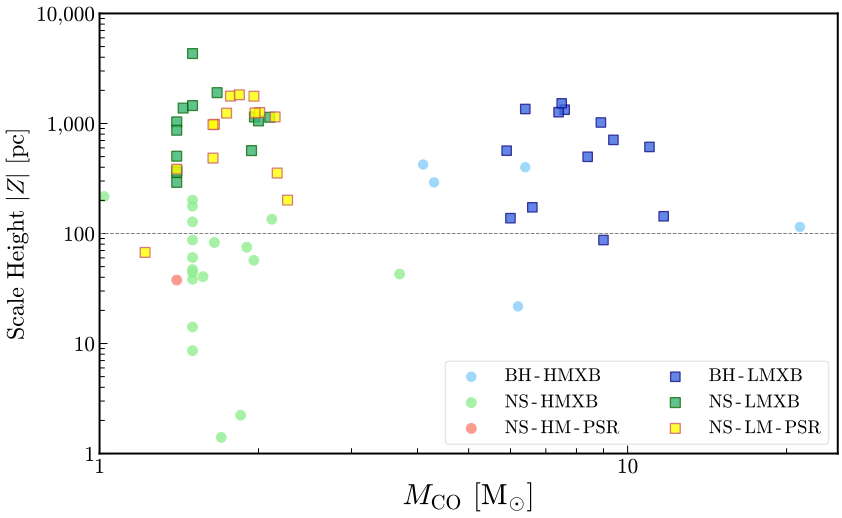

Figure 2.15: **Galactic scale height of 68 compact objects within this sample**: Distance from the Galactic plane (parsecs), with black holes, neutron stars, and pulsars distinguished by colour, and companion mass distinguished by shape.

are neutron stars. However, all but one of the neutron star systems have high mass companions ($M_2 \geq 7.5\,M_\odot$), suggesting the challenges associated with observing LMXBs in the obscured Galactic disc are just as applicable to neutron stars (see Figure 2.15). Additionally, the natal kick distributions for the systems close to the Galactic plane span a range of magnitudes ($15 \leq \langle \upsilon_{NK} \rangle \leq 500\,km\,s^{-1}$), further highlighting that systemic velocity and, consequentially, Galactic location are not directly proportional to natal kick velocity. For these reasons, whilst further observations of LMXBs in the Galactic disc are, of course, desirable, the potential biases introduced by their absence are unlikely to affect the results presented here.

As discussed, population synthesis is intrinsically limited based on the assumptions made. Specifically, the assumption of binary formation via isolated evolution (i.e., these compact objects were formed in binaries, rather than through the dynamical capture of another star at some unknown stage of the system's evolution).

It is currently unclear how many massive stars exist in triples or higher-order systems. It has recently been proposed that V404 Cygni is part of a hierarchical triple, with a third companion existing approximately 3500 AU from the inner binary [38]. This has been used as evidence for a low natal kick since it is theorised that the tertiary component would be ejected in the case of a strong natal kick. This is consistent with this study; the natal kick applied to V404 Cygni is within the range $0 \leq \upsilon_{NK} \leq 30\,km\,s^{-1}$. It has

also been proposed that HD96670 exists as part of a triple system [111]. This system's observed systemic velocity is consistent with zero (once accounting for Galactic dispersion velocity), however natal kick constraints that result in a systemic velocity less than $30\,\mathrm{km\,s^{-1}}$ are elusive (see Table 2.4). This may highlight the issues with neglecting the impact of a third companion in determining the system's evolution.

However, the dynamics and evolution of a triple system are far from trivial, and one cannot simply scale up the physics of binary evolution to incorporate this third component - this is particularly the case when considering the dynamics associated with natal kicks. Interactions between the three components will influence the evolution of the system (e.g. eccentricity excitations associated with Lidov-Kozai oscillations [179; 171]), and may even impart some momentum to a system, increasing its peculiar velocity and inaccurately suggesting a higher natal kick. A comprehensive investigation into how a tertiary component may influence the observed characteristics, particularly the peculiar velocity, is beyond the scope of this study - nevertheless, should more evidence of triples within the sample come to light this may necessitate a revision of the above analysis.

2.2 Implications for natal kick mechanisms

A variety of potential mechanisms behind natal kicks have been put forward including; recoil due to baryonic ejecta [24; 31; 214]; anisotropy in gravitational attraction due to asymetrically ejected mass [143; 309]; and, asymmetric neutrino emission (related to the hydrodynamic processes within the SN) [58; 73; 3; 175; 219].

That black holes and neutron stars receive comparable natal kicks is in tension with previous schools of thought, and has broad implications, particularly for supernova physics. Previous studies of supernovae, notably those involving advanced hydrodynamical simulations, predict substantial natal kicks only for neutron stars, with black holes typically being subject to kicks of only a few km/s. [65; 45; 144; 274].

These hydrodynamical simulations suggest natal kicks are the result of, and proportionate to, asymmetries in the explosion (both neutrino and baryonic matter). Rayleigh-Taylor instabilities are a well-established phenomenon occurring within supernovae [129; 42; 146]. Burrows and Hayes [40] demonstrated that even small anisotropies ($< 0.1\%$) can grow during collapse (and further perturbed as stellar rotation interacts with convection processes) and result in substantial natal kick velocities ($500\,\mathrm{km\,s^{-1}}$) via the rocket effect. Studies focused on neutron stars have reported that lower-compactness progenitors experience smaller recoil kicks (100–$200\,\mathrm{km\,s^{-1}}$) than their higher-compactness counterparts

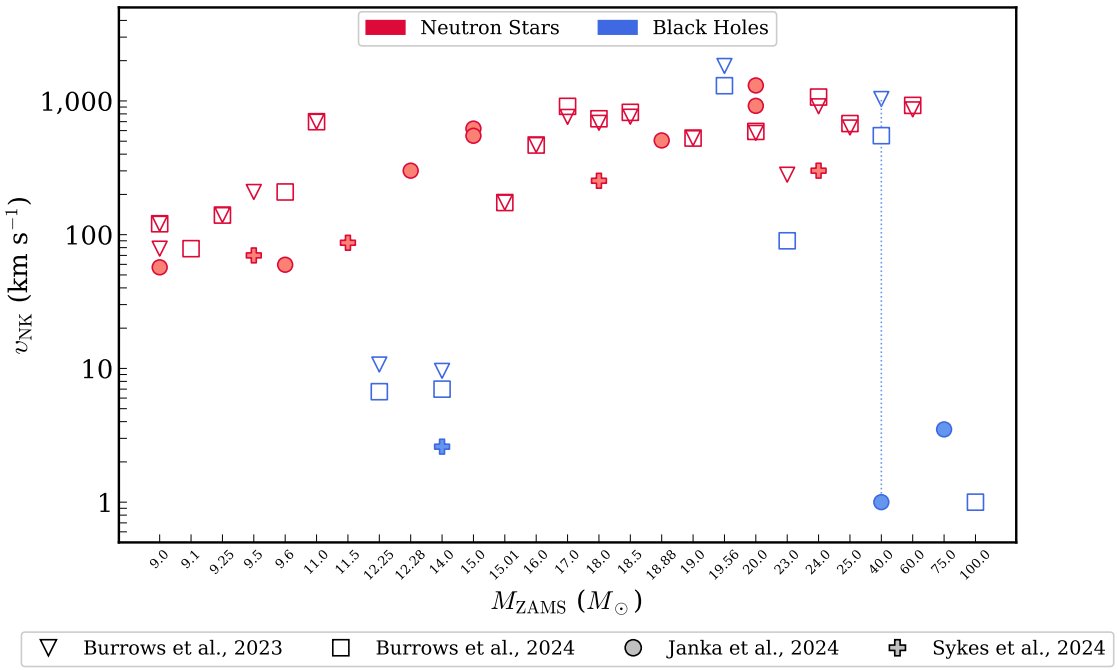

Figure 2.16: **Predicted natal kick magnitudes based on hydrodynamic simulations of supernovae, as a function of model ZAMS mass**: based on the publications of [44; 38; 144; 274]. The ZAMS (Zero-Age Main Sequence) mass indicates the mass of the star as it begins hydrogen burning. The marker shape indicates the relevant study, black hole & neutron star models are distinguished by colour. The blue dotted line highlights the differences between the natal kick associated with a 40 $M_\odot$ model in different studies.

- this may be attributed to the later explosions in the latter instance: any post-shock turbulence have more time to develop and grow to sufficient strength & Mach number, reducing the sphericity and eliciting stronger natal kicks [45].

Much of this discussion hinges upon the relative contribution of anisotropic emission of matter vs neutrinos to any recoil velocity, which remains an ongoing point of contention[3]. In the case of black holes, natal kicks are expected to be predominantly associated with neutrino emission, with typical values being only a few km s^{-1} [65; 144]. In contrast, the hydrodynamically-driven kicks applied to neutron stars are predicted to exceed 100 km s^{-1} in the majority of cases [144; 274]. The results of these simulations are summarised in Figure 2.16.

[3]Early simulations suggested radiating neutrinos contributed at most 16% to overall anisotropies, though more recent results have argued for neutrinos being the presiding influence - to the extent that, if net neutrino emission is directed in opposition to matter recoil, neutron star recoil may be aligned with the associated mass ejecta.

2.2.1 Success of the explosion

The success of the explosion is a decisive factor in predicting the magnitude of natal kicks. There exist numerous simulations in which black hole progenitors (range 12-15 $M_\odot$) do not explode, resulting in minimal matter kicks, and neutrino kicks being dominant (though still smaller than those applied in explosive models). Direct-collapse supernova (sometimes referred to as "silent" or quiescent supernovae) may be associated with specific mass regimes (progenitor or remnant) and have often been touted as the primary mechanism through which black holes form. Given the substantial number of black holes that appear to have received kicks beyond those which are predicted for direct-collapse supernova, this assumption ought to be revised.

2.2.1.1 "Channel 1"

Whilst this 'silent' scenario can lead to 5-15$M_\odot$ black holes [45; 46] (i.e. within the relevant mass regime in this study), it is not the only scenario by which black holes may form. When presenting the results of these simulations, Burrows et al. [46] propose four distinct black hole formation channels, distinguished by the characteristics of the formative supernova and the rigour of the associated explosion, with the silent supernova being but one.

In the majority of cases, natal kicks imparted with black holes are expected to be small. However, Channel 1 is predicted to result in natal kicks $> 1000\,\mathrm{km\,s^{-1}}$. This scenario involves a highly asymmetric and vigorous explosion with substantial mass loss and remnant masses within the lower-mass gap (or slightly higher if the black holes experience fallback). Two of the models in Burrows et al., 2023 & 2024, undergo this channel. These models are defined by ZAMS masses of 19.56 $M_\odot$ and 40 $M_\odot$, and receive natal kicks of 1300-1900 $\mathrm{km\,s^{-1}}$ and 550-1500 $\mathrm{km\,s^{-1}}$ respectively. The large ejecta mass means a binary would likely be disrupted, and therefore this channel cannot easily explain this population of X-ray binaries (though could plausibly generate isolated black holes).

In contrast, simulations by Janka and Kresse [144] involving a model with a ZAMS mass of 40 $M_\odot$ yield natal kicks $< 5\,\mathrm{km\,s^{-1}}$. It may be the case that the parameter space and conditions in which Channel 1 occurs are extremely narrow, which would explain the lack of observations of black holes associated with natal kicks $> 1000\,\mathrm{km\,s^{-1}}$.

In any case, the differences between the predicted natal kicks associated with neutron stars or black holes are substantial (regardless of whether the natal kicks associated with black holes are consistently low or, perhaps, bi-modal, depending on the specific details

of the supernova). That the results point to similar kick distributions and a significant number of black holes with *moderate* natal kicks may be indicative of formation channels beyond those identified through models of supernova.

2.2.1.2 Fallback

The success of an explosion during core-collapse supernovae is not dichotomous. Even if black hole progenitors do not explode as vigorously as their neutron star fellows, there exists a realm in which the progenitor exhibits non-negligible mass-loss and are perhaps subject to baryonic asymmetries. Prior studies have proposed that black holes formed via fallback (where some of the material lifted during the supernova is not sufficiently energetic to escape and falls back onto the compact object, further increasing its mass) will involve smaller kicks than neutron stars [96; 143]. Fryer et al. [96] proposed that natal kicks are moderated by the amount of matter that falls back onto the proto-neutron star according to Equation 2.6.

$$\upsilon_{\rm NK} = (1 - f_{\rm fb}) \sqrt{\upsilon_x^2 + \upsilon_y^2 + \upsilon_z^2} \tag{2.6}$$

Here, $f_{\rm fb}$ is the fraction of matter that falls back onto the compact object, and $\upsilon_x, \upsilon_y, \upsilon_z$ are three velocity components drawn from some 'intrinsic' kick distribution (e.g. the Maxwellian distribution from Hobbs et al. [133]). The amount of fallback is expected to be significant for black holes, and therefore natal kicks would be smaller than those applied to neutron stars (and will be non-existent in the case of direct collapse supernovae). This is in conflict with the above findings and is perhaps suggestive of an incomplete understanding of fallback formation channels or related to the ambiguity surrounding an 'intrinsic' natal kick distribution (i.e. the natal kicks prior to modulation via fallback). That being said, both the mass and fraction of matter which may be totally ejected or fallback onto the black hole are dependent on the progenitor mass as well as the final mass, and it is therefore difficult to make inferences on the entire population of black holes based on the (relatively) low mass ones included in this study.

2.2.2 Electron Capture Supernovae

Whilst most X-ray binaries are considered to be the result of core-collapse supernovae, electron capture supernovae (ECSN) may be responsible for some neutron stars. These ECSN involve an ultra-stripped progenitor and very little ejecta mass (0.01–0.2 $\rm M_\odot$) and weaker natal kicks (a few kilometres per second) [216; 231; 277; 140]. ECSN are unlikely

to be responsible for any of the neutron stars in this study. Only a handful of systems in this study experience mass loss $< 0.2\,\mathrm{M}_\odot$; 5 NS-HMXB & 1 NS-LMXB. Whilst the ejecta mass could suggest that these systems were formed via ECSN, only 2 of the 6 systems may be formed without a natal kick; the remainder require natal kicks $\upsilon_{\rm NK} > 20\,\mathrm{km\,s^{-1}}$, (averaging around $45\,\mathrm{km\,s^{-1}}$). It may be that low ejecta mass is not necessarily a smoking gun for ECSN, and that these systems could have experienced core-collapse supernovae. Alternatively, it may indicate that ECSN result in smaller, but non-negligible, natal kicks - this would be at odds with hydrodynamical simulations.

2.3 Natal kicks in gravitational wave astronomy

Natal kick distributions are intertwined with gravitational wave astronomy. Further simulations were undertaken to investigate the impact that black hole natal kicks will have on double compact object merger (and related gravitational wave) rates. Using `cosmic`, six Galactic populations of compact object binaries were simulated assuming a variety of different kick distributions: a) and b) Hobbs et al. [133] (Maxwellian), both with and without mediation by fallback; c) and d) Giacobbo & Mapelli [108] equations 1 & 2 (where $\upsilon_{\rm NK} \propto M_{\rm ejected}/M_{\rm CO}$ and $\upsilon_{\rm NK} \propto M_{\rm ejected}$); e) Bray & Eldridge [32] ($\upsilon_{\rm NK} \propto M_{\rm ejected}/M_{\rm CO}$). Additional simulations were carried out, under the assumption that natal kicks are drawn from a Gamma distribution with mean $147\,\mathrm{km\,s^{-1}}$. Across the simulations, the natal kicks span $0 \leq \upsilon_{\rm NK} \leq 2000\,\mathrm{km\,s^{-1}}$. These simulations are normalised to a Galactic population of 10 billion stars, and are based on the assumption that these descriptions of natal kicks are valid for systems in the LIGO/Virgo mass regime.

2.3.1 Simulated Galactic populations

The Galactic population is synthesised according to the following: the mass of the primary is dictated by a power-law initial mass function (IMF) with three breaks, as described by Kroupa [174]; this differs slightly from the IMF employed for the `StarTrack` simulations (two breaks), with marginally different exponent α for $M \geq 0.5\,\mathrm{M}_\odot$ and the inclusion of the lowest mass regime ($M < 0.08\,\mathrm{M}_\odot$): The exponent α_i takes values of:
$\alpha_0 = -0.3$ for $\mathrm{M} \in [0.01, 0.0.08]\,\mathrm{M}_\odot$
$\alpha_1 = -1.3$ for $\mathrm{M} \in [0.08, 0.5]\,\mathrm{M}_\odot$
$\alpha_2 = -2.3$ for $\mathrm{M} \in [0.5, 1.0]\,\mathrm{M}_\odot$

$\alpha_3 = -2.3$ for M $\in [1.0, 150.0\,\mathrm{M}_\odot$

The mass of the secondary component is randomly sampled from a uniform distribution $q \in [M_{2,\mathrm{min}}/M_1, 1]$, where $M_{2,\mathrm{min}}$ is determined such that the pre-main sequence lifetime of the secondary star does not exceed the full lifetime of the primary star (if each were to evolve as a single star). Orbital periods and eccentricities adhere to the distributions proposed by Sana et al. [251] where $\mathrm{P}(\log P_{\mathrm{orb}}) \sim (\log P_{\mathrm{orb}})^{-0.55}$ and $\mathrm{P}(e) \sim e^{-0.42}$. The binary fraction is considered constant, at 0.5 (although in practice the binary fraction is a function of mass and Galactic position [174; 200; 29]).

Evolutionary prescriptions and assumptions are all consistent with those used in prior simulations (see Section 2.1.2). More detailed study, including comparing the results under a broader range of evolutionary channels (e.g. initial mass functions, stellar wind descriptions, magnetic braking, supernovae mechanisms), will enhance the validity of these predictions, and potentially provide useful information regarding how the population of compact objects identified through gravitational waves may contribute to the understanding of binary evolution.

Within the populations, gravitational wave sources are defined as systems that exist as double compact object binaries (DCO; BH-BH, BH-NS, or NS-NS - merger events associated with white dwarfs are excluded) and go on to merge within a Hubble time, (here meaning 13.7 Gyr after the initialisation of the binary).

2.3.2 Predictions

The expected number of DCO mergers and associated gravitational wave signals varies significantly depending on the assumed distribution of natal kicks - for instance, if natal kicks are indeed drawn from the proposed Gamma distribution there will be nearly twice as many DCO mergers compared to the numbers predicted using the distribution presented by Hobbs et al. [133]. However, neither the number of compact object mergers (N_{GW}) nor the fraction of double compact object binaries that will eventually merge ($N_{\mathrm{GW}}/N_{\mathrm{DCO}}$) vary linearly with natal kick velocity (Figures 2.17 & 2.18).

Systems subjected to high natal kicks are more often disrupted by either the first or second supernova (as expected) (up to $\geq 99\%$; typically due to the first supernova), resulting in fewer DCO binaries. However, if binaries survive both supernovae without being disrupted (i.e. perhaps due to more moderate kicks being imparted by the first supernova), a greater proportion will merge, resulting in gravitational wave emission, if the second natal kick is large ($\geq 100\,\mathrm{km\,s^{-1}}$). This could be attributable to the fact that

these large kicks result in highly eccentric orbits, such that the periastron separation is sufficiently close that gravitational waves act to circularise the orbit rapidly, resulting in closely separated binaries which are conducive to mergers. For Figure 2.17, both the first and second natal kicks are binned in log-uniform space, width of 0.1dec, and determine the number of systems that form DCO binaries, and the number which will merge within a Hubble time to emit gravitational waves. That higher natal kicks may be favourable for producing gravitational waves (subject to other conditions) is perhaps counterintuitive; nevertheless, this is what the simulations predict.

These are predictions of the intrinsic number of events which may occur and do not directly translate to the expected number of observations by gravitational wave missions such as LIGO/Virgo/Kagra & the upcoming LISA. Quantifying the numbers of these systems which may be observed, (and, consequently, the likelihood of being able to discern natal kick magnitudes based purely on gravitational wave data) depends on a broad range of factors including specific information about the merging systems, inclusion of realistic star-formation rates within a suitable cosmological evolutionary model, and the limiting sensitivities of gravitational wave detectors.

Small effective spins have been measured in the LIGO population [e.g. 84] and this has been used in favour of dynamical binary formation channels. However, strong natal kicks in black holes could instead also be a natural means to explain the small effective spins (subject to uncertainties on the physics of binaries in the strong gravity regime, such as the efficiency of tidal synchronisation [48; 271]). Given that findings suggest systems which have been subject to strong natal kicks can remain coupled and go on to merge, such kicks may offer an explanation for the distribution of spins within the LIGO population.

2.3.3 Natal kick estimates in GW sources

Wong and Gerosa [307] present inferred natal kick magnitudes from LIGO/Virgo sources, finding a velocity dispersion $\sigma = 105^{+44}_{-29}\,\mathrm{km\,s^{-1}}$. This is consistent with the findings presented here, and whilst it would be premature to assert that natal kicks applied to these populations are consistent with those in the X-ray binary regime, the lack of a significant discrepancy is promising. That being said, the model was trained on population synthesis simulations using a Maxwellian distribution of natal kick velocities 0, 25, 50, 70, 130, 200, 265 $\mathrm{km\,s^{-1}}$ so the inputs are likely at least partially responsible for the order of magnitude agreement,

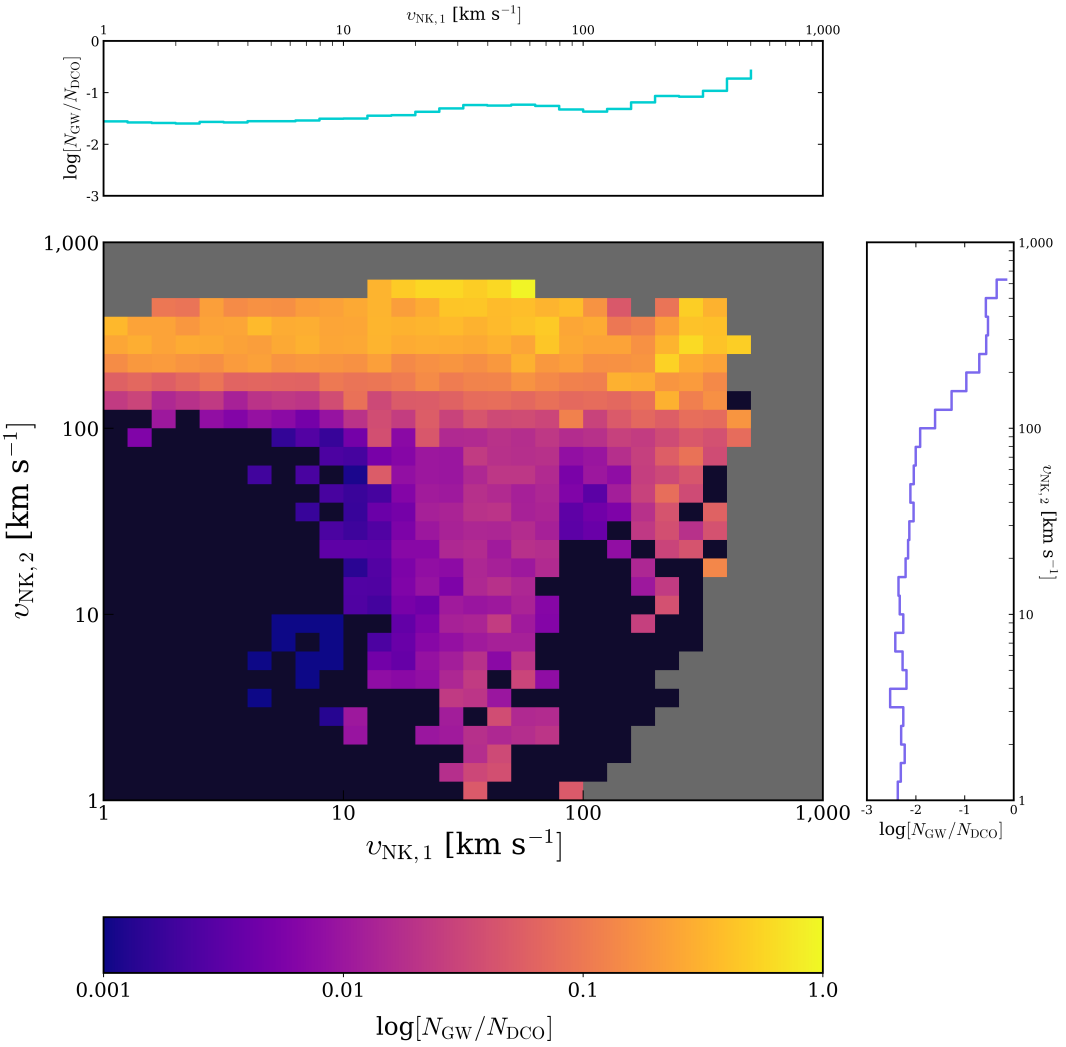

Figure 2.17: **Fraction of DCOs that will merge as a function of natal kick velocity**: The fraction of simulated double compact object (DCO) binaries which will merge within a Hubble time to emit gravitational waves (see colour-bar) as a function of the first and second natal kick. Dark navy shading indicates regions where no DCOs merge; grey regions indicate parameter space without simulated DCOs. The one-dimensional projection of the effect of the first and second natal kicks are indicated in the upper and right panels respectively.

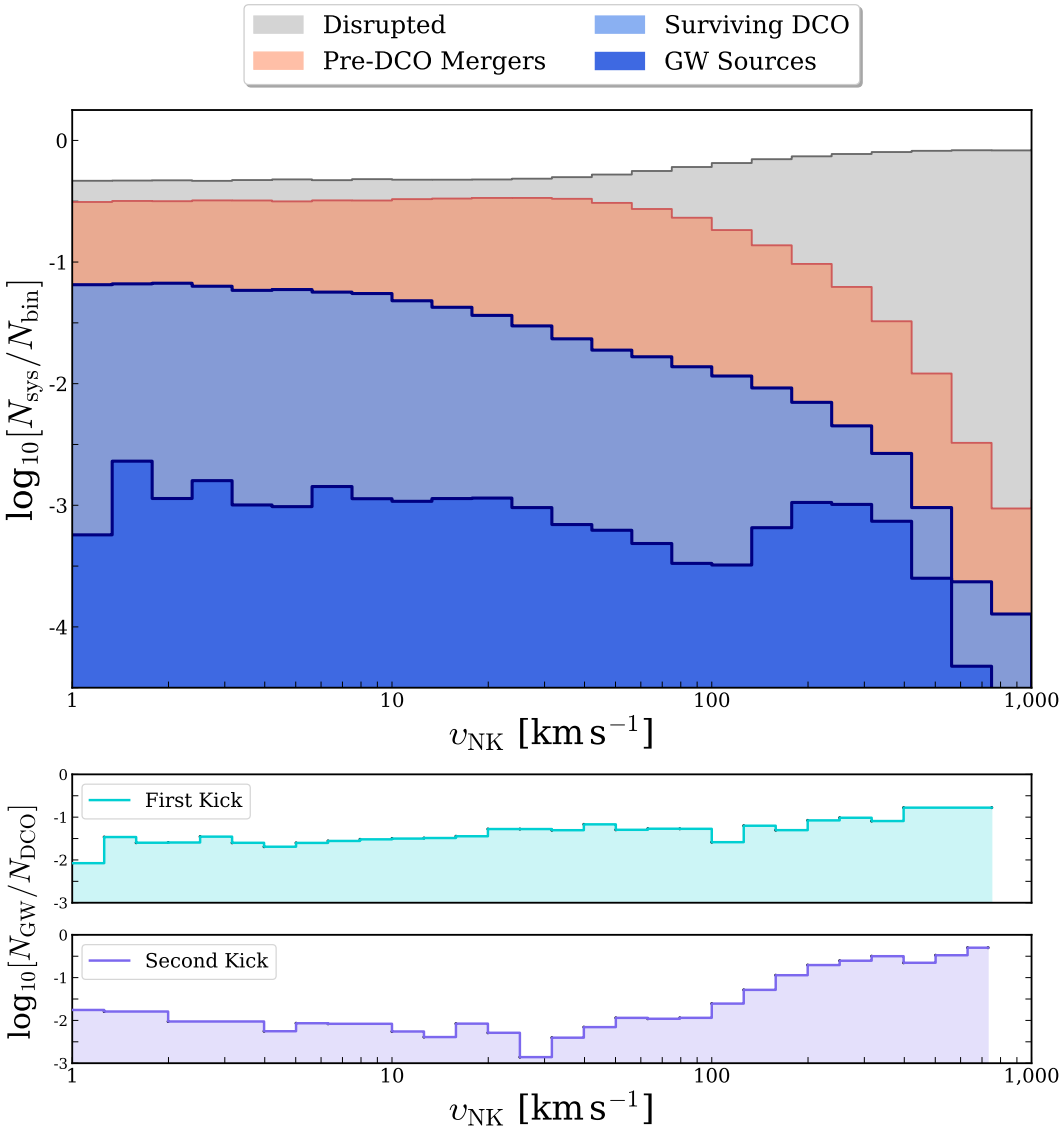

Figure 2.18: **Outcome of double compact object systems for various natal kicks**: Upper: Number of systems which are disrupted due to the supernovae (grey), merge prior to forming double compact objects (orange), and double compact object systems (blue) as a function of natal kick velocity. Darker blue indicates those systems which will merge and emit gravitational waves within a Hubble time. Lower: Fraction of double compact object binaries which will merge within a Hubble time as a function of the first (middle panel) and second (lower panel) natal kick.

Belczynski et al. [21] find that LIGO observations are inconsistent with very high natal kicks ($\upsilon_{\rm NK} \geq 400\,{\rm km\,s^{-1}}$). A significant obstacle in constraining the magnitude of natal kicks from gravitational wave populations is that these systems have, by definition, been subject to two natal kicks (although one or both of them may be negligible). Disentangling the effects of two distinct natal kicks is non-trivial, and these findings suggest that gravitational wave sources may favour different natal kick distributions for different supernovae (see Figures 2.17 & 2.18).

There has been discussion around whether kicks may be able to explain the spin-orbit misalignment distribution, however, this is generally thought to be unlikely, as kicks would have to have very large and likely unphysical velocities [48]. Additionally, Belczynski et al. [21] studied the likely evolution of the merger that caused GW160914, proposing that it involved no natal kicks, however, the binary is believed to have exhibited spin-orbit misalignment prior to the merger. Given that accretion processes can only serve to reduce misalignment, this may indicate dynamical capture evolution. Evidence for strongly misaligned spins is supported by spins observed in X-ray binaries being typically large, however preliminary evidence from the study of merger signals indicates effective spins are near-zero [84]. Belczynski et al. [22] found that efficient angular momentum transfer in binary systems may reduce near-effective spins, but the exact mechanisms of this are unknown. Studies appear to favour isotropic spins as an explanation of these results, and Callister et al. [48] suggests there may be an anti-correlation between binary mass-ratio and effective spin.

2.3.4 Kicks due to gravitational recoil

It should be noted that compact object mergers may be accompanied by a 'recoil' kick, associated with the loss of linear momentum through radiating gravitational waves [e.g 17; 106; 290]. While the impact of these kicks on a merging system is likely to be governed by similar underlying physics, these are unrelated to the natal kicks discussed herein.

2.4 Conclusions

The primary result of this study is that black holes and neutron stars appear to share similar natal kick distributions (see Figures 2.9 & 2.14) which are well-described with a Gamma distribution of mean $147^{+29}_{-26}\,{\rm km\,s^{-1}}$ (see Equation 2.5 and Figures 2.14 & 2.10).

In the absence of a comprehensive and established description of the physical drivers of kicks and their expected direction & velocity, the Gamma distribution of mean $\approx 147\,\mathrm{km\,s^{-1}}$ provides a robust observationally motivated model, suitable for implementation in population synthesis studies and related modelling. At the very least, it seems wise to draw natal kicks from a common distribution, regardless of the nature of the compact object.

Studies of supernova mechanisms and the associated natal kicks have propounded the idea that neutron star natal kicks are primarily attributed to asymmetries in baryonic matter, whereas black hole natal kicks are dominated by neutrino emission, and, consequently, smaller. Whilst the specific drivers of these natal kicks and their relative contribution cannot be exactly constrained, the fact that evidence shows black holes can receive kicks consistent with those imparted to neutron stars upon formation points to an incomplete understanding of some supernovae processes. Specifically, there is evidence that the dominant channel for black hole formation is one that imparts moderate kicks (a few 10s to $200\mathrm{km\,s^{-1}}$).

It has been suggested that a delayed explosion may be more conducive to larger natal kicks [94; 255] - if this holds true for black holes, this may be responsible for the larger natal kicks they are subject to. However, it is these delayed supernovae that are expected to populate the observed mass gap between 3-5 $\mathrm{M_\odot}$, the validity of which remains contentious.

Whilst hydrodynamic simulations and theoretical studies of black hole formation are valuable, the high-precision kinematic observations of the Galactic population have proved, once again, that these must be complemented by data. A reckoning regarding the disparate behaviour of natal kicks for black holes and neutron stars now seems unavoidable. Any future work constraining the mechanisms behind natal kicks ought to be consistent with the possibility of equivalent natal kicks for neutron stars and black holes.

The legitimacy (and precision) of these constraints will be reinforced with further study; in particular, extending the above analysis to populations of non-interacting compact objects will remove some of the biases associated with X-ray binaries. Additionally, any velocity constraints provided by gravitational wave sources will further clarify the intrinsic distribution of natal kicks across various mass regimes.

Table 2.5: **Systems requiring weak natal kicks:** System properties and natal kick constraints for 23 compact objects (8 black holes and 15 neutron stars) that may have formed without a natal kick (i.e. $v_{\rm NK,min} \leq 5\,{\rm km\,s^{-1}}$. M_1 and M_2 refer to the mass of the compact object and the companion star respectively. d & $|Z|$ indicate the distance to the source and the modulus of the Galactic scale height, both in kpc. We present the mean and 68% confidence intervals of the mass-loss-kick (Blaauw kick), and the minimum, mean, and 68% confidence intervals of the natal kick. All velocities are in ${\rm km\,s^{-1}}$.

Name	Type	$v_{\rm pec}$	M_1	M_2	$P_{\rm orb}$	d	$\lvert Z\rvert$	$v_{\rm NK}$		
			[$M_\odot$]	[$M_\odot$]	[days]	[kpc]	[kpc]	Min.	Mean	68%
1A 0535+262	NS-HMXB	45 ± 4	1.7 ± 0.6	7.5 ± 2.5	111	1.8 ± 0.1	-0.1	0	44	25-63
1E 1145.1-6141	NS-HMXB	56 ± 10	1.7 ± 0.3	14 ± 4	14.37	8.3 ± 0.6	0	0	139	82-196
2S 0114+650	NS-HMXB	22 ± 2	1.5 ± 0.4	16 ± 5	11.59	4.5 ± 0.2	0.2	0	98	26-172
2S 0921-630	NS-LMXB	38 ± 7	1.4 ± 0.1	0.4 ± 0.0	9	8.5 ± 1.5	-1.4	0	3	1-6
4U 1538-52	NS-HMXB	77 ± 10	1.0 ± 0.2	16 ± 2	3.7	5.7 ± 0.5	0.2	0	286	106-433
4U 1700+24	NS-LMXB	39 ± 9	1.4 ± 0.3	1.6 ± 0.2	4391	0.5 ± 0	0.3	0	18	3-34
4U 1735-444	NS-LMXB	60 ± 31	1.4 ± 0.3	0.5 ± 0.1	0.2	8.5 ± 1.3	-1	0	42	13-71
4U 2206+543	NS-HMXB	28 ± 4	1.5 ± 0.4	23.5 ± 8	9.6	3.1 ± 0.1	-0.1	0	33	10-56
A 0620-00	BH-LMXB	44 ± 7	6.6 ± 0.3	0.5 ± 0.1	0.3	1.5 ± 0.2	-0.2	0	14	4-23
Aql X-1	NS-LMXB	42 ± 12	1.4 ± 0.0	0.76 ± 0	0.8	5.2 ± 0.8	-0.4	0	38	11-65
B1259-63	NS-HM-PSR	25 ± 8	1.4 ± 0.3	23 ± 8	1236.7	2.2 ± 0.1	0	0	26	8-43
Cyg X-1	BH-HMXB	22 ± 3	21.2 ± 0.2	40.6 ± 7.1	5.6	2.1 ± 0.1	0.1	0	5	2-9
GRS 1915+105	BH-LMXB	32 ± 15	12.4 ± 0.8	0.5 ± 0.3	33.8	8.6 ± 2	0	0	3	1-4
Her X-1	NS-LMXB	125 ± 11	1.5 ± 0.3	2.3 ± 0.3	1.7	7.1 ± 0.6	4.3	0	127	22-274
J2339-0533	NS-LM-PSR	64 ± 13	1.6 ± 0.3	0.35 ± 0.1	0.19	1.1 ± 0.2	-1	0	33	6-63
LS 5039	NS-HMXB	88 ± 3	3.7 ± 0.1	22.9 ± 2.9	3.9	1.9 ± 0.1	0	0	102	24-202
MAXI J1305-704	BH-LMXB	58 ± 22	8.9 ± 0.1	0.4 ± 0.2	0.4	7.7 ± 1.6	-1	0	38	16-62
MWC 656	BH-HMXB?	26 ± 13	4.1 ± 0.4	7.8 ± 2	60.4	2 ± 0.1	-0.4	0	18	6-30
RX J0146.9+6121	NS-HMXB	12 ± 4	1.5 ± 0.4	11 ± 2	330	2.8 ± 0.2	0	0	17	5-30
SS 433	BH-HMXB?	44 ± 16	4.3 ± 0.4	11.3 ± 0.6	13.1	7.4 ± 1.1	-0.3	0	24	7-41
V404 Cyg	BH-LMXB	45 ± 3	9 ± 2.6	0.6 ± 0.1	6.47	2.4 ± 0.1	-0.1	2	21	15-26
V4641 Sgr	BH-HMXB	92 ± 7	6.4 ± 0.6	2.9 ± 0.4	2.8	4.8 ± 0.5	-0.4	0	72	49-93
Vela X-1	NS-HMXB	59 ± 7	2.1 ± 0.2	26 ± 1	9.0	2 ± 0.1	0.1	0	157	61-247

Table 2.6: **Systems requiring high natal kicks:** System properties and natal kick constraints for 22 compact objects (5 black holes and 17 neutron stars) that require natal kicks $v_{\rm NK} \geq 100\,{\rm km\,s^{-1}}$. M_1 and M_2 refer to the mass of the compact object and the companion star respectively. d & $|Z|$ indicate the distance to the source and the modulus of the Galactic scale height, both in kpc. We present the mean and 68% confidence intervals of the mass-loss-kick (Blaauw kick), and the minimum, mean, and 68% confidence intervals of the natal kick. All velocities are in ${\rm km\,s^{-1}}$.

Name	Type	$v_{\rm pec}$	M_1	M_2	$P_{\rm orb}$	d	$\lvert Z\rvert$	$v_{\rm NK}$		
			[$M_\odot$]	[$M_\odot$]	[days]	[kpc]	[kpc]	Min.	Mean	68%
2A 1822-371	NS-LMXB	254 ± 33	2.0 ± 0.4	0.5 ± 0.1	0.2	5.9 ± 0.9	-1.1	182	258	227-286
4U 1700-37	NS-HMXB	71 ± 11	2.0 ± 0.2	46 ± 5	3.4	1.5 ± 0.1	0.1	163	504	360-652
BW Cir	BH-LMXB	352 ± 99	7.6 ± 0	0.9 ± 0.3	2.5	27.5 ± 2.5	-1.3	267	366	297-442
Cen X-3	NS-HMXB	102 ± 4	1.6 ± 0.1	24 ± 1	2.1	6.9 ± 0.6	0	246	530	407-673
Cen X-4	NS-LMXB	419 ± 69	1.94 ± 0.9	0.34 ± 0.2	0.6	1.4 ± 0.3	0.6	372	447	398-500
Cyg X-2	NS-LMXB	164 ± 9	1.67 ± 0.2	0.6 ± 0.1	9.8	9.7 ± 1.4	-1.9	173	192	185-200
GRO 1655-40	BH-LMXB	162 ± 6	6 ± 0.4	2.5 ± 0.3	2.6	3.2 ± 0.4	0.1	162	192	182-201
GX 1+4	NS-LMXB	189 ± 8	1.4 ± 0.3	1.2 ± 0	1160.8	4.3 ± 0.9	0.4	176	289	272-310
GX 301-2	NS-HMXB	58 ± 4	1.9 ± 0.6	43 ± 10	41.5	3.6 ± 0.2	0	221	407	305-503
GX 339-4	BH-LMXB	166 ± 35	5.9 ± 3.6	1.1 ± 0.76	1.8	7.5 ± 2.5	-0.6	109	172	144-201
J1023+0038	NS-LM-PSR	131 ± 6	1.7 ± 0.2	0.2 ± 0.0	0.2	1.4 ± 0	1	145	182	169-194
J1048+2339	NS-LM-PSR	158 ± 35	2.0 ± 0.2	0.4 ± 0.0	0.3	2 ± 0.4	1.8	125	230	191-271
J1653-0158	NS-LM-PSR	178 ± 9	2.2 ± 0.2	0.01 ± 0	0.1	0.8 ± 0.2	0.4	246	404	315-481
J1723-2837	NS-LM-PSR	110 ± 11	1.2 ± 0.2	0.4 ± 0.1	0.6	0.9 ± 0	0.1	126	174	154-192
J1816+4510	NS-LM-PSR	165 ± 26	1.8 ± 0.11	0.2 ± 0.1	0.4	4.4 ± 0.9	1.8	143	173	154-193
J2129-0429	NS-LM-PSR	201 ± 24	1.7 ± 0.18	0.4 ± 0.0	0.6	2.1 ± 0.3	-1.2	192	232	209-252
MXB 1659-298	NS-LMXB	260 ± 204	2.1 ± 0.9	0.6 ± 0.3	0.3	9 ± 2	1.1	102	359	254-468
Sco X-1	NS-LMXB	168 ± 10	1.4 ± 0.3	0.4 ± 0.1	0.8	2.2 ± 0.1	0.9	158	177	168-186
Swift J1727.8-1613	BH-LMXB	207 ± 7	3.1 ± 0.1	0.8 ± 0	0.5	0 ± 0	0	201	218	211-224
XSS J12270-4859	NS-LM-PSR	131 ± 21	1.4 ± 0.3	0.3 ± 0.0	0.3	1.6 ± 0.3	0.4	131	196	167-226
XTE J1118+480	BH-LMXB	143 ± 11	7.5 ± 0.6	0.2 ± 0.1	0.2	1.7 ± 0.1	1.5	118	136	128-144
XTE J1814-338	NS-LMXB	171 ± 51	2 ± 0.5	0.2 ± 0.1	0.2	8 ± 1.6	-1.1	144	186	167-200

ID	$\upsilon_{\rm pec}$	$\upsilon_{\rm NK,lit}$	$\upsilon_{\rm NK,mean}$	$\upsilon_{\rm NK,68\%}$
1E 1145.1–6141	56 ± 10	50^{+85}_{-32} [86]	139	82 - 196
2FGL J1019.0–5856	31 ± 3	85^{+109}_{-39} [86]	43	29 - 56
4U 1538–52	77 ± 10	76^{+112}_{-53} [86]	286	106 - 433
4U 1700–37	71 ± 11	79^{+113}_{-56} [86]	504	260 - 652
4U 2206+543	28 ± 4	87^{+85}_{-35} [86]	33	10 - 56
A 0620–00	44 ± 7	20-43 [244]	14	4 - 23
B1259–63	25 ± 8	57^{+44}_{-21} [86]	26	8 - 43
Cyg X–1	22 ± 3	<75 [308]; 0-60 [21]	5	2 - 9
GRO 1655-40	162 ± 6	30-50 [206]; 40-140 [303]; 0-210 [21]; ≥62[211]	192	182 - 201
GRS 1124-684	119 ± 15	≥48 [211]	118	106 - 130
GRS 1915+105	32 ± 15	0-75 [21]; 0 [71]	3	1 - 4
GX 301–2	58 ± 4	136^{+194}_{-68} [86]	407	305 - 503
H 1705–250	221 ± 109	415-515 [244]; 295 [70]	221	144 - 298
IGR J00370+6122	23 ± 8	132^{+121}_{-51} [86]	50	41 - 48
IGR J08408–4503	39 ± 5	235^{+170}_{-91} [86]	143*	61 - 229
IGR J17544–2619	44 ± 4	142^{+161}_{-57} [86]	211	119 - 305
LS 5039	88 ± 3	162^{+202}_{-94} [86]	102	24 - 202
LS I +61 303	9 ± 4	88^{+57}_{-31} [86]	43	32 - 53
MAXI J1305–704	58 ± 22	30 [161]; ≥0[211]	38	16 - 62
MAXI J1820+070	72 ± 16	≥0 [211]	59	45 - 74
Swift J1727.8–1613	207 ± 7	220^{+40}_{-50} [252]; ≥77 [211]	218	211 - 224
Swift J1753	110 ± 57	110^{+69}_{-37} [315];76-243[5]	111	68 - 150
V404 Cyg	45 ± 3	0-45 [21]; <5 [38]; ≥0[211]	21	15 - 26
V4641 Sgr	92 ± 7	123 [250]; ≥23 [211]	72	49 - 93
Vela X–1	59 ± 7	59^{+92}_{-41} [86]	157	61 - 247
X Per	18 ± 8	17^{+25}_{-11} [86]	34	23 - 44
XTE J1118+480	143 ± 11	80-310 [90]; 93-106 [244]; ≥36 [211]	136	128 - 144

Table 2.7: **Literature Comparison:** Comparison between υ_{NK} values determined in this study and those quoted in literature [206; 303; 71; 90; 308; 244; 21; 250; 5; 161; 70; 38; 211; 315; 252; 86] - all velocities are in $\mathrm{km\,s^{-1}}$. *The natal kicks derived for IGR J08408–4503 are based on a system velocity $\upsilon_{\rm pec} \leq 40\,\mathrm{km\,s^{-1}}$ rather than the observed peculiar velocity (Table 2.4).

Chapter 3

Searching for non-interacting black holes

The mass of black holes underpins their entire existence, yet the distribution of stellar mass black holes in our Galaxy remains unclear. One of the issues associated with surveying black hole masses is that observations typically favour X-ray binaries, as their strong X-ray emission makes them beacons for accretion in a sky full of ordinary stars. This means any inferences on mass are subject to this selection bias and not necessarily applicable to all black holes within the Galaxy.

Section 1.4 describes the methods for determining the mass of black holes. These dynamical mass measurements, relying on observations of the radial velocity of the companion star, are not contingent on any interaction. To that end, the spectra of the luminous companion are just as useful in non-interacting systems. Any luminous stars thought to be coupled to a black hole can be studied, their motion detected and described, and the presence of a black hole may be confirmed or refuted.

In this Chapter, the state of the art astrometric mission *Gaia* is discussed, and its potential in finding black holes is outlined. The confirmation of the first astrometrically identified black hole [78] is discussed in Section 3.3, and this system acts as a blueprint for further searches.

Six systems, identified as interesting through the same methods implemented by El-Badry et al. [78], are subject to spectroscopic observations, and their radial velocities constrained. Disappointingly, none of these systems appear to host compact objects and the Gaia astrometric solutions appear to be poor fits to observational data. Section 3.4 describes these data and discusses the potential characteristics of each of these systems; they are most likely stellar binaries comprising two small $\leq 1.5 M_{\odot}$ stars. The implications

for this in the wider context of the *Gaia* mission is outlined at the end of the Chapter.

3.1 Identifying black holes without X-ray emission

Whilst the energetic emission from X-ray binaries makes them attractive targets for studies of black holes, they are not the only type of black holes within our Galaxy. Indeed, their contribution to the overall population of Galactic black holes (expected to be of order 100 million) remains unclear. There exists another group of black holes, also in binaries, that are widely separated from their companion star such that they do not interact. Their distance means there is no mass transfer, no related X-ray emission, and no obvious evidence of a black hole at all.

One could be forgiven for wondering, without this X-ray lighthouse, how we can hope to find them, let alone understand them. The answer, once again, lies in the dependable motion that is intrinsic to physics. Despite not accreting matter, these black holes still influence their companion stars; the laws outlined by Kepler and Newton are undeterred.

3.2 *Gaia* astrometric mission

The Global Astrometric Interferometer for Astrophysics (*Gaia*) is a European Space Agency observatory mission designed to use high-precision astrometry to create a detailed, three-dimensional map of our Galaxy [97]. Whilst not the first astrometric observatory, *Gaia* is pioneering; *Gaia* Data Release 3 (DR3) included the full astrometric solution (position, proper motion, distance) for over 1.4 billion sources, with magnitudes between 3 - 21, in addition to newly defined quality indicators [98]. The data release also included astrophysical parameters for over 450 million sources, such as effective temperature, colour, spectral type, and variability analysis.

However, it is well-established that huge swathes of stars exist in binaries; for these systems, the above model is insufficient. In DR3 a new class of objects was introduced; 800,000 'Non-Single Solutions'.

3.2.0.1 Non-Single Solutions

Gaia DR3 included over 800,000 sources with 'Non-Single Solutions' (NSS); that is, sources undergoing non-linear motion and orbital perturbations that were not adequately accounted for by fits of single stars. There exist numerous alternative models [121], which can be broadly characterised as follows:

Acceleration: These sources are better described using quadratic or cubic models than the linear models applicable for single stars, including $\vec{\gamma}$ to describe the curvature of motion, in the equation:

$$\vec{b}(t) = \vec{b}_0 + \vec{v}(t - t_0) + \frac{\vec{\gamma}}{2}(t - t_0)^2 \tag{3.1}$$

As is the case in Equation 1.12, $\vec{b}$ is the star's barycentric position and $\vec{v}$ is the constant space velocity, with '0' denoting the reference values.

These models are suited to longer-period binaries, and the abscissa w (defined as the astrometric coordinate along the *Gaia* scan axis) is usually described with:

$$\frac{\partial w}{\partial g_\alpha} = \frac{\partial w}{2\partial \alpha}\left[(t - t_0)^2 - \frac{\Delta T^2}{3}\right]$$
$$\frac{\partial w}{\partial g_\delta} = \frac{\partial w}{2\partial \delta}\left[(t - t_0)^2 - \frac{\Delta T^2}{3}\right]$$

where g_α and g_δ are the acceleration in the RA and Dec components, and ΔT indicates half the observing time across all transits of the star.

Variability Induced Mover (VIM): Photometric variability indicates the presence of a binary. This variability may appear as fluctuations in the total brightness of the source, or there may be additional observable motion of the photocenter. The equations of motion for these sources are described using the brightness fluctuations:

$$\frac{\partial w}{\partial D_\alpha} = \frac{\partial w}{\partial \alpha}\left[\frac{\tilde{\mathcal{F}}}{\mathcal{F}} - 1\right]$$
$$\frac{\partial w}{\partial D_\delta} = \frac{\partial w}{\partial \delta}\left[\frac{\tilde{\mathcal{F}}}{\mathcal{F}} - 1\right]$$

where $\tilde{\mathcal{F}}$ and $\mathcal{F}$ are the reference photometric flux (i.e. median of observed fluxes) and the photometric flux of a given transit (observation). D_α & D_δ are the location of the photocenter (RA and Dec components).

Orbital: Discovered by searching *Gaia*'s observations for periodic modulations that may be associated with binary motion. For these systems, the movement of the sources' photocenter displays elliptical variations around a common centre; these orbits are expressed in terms of the Thiele-Innes coefficients (for derivation, see Appendix C):

$$w = w_{\mathrm{B}} + (\cos E - e)\left(A\frac{\partial w_{\mathrm{B}}}{\partial \delta} + B\frac{\partial w_{\mathrm{B}}}{\partial \alpha}\right) + \sqrt{1 - e^2}\sin E\left(F\frac{\partial w_{\mathrm{B}}}{\partial \delta} + G\frac{\partial w_{\mathrm{B}}}{\partial \alpha}\right) \tag{3.2}$$

where w_B is the abscissa of the barycentre, A, B, F & G are the four primary Thiele-Innes coefficients, e is the eccentricity, and E the eccentric anomaly. From them, one can derive; the orbit's photocenter a_0, the inclination i, the ascending node Ω and the argument of periastron ω (not to be confused with the abscissa w). Along with the orbital period, source distance, and eccentricity (where applicable) determined by *Gaia*, these provide a complete description of a binary system, except for well-measured component masses. These solutions led to the first astrometrically identified black hole: *Gaia* BH1 (see Section 3.3).

Spectroscopic & Eclipsing: Binaries may be identified by Doppler variations in stellar spectra indicating binary motion, or fluctuations in luminosity due to the eclipse of one star by another.

3.2.0.2 Data Limitations

The process of deriving NSS for sources goes as follows: where the goodness-of-fit (GoF) for a Single Star Solution is poor, the data is tried against a series of increasingly complex models, until the GoF is acceptable. A source is rejected as a single star based on the GoF and is then fit using an 'Acceleration' solution; if this is unsuccessful based on the GoF, the next model tried is a 'VIM' model, followed by an 'Orbital' solution, and so on until a good fit is found.

This means that there are likely solutions for which more parameters could be known, with more complex solutions being fit (i.e. eclipsing or spectroscopic binaries). The cascading nature of the model fitting, however, means the first (and therefore simpler) suitable model was accepted, and this is how the source appears in the data set.

The *Gaia* data set includes estimates for mass, radius, luminosity, and age as derived from Astrophysics Parameters Inference System (Apsis [9]) & Final Luminosity Age Mass Estimator (FLAME [229]) models. The luminosity and effective temperature derived from the *Gaia* data, and the metallicity given in the *Gaia* catalogue are used to place the object on the Hertzsprung-Russell diagram, and evolutionary tracks are used to estimate the masses, radii, luminosities, and ages of each of the *Gaia* sources. This method is based on single stars and is therefore unlikely to be suitable for binary systems, which may consist of stars at different stages of evolution, different sizes, temperatures, luminosities, etc. Given that the *Gaia* data gives one set of parameters for the NSS source, it is impossible to know with any certainty whether these astrophysical parameters pertain to one of the objects within the binary, if both objects have identical parameters, or if the

measurements are the result of combined observations of the two components. Therefore, photometrically inferred parameters are, unfortunately, of limited use.

Nonetheless, these NSS sources provide a huge catalogue of (candidate) binary systems and, consequently, a wealth of information on binary evolution. They may also be used in the search for compact objects and for studying the evolution of these particular systems. Such systems being identified using astrometry provides a unique opportunity to study compact objects in non-interacting systems (i.e. where the luminous stellar companion is sufficiently far from the compact object that accretion processes are absent). Expanding the population of known compact objects beyond X-ray binaries to include such systems is vital in developing theories of binary evolution, pre-supernova interactions, natal kicks & related supernovae mechanisms, & expected gravitational wave populations.

Given that our Galaxy is expected to harbour of order 100 million stellar mass black holes, the run-up to DR3 was characterised by huge excitement. Individual search strategies aside, *Gaia* DR3 was sure to contain scores of black holes and a wealth of information on compact objects and the binaries that host them.

3.3 Gaia BH1

3.3.1 Identification of Gaia Black Hole 1

In October 2023, El-Badry et al. [78] presented their findings of a $9.6 \pm 0.18\,\mathrm{M}_\odot$ black hole, identified through analysis of the astrometric solutions in the *Gaia* NSS catalogue. Specifically, they searched the catalogue of NSS systems with *Orbital* solutions for systems with a large apparent semi-major axis (determined by the elliptical motion of the photocenter) compared to their orbital periods, which indicate a large central component (see Figure 3.1).

Using archival observations and dedicated spectroscopic follow-up of a handful of promising black hole candidates, they characterised one system as a binary consisting of a black hole and solar mass G-type star, with a semi-major axis of 1.4 au (corresponding to an orbital period of 185 days, in good agreement the period presented in the *Gaia* catalogue) and a moderate eccentricity (~ 0.4); this has since been designated Gaia BH1.

As one of the first dynamically confirmed non-interacting compact object binaries, Gaia BH1 marked a major advancement in the field and highlighted the promise of using high-precision astrometry in the search for such systems. That being said, this system is

not without controversy, and there remains significant discussion around the system's characteristics and the pathways through which it may have formed and evolved.

3.3.2 Evolution of Gaia BH1

The evolutionary history of Gaia BH1 is far from obvious; given the lack of observational data, the evolution of non-interacting compact objects and any deviation from the channels associated with X-ray binaries are poorly understood. The present-day orbital separation implies previous interaction between the companion star and the large ($\geq 20\,\mathrm{M}_\odot$) black hole progenitor. A sub-solar star is expected to be engulfed during a common envelope phase of pre-supernova binary evolution, ultimately resulting in its destruction.

That the system apparently survived this common envelope phase seems only plausible in the case of high-efficiency common envelope ejections. The ratio of the separation between the two components of the binary before and after a common envelope phase is described by the following:

$$\frac{\alpha_f}{\alpha_i} = \frac{M_c}{M_1}\left(1 - \frac{2M_e}{\alpha\lambda r_L M_2}\right)^{-1} \tag{3.3}$$

where M_1 is the total mass of the compact progenitor (comprising core mass, M_c, and envelope mass, M_e), M_2 is the companion mass, and r_L denotes the Roche lobe radius. Constants α & λ describe the fraction of the companion star's energy that is used to eject the black hole progenitor's envelope and the binding energy of this envelope respectively. The modelling presented in El-Badry et al. [78] implies a scenario where $\alpha \approx 14$ - the physical interpretation of this is that an additional source of energy is required to eject the envelope, which currently eludes explanation.

Since this initial publication, there have been a number of studies attempting to understand the evolutionary channels through which this system formed. Kotko et al. [170] suggest that a common envelope scenario is equally probable to formation due to dynamical capture in a stellar cluster; the former does not require $\alpha > 10$ due to the apparently low binding energy of the envelope. The study by Kotko et al. [170] suggest Gaia BH1 (and Gaia BH2) favour moderate natal kicks, 20-40 $\mathrm{km\,s^{-1}}$. Alternatively, the common envelope conundrum was addressed by Generozov and Perets [104], which proposed that if Gaia BH1 was part of a hierarchical triple system, the common envelope phase could be avoided, although the presence of a triple was reported to be unlikely in Nagarajan et al. [212].

As discussed previously, population synthesis software is a valuable tool in understanding the evolution of binaries. However, Gaia BH1 proved difficult to replicate with

COSMIC from general populations; only a very targeted simulation was able to produce systems resembling Gaia BH1, implying a narrow region of parameter space in which this system may have formed. These simulations include two distinct evolutionary pathways, both of which result in systems in which masses and orbital periods are (somewhat) consistent with the observed values for Gaia BH1 (though the systemic velocity and eccentricity remain troublesome).

Each of these evolutionary pathways is briefly summarised below. Table 3.1 shows the system parameters at ZAMS, just prior to supernova, and after supernova for systems analogous to Gaia BH1.

Table 3.1: **Gaia BH1 progenitor properties:** as identified through population synthesis investigation using COSMIC.

	Common Envelope			**Direct Supernova**		
	ZAMS	Supernova	Post-SN	ZAMS	Supernova	Post-SN
Primary Mass [$M_\odot$]	25	19	5.1	22.1	18.1	8.2
Secondary Mass [$M_\odot$]	1.7	1.8	1.8	0.7	0.8	0.8
Orbital Period [days]	2500	4.1	205	3250	4480	224
System Velocity [$\mathrm{km\,s^{-1}}$]		260			31	

3.3.2.1 Common Envelope Channel:

In this scenario, the initial binary likely had a primary mass of around $25\,M_\odot$; a mass ratio of around 14; and a period of 2500 days. The radius of the primary expands such that it supersedes its Roche lobe, and mass-transfer begins (this has been considered unlikely when considering the metallicity of the luminous star [78]). This shrinks the period down to only a few days, and the majority of systems merge during this phase (although it is not exactly clear if there is any definitive parameter space that causes these mergers). The primary loses a significant amount of mass during this phase (which results in smaller masses post-SN), some of which is gained by the secondary, and eventually undergoes core-collapse SN.

Following the supernova, the fate of binaries is highly dependent on the natal kicks they receive. Systems that evolve to be analogous to BH1 receive a natal kick in excess of $125\,\mathrm{km\,s^{-1}}$, resulting in system velocities well above $150\,\mathrm{km\,s^{-1}}$, as well as highly eccentric orbits (0.75-0.95). Whilst other systems may survive if they receive smaller kicks, the vast majority merge.

3.3.2.2 Direct Supernova Channel:

Though the common envelope phase is often considered synonymous with compact object evolution, there exists a potential evolutionary channel involving no mass transfer prior to the formation of the compact object [157]. This 'direct supernova' channel is thought to be a viable pathway for LMXBs, and is characterised by widely separated binaries in which neither star exceeds its Roche lobe. Survival of the binary is highly dependent on the natal kick magnitude and direction - it must be fine-tuned such that the binary is not disrupted (despite potentially significant mass loss from the compact progenitor) and, for the case of Gaia BH1, result in an orbital period that remains wide enough to preclude mass transfer. This formation channel appears to be feasible in the case of Gaia BH1.

Here, the initial binary hosts a primary star of mass of around $22\,M_\odot$; a mass ratio of around 28; and a period of 3250 days. This widely separated binary evolves without interaction; as the primary evolves into a giant and begins core helium burning there is a decrease in orbital period (a few hundred-1000 days). Eventually, the primary undergoes a core-collapse supernova; 82% of simulated systems were either widened or disrupted as a result of the supernova. Of the remainder, it is only those that shrink to at least 60% of their supernova orbital separation that go on to resemble Gaia BH1. As the newly formed non-interacting black hole binary evolves, the orbit shrinks further to a period of a few hundred days (i.e. that which we observe). As the orbital separation continues to decrease, some of these systems will evolve to interact via Roche Lobe overflow.

This appears to be the preferred evolutionary channel, and it is only formation via a direct supernova mechanism that allows for systems with a primary mass greater than $6\,M_\odot$, as the primary progenitor does not suffer the same mass loss as in the CE channel.

Whilst recreating systems with masses and orbital periods that are consistent with the observed BH1 characteristics is possible (albeit challenging), the observed peculiar velocity and eccentricity are at odds with predictions, and an evolutionary pathway involving a moderate kick and eccentricity remains elusive.

If Gaia BH1 underwent a common envelope phase prior to supernova, then a kick of greater than $125\,km\,s^{-1}$ must have been imparted to the system for it to have survived this phase and gone on to form the observed binary. This large kick results in a system with a peculiar velocity in excess of $150\,km\,s^{-1}$, which is far greater than the observed value. Alternatively, if Gaia BH1 was formed via a direct supernova, the magnitude of the imparted natal kick cannot have exceeded $50\,km\,s^{-1}$, otherwise, the system would have been disrupted due to its wide separation. The resulting peculiar velocity would be closer to $30\,km\,s^{-1}$, below the observed value of $75\,km\,s^{-1}$.

That the observed peculiar velocity of Gaia BH1 lies outside the regions of (apparently) explainable peculiar velocities is puzzling, to say the least. The evolution of Gaia BH1 remains uncertain, and the system highlights how much remains to be understood about binary evolution. It is apparent that the system can only be produced from a very narrow range of initial conditions; however, whether the system interacts prior to the supernova or not cannot be determined from the available data. The observed masses of the binary components seem more akin to the simulated systems that do not experience a common envelope phase, and one might naively assume this is a smoking gun for that evolutionary pathway. However, the kinematics and eccentricity of the system cannot be reproduced in either scenario. The uncertainty regarding how supernova kicks affect the system and its future kinematics makes it difficult to ascertain which (if any) evolutionary channel could result in a peculiar velocity similar to the measured value and whether it is fair to rule out potential pathways based on the velocity measurements alone.

Finally, there is always the potential that the observed characteristics of Gaia BH1 are incorrect. The wide orbit means constraining system parameters via radial velocity measurements alone is challenging. The initial fits to radial velocity data appear to rely heavily on the *Gaia* astrometrically determined parameters, and it may be the case that the eccentricity or even orbital period has been incorrectly measured. This can only be addressed with more data and radial velocity measurements spanning the full nominal orbital period; future observations are essential in understanding this system and its history.

3.3.3 Gaia BH2

Following the identification of Gaia BH1, another candidate system from the same sample was later identified as a non-interacting black hole. *Gaia* BH2 [79], is thought to be a $8.9 \pm 0.3\,\mathrm{M}_\odot$ black hole, accompanied by a solar mass red giant, orbiting with a period of 1277 days, making it the longest-period binary to host a compact object discovered to date.

This identification also relied upon combined astrometry and radial velocity observations; however, unlike Gaia BH1 the phase coverage is limited to only 10% of the assumed orbit. The radial velocity curve used to characterise the central object relies heavily on the orbital properties measured by Gaia, including the orbital period (which exceeds the timespan of astrometric observations). Consequently, any inaccuracies in the *Gaia* astrometry may impact the radial velocity fit and inferred black hole mass and one ought

to bear this in mind when making inferences on black hole and binary evolution from such a system.

3.3.4 Gaia BH3

In 2024, the *Gaia* collaboration published their findings of a $33\,M_\odot$ black hole existing in a binary with an orbital period $P_{\rm orb} = 11.6\,{\rm yr}$, in advance of the larger data release.

3.4 Searching for non-interacting black holes

3.4.1 Astrometric searches

As of March 2025, Gaia BH1, Gaia BH2, and Gaia BH3 remain the only dynamically confirmed black holes identified through the astrometry provided in *Gaia* DR3 (though there exist several other candidates and samples which may yet prove to be compact in nature). Searching the putative binaries for systems with large mass functions has the highest success rate when searching for black holes; Gaia BH1 exists as a blurred photograph of a needle, and the haystack remains formidable and enticing in equal measure.

The NSS catalogue published by the *Gaia* collaboration includes 169,227 sources flagged as *Orbital* or combined *Orbital & Spectroscopic* solutions. The inclusion of systems where the NSS solution is somewhat more complex, flagged as one of *OrbitalAlternative, OrbitalAlternativeValidated, OrbitalTargetedSearch, OrbitalTargetedSearchValidated*, increases the sample size used by El Badry et al. by ~ 1000. For a more detailed discussion of the NSS processing pipeline and related astrometric solutions, uncertainties, and implications, refer to Section 1.6.3.

3.4.1.1 Selection Criteria

As discussed in Section 1.4, the nominal orbital periods and semi-major axes may be used to estimate the mass of the central object in the binary; the small number of systems with a predicted mass $M_1 \geq 1\,M_\odot$ are easily distinguishable by eye, existing above the locus of sources (see Figure 3.1). Having identified systems which may host super-solar components, these underwent 'quality' cuts with the aim of focusing on the systems most likely to be of interest.

Candidates were selected from the subsample provided that they met the following criteria:

- Visibility Periods Used > 12
- Parallax > 0
- Parallax Over Error > 12
- Well-measured semi-major axis: $a_0/a_{0,error} > 4$
- $10 \leq P_{\rm orb} \leq 350$ days
- Periods unlikely to be related to the *Gaia* scanning period: $P_{\rm orb} - 2 < k \times 63 < P_{\rm orb} + 2$ (where k is some integer and $\rm P_{orb}$ is measured in days).

These cuts were chosen to: ensure the robustness of the data (i.e. from good parallax and orbital elements measurements); discard candidates that would require long-term observations to verify orbital periods; and to exclude those whose periods are likely to be an artefact. This latter point is significant; Gaia BH1 was excluded from previous studies

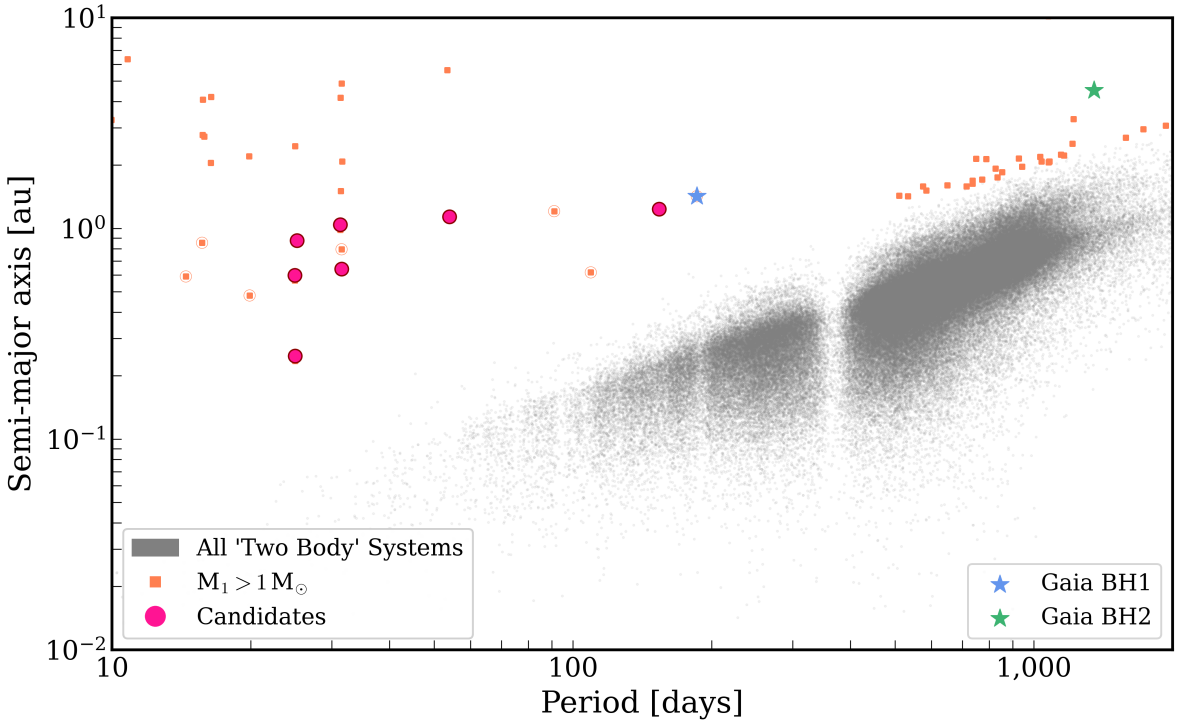

Figure 3.1: **Candidate non-interacting black holes**: Sample of all *Gaia* NSS sources with *Orbital* solutions described by the Thiele-Innes coefficients). The semi-major axis, a_0, is determined from the orbital motion of the photocenter and the distance. Systems whose parameters suggest a massive central object are highlighted, and the 7 candidates selected for follow-up observations are indicated as pink circles. Gaia BH1 & Gaia BH2 are indicated with a blue and green star respectively.

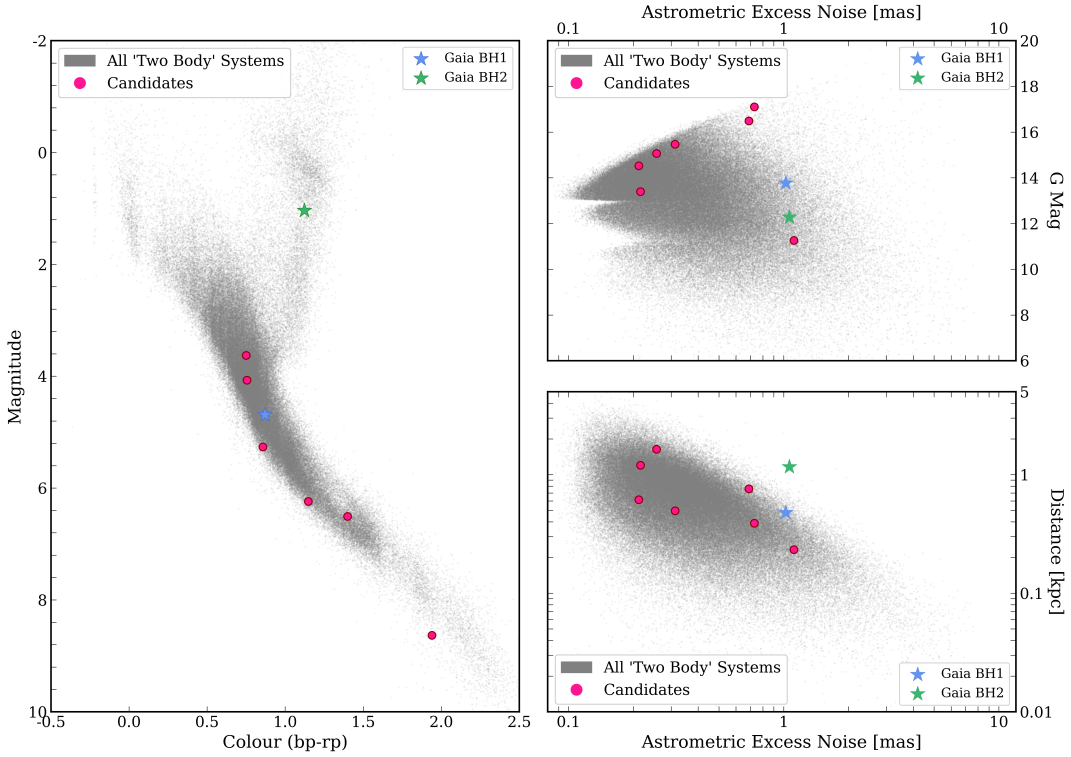

Figure 3.2: **Candidate non-interacting black holes**: Sample of all *Gaia* NSS sources, with the 7 candidates selected for follow-up observations indicated as pink circles, and Gaia BH1 & Gaia BH2 are indicated with a blue and green star as before. Their positions on the Hertzsprung–Russell diagram identify them as main sequence stars (with the exception of Gaia BH2, accompanied by a red giant). None of the sources show significant astrometric excess noise with respect rest of the NSS catalogue.

due to its orbital period being close to an integer multiple of the *Gaia* scanning law (∼63 days). Previous papers have highlighted this as a potential source of contamination, suggesting that systems with periods that fall close to the scanning law are likely to produce seemingly high mass functions but be non-physical [121; 135]. Whilst subsequent radial velocity campaigns have verified the orbital period of Gaia BH1, there remains reason to be cautious when studying systems that may be influenced by this artifice. Ultimately, these quality cuts are perhaps stricter than necessary, in order to identify a handful of the best candidates for spectroscopic follow-up. Sources that were rejected based on the above may still be good candidates for non-interacting black holes, and may be subject to further investigation in the future.

The decision to exclude sources with orbital periods longer than 1 year was based on a) the reliability of measured orbital periods which exceed the *Gaia* DR3 baseline and b) considering the practicalities of follow-up observational campaigns. Gaia BH2 is subject

to scrutiny, given that its orbital period is longer than the nominal *Gaia* DR3 baseline. El-Badry et al., 2023 comment that Gaia BH2 suggests the *Gaia* baseline of 1000 days does not preclude reliable analysis of binaries with periods in excess of 1000 days [79] [1]. However, given the extensive time coverage needed to confirm such long orbital periods through radial velocity measurements (particularly for eccentric systems such as BH2), Gaia BH2 and two other sources are excluded from the sample, leaving 12 sources. None of these have been subject to significant previous study and there are no co-located X-ray sources.

3.4.2 Observations

Whilst the astrometric solutions provide promising, high-precision constraints on the properties of these binaries, dedicated radial velocity campaigns remain the most effective and reliable way to identify and characterise the orbital period and component masses.

The Southern Africa Large Telescope (SALT) is a 9.2-meter telescope, the largest in the southern hemisphere, optimised for spectroscopy in the 3200-9000 Å wavelength range.

7 of 12 sources had declinations $\delta < +10°$, making them visible to the SALT observatory - these are highlighted in Figures 3.1 & 3.2. These sources are summarised in Table 3.2. These 7 candidates were then subject to an observing campaign using the Robert Stobie Spectrograph (RSS) [39; 36]. The aim of this investigation was to use high-precision optical spectra to constrain the radial velocities associated with orbital motion and derive mass functions for each system, which could be used to identify non-interacting black holes similar to Gaia BH1.

For this campaign, observations were carried out using the pg1300 grating, with a resolving power 1200-2000 over a wavelength range of 4900-7000 Å, encompassing the Hα line (6562 Å) as well as 5000–5900 Å region which includes typical metal lines (Mg, Na, etc.).

Given the stars observed had magnitudes ranging 11-16, exposure times of 500s translated to signal-to-noise ratios of $\sim$100. The rms of the wavelength calibration ranged 0.1-0.2 across observations, and the orbital velocity of these stars was therefore

[1] They also comment that the fact Gaia BH1 & BH2 have orbital periods at both long- and short-period edges of the observational sensitivity curve is suggestive of a bimodal distribution of non-interacting binary periods, with a dearth of sources with $P_{\rm orb}$=1–3 yrs. Drawing conclusions on the intrinsic period distribution of these binaries seems premature, given that there are only 2 robust candidates (neither of which have radial velocity measurements encompassing all phases); future observations & candidates will allow for a more developed understanding of period distributions.

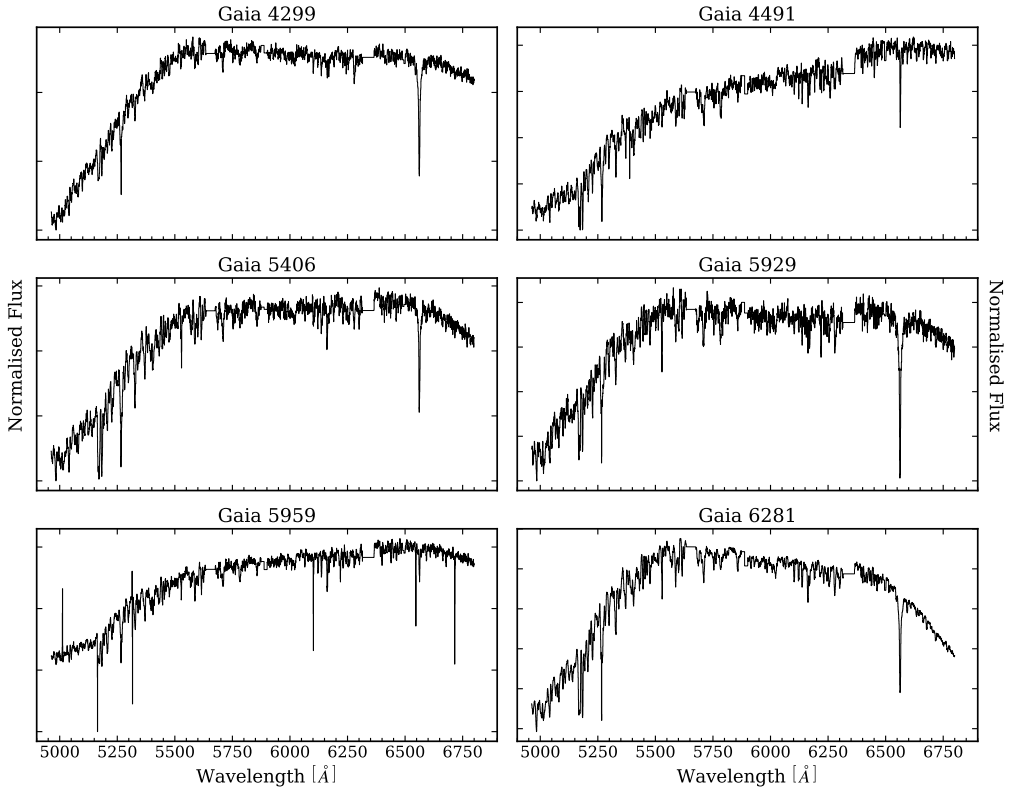

Figure 3.3: **SALT spectra for candidate non-interacting black holes**: Optical spectra for 6 of 7 candidate non-interacting black holes, selected based on *Gaia* measurements of orbital periods and semi-major axes.

measurable to within $10\,\mathrm{km\,s^{-1}}$, which is sufficient to understand the nature of these systems and to determine the presence of a compact object for most configurations of systems like Gaia BH1.

3.4.3 Radial velocity measurements

Optical spectra for 6 of 7 sources were obtained, the number of epochs for each source ranging 4-10 (see Table 3.3). Typical spectra are shown in Figure 3.3.

Table 3.3: **Summary of SALT observations:** the date of observation (including Heliocentric Julian Date, HJD); the ID of the source in question; the observed radial velocity (V_r); and the heliocentric velocity (RV Helio), referring to the motion of the source relative to the Sun.

Date	HJD	Source	V_r	RV Helio

			[km s^{-1}]	[km s^{-1}]
01/05/2023	2460066.34	Gaia 6281	1 ± 3	3.57
01/05/2023	2460066.41	Gaia 5929	-3 ± 6	16.09
01/05/2023	2460066.43	Gaia 5959	-90 ± 4	19.14
02/05/2023	2460066.65	Gaia 4299	-48 ± 9	25.76
09/05/2023	2460073.63	Gaia 4299	-50 ± 5	25.39
09/05/2023	2460073.66	Gaia 5959	-80 ± 5	16.03
09/05/2023	2460074.36	Gaia 5406	-33 ± 5	-12.2
09/05/2023	2460074.42	Gaia 5929	-8 ± 4	13.25
10/05/2023	2460074.53	Gaia 4491	21 ± 2	13.2
15/05/2023	2460080.41	Gaia 5959	-2 ± 5	13.7
16/05/2023	2460080.66	Gaia 4299	-65 ± 4	24.33
16/05/2023	2460081.33	Gaia 5406	-16 ± 5	-13.46
17/05/2023	2460081.53	Gaia 4491	-5 ± 3	10.5
19/05/2023	2460084.30	Gaia 6281	-31 ± 3	-5.4
19/05/2023	2460084.37	Gaia 5929	-40 ± 5	9.45
23/05/2023	2460088.30	Gaia 5406	-22 ± 5	-14.52
26/05/2023	2460091.47	Gaia 4491	43 ± 7	6.66
27/05/2023	2460091.61	Gaia 5959	-24 ± 4	8.41
27/05/2023	2460092.35	Gaia 5929	-32 ± 4	6.18
01/06/2023	2460096.56	Gaia 4299	-61 ± 5	21.07
05/06/2023	2460101.48	Gaia 6281	-14 ± 3	-13.89
06/06/2023	2460101.55	Gaia 5929	-12 ± 4	-2.06
06/06/2023	2460102.33	Gaia 5959	-47 ± 4	3.89
11/06/2023	2460106.56	Gaia 4299	-32 ± 3	18.52
20/06/2023	2460116.23	Gaia 5406	-16 ± 5	-16.71
22/06/2023	2460118.41	Gaia 4491	0 ± 3	-4.54
24/06/2023	2460120.21	Gaia 6281	-4 ± 4	-20.83
24/06/2023	2460120.28	Gaia 5959	-60 ± 4	-4.52
01/07/2023	2460126.51	Gaia 4299	-35 ± 3	11.54
01/07/2023	2460127.40	Gaia 6281	3 ± 4	-23.57
02/07/2023	2460128.47	Gaia 5929	-21 ± 4	-8.34
04/07/2023	2460130.25	Gaia 5959	-44 ± 4	-9.02
06/07/2023	2460132.38	Gaia 4491	-	-10.09
10/07/2023	2460136.46	Gaia 4299	-42 ± 4	7.64

10/07/2023	2460136.47	Gaia 5929	-38 ± 4	-12.2
11/07/2023	2460137.36	Gaia 6281	7 ± 4	-26.18
13/07/2023	2460139.38	Gaia 4491	16 ± 3	-12.72
21/07/2023	2460147.35	Gaia 6281	-1 ± 4	-28.15
22/07/2023	2460148.33	Gaia 4491	20 ± 3	-15.75
01/08/2023	2460158.31	Gaia 6281	16 ± 4	-29.3
13/08/2023	2460170.27	Gaia 4491	14 ± 4	-21.63
13/08/2023	2460170.29	Gaia 6281	21 ± 4	-29.54
13/08/2023	2460170.39	Gaia 5959	-7 ± 4	-23.92
14/08/2023	2460171.26	Gaia 4491	-9 ± 4	-22.02
14/08/2023	2460171.28	Gaia 6281	5 ± 2	-29.44
19/08/2023	2460176.24	Gaia 4491	5 ± 3	-22.73
23/08/2023	2460180.38	Gaia 5959	-2 ± 6	-26.12
03/09/2023	2460191.35	Gaia 5959	-5 ± 4	-27.64

3.4.3.1 Determining Radial Velocities

Radial velocities may be deduced from spectra in various ways, with the most fruitful results incorporating multiple techniques.

Line Fitting: Each of the spectra shows absorption features associated with various metals and the Hα line (see Figures 3.3 & 3.4) - the latter is the strongest spectral feature in all observations, with relative change in flux $\sim$ 40%, as shown in Figure 3.5. These absorption lines may be fit as Lorentzians, and their centroids constrained and compared to the nominal rest wavelengths. These lines may be fit independently of one another or collectively (i.e. fit with consistent velocity variation regardless of wavelength) - Figure 3.6 demonstrates line fitting techniques for spectrum. Whilst fitting individual lines may offer more precise estimates of radial velocities (particularly in the case of the well-defined Hα line), fitting all strong absorption features collectively is favourable, offering radial velocity measurements that are less susceptible to inter-epoch variability of individual lines, at the expense of somewhat larger errors.

Cross Correlation: Radial velocities can also be determined by cross-correlating the observed spectra with either a template (of the same spectral type as the star in

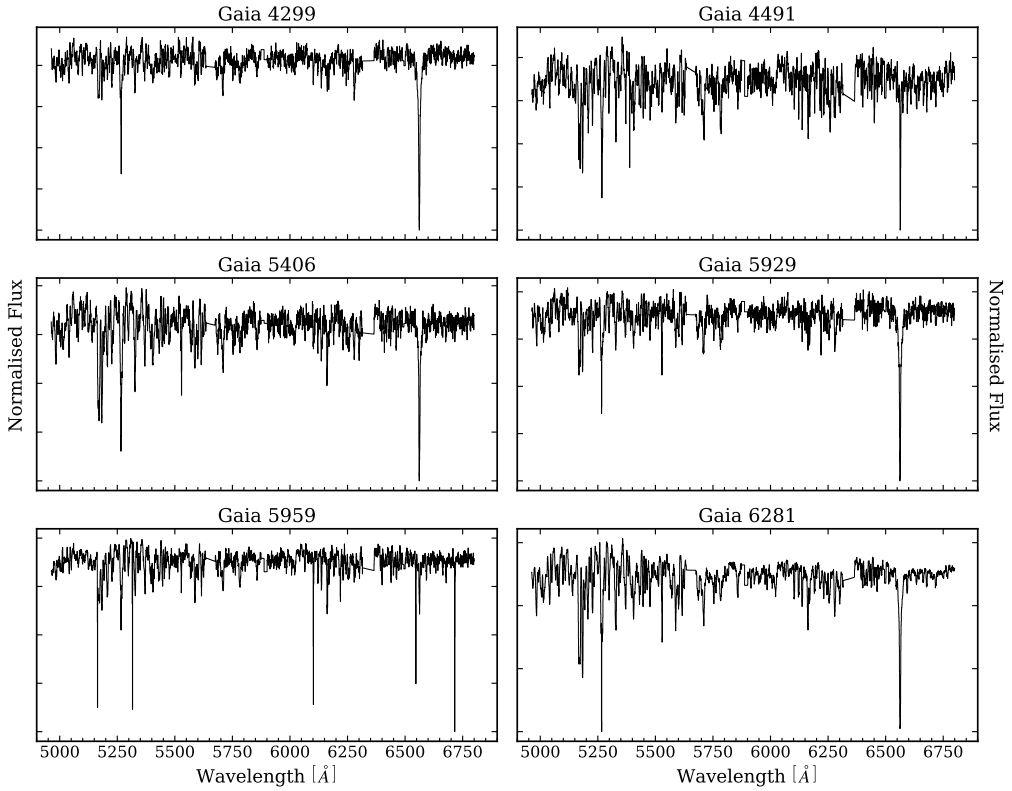

Figure 3.4: **SALT spectra for candidate non-interacting black holes**: Same as Figure 3.3, with background continuum subtracted to better highlight absorption features associated with the star. Background was subtracted by fitting the continuum to a polynomial and subtracting this from the spectrum.

question) or a spectrum from some previous epoch of the same source - Figures 3.7 & 3.8 demonstrate cross-correlation analysis of one system (G6281). Whilst the former provides a measurement of radial velocities compared to a stationary system at rest, the latter offers only *relative* changes in velocity. Though this must be accounted for when fitting radial velocity curves, it has the advantage of excluding any additional velocity associated with the motion of the entire system around the Galaxy.

3.4.3.2 Validating wavelength calibration

The wavelength calibration for each spectrum can be validated by checking the observed wavelengths (and consequently velocities) of telluric lines; that is, absorption features associated with the composition of Earth's atmosphere. These lines ought to be consistent between epochs and exhibit no changes in centroid wavelength (within errors). The telluric features present in all spectra showed no inter-epoch variation in wavelength, implying

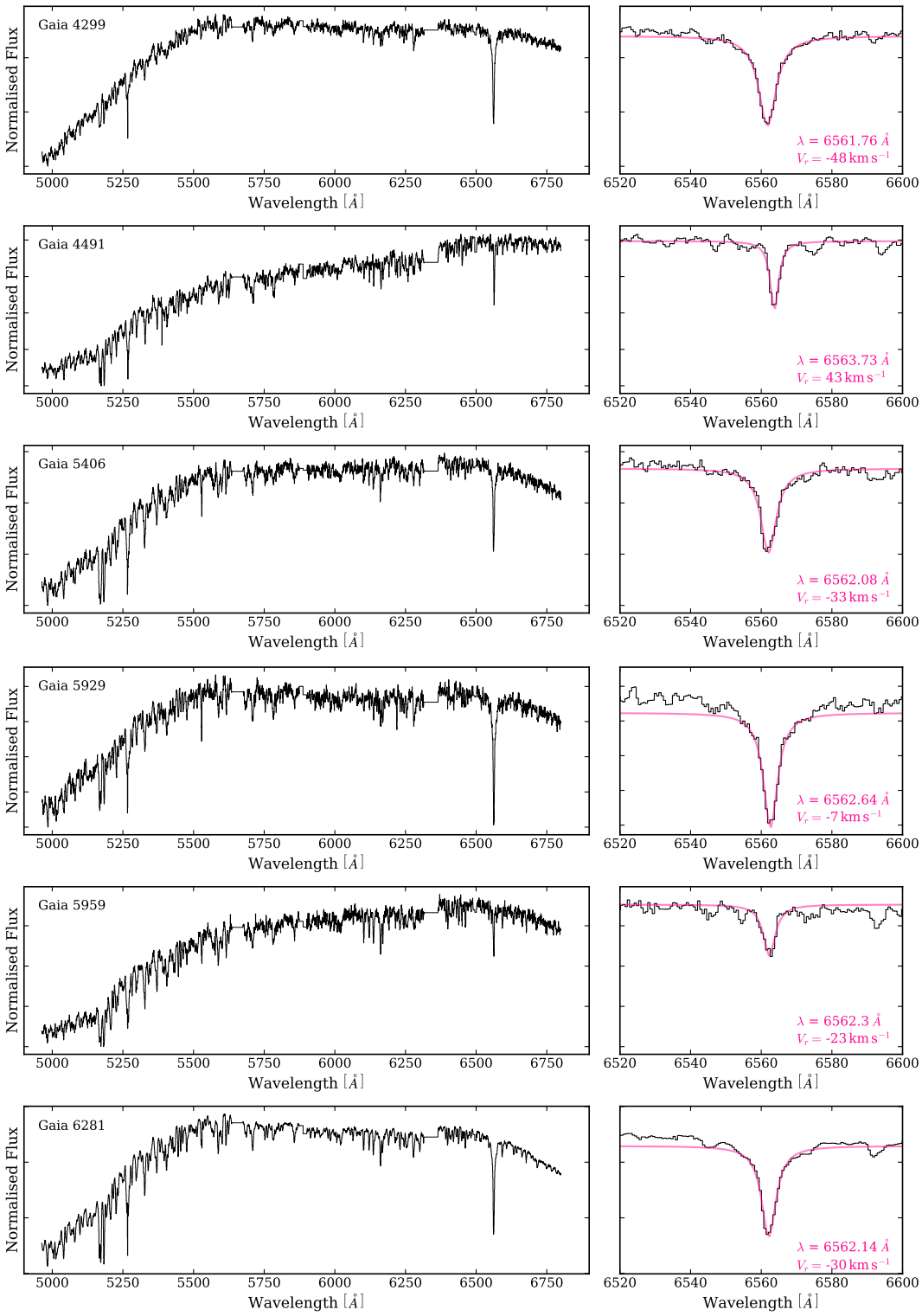

Figure 3.5: **SALT spectra and Hα absorption line**: Optical spectra of each of the 6 sources (left). Hα absorption feature around 6562.8 Å fit with a Lorentzian (right), including the associated radial velocity (based on only this feature).

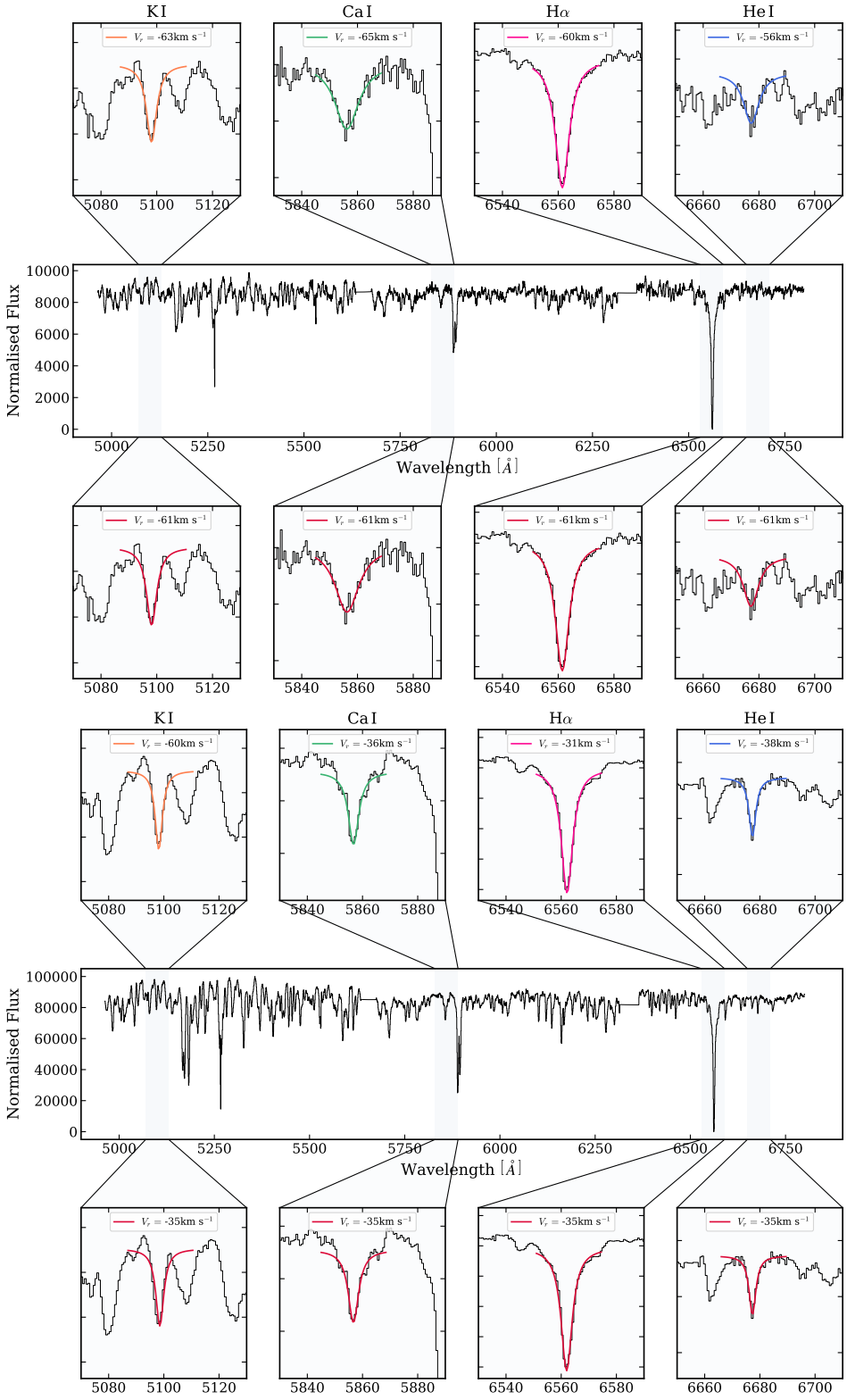

Figure 3.6: **SALT spectra line-fitting**: Typical spectrum (with background continuum subtracted) of two candidates. Upper panels show independent fits of absorption features, lower panels show results of combined fitting, with multiple lines fit to the same Lorentzian.

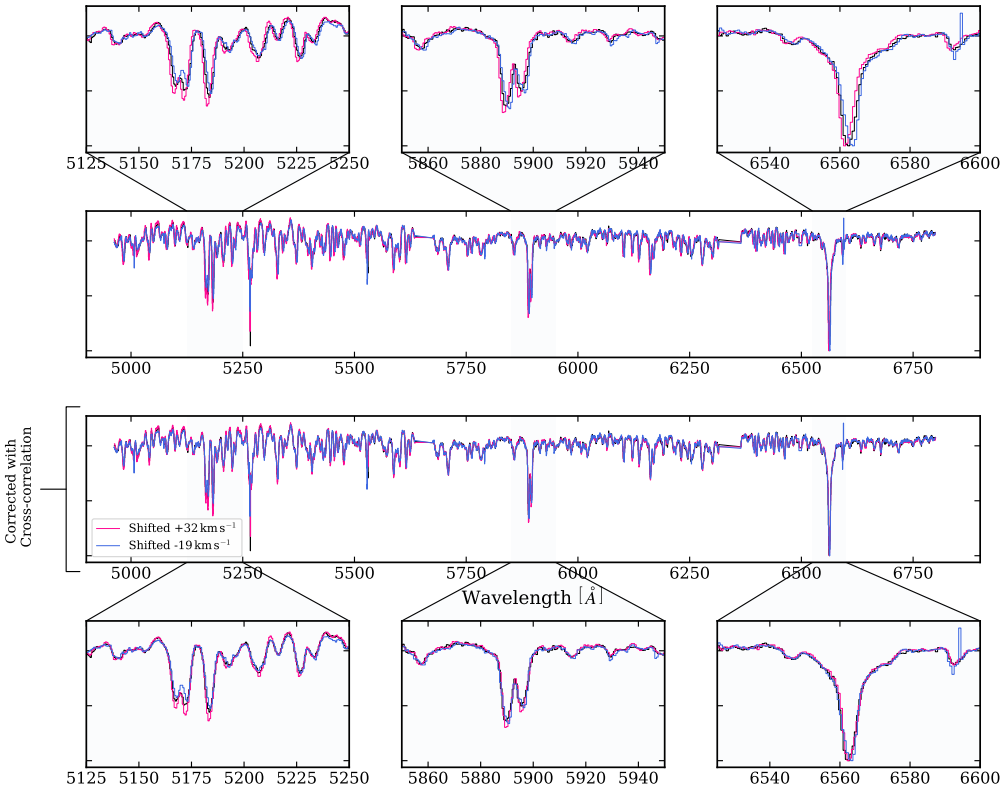

Figure 3.7: **Cross-Correlating Spectra**: Upper panels show the entire spectrum and some absorption features (associated with magnesium, sodium, and hydrogen) for three observations of G6281, with inter-epoch shifts in velocity identifiable by eye. Lower panels show spectra and line features after two epochs have been red-shifted according to the results of the cross-correlation (i.e. by 32 km s^{-1} and -19 km s^{-1} respectively).

consistent wavelength calibration for each spectrum and, therefore, authenticating any inferences made by studying absorption features associated with the visible star (e.g. see Figure 3.9).

3.4.3.3 Resultant Radial Velocities:

The observed radial velocities and associated errors are summarised in Table 3.3. Errors are generally well-constrained, typically averaging 5 km s^{-1}.

3.4.4 Fitting orbital solutions

There exist numerous techniques to fit radial velocity curves to data. `Joker` is a publicly available Monte Carlo sampler, developed to generate posterior samplings of Keplerian orbits given radial velocity observations of stars [234], and is the method employed here.

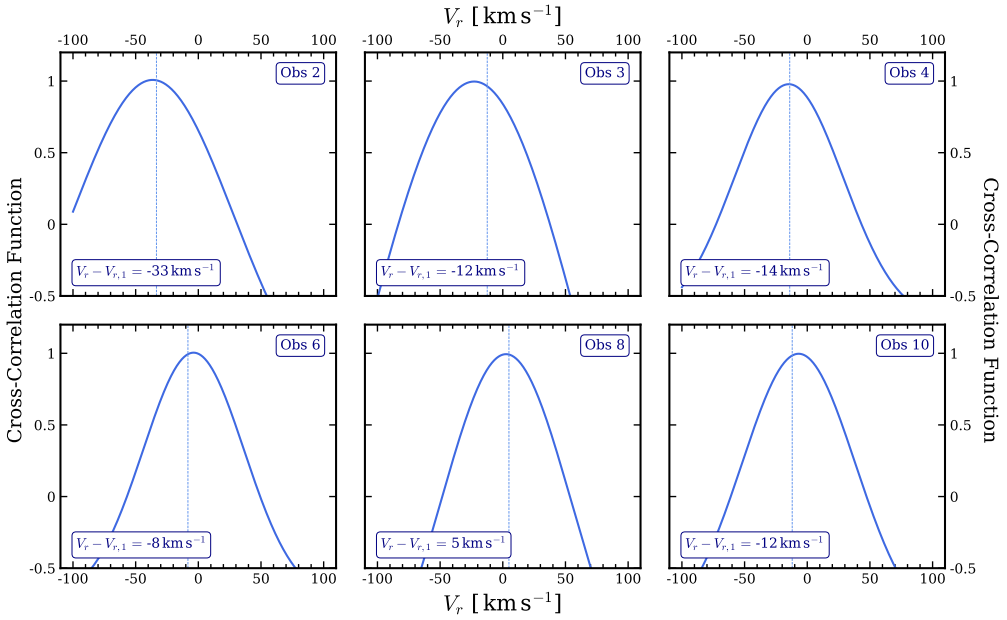

Figure 3.8: **Cross-Correlating Multiple Epochs**: 6 spectra from source Gaia 6281, cross-correlated against a template epoch. The peak of the Gaussian indicates the best-fit cross-correlation value, corresponding to the radial velocity shift from the template spectrum (in this case, the first observed spectrum).

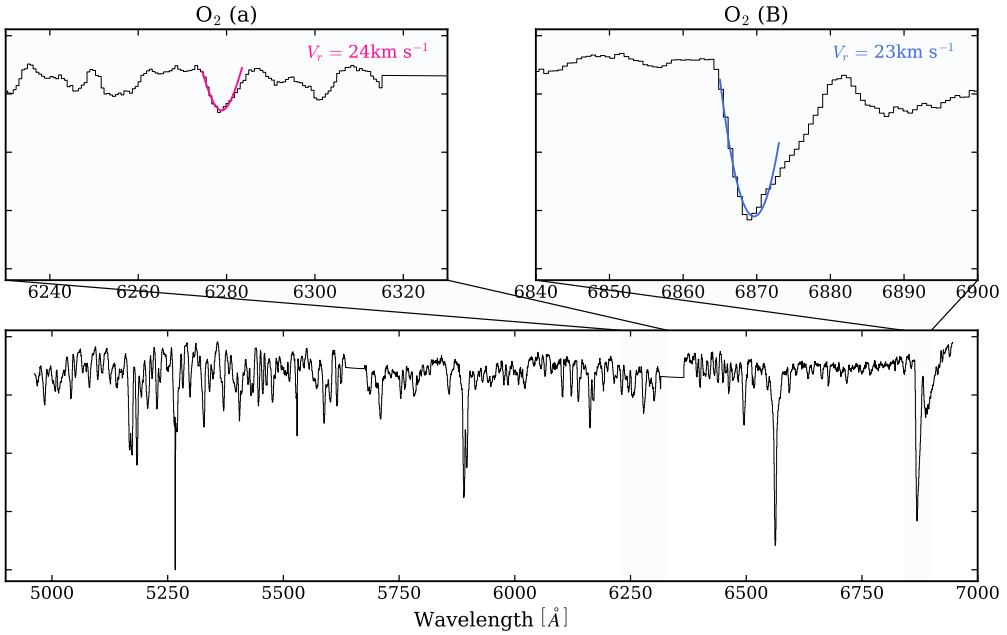

Figure 3.9: **Telluric lines**: Epoch # 5 of source Gaia 6281. Upper panels show absorption features associated with Earth's atmosphere (Fraunhofer lines at 6278 Å & 6869 Å). Fitting these lines with Lorentizans results in radial velocities consistent with those applied during reduction to account for heliocentric correction (see Table 3.3).

3.4.4.1 *Gaia* solutions

The *Gaia*-derived astrometric solutions offer a prediction of the systems' parameters and, therefore, the expected radial velocity curves. These solutions (in particular, the tightly constrained orbital periods) provide a natural starting point for fitting the data.

In practice, this involves using `Joker` to fit radial velocity curves and restricting the parameter space such that the fits match the orbital periods measured by Gaia (± 3 days). Whilst the Thiele Innes coefficients also provide estimates of semi-major axis (and, consequently, radial velocity semi-major amplitude) and eccentricity, these are *not* used as priors for fitting.

The results of fitting radial velocity curves using the *Gaia* period estimates are shown in Figures 3.10 & 3.11, and the mass functions derived from these fits are shown in Figure 3.12. Of six systems, the nominal orbital periods presented by *Gaia* are consistent with observations for only three sources. Details of these fits are summarised below.

Gaia 4299: The radial velocities for each of the seven epochs are well-constrained, with errors of order 10%. The *Gaia* orbital period of 31.5 days is consistent with observations, as is the moderate eccentricity (0.4). The orbit is consistent with a semi-major amplitude of 10-20 $\mathrm{km\,s^{-1}}$, resulting in a mass function $f(M) \leq 0.025\,\mathrm{M_\odot}$. This is a far cry from the predicted $f(M) \geq 20\,\mathrm{M_\odot}$, and indicative of a poorly fit astrometric solution determined by Gaia, albeit with a well-measured orbital period.

Gaia 5406: There are only four observations of this source, and the inter-epoch radial velocity shifts are comparable to their associated errors. Nevertheless, it is possible to fit a radial velocity consistent with $P_{\mathrm{orb}} = 25 \pm 2$ days and $e = 0.25 \pm 0.1$. The semi-major amplitude of this velocity curve is less well-constrained, ranging $0 - 40\mathrm{km\,s^{-1}}$. Even the largest of these provides a mass function of only $f(M) \approx 0.1\,\mathrm{M_\odot}$. Neglecting the *Gaia* measured eccentricity, K_2 may be up to $50\,\mathrm{km\,s^{-1}}$, though the higher eccentricities required for these orbital solutions to be viable still lead to a mass function of only $f(M) \approx 0.1\,\mathrm{M_\odot}$. This is inconsistent with the astrometric solution presented in the *Gaia* catalogue, which predicts a wider binary and a large mass function.

Gaia 5929: The radial velocity observations suggest the binary may indeed have an orbital period of 54 days, as predicted by Gaia, with an eccentricity consistent with the lower end of the expected range. The Keplerian velocity does not exceed $50\,\mathrm{km\,s^{-1}}$ (rarely does it exceed $25\,\mathrm{km\,s^{-1}}$) making it consistent with a low-mass stellar binary, where $0.01 \leq f(M) \leq 0.1\,\mathrm{M_\odot}$.

Gaia 6281: The longest-period source in this sample, the observations of Gaia 6281 corroborate the *Gaia* orbital period of 154 days, though fitting a radial velocity curve

to this period requires an eccentricity >0.4, which lies outside the range suggested by Gaia. The best-fit parameters for this source indicate a mass function $f(M) \approx 0.1\,\mathrm{M}_\odot$, although it may be as great as $0.5\,\mathrm{M}_\odot$ (as is discussed further below).

3.4.4.2 Fitting Alternative solutions

In the wake of apparently ill-matched *Gaia* orbital solutions (including poorly matched orbital periods in some instances), the allowed parameter space for fitted radial velocity curves is expanded; instead, orbital periods are restricted to $10 \leq P_{\mathrm{orb}} \leq 100\,\mathrm{days}$ (maximum of 200 days for Gaia 6281) and further refined for each system based on the outcome of these fits. The results of fitting radial velocity curves without using the *Gaia* period estimates are shown in Figures 3.13 & 3.14, and the associated mass functions are shown in Figures 3.15 & 3.16.

Gaia 4299: Whilst the *Gaia* observed orbital period can be used to fit radial velocities, there is greater success and improved goodness-of-fit when increasing the range used in the priors. Gaia 4299 is better described as a binary with an orbital period 60^{+20}_{-10} days - that the likelihood peaks around an integer multiple of the *Gaia* orbital period (at $P_{\mathrm{orb}} \approx 61$ days is interesting, being an integer multiple of the nominal period of ~ 30 days, though this may be coincidental). Despite the longer period, the mass function remains low, and the mass of the central component is unlikely to exceed $0.5\mathrm{M}_\odot$.

Gaia 5929: Whilst the nominal period of 54 days is plausible, the seven radial velocity observations suggest this system is more likely to have a slightly shorter orbital period; 42–50 days. As is the case with other systems, that the orbital period lies outside the *Gaia* predictions provides food for thought when considering the challenges in fitting complex astrometric solutions. Still, this minor variation in possible orbital periods does little to affect the analysis of the system - Keplerian velocities remain low, and the mass estimates suggest the binary comprises ordinary stars.

Gaia 5959: With radial velocity variations of $\approx 70\,\mathrm{km\,s^{-1}}$, there exist only a handful of radial velocity solutions for the 10 measurements of this source when using the nominal *Gaia* orbital period. The observations appear to favour a longer period binary, 100-125 days (likelihood peaking around 112 days), with moderate Keplerian semi-major amplitude ($K_2 \approx 30$) and low-medium eccentricities (< 0.5). This source, therefore, yields the largest mass function, $f(M) \geq 0.15\,\mathrm{M}_\odot$, with a predicted central mass $0.5 \leq M_1 \leq 2\,\mathrm{M}_\odot$. This is still below the expected mass range for black holes, and therefore this system is unlikely to host a compact object - that being said, questions arise as to the nature of

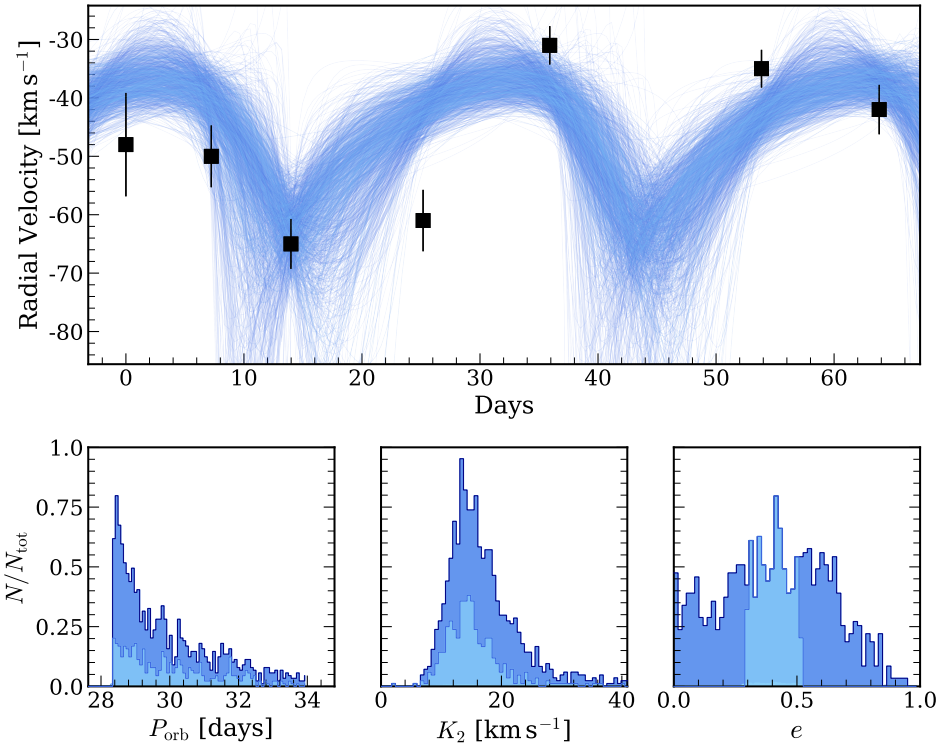

(a) Gaia 4299

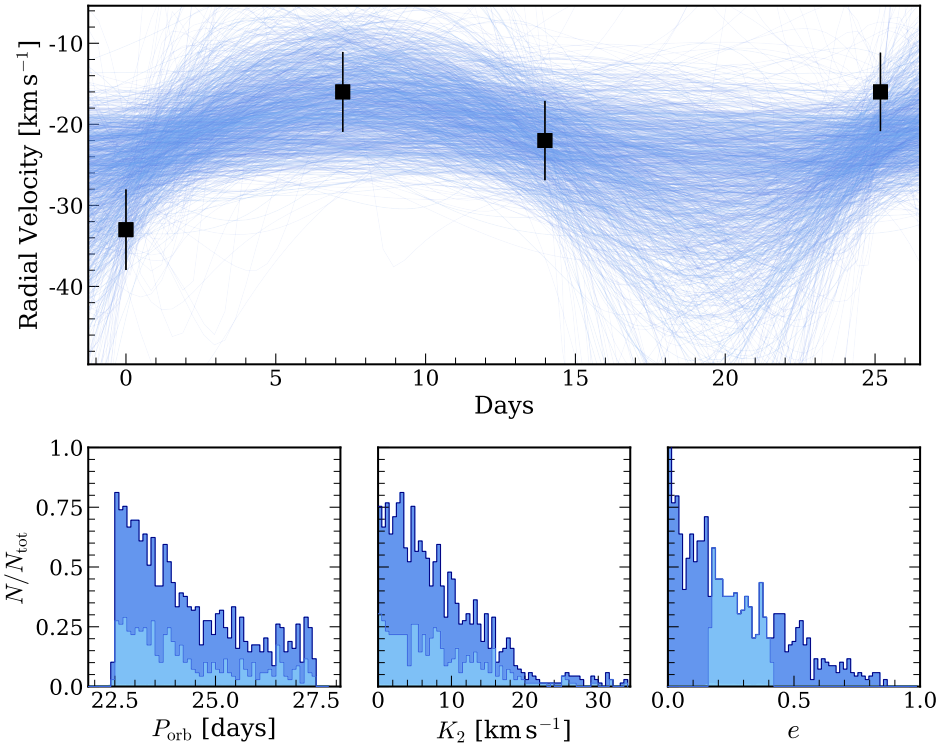

(b) Gaia 5406

Figure 3.10: **Best-fit orbital solutions (*Gaia* priors)**: Results of fitting Kelperian orbits to radial velocities, based on *Gaia* orbital period priors for Gaia 4299 and Gaia 5406. Upper panel shows possible solutions. Middle panels show distributions of orbital period, semi-major amplitude velocity, and eccentricity for all possible fits (sources in light blue indicate orbital solutions consistent with the *Gaia* observed eccentricities as well as orbital periods).

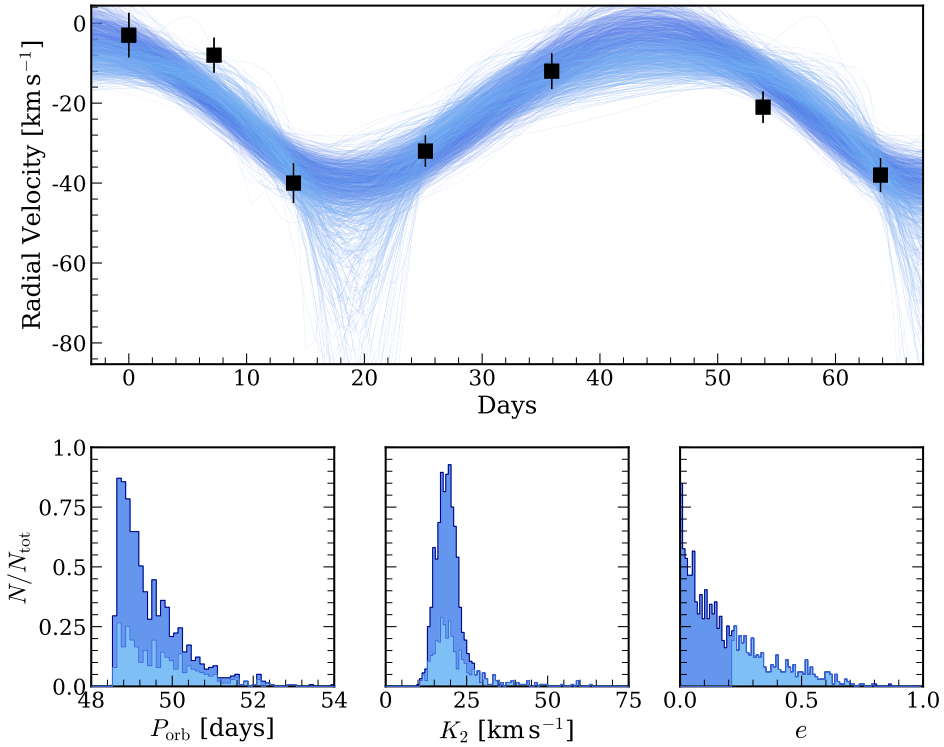

(a) Gaia 5959

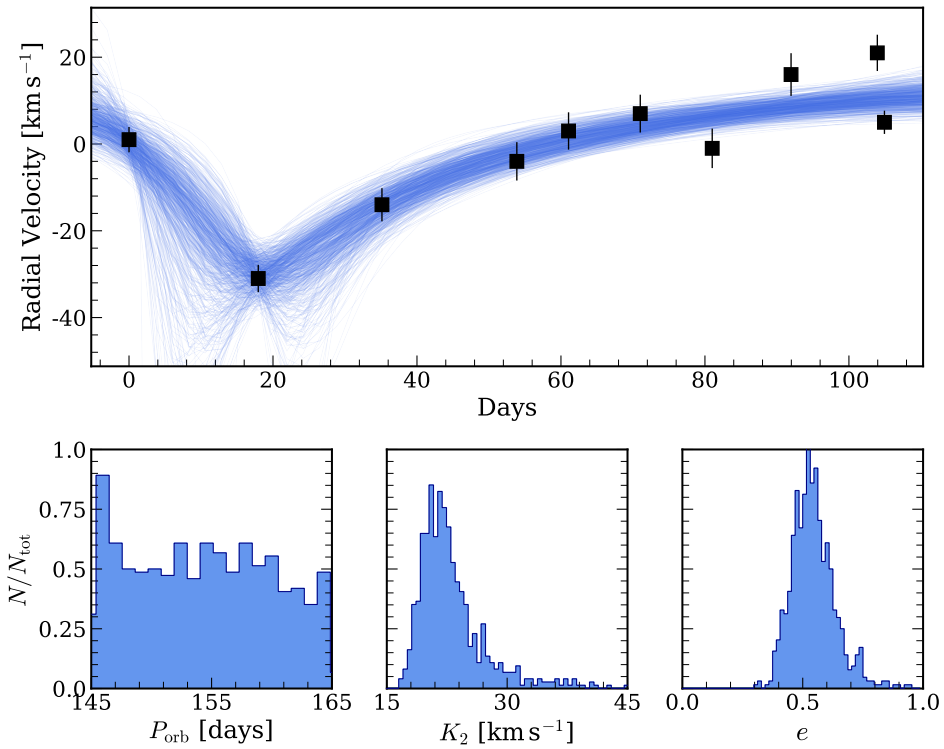

(b) Gaia 6281

Figure 3.11: **Best-fit orbital solutions (*Gaia* priors)**: Same as Figure 3.10, for sources Gaia 5929 and Gaia 6281.

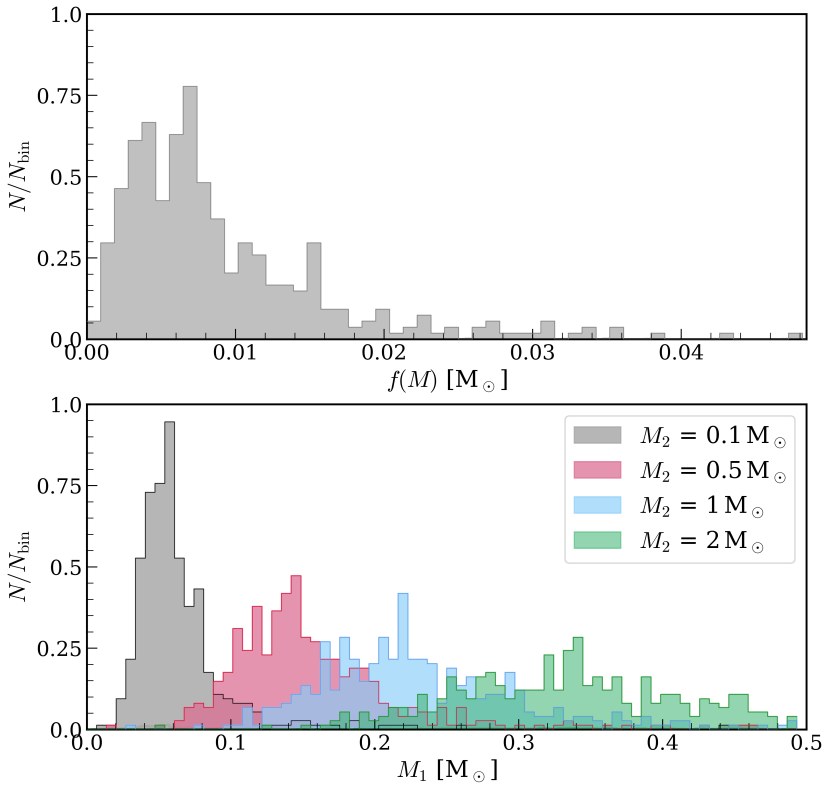

(a) Gaia 4299

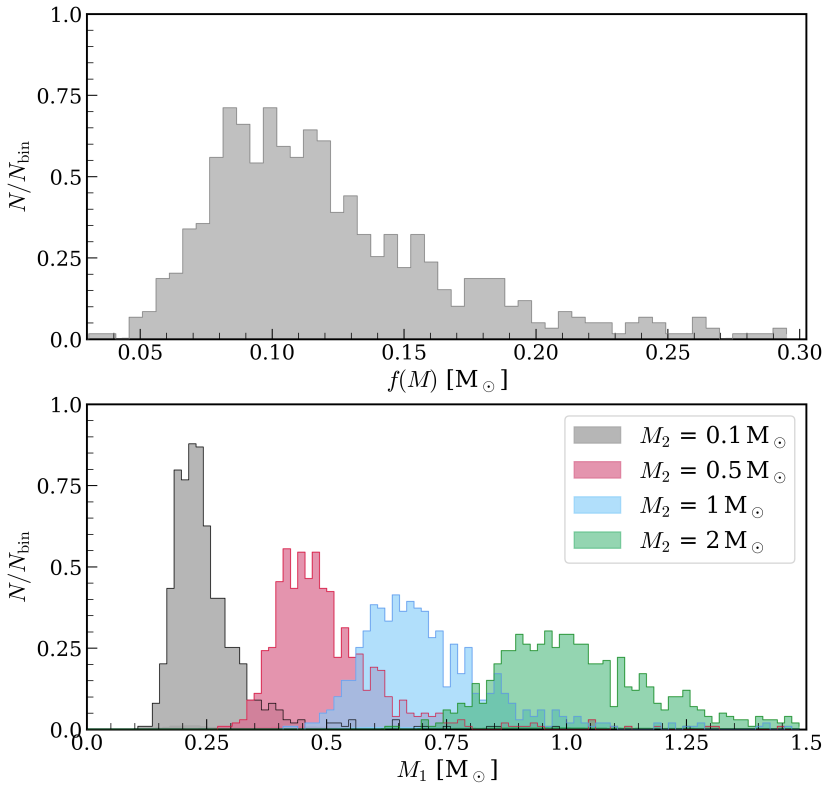

(b) Gaia 6281

Figure 3.12: **Astrometric mass estimates**: Upper panels: distribution of mass functions for orbital solutions (consistent with Gaia). Lower panels: distribution of potential central object masses under different assumed primary mass.

this system when considering the unusually bright luminosity. [2]

Gaia 4491: It is intriguing yet vexatious that, despite 10 observations (which happen to be mostly uniform in time), Gaia 4491 eludes explanation through conventional radial velocity fitting. The quality of constraints on radial velocity magnitudes are comparable with the rest of the sample, yet this system cannot be easily described as a binary of orbital period 32 days, or indeed any other $P_{\rm orb}$. Precise characterisation the orbit is somewhat academic; the radial velocities span -10 $\mathrm{km\,s^{-1}}$ to +45 $\mathrm{km\,s^{-1}}$, so a large mass function is unlikely.

3.4.5 Stellar binaries with two luminous components

Luminosity Predictions: The lack of evidence for large 'unseen' companions implies that these ought to be visible stars, though perhaps less luminous than the primary. One can calculate the expected luminosity (and apparent magnitude) for a binary system as a function of the component masses, as shown in Figure 3.17. *Gaia* photometry indicates these systems have optical luminosities in the range 0.02-3 $\mathrm{L_\odot}$. If they comprise only one luminous component, these would range 0.4-1.4 $\mathrm{M_\odot}$, but assuming the standard mass-luminosity relation, individual component masses may be estimated.

At a distance of $>$ 1.6 kpc and with an apparent magnitude of 15, Gaia 6281 requires at least one star greater than 1 $\mathrm{M_\odot}$. Given that the mass function expresses the relative masses of two components in a binary, this may be used in tandem with luminosity-based mass constraints to further refine the possible parameter space (see Figure 3.18). Similar mass estimates can be determined for Gaia 5929 and Gaia 5959 (NB For Gaia 4299 there is no photometric information from *Gaia*, Gaia 4491 has no well-described orbit, and Gaia 5406 encompasses such a vast range of parameters that errors on mass estimates will be of little value).

If both components of the binary are contributing to the overall luminosity, their masses may be limited as follows:

- **Gaia 5929**: $1.2 \leq M_1 \leq 1.5\,\mathrm{M_\odot}$, $0.3 \leq M_2 \leq 0.6\,\mathrm{M_\odot}$
- **Gaia 5959**: $0.5 \leq M_1 \leq 0.8\,\mathrm{M_\odot}$, $0.1 \leq M_2 \leq 0.7\,\mathrm{M_\odot}$

[2]These solutions were fit using only 8 of the 10 epochs - the signal-to-noise of the first spectrum made both line-fitting and cross-correlation unreliable and analysis of the second suggested a Keplerian velocity of -80 $\mathrm{km\,s^{-1}}$. Whilst this is of a similar magnitude to later epochs, it is in stark contrast to the subsequent observation in which the system is consistent with rest wavelengths, with no Keplerian motion along the line of sight. Preliminary analysis of the spectrum suggests improper wavelength calibration, and though the offset measured by the telluric lines is not sufficient to explain such an apparently large inter-epoch velocity shift, it is enough to leave the velocity errors too large to be meaningful, at least at this stage.

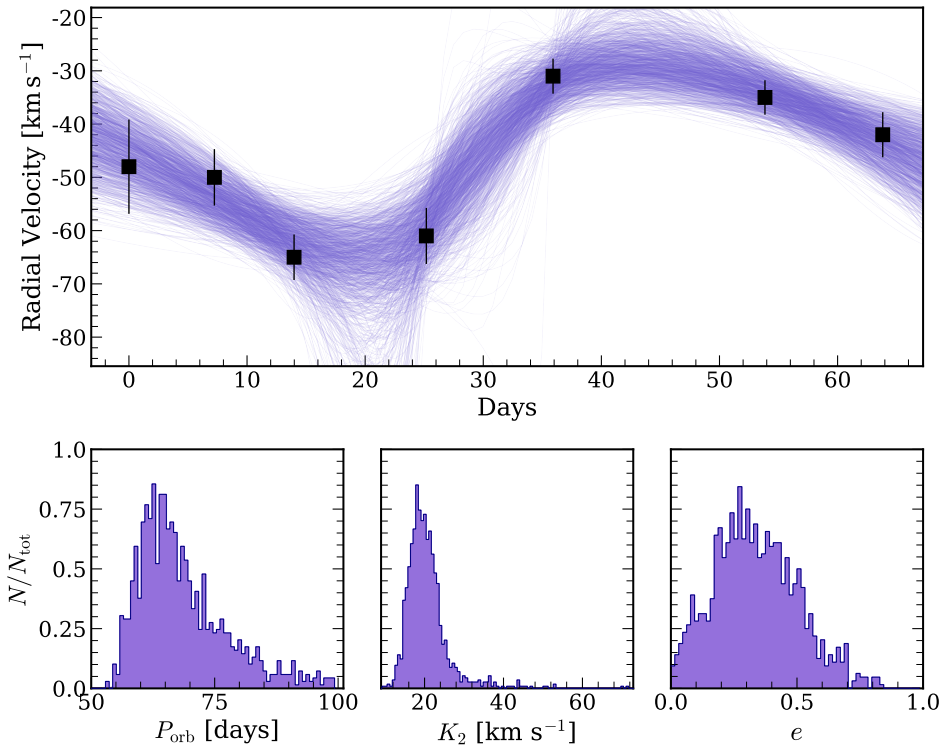

(a) Gaia 4299

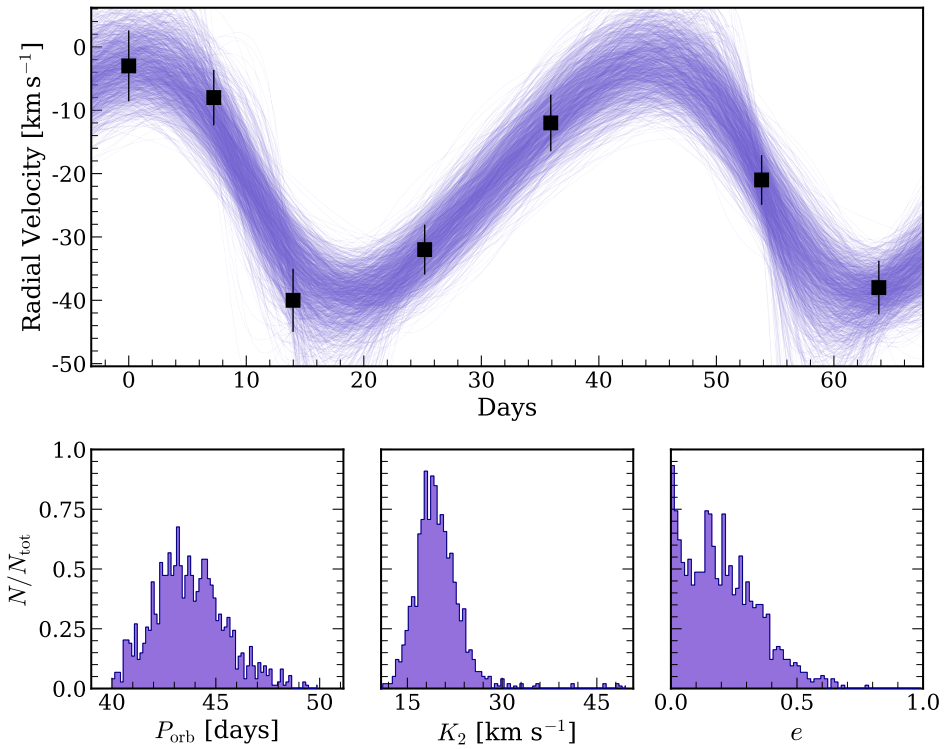

(b) Gaia 5929

Figure 3.13: **Best-fit orbital solutions (uniform priors)**: Results of fitting Kelperian orbits to radial velocities of Gaia 4299 and Gaia 5929, based on uniform priors for orbital period. Upper panel shows possible solutions. Middle panels show distributions of orbital period, semi-major amplitude velocity, and eccentricity for all possible fits.

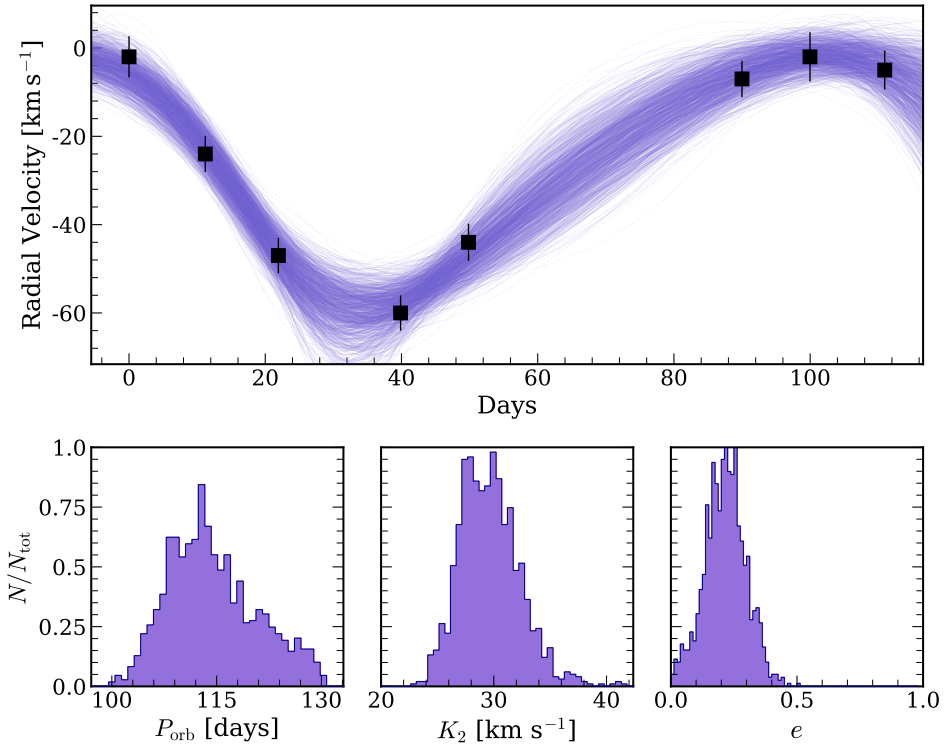

(a) Gaia 5959

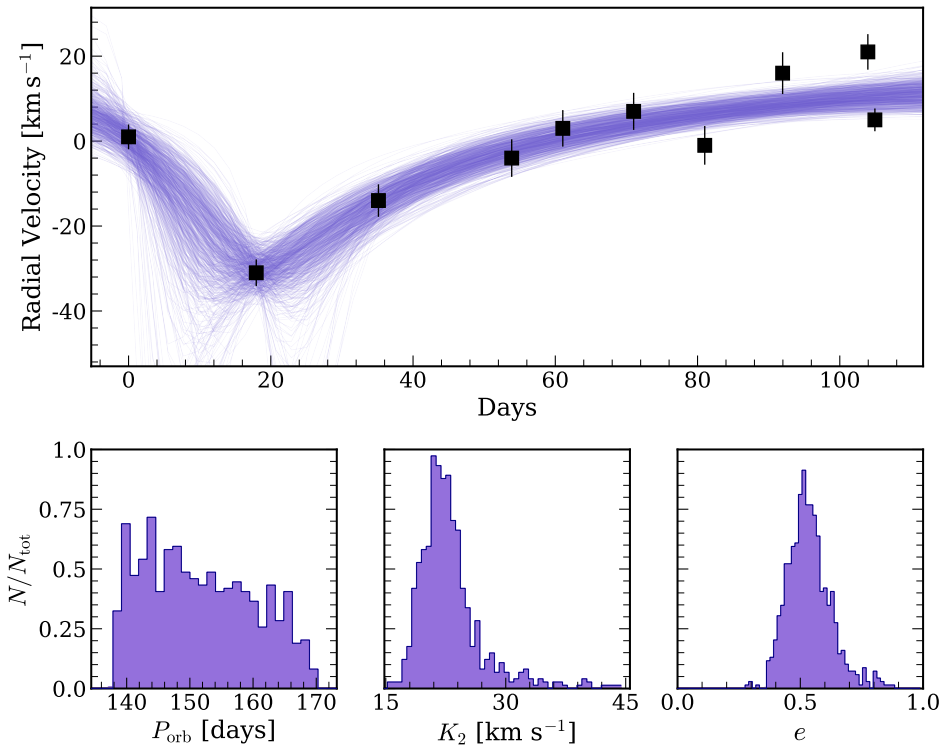

(b) Gaia 6281

Figure 3.14: **Best-fit orbital solutions (uniform priors)**: Same as Figure 3.13, for sources Gaia 5959 and Gaia 6281.

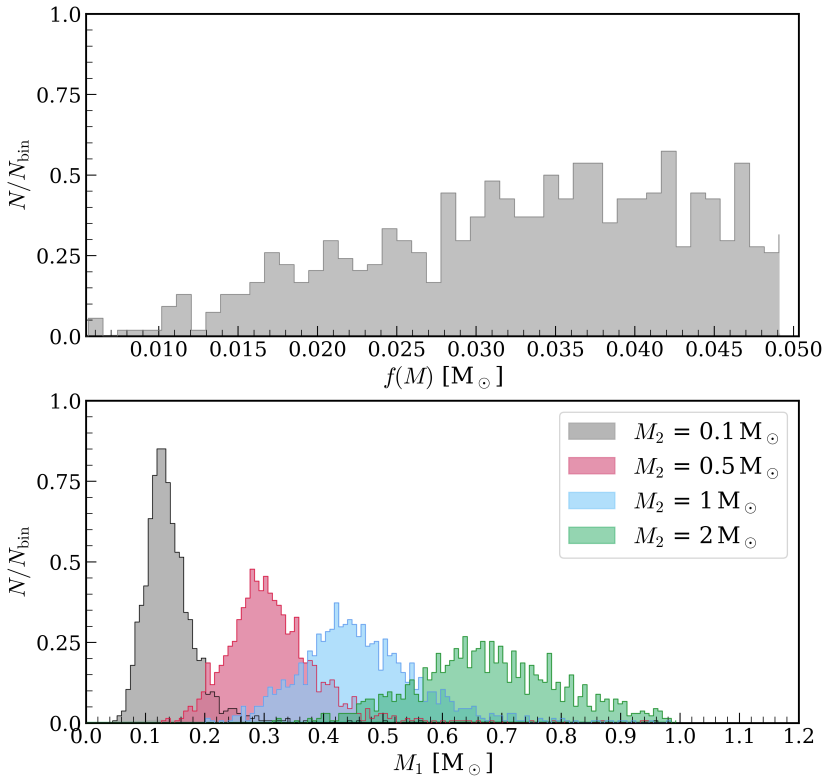

(a) Gaia 4299

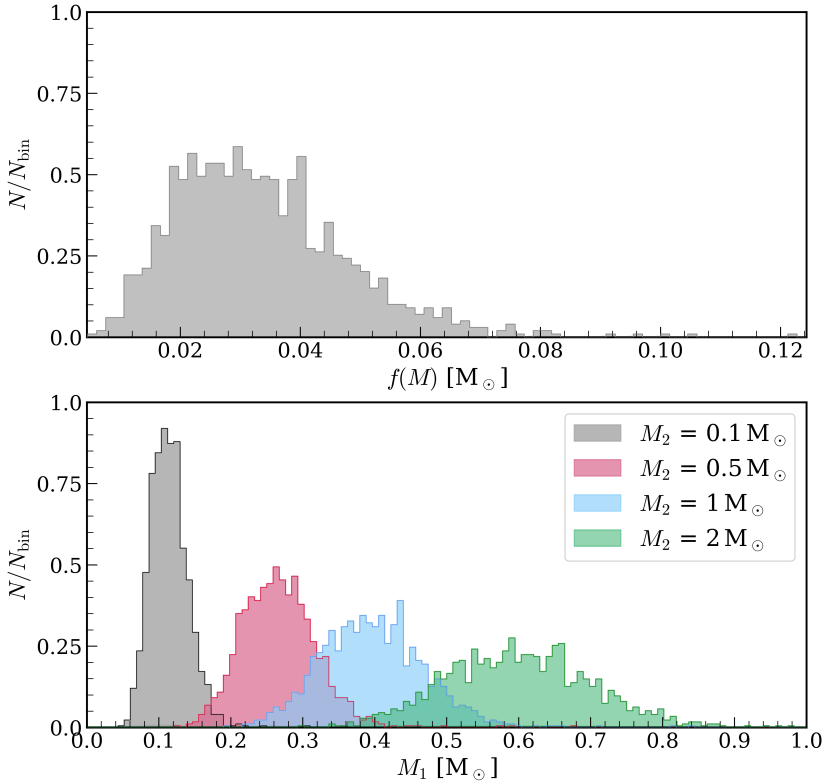

(b) Gaia 5929

Figure 3.15: **Astrometric mass estimates**: Upper panel: distribution of mass functions for orbital solutions (not necessarily consistent with Gaia). Lower panel: distribution of potential central object masses under different assumed primary mass.

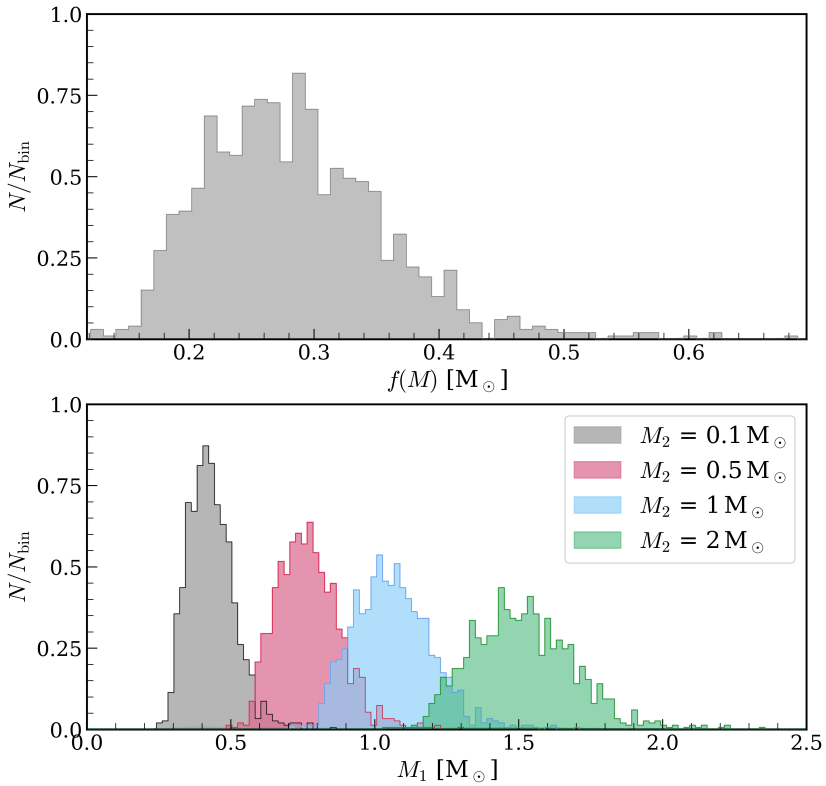

(a) Gaia 5959

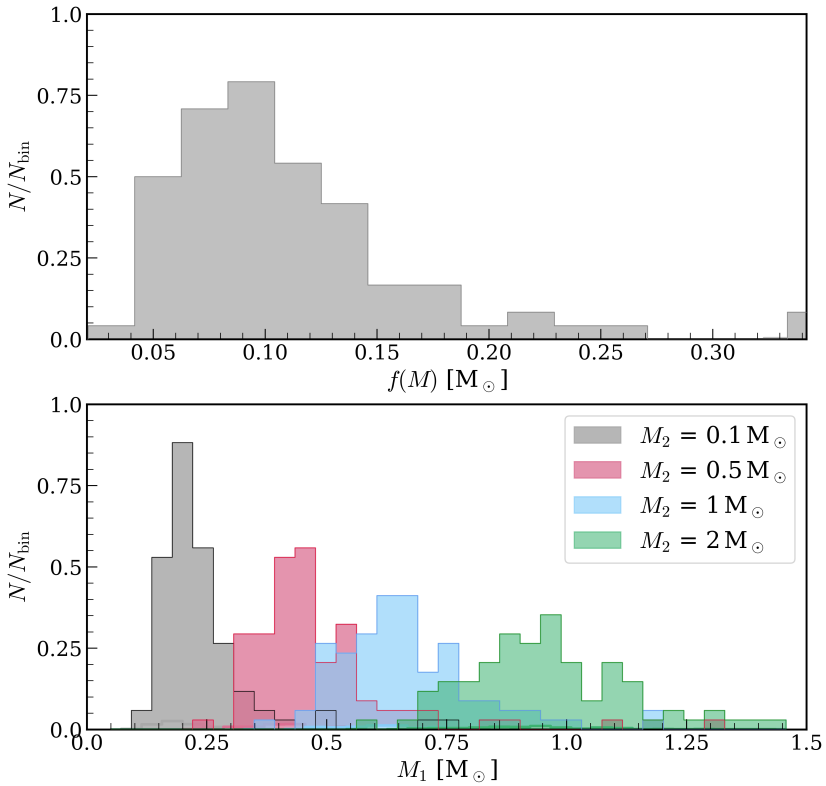

(b) Gaia 6281

Figure 3.16: **Astrometric mass estimates**: Same as Figure 3.15, for Gaia 5959 and Gaia 6281.

- **Gaia 6281**: $0.9 \leq M_1 \leq 1.3\,\mathrm{M}_\odot$, $0.5 \leq M_2 \leq 1\,\mathrm{M}_\odot$

Mass-transfer: The estimated masses of each of the components of the binary leads to an estimation of their stellar radii, as well as an estimated size of the Roche Lobe, and predict whether the system is likely to be experiencing mass transfer. For mass ratios between 0.3-4, the L1 Lagrange point ranges $0.2a \leq R_{L1} \leq 0.5a$, and the stellar radii range $0.55 \leq R_* \leq 1.4\,\mathrm{R}_\odot$, meaning each star fits well within its Roche Lobe and mass-transfer is unlikely.

Stellar Spectra: When comparing the observed spectra with templates for stars of a similar type (class, temperature, etc.) there appears to be no evidence of an additional luminous component. There is also no evidence of contamination from another star when comparing the *Gaia* colours and the colours from archival *2MASS* observations. This appears to rule out the possibility of a second luminous star of a different type than the primary, although it may still be the case that the 'unseen' object is a star of the same type as the luminous primary star.

The exception to the above is **Gaia 4299**: there is no photometric information on this source in the *Gaia* catalogue (i.e. no colour, no magnitude, no temperature, etc.) and it is, therefore, difficult to compare its spectra to an 'expected' spectrum. Comparing these spectra to other stellar templates suggests there may be an additional luminous component; however, without confirmation of the spectral type, this can't be confirmed.

Resolvable binary: Combining the orbital period, distance, and mass estimates suggests semi-major axes of:

- **Gaia 5929**: $0.28 \leq a \leq 0.33\,\mathrm{AU}$
- **Gaia 5959**: $0.36 \leq a \leq 0.57\,\mathrm{AU}$
- **Gaia 6281**: $0.6 \leq a \leq 0.78\,\mathrm{AU}$

In each of these instances, the separation < 0.01 arcsec - substantially less than both the nominal resolving power of *Gaia* and predictions of the resolving potential for binaries [320]. This raises an intriguing question - if the radial velocity data are to be believed, then these are likely ordinary stellar binaries existing too close together to be resolved as individual components. This implies they would appear in the Gaia catalogue as single stars; the astrometry should show no evidence of this binarity. And yet, binary characteristics and periodicities have been identified through the *Gaia* data processing to a high level of precision. The question then becomes: why does *Gaia* identify

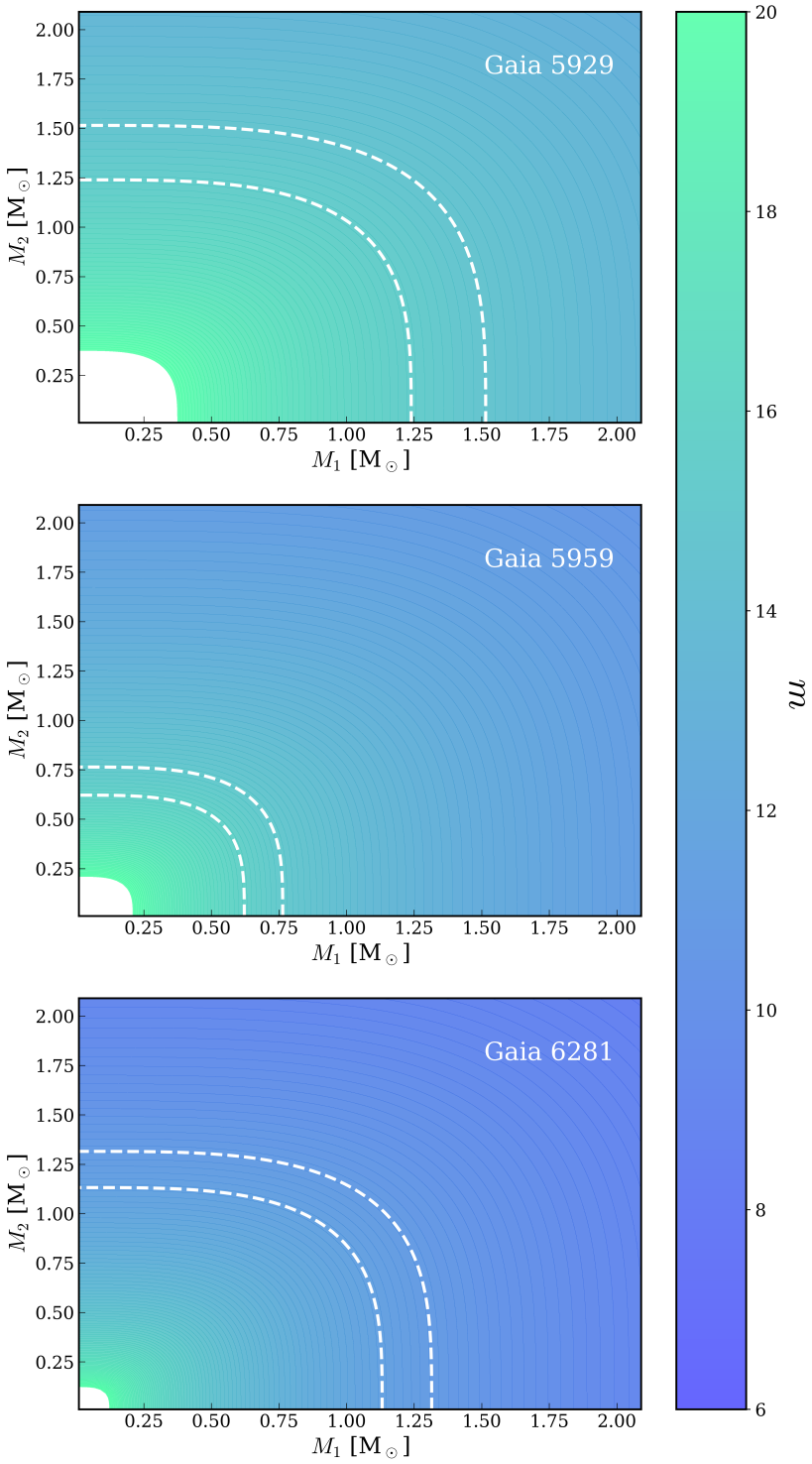

Figure 3.17: **Photometric mass estimates**: Expected apparent magnitude for three sources (Gaia 5929, Gaia 5959, and Gaia 6281), assuming two luminous components. White dashed lines encompass regions consistent with the apparent magnitude for *Gaia* G band.

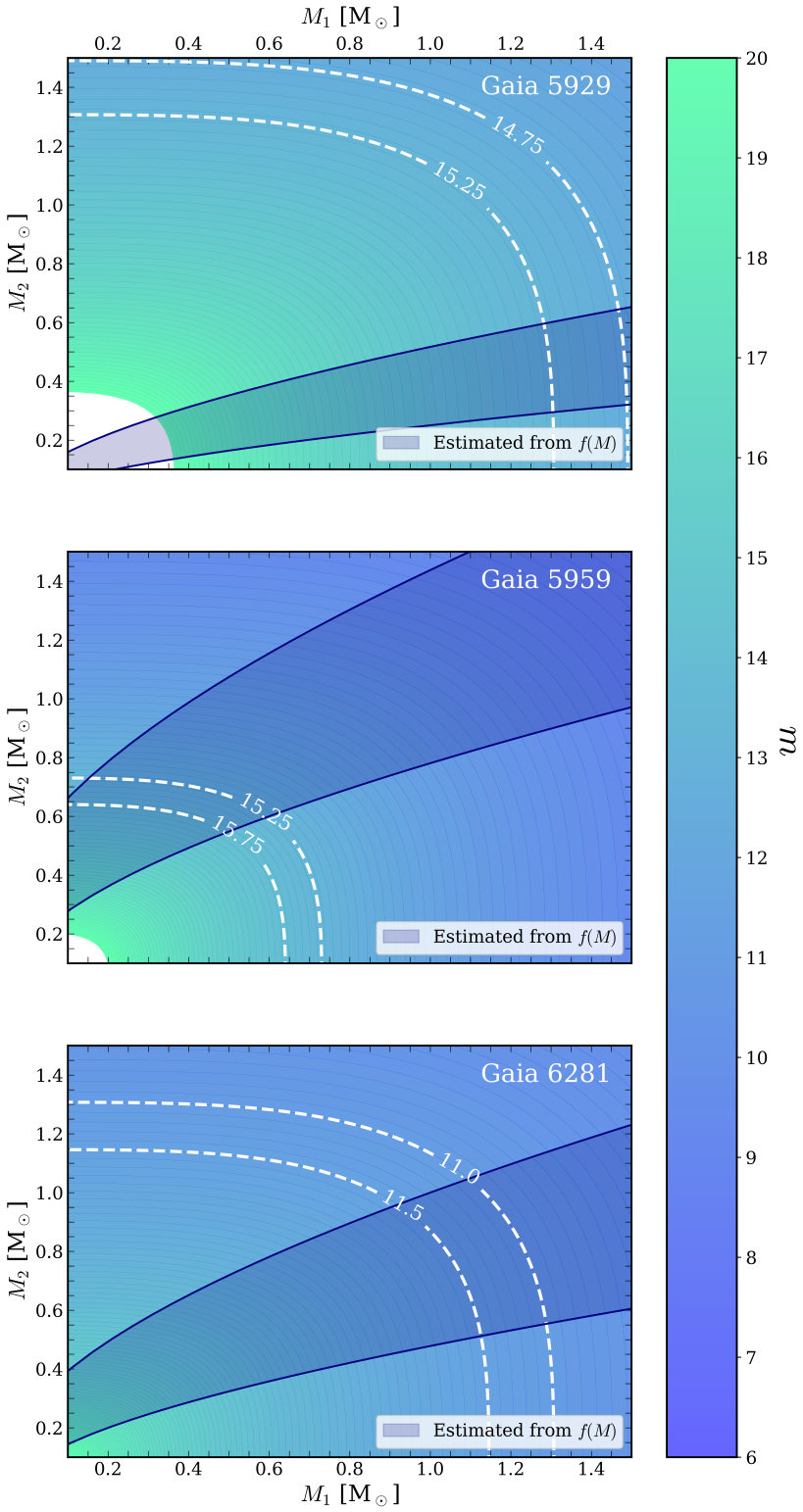

Figure 3.18: **Combined photometric & astrometric mass estimates**: Expected apparent magnitude for three sources (Gaia 5929, Gaia 5959, and Gaia 6281), assuming two luminous components. White dashed lines encompass regions consistent with the apparent magnitude for *Gaia* G band. Blue-shaded regions indicate parameter space consistent with radial-velocity derived mass functions.

a binary system, when the tight stellar binary is beyond its detection capabilities? If the astrometric solutions are not associated with these stellar binaries, are they associated with something else? One may speculate on the possibility that the *Gaia* data pipeline has found something that we cannot yet define - but for now, these systems must be attributed to teething problems in the astrometric fitting processes.

3.4.6 Conclusions

Where *Gaia* astrometry pointed to these 6 systems hosting a massive dark companion (Figure 3.1), the subsequent radial velocity campaign proved that they are, in all likelihood, ordinary stellar binaries (though the exact nature is not easy to confirm) - plausible masses are summarised in Figures 3.12, 3.15, 3.16, & 3.18. This null-detection is not without value, however. Whilst the aim was to identify and characterise a new sample of black holes, the data instead provides an insight into the reliability and fallibility of fitting astrometric solutions to binaries.

The precision astrometry provided by *Gaia* is unparalleled and opens the door for the identification of new types of black hole systems. However, the best way of exploiting the *Gaia* catalogue, particularly the Non-Single Solutions remains unclear.

Where the astrometrically measured orbital periods and semi-major axes were successful in the identification of BH1 & BH2, other systems within the same parameter space have been excluded as compact object sources (by both El-Badry et al. [78] and the above study). This, in tandem with the (at times obviously) poorly-fit astrometric solutions provided by *Gaia* highlights the uncertainty within astrometrically measured parameters and that researchers must remain cautious.

Future studies of these systems in particular, both astrometric and radial velocity, will hopefully shed further light on their specific characteristics, in turn supporting, or refuting, various evolutionary channels.

3.4.6.1 *Gaia* Data Release 4

These findings are significant, not only for the catalogues presented in *Gaia* DR3, but also in anticipation of *Gaia* DR4 (expected 2026). Astrometric fitting is a non-trivial and the techniques used to describe multi-component systems are in their infancy.

Section 3.2 explained the cascading nature of astrometric fitting of non-single solutions for putative binaries, which is perhaps one of the most obvious drawbacks of the current pipeline - there may be numerous systems for which more data is available, and the

binaries may be better characterised than the 'first-past-the-post' solutions presented in the official catalogue. This is, of course, speculative; *Gaia* DR4 will include individual epoch astrometry, allowing one to carry out fitting beyond that which is included in the *Gaia* pipeline.

The next stage of the above investigation will be to study the updated information provided by *Gaia* DR4; should the astrometric solutions remain unchanged, individual epoch astrometry will be subject to intense scrutiny in the hopes of fitting an astrometric solution that is consistent with the observed radial velocities.

That the present astrometry is at odds with the orbital characteristics derived from radial velocity observations is troublesome, though the value in the former should not be underestimated. The groundbreaking high-precision astrometry undertaken by the *Gaia* mission is without equal and has enabled studies of stellar populations (both individual and binary), stellar variability, globular clusters, Galactic structures, interstellar material, and much more. The application of such rigorous observations to compact objects is just part of the *Gaia* mission, and the work is far from over.

A positivist perspective would be that perhaps the lack of obvious black holes present in the *Gaia* NSS catalogue is the result of underdeveloped astrometric fitting techniques and that future data releases and investigations may reveal black holes in the numbers predicted prior to DR3. Gaia BH1, Gaia BH2, & Gaia BH3 are pioneering and, though not immune from the challenges associated with astrometric observation and analysis, are only the first of what is sure to be a vast catalogue of black holes, interacting and otherwise, identified with *Gaia*. Thus, with that in mind, the search continues.

Table 3.2: Candidate non-interacting black holes

Gaia ID	Name	α [deg]	δ [deg]	$\bar{\omega}$ [mas]	Mag	$P_{\rm orb}$ [days]	e	a [mas]	i [deg]
4299244434901041024	Gaia 4299	300.87	9.39	0.83 ± 0.03	13.39	31.5 ± 0.03	0.4 ± 0.07	0.5 ± 0.1	92.5 ± 5.0
4491401821468887552	Gaia 4491	261.5	9.56	1.32 ± 0.08	16.49	31.31 ± 0.02	0.24 ± 0.08	1.4 ± 0.1	96.3 ± 4.3
5406907085973524224	Gaia 5406	151	-49.79	1.63 ± 0.02	14.53	24.98 ± 0.02	0.28 ± 0.1	0.4 ± 0.1	77.6 ± 13.5
5591318172608607232	Gaia 5591	112.21	-34.83	2.57 ± 0.07	17.1	24.95 ± 0.02	0.25 ± 0.1	1.5 ± 0.4	87.7 ± 13.7
5929746958324419200	Gaia 5929	254.29	-54.41	0.61 ± 0.03	15.06	54 ± 0.15	0.48 ± 0.24	0.7 ± 0.1	86.4 ± 4.8
5959603097090964992	Gaia 5959	260.66	-41.99	2.02 ± 0.05	15.47	25.23 ± 0.01	0.33 ± 0.12	1.8 ± 0.3	92.7 ± 3.9
6281177228434199296	Gaia 6281	223.21	-19.37	4.28 ± 0.03	11.26	153.95 ± 0.36	0.18 ± 0.04	5.3 ± 0.6	72.2 ± 8.4

Chapter 4

Measuring masses with X-ray spectroscopy

As discussed in Section 1.4, the masses of compact objects provide extensive information on their evolutionary history, their formation, the mass lost during supernova, the mass gained through accretion, and has consequences for various areas of astronomy.

These masses are best measured through studies of the companion star (using the mass function, Equation 1.9). Whilst radial velocity observations are commonplace in the optical waveband (e.g. as is the case in Chapter 3), spectral features are also present in the X-ray emission from interacting binaries. X-rays open up the possibility to probe masses for sources which are otherwise too obscured in the optical, thereby expanding the sample of black holes with mass measurements.

This Chapter discusses the potential to use cutting-edge X-ray spectrographs to constrain radial velocity motions to high precision. The plausibility of this method hinges on the equivalent width of the spectral feature in question (in this case, the iron fluorescent line at 6.4 keV). This equivalent width describes the strength of the emission line with respect to the underlying continuum (mathematically defined as the width of a rectangle under the continuum with the same area as that of the emission line profile), and is derived considering the geometry of an X-ray binary, including distortion of the donor star, in tandem with the composition of the stellar surface and the nature of the X-ray emission.

The equivalent width of the iron Kα emission feature is predicted to range 2-40 eV (dependent on the binary's mass ratio, inclination, and orbital phase). As shown in Section 4.7, the latest X-ray mission *XRISM* is sensitive to energy shifts within 5-30 km s^{-1}, which are sufficient to fit radial velocity curves and calculate mass functions; this method can

be applied to systems that are more obscured in other wavebands, potentially mitigating some of the biases of previous studies. Though there are caveats (discussed in Section 4.9), the potential of this method is significant, and will likely contribute to our understanding of the mass distribution of compact objects.

4.1 Measuring the masses of X-ray binaries

Whilst the catalogue of black holes with well-constrained masses is growing, there remain numerous questions regarding the overall mass distribution of black holes, and the implications therein. As mentioned previously, a perhaps disproportionate number of black hole mass measurements come from LMXBs, due to their transient nature being more conducive for radial velocity studies. Additionally, if one assumes formation in the Galactic plane and a broadly consistent natal kick distribution for black holes, in follows that heavier systems are likely to be less displaced due to a natal kick, leaving them closer to their natal site and more affected by extinction. These heavier black holes may therefore be harder to find (although smaller black holes in high-mass X-ray binaries are also susceptible to this bias).

Enhancing the sample size of black hole masses will provide further evidence for and against various mass distributions, the presence of a lower mass gap, and related supernova processes. It is therefore wise to consider new ways of measuring the masses of black holes. Once again, the movements of the Universe offer support.

Though these masses cannot be measured directly, radial velocity observations of the companion star can provide constraints, both in non-interacting as well as interacting (X-ray) binaries. Thus far, the majority of characterised black holes exist in the latter (though this is *not* attributable to these being the dominant population of compact objects, but rather reflective of the challenges associated with observing compact objects).

As described in Section 1.4, the mass function of a system can be expressed as:

$$f(M_1) = \frac{M_1^3 \sin^3 i}{(M_1 + M_2)^2} = \frac{P_{\rm orb}\ K_2^3}{2\pi G} \tag{4.1}$$

where M_1 is the mass of the compact object, M_2 is the observed mass of the companion, K_2 is the peak Keplerian velocity of the companion and P_{orb} is the orbital period. By reducing the assumed companion mass to 0, $f(M_1)$ provides a minimum mass for the compact object.

Mass functions have been derived for many XRBs, with the radial velocity curve typically relying on optical or infrared spectra, including absorption features and fluorescent emission lines [e.g. 54; 202; 55; 127].

4.2 Opportunities in X-ray

Thus far, there have been limited attempts to extend this method to other wavelength ranges. Zhang et al. [317] used the Doppler shift in X-ray absorption features associated with an accretion disc to constrain the mass of the compact object and the inclination of GRO J1655–40. This method was attempted again by Madej et al. [192] in 2014, though the results appeared to be dominated by variability in the X-ray luminosity. In 2018, Ponti et al. [233] used absorption features in the X-ray spectra of an LMXB to derive radial velocity measurements and therefore constrain the mass of the companion. Their findings are consistent with previous estimates from other methods, indicating promise in the idea of expanding mass function methodologies to different wavebands.

XRB X-ray spectra also often exhibit *emission* features. In particular, the fluorescent iron emission is prominent as a result of a high iron (Fe) abundance and fluorescence yield. This emission occurs following photoelectric absorption of X-rays (greater than 7.1 keV) by an iron atom/ion, which causes the ejection of an electron from one of the inner K shells - shells indicate the orbits that electrons follow around the atomic nucleus, existing at different energy levels. A higher energy electron falls from the L shell, and this transition results in the emission of the Kα line at 6.4 keV. In practice, there exist two potential pathways by which the energy released by the transition may be emitted: emission line photons or, more commonly, Auger electrons (electrons ejected having received the excess energy). Strictly speaking, the iron Kα line comprises two distinct energies, 6.404 keV & 6.391 keV [15; 257], however, this distinction is purely academic.

The Kα emission feature at a rest energy of $\approx$6.4 keV (or a wavelength of 1.9387 Å) has been observed in a large number of XRBs. It is, therefore, a potentially valuable means to derive system properties, especially the Doppler-broadened component that arises deep within the potential well of the binary close to the compact object [12; 226; 195; 81; 105; 150]. Any narrow line component that might arise farther out from the core (for example, from the X-ray irradiated surface of a companion star), with a full-width half maximum (FWHM) of a few eV, is best suited to observations at high spectral resolution [204; 50; 124].

Torrejón et al. [282] provide a comprehensive summary of Kα detections in bright

XRBs using *Chandra* gratings, finding the narrow component to be present in all high-mass systems (HMXBs), and a small number of LMXBs. They attribute the source of the lines to the reprocessing of X-ray photons in cold stellar winds, arguing that this explains the lack of observations in low-mass systems, which typically do not have substantial stellar winds. The equivalent widths (EWs) of these are large, sometimes exceeding 200 eV, a fact that has interesting consequences for their origin, as will be discussed herein. Conversely, Torrejón et al. [283] examine *Chandra* observations of QV Nor, and present evidence that the main part of the Fe Kα emission comes from the illuminated side of the donor, in agreement with the assumptions made here.

It is encouraging that narrow-line components have already been successfully isolated and studied using gratings. But, thus far, observations have very likely found only the 'lowest hanging fruit', with other fainter and narrower components remaining to be detected. This is set to change with major advancements in X-ray astronomy, including the launch of *XRISM* in 2023 [313] & the highly anticipated launch of *Athena* [4] in the next decade. With these, high-precision X-ray observations will be used to address a number of underlying questions related to accretion processes and compact objects [e.g., 101]. These will be enabled by novel microcalorimeter technologies, with an approximate order-of-magnitude improvement in spectral resolution around the important Fe K band energies $\sim$6–7 keV, relative to best current grating capabilities [50].

Micro-calorimeters rely on the conversion of high-energy incident photons into heat by an absorber (with low heat capacity to prevent energy loss). They are advantageous over grating spectrometers due to their being non-dispersive, meaning the energy resolution remains largely consistent across the energy range (rather than being optimised for below 2.5 keV, such as *XMM Newton*). The *XRISM Resolve* spectrometer consists of a 36-pixel micro-calorimeter array using silicon thermistors, providing an energy resolution 5-7 eV in the 0.5-10 keV bandpass. *XRISM* was launched in September 2023, and achieved energy resolution of < 5 eV. Iron emission lines were measured to within a handful of eV ([312] - although this did *not* include the 6.4 keV iron line but rather higher energy emission features (6.6-7.8 keV). The energetic (i.e. kinematic) accuracy has, thus far, fulfilled expectations, and, with the mission now receiving proposals from the wider community, it is fitting to present novel techniques to maximise the scientific output of this state of the art instrument.

To determine whether the energy resolution is sufficient for mass function studies, the expected equivalent width of the iron Kα line can be calculated by considering the geometry of the binary system, accounting for the deviation of a companion star due to

Roche lobe overflow, and determining the apparent solid angle of the companion star. One can then estimate the intensity of the Kα line relative to the background continuum and conduct simulations in `XSPEC` to determine the accuracy with which one may be able to resolve the fluorescent line and measure radial velocities.

4.3 Equivalent width of iron Kα line

The potential in this method is subject to the strength of the fluorescent component from the donor star in XRBs; determining the expected strength is non-trivial and is dependent not only on the X-ray flux but also on the composition & characteristics of the star and the geometric configuration of the system (including the observer). The expected intensity profile of the Kα emission from the secondary star within a binary system comprises three main terms; (i) the equivalent width expected from any part of the companion's surface, given the chemical composition of the reprocessing surface and the X-ray continuum flux; (ii) the solid angle presented by the companion star to the X-ray source; and (iii) the 'geometric albedo': a term encompassing the variations in equivalent width associated with the viewer (i.e. changes with phase, inclination, etc.). One therefore has:

$$EW_{obs} = EW_I \times \Omega(q) \times \alpha(q, i, \Phi) \tag{4.2}$$

where EW_I is the equivalent width of the Kα line per unit area of reprocessing material (see below, and also Sunyaev and Churazov [273]; Kallman et al. [155]). Ω is the solid angle for a given system (a function of mass ratio, q), and α describes the luminosity of the iron line directed toward the observer (a function of q, inclination i, and orbital phase Φ). The X-ray source is considered to be a point-source, approximately co-located with the compact object [301; 241]. Basko [12] presented a pioneering study which computed the expected equivalent width of the Fe Kα line from donor stars. This work is broadly consistent (the comparisons are further discussed below) but improves upon it in various ways, e.g., considering changes in the shape of the companion star due to the gravitational potential around the compact object rather than assuming a perfect sphere and incorporating the effects of an accretion disc.

4.4 Surface composition

The first of the terms in Equation 4.2 is a function of the composition of the reflecting surface, the continuum flux, and other characteristics intrinsic to the system and reprocessing material.

$$EW_I = N_H A_{Fe} Y \frac{\int_{E_K}^{\infty} E^{-2} \sigma_{ph} dE}{I(6.4)} \tag{4.3}$$

where N_H is the hydrogen column density ($\mathrm{N}_H = 10^{22}$–$10^{24}\,\mathrm{atoms\,cm^{-2}}$) [311; 282]; A_{Fe} is the iron abundance relative to hydrogen (2×10^{-5}) [194]; Y is the fluorescence yield (typically 0.3) [172; 201; 225]; $I(E)$ is the photon flux spectrum of the X-ray source (assumed to be a power law, of form E^{-2} $\mathrm{photons\,s^{-1}\,cm^{-2}\,keV^{-1}}$); and σ_{ph} is the photo-absorption cross-section for the iron K-shell for photons of a given energy ($\sigma_{ph}(E) = 3.5 \times 10^{-20} \times \frac{E_K^3}{E^3}$ $\mathrm{cm^2\ atom^{-1}}$) [118; 273; 194]. E_K is the iron K-shell absorption energy ($\approx 7.11\,\mathrm{keV}$), and EW_I is typically of order 30–300 eV [12; 273; 204; 155; 282].

4.5 Geometry

4.5.1 The Roche potential

In closely separated binaries (e.g. many of the observed Galactic XRBs), the companion star becomes distorted such that it can no longer be approximated as spherical. The outer layers remain gravitationally bound to the gravitational centre of the star but experience the effects of the compact object, leading to stars with a 'tear-drop' shape [168], characterised by the Roche lobe.

The gravitational potential around the system (in the case of synchronous rotation) at any point is given by:

$$\Phi = -\frac{GM_1}{r_1} - \frac{GM_2}{r_2} - \frac{\omega^2}{2}\left[\left(x - \frac{M_2}{(M_1 + M_2)}\right)^2 + y^2\right] \tag{4.4}$$

This can be converted to spherical polar coordinates (centred on the compact object (M_1), with the x-axis directed towards the companion star (M_2), and the z-axis perpendicular to the orbital plane), and made dimensionless by dividing by GM_1/a and substituting in $q = M_2/M_1$, leaving:

$$\Phi(r,\theta,\phi) = \frac{1}{r} + q\left(\frac{1}{\sqrt{1-2r\sin(\theta)\cos(\phi)+r^2}} - r\sin(\theta)\cos(\phi)\right) + \frac{q+1}{2}r^2\sin^2\theta \quad (4.5)$$

The above describes equipotential surfaces with some constant potential Φ, for systems of a given mass ratio, q, in terms of the orbital separation, a, as shown in Figure 1.2 [168]. θ describes the angle from the z-axis in the x-z plane, and ϕ is the angle from the x-axis in the x-y plane. Figure 4.1 shows a distorted star whose surface is described by the Roche potential, with R_{L1} indicating the most distorted part of the star as it extends towards the compact object.

There is a point at which the contours of constant potential surrounding each mass are in contact; the L_1 Lagrange Point (see Figure 1.2). This is defined by the saddle point in the potential equation, and is a point at which material will find it much easier to pass between the lobes than to escape the surface entirely, and is thus the route through which Roche lobe overflow occurs [92] (it is this accretion which results in the characteristic X-ray emission from interacting compact object binaries). This can be found from the minimum of the potential equation, where $\theta = \pi/2$ and $\phi = 0$. The differential of the potential equation at this point gives:

$$d\Phi = -\frac{1}{r^2} - q\left[\frac{2r-2}{2(r^2-2r+1)^{\frac{3}{2}}} - 1\right] + (q+1)r \quad (4.6)$$

Solving this for at a given q will specify the radius at which the L_1 Lagrange point occurs (R_L, expressed in units of orbital separation). At this point, Φ_{L_1} is the Roche potential and defines the Roche lobe.

In a binary system, any matter outside the Roche lobe is gravitationally unbound from the star and will be lost, meaning the physical surface of the companion star may be defined by the Roche lobe or by another equipotential within [208]. This is described with the 'filling factor': the ratio between the potential at the companion star's surface and the potential at the Roche lobe surface; $F = \Phi_*/\Phi_{L_1}$.

In the case of the dimensionless potential equation:

$$\Phi_F = F\left[\Phi_{L_1} + \frac{q^2}{2(q+1)}\right] - \frac{q^2}{2(q+1)} \quad (4.7)$$

Having found the potential that defines the surface of the star (either the potential at the L_1 point or the potential at some nearer point if $F < 1$) one can solve the Roche potential equation to determine R (radius of the star) for any given θ and ϕ (angular

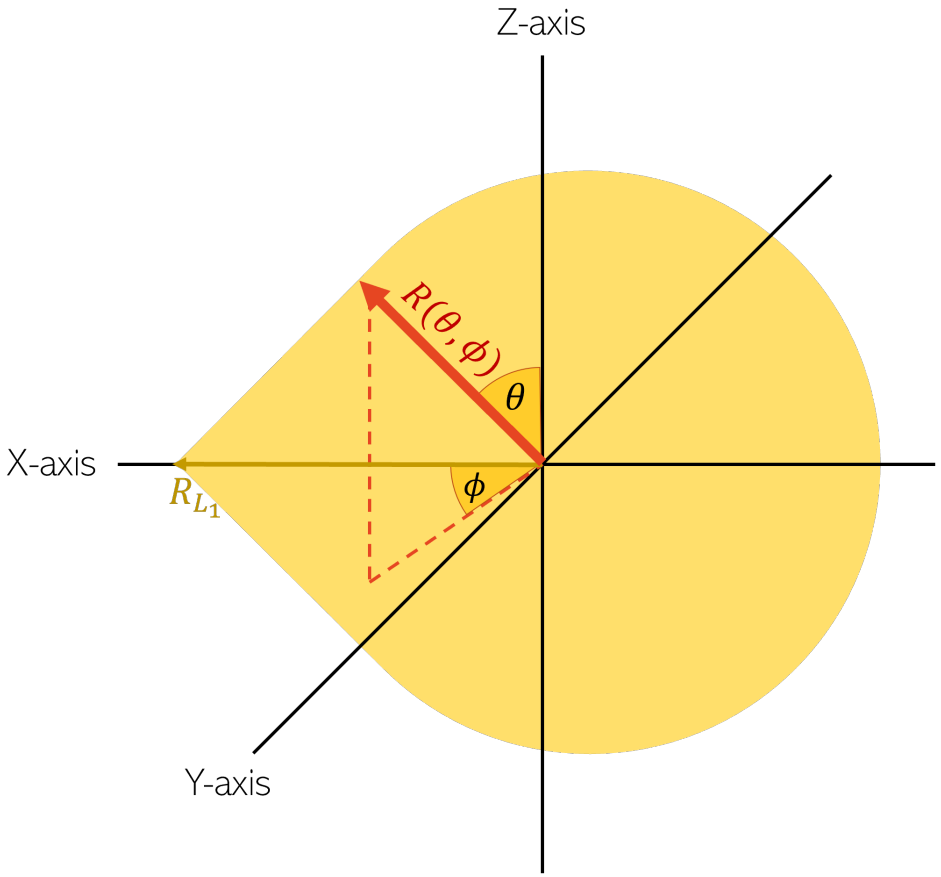

Figure 4.1: **Roche lobe filling star**: Diagram of a star existing in an X-ray binary and being distorted by the presence of a compact object indicating the coordinate system and the location of the L_1 Lagrangian point.

position from the centre of companion). This provides a complete picture of the geometry of the distorted star, from which it is possible to determine the solid angle the companion presents to the X-ray source.

4.5.2 Calculating the solid angle

The solid angle defines the field of view that a given object (in this instance, the companion star) covers as viewed by some observer (in this instance, the X-ray source). Measured in steradians, the solid angle is given by: $\Omega = \frac{A}{r^2}$ (where A is the apparent surface area of the companion star and r is the distance from the compact object). Taking advantage of the assumed symmetry about the x-axis, and setting $\theta = \pi/2$ one can determine the radius at any given ϕ (for all θ):

$$\Phi_S = \frac{1}{r} + q\left(\frac{1}{\sqrt{1-2r\cos(\phi)+r^2}} - r\cos(\phi)\right) + \frac{q+1}{2}r^2 \tag{4.8}$$

where Φ_S is the potential at the stellar surface and $q = \mathrm{M}_2/\mathrm{M}_1$.

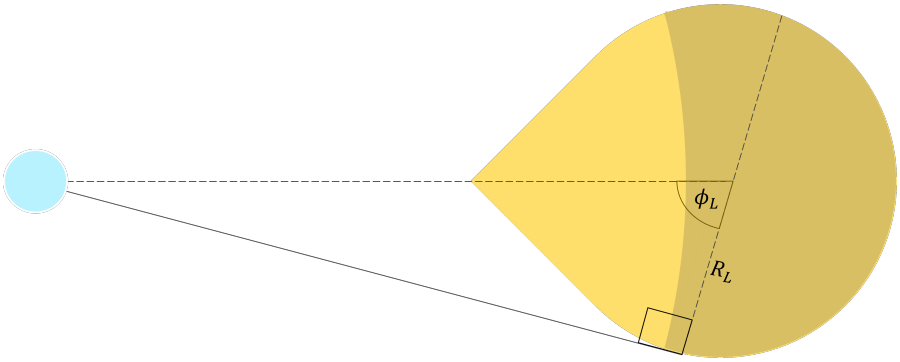

Figure 4.2: **Stellar 'limbs'**: Diagram indicating the location of the 'limbs' which define the illuminated region of the star.

The above can be solved to find the radius at a given ϕ, and leads to:

$$\Omega = \frac{1}{(r')^2} \int R(\phi)^2 \sin(\phi) d\phi \tag{4.9}$$

where r' is the distance to the compact object (1-R_L) and R (in units of orbital separation) is a function of ϕ and q only.

The above integral can be carried out within the limits that define the reflective region of the stellar surface - that is, the region of the star which will be irradiated. One can identify these limits by considering the geometry of a point source emitting light onto a star - the 'limbs' are defined by the point at which a line subtended from the surface of the star to the point source (i.e. a compact object) is perpendicular to a line from the centre of the star to the surface at that point, as shown in Figure 4.2 (Hamme [122] and references therein); i.e. where $\cos(\phi) = R(\phi)$ (given that radii are expressed in term of a and the distance between the stellar centre and the compact object is, by definition, 1).

Therefore, the integral is from $-\phi_L$ to ϕ_L (where ϕ_L is typically 60-80°, i.e. Figure 4.3). This gives us the surface area of the star that is illuminated by a source directly in front of it and is, therefore, the maximum area of the star in which X-ray reprocessing and Kα emission may occur.

4.5.3 Effects of the accretion disc

Where the above gives a description of the solid angle of the companion star in a binary, the accretion disc surrounding the compact object must also be considered. An accretion disc will have the effect of casting a shadow over the companion star, such that there is a region on the surface that will not be irradiated by the X-ray source, and, depending

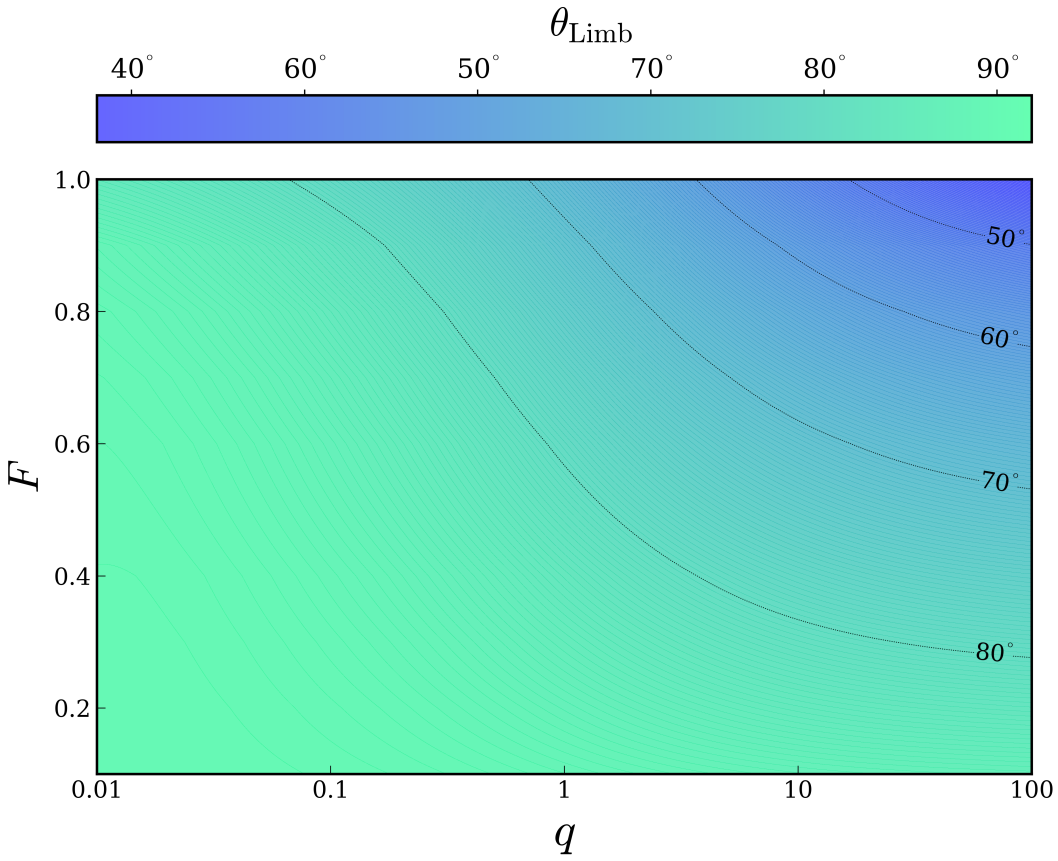

Figure 4.3: **Stellar limb angle**: Contour plots indicated the location of the 'limbs' of a companion star as a function of mass ratio and filling factor.

on the orbital phase, additional areas of the stellar surface will be obscured from the observer (e.g. Figures 4.4 & 4.6).

Firstly, consider that a small region of the star will sit in the shadow of the accretion disc and, consequently, not be irradiated by the X-ray source. This effect is minimal for HMXBs, where the companion star is significantly larger than the accretion disc. Conversely, the donors in systems where $q < 0.01$ are so much smaller that they are totally in the shadow of the disc and see no X-radiation at all. This is dependent on outer disc elevation or flaring angle, e.g. de Jong et al. [151] derives an average flaring angle of 12° for LMXB. This effect can be approximated with some assumptions about the nature of the disc. Using the equation from Frank et al. [92]:

$$D_H \cong C_s(GM)^{-0.5} R_D^{1.5} \tag{4.10}$$

where D_H is the disc height, C_s is sound speed ($\sim$1000 km s^{-1}), and M is set as 5 $M_\odot$.

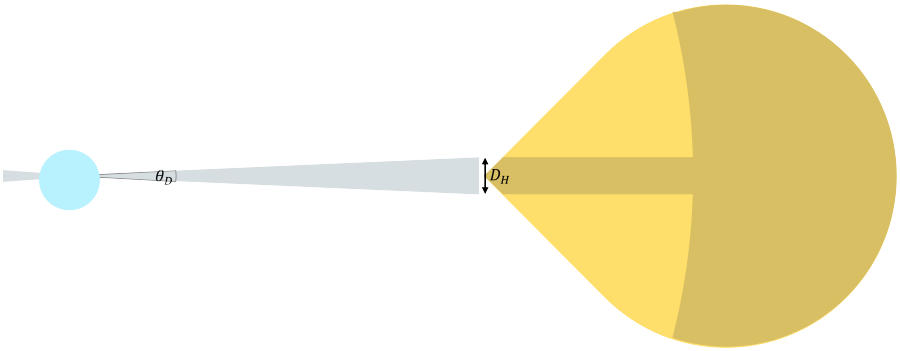

Figure 4.4: **Effects of disc shadowing**: Diagram showing the effects of an accretion disc casting a shadow over part of the star, preventing iron fluorescence emission in this region.

By substituting R_D (radius of the disc) as 1-R_{L1}[1] where R_{L1} is the radius at the most elongated point of the star (the L_1 point), this gives us the thickness of the disc at the outer edge, toward the companion star (i.e. angle α_D in Figure 4.4). The area of this 'strip' can be approximated and subtracted from the total solid angle, as follows:

$$\Omega = \frac{1}{(r')^2}\left(\int_{-\phi_L}^{\phi_L} R(\phi)^2 \sin(\phi) d\phi - 2R(\phi_L)D_H\right) \tag{4.11}$$

One therefore has an expression for the solid angle presented to the X-ray source, and the area which may undergo X-ray reprocessing (Figure 4.5).

4.5.4 'Geometric albedo' α

The intensity of reprocessed flux from a companion star is a function of both solid angle and albedo, the latter of which comprises the effects of molecular composition and the angular distribution of radiation that is emitted from the surface [306; 62]. The effects of molecular composition are included in EW_I, however, this additional term describes the geometric albedo, i.e. the effect that observation geometry has on the projected area of the companion star, which will depend on q, inclination, and phase. With this in mind, it is necessary to consider the angles between the Kα emitted flux and an observer.

The companion star is assumed to be a Lambertian radiating surface [310] (i.e. emission from the surface of the star is isotropic at each small surface element), defined by the normal to the surface element. The normal vector from any surface $f(x, y, z)$ at a

[1]This assumes the disc extends from the compact object all the way to the surface of the star; this is an overestimate, as the disc is typically truncated to around 2/3 of the orbital separation due to the resonance processes [222].

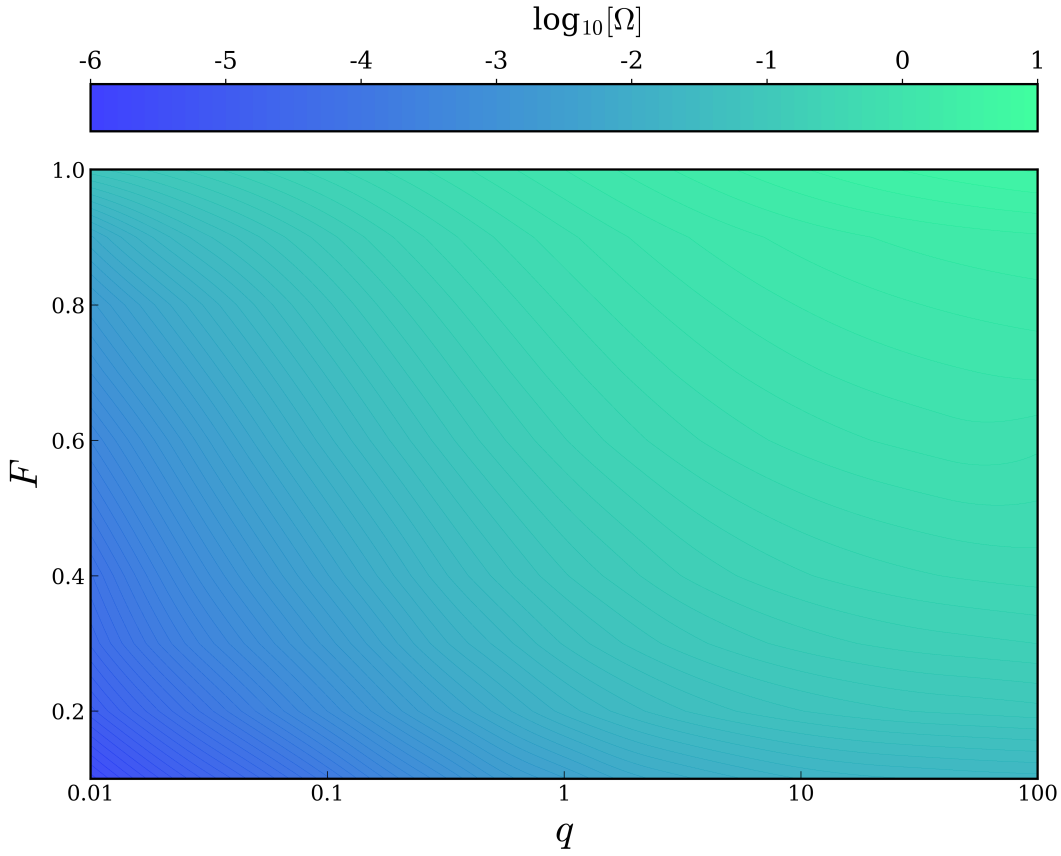

Figure 4.5: **Expected solid angle**: Contour plots indicated the solid angle presented to the central X-ray source as a function of mass ratio and filling factor.

given point is given by ∇f. The unit normal vectors θ_N and ϕ_N are given by $\frac{1}{|\nabla f|}\frac{\partial f}{\partial \theta}$ and $\frac{1}{|\nabla f|}\frac{\partial f}{\partial \phi}$ respectively. Integrating both of these components over the illuminated surface gives the proportion of Kα emission that reaches the observer:

$$\alpha = \iint_{S_R} \sin(\theta_N)\cos(\phi_N)\, d\phi\, d\theta \tag{4.12}$$

All of the above can be adapted to consider the effects of inclination and orbital phase. The apparent area of the irradiation (from the perspective of an observer) will change with orbital phase; this effect is exaggerated by the distortion of the star and is dependent on the inclination of the system (see Figure 4.6). In the case of a perfectly edge-on system, the albedo will be unaffected by the accretion disc; at phase $\Phi = [0, 2\pi]$, the apparent area to an observer will be equivalent to the solid angle presented to the X-ray source and at phase $\Phi = \pi/2$, there will be no X-ray flux directed towards an observer. In the event of inclination $i = \pi$, the albedo and X-ray flux from the perspective of an observer will remain constant regardless of orbital phase. Any intermediary inclinations will determine

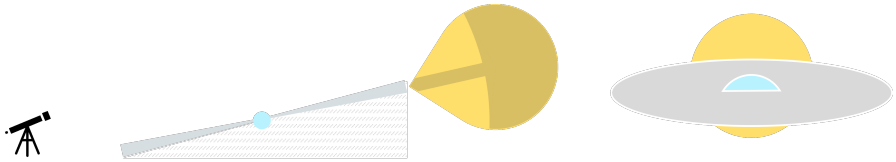

Figure 4.6: **The impact of perspective**: Diagram showing how the inclination of a system impacts the emission directed toward an observer, as the disc acts as a barrier to parts of the luminous and irradiated star.

how much of the reprocessing area is visible to an observer and how much is obscured by the accretion disc. This effect can be incorporated by calculating the size of the disc from the observer's point of view and comparing this to the reflecting area. Figure 4.7 shows the 'geometric albedo' at phase 0 (i.e. superior conjunction) as a function of mass ratio & filling factor, at two different inclinations.

The combined effects of the accretion disc and the distortion of the companion star due to the Roche potential mean that the reprocessing area visible to the viewer (in essence, α) will change with phase, resulting in a light curve with ellipsoidal variations (Figure 4.8). This is a purely geometrical effect, however, there may be additional drivers of further variation in equivalent width, such as changing ionisation levels or N_H, as will be discussed later.

4.6 Expected Equivalent Width

All of the above allows us to determine the expected equivalent width of the Kα line produced from the companion star with respect to the continuum reflected off the disc (Equation 4.2). The final outcome of the equivalent width for each orbital phase is based on the mass ratio q, filling factor F, and inclination i only.

Figure 4.9 shows the fraction of the intrinsic equivalent width of the iron line which will be directed towards an observer. Figure 4.10 shows the expected equivalent width of the Kα line as seen by the observer for systems with an inclination of 90°. The presence of an accretion disc and the Roche distortion of the companion star result in significant ellipsoidal variations of intensity as a function of orbital phase, as demonstrated in Figure 4.11. Such light curves of XRBs (specifically Cyg X-3, Her X-1 and 4U 1700-37) were first calculated by Basko et al. [13].

This ranges from approximately 2–40% of EW_I, depending on mass-ratio and phase; unsurprisingly, for systems with a low q (i.e. $q < 1$, indicating a smaller companion star) the smaller solid angle and reduced albedo mean $\leq$10 % of the source emission is directed

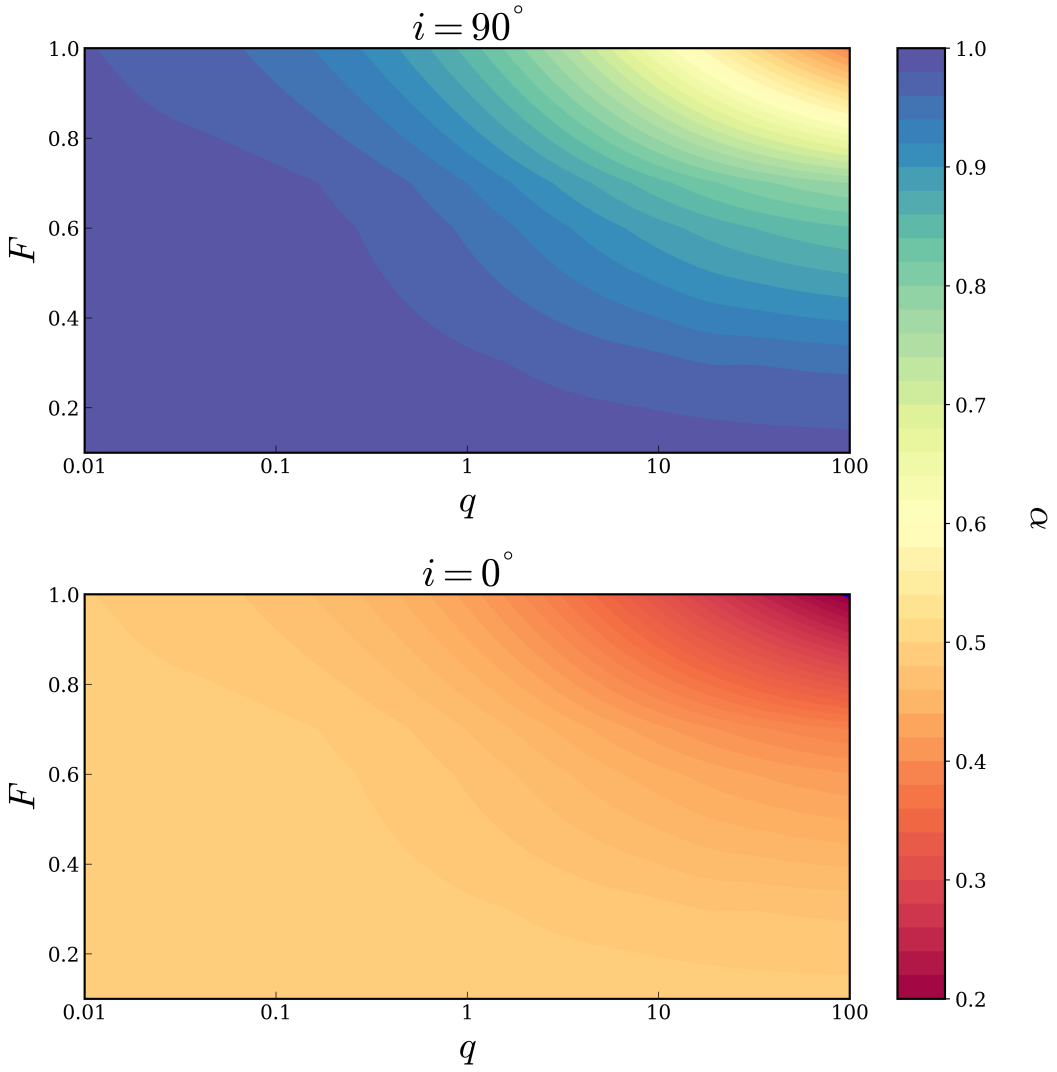

Figure 4.7: **Geometric Albedo**: Contour plots showing the geometric albedo of a system with a given mass ratio and filling factor (as phase 0). Upper panel: inclination $i = 90°$ (edge-on). Lower panel: inclination $i = 0°$.

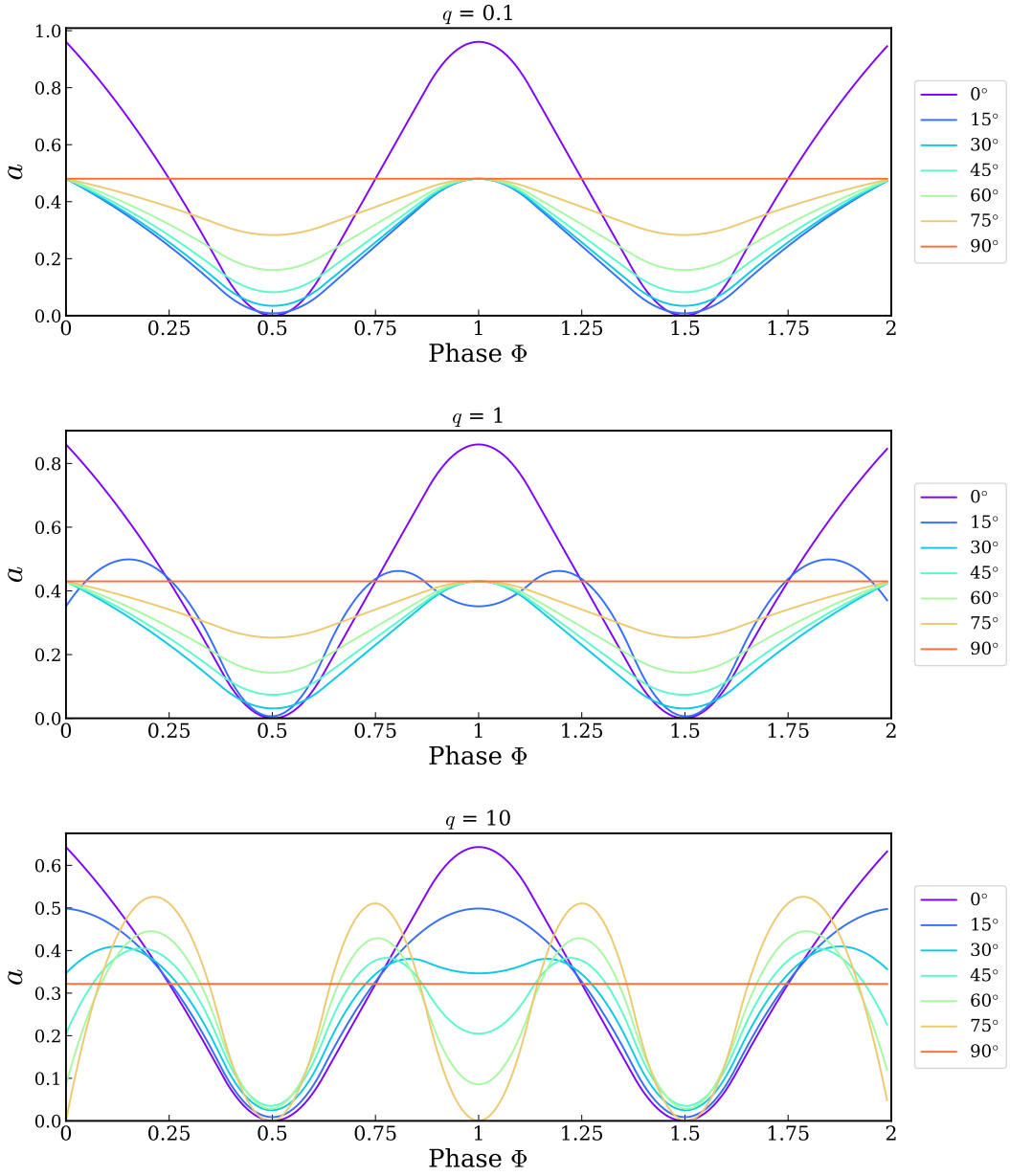

Figure 4.8: **Geometric albedo curves**: Geometric albedo alpha as a function of orbital phase for three different mass ratios: 0.1 (upper), 1 (middle), 10 (lower). Different inclinations are distinguished by colour (see legend). At higher mass ratios (i.e. a more massive companion star) the system experiences sinusoidal variations associated with the partial obscuration of the accretion disc.

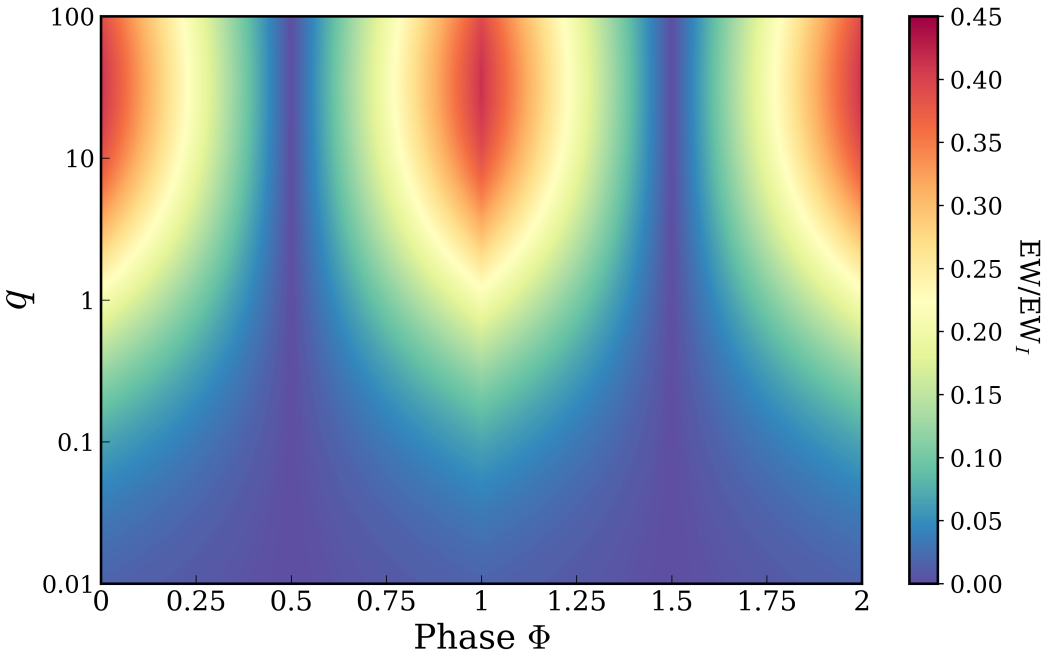

Figure 4.9: **Equivalent width fraction**: Contour plots showing the expected equivalent width of the Kα line as a function of mass ratio and orbital phase.

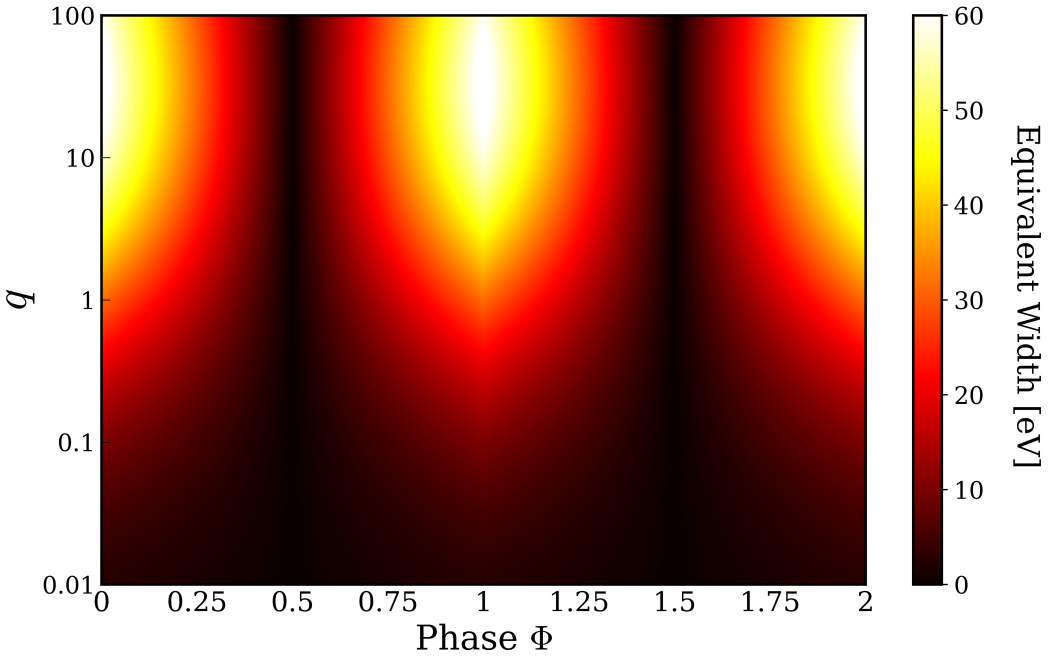

Figure 4.10: **Equivalent width**: Contour plots showing the expected equivalent width of the Kα line as a function of mass ratio and orbital phase (assuming $EW_0 = 150\,\mathrm{eV}$)

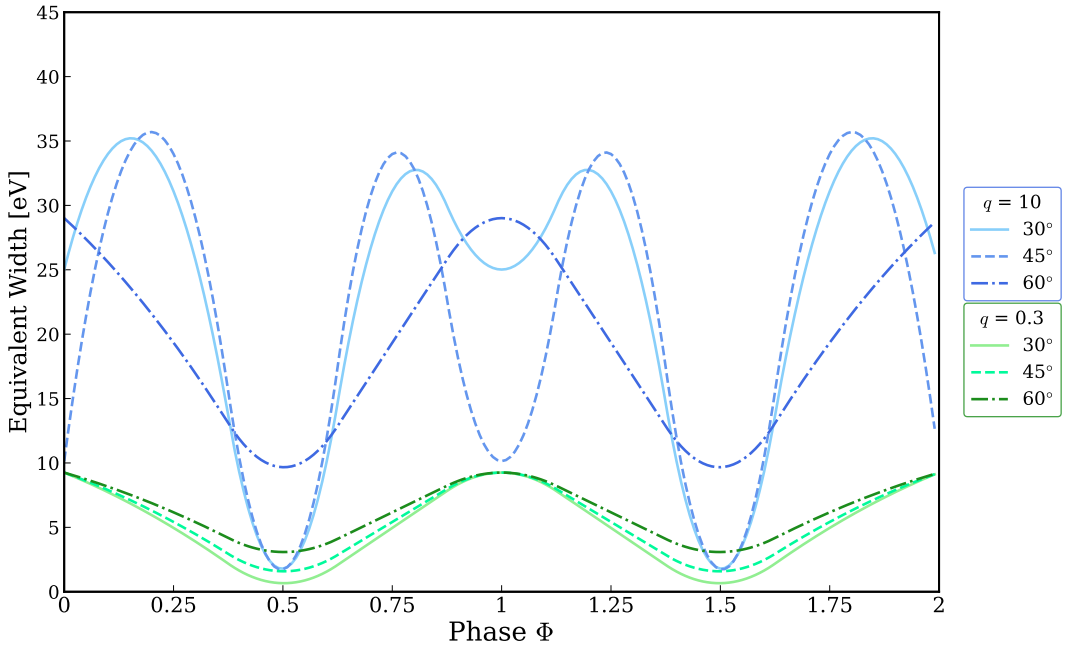

Figure 4.11: **Equivalent width curve**: Equivalent width of the iron Kα emission feature as a function of phase for a typical HMXB (blue) and LMXB (green), for three distinct inclinations (30,45,60 – distinguished by shade and line-style). At higher masses, particular obscuration of the companion by the accretion disc leads to complex line profiles. For LMXBs the accretion disc obscures at least half of the star at all inclinations $> 15°$, leading to equivalent widths with less inter-phase variation.

towards an observer, and the Kα EW is less than 15 eV (assuming $\mathrm{EW}_I \approx 150$ eV). For systems with $q > 1$, the observed EW is of order 15-40 eV, due to the significant stellar surface area and solid angle, and EW may exceed 50 eV in the case of $q > 5$.

HMXBs (i.e. systems with $q > 2$) are expected to see EW up to 20-30 eV. The distribution of XRB inclinations indicates a majority have $i \sim 30$–$60°$, meaning these values decrease (to around 50–80% of their maximum value) but remain of the same order of magnitude.

Figure 4.11 shows a plot of the observed EW for two distinct mass ratios ($q = 0.2$ & $q = 5$, representing a typical LMXB and HMXB, respectively), and at 3 different inclination angles (i.e. 60°, 45°, and 30°). These clearly show the ellipsoidal variations with phase due to the distortion of the companion. Inclination has a greater effect on systems with larger q, but the observed EW is expected to be of the same order of magnitude, regardless of inclination.

XRB source emission can vary significantly in intensity. During quiescence, fluxes are typically of the order 10^{-10} – 10^{-12} ergs cm^{-2} s^{-1}, but during outburst, they can increase

by 2 to 3 orders of magnitude, or even brighter in some instances [92]. The narrow-line Kα emission from the companion star is expected to have an EW with respect to the background continuum reflected off the disc of 2-50 eV. Whether this is sufficiently bright to be resolved and used to constrain the mass function of the system can be investigated by considering the nominal instrument specifications and testing the feasibility using the publicly available response files (Redistribution Matrix Files (RMFs) and Ancillary Response Files (ARFs))[148].

4.7 Efficacy of X-ray spectrographs

NASA's HEASARC [213] provides various tools for research into high-energy astrophysics, including `XSPEC` [2], which may be used to predict the expected output spectrum of a given X-ray source observed by *XRISM*. This provides a useful tool to investigate the potential validity of this method by simulating a source with a Kα fluorescent line consistent with the predicted flux & equivalent width and estimating the errors in line energy (and, therefore, radial velocity). Whilst they are only predictions based on the response files for *XRISM*, these simulations indicate the potential validity of using the Doppler shift in this line to find the mass function and thereby constrain the mass of the compact object.

The X-ray spectrum from the stellar companion in an XRB is broadly described by an underlying continuum flux, described by a power-law with index ~ -2, and additional Gaussian line features of varying strengths. The Kα emission is modelled as a Gaussian, centred on 6.4 keV, with a width of 5 eV. The continuum flux in these models ranges from $F_{2-10\,\mathrm{keV}} = 10^{-8} - 10^{-12}\,\mathrm{ergs\,cm^{-2}\,s^{-1}}$, in order of magnitude increments. Two equivalent widths are modelled for each of these fluxes: 20 eV and 5 eV.

Using the *XRISM* high-resolution (7 eV) response files [278; 148] and `FAKEIT` (an `XSPEC` package used to simulate X-ray spectra), one can analyse these simulated spectra and determine the fluxes at which the iron line may be detected and resolved, as well as the associated errors in energy and velocity.

Figure 4.12 shows a contour plot with 1-σ and 2-σ confidence intervals in velocity measurements (converted from line energy) against line-width, for four different flux levels (10^{-8}, 10^{-9}, 10^{-10}, and $10^{-11}\,\mathrm{ergs\,cm^{-2}\,s^{-1}}$).

These simulations indicate that for higher fluxes (i.e. during outbursts, $F_{2-10\,\mathrm{keV}} \sim 10^{-8}$ – $10^{-10}\,\mathrm{ergs\,cm^{-2}\,s^{-1}}$), if *XRISM* is able to detect and resolve the narrow line, the errors in energy will be $0.01 - 0.1$ eV. This corresponds to velocity errors for the companion

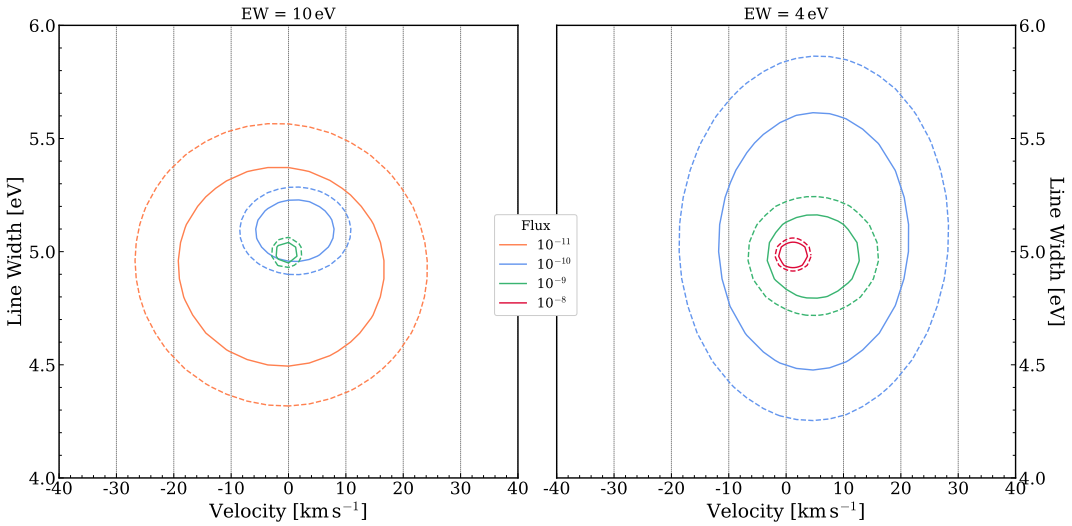

Figure 4.12: ***XRISM* velocity confidence intervals**: Contours showing the 1-σ (solid) and 2-σ (dashed) confidence intervals for orbital velocity measurements from the KA line, with different source flux.

star of 5–40 km s^{-1}. In the best case scenario (outbursts of $10^{-8} - 10^{-9}$ ergs cm^{-2} s^{-1} and $q > 4$) *XRISM* may be able to resolve the Kα line with velocity errors within a few km s^{-1}. This relies on exposure times of 100 ks; but further simulations are carried out with exposures of 50 ks and 20 ks, which show that if the X-ray flux is bright (i.e. $F_{2-10\,keV} = 10^{-8}$–10^{-9} ergs cm^{-2} s^{-1}) velocity errors remain well-constrained.

The 1-σ, 2-σ uncertainties as shown in Figure 4.12 are given in Table 1. Note, higher fluxes rely on exposure times exceeding 50 ks - this is therefore considered the limiting flux for which *XRISM* may calculate radial velocity measurements:

$F_{2-10\,keV}$ ergs cm^{-2} s^{-1}	1-σ km s^{-1}	2-σ km s^{-1}
10^{-8}	2	3
10^{-9}	5	9
10^{-11}	19	24
10^{-12}	40	46

Table 4.1: 1-σ and 2-σ errors in velocity for various X-ray fluxes, given 50 ks exposure time.

Typical HMXB companion star velocities range from 10–100 km s^{-1}, meaning radial velocity errors may be of order 5-10%. However, given sufficient orbital phase coverage,

it should still be sufficient to produce a radial velocity curve, from which the amplitude and period can be determined.

4.7.1 Simulated radial velocity curves

Having calculated the equivalent width as a function of phase, one can simulate the expected spectrum as would be observed by *XRISM* and determine the extent to which the narrow component may be used to constrain energies and radial velocities.

Consider two HMXBs (as explained further later, these are the most promising candidates for this technique), each with mass ratio $q = 4$ and orbital period $P_{\rm orb}$ of 5 days, but different compact object mass and therefore different K_2 values. Having found the expected equivalent width of the Kα line as a function of phase, this is reduced by 20% to account for changes in flux at the peak line energy due to the complex profile of the emission line (such as the Compton Shoulder, resulting from the down-scattering of fluorescent photons [297; 248]). 10 epochs are chosen randomly over 4 orbital cycles, and the expected strength and Keplerian velocity of the Kα feature are calculated. Having introduced some scatter (mimicking small velocity changes associated with winds, etc.), spectra were simulated and analysed with the intention of fitting the Kα line and calculating the radial velocity measurements and errors. The results of these are shown in Figure 4.13.

Where the flux of the X-ray source is $10^{-10}\,\mathrm{ergs\,cm^{-2}\,s^{-1}}$, errors in velocity range from 10 to $30\,\mathrm{km\,s^{-1}}$ (changing as a function of phase in response to the modulation of EW). For systems with a K_2 of order $100\,\mathrm{km\,s^{-1}}$, these errors are small enough to produce good radial velocity curves, with fits in good agreement with the 'correct' system parameters (Figure 4.13). Where Keplerian velocities are smaller, $\sim$$30\,\mathrm{km\,s^{-1}}$ (i.e. as would be more typical for systems with larger companion star masses), these errors cast doubt on the resultant radial velocity curves. Figure 4.14 shows a comparison between velocity errors produced with *XRISM* and *Athena* response files, indicating the significant improvement that *Athena* will provide, particularly for fainter fluxes and/or smaller velocities.

4.8 Discussion

These calculations indicate that if narrow, fluorescent X-ray emission lines from the companion star can be isolated, they provide a viable method for measuring binary mass

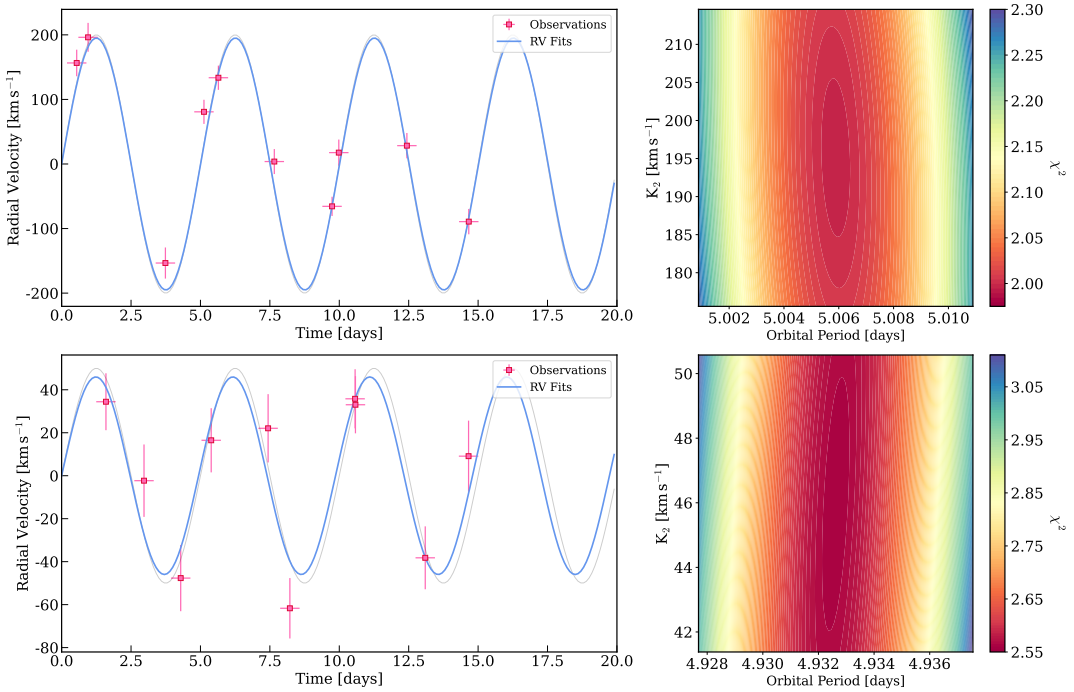

Figure 4.13: **Simulated Radial velocity fits**: Simulated radial velocity observations of two sources (both with orbital period $P_{\rm orb} = 5$ days.). Left panels: Simulated radial velocities and errors (derived using `XSPEC`) (pink markers) and best-fit orbital solution (fitting K and P only)(blue). The 'correct' solution is shown (grey). Right Panels: goodness-of-fit (χ^2) of orbital fits for K_2 and $P_{\rm orb}$.

functions. This then makes it possible to investigate many systems that are too obscured and/or faint to be studied in the optical.

The most viable candidates are those systems (mostly HMXBs) where the companion star presents a significant reflecting surface to incident X-rays, i.e., the line EW increases with mass ratio q, and where their inclinations are $> 60°$, (particularly if the mass ratio is smaller). This needs to be balanced against the fact that more massive systems will have lower K_2 values, and there could be other, more complex, emission components such as stellar winds, as is discussed below. Hence, the ideal systems could be objects with more intermediate mass ratios q and mid-spectral types. Exposure times of 100 ks yield sufficient energy precision with *XRISM*, although shorter observations can provide useful constraints, especially with *Athena*. Additionally, full orbital phase coverage is essential.

After the launch of *XRISM* and *Athena*, it would be prudent to validate observations of systems with already well-established optical ephemerides, e.g. GRO J1655–40 ($q = 0.4$, $P = 2.6$ days, $K_2 = 228\,{\rm km\,s^{-1}}$), Cyg X - 1 ($q = 1$–$2$, $P = 5.6$ days, $K_2 = 76\,{\rm km\,s^{-1}}$),

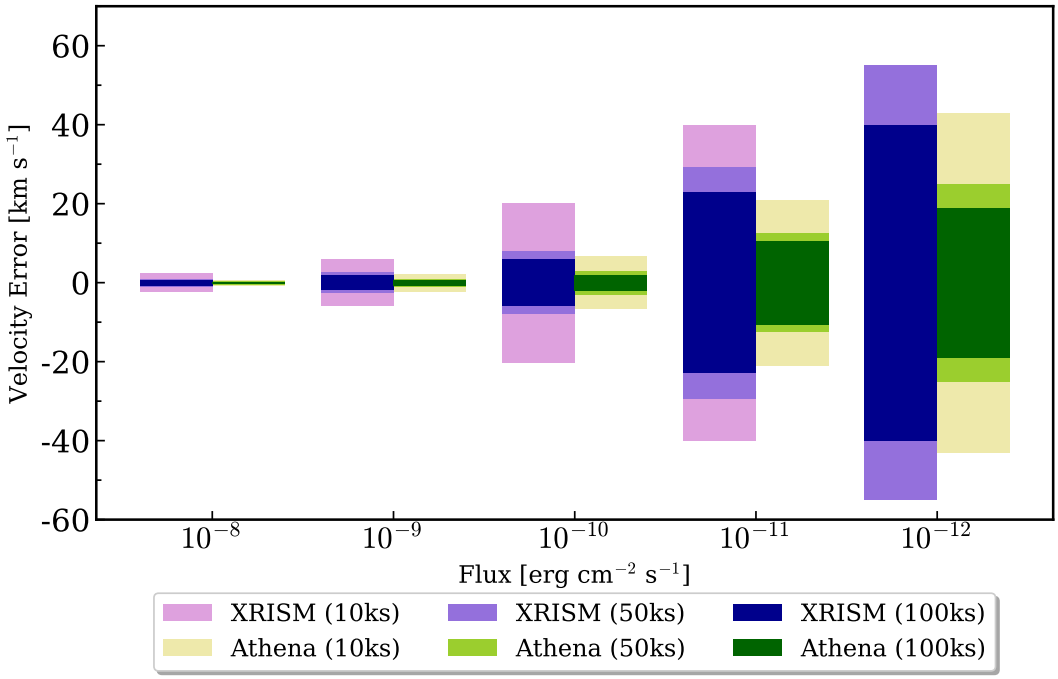

Figure 4.14: **Expected RV errors**: Predicted uncertainties in radial velocities as a function of flux and exposure time, for both *XRISM* (blue) and *Athena* (green)

or V404 Cyg ($q = 0.1$, $P = 6.5$ days, $K_2 = 210\,\mathrm{km\,s^{-1}}$)[2]. These will provide a wealth of information on the viability of isolating the narrow component of the Fe line and its location since the binary solution is known from the optical. In the cases of the two X-ray transient LMXBs (GRO J1655–40, V404 Cyg), observing in *quiescence* is also potentially valuable, as it would minimise potentially confusing emissions from the (still present) accretion disc. Additionally, during quiescence, discs may have lower flaring angles, thereby increasing the irradiated area of the companion [6]. This would, however, be challenging, as the X-ray fluxes would be lower. If velocity errors from observations of Kα are too large, other spectral features at lower energies (O, Ne, Fe-L at 0.5–1 keV) associated with intrinsic coronal emission from the donor might also be detectable.

Two further XRB candidates of particular interest for an X-ray spectroscopic study include Cyg X-3, and Her X-1. Cyg X-3 is an optically obscured, short period (4.8 hrs), HMXB, comprising a (candidate) black hole and a Wolf-Rayet donor. Even though it is X-ray bright, Cyg X-3's ephemeris is well established, so phase-binning could be used to search for weak, sharp features within the spectra. Her X-1 is eclipsing (1.7 day period), and it exhibits a well-known 35-day super-orbital periodicity [178], which is attributed to

[2]System parameters from [53].

the tilting and precessing of its accretion disc, which causes variable X-ray obscuration. Her X-1 is also an X-ray pulsar, and falls into the rare category of 'intermediate-mass X-ray binaries'.

Findings of an expected equivalent width of 5–40 eV are in good agreement with the first calculations of this effect [12]; e.g., for Her X-1 with a mass ratio $q = 1.8$, a calculated EW of ≈ 16 eV, sits very close to Basko [12]'s estimate of 14 eV. Interestingly, Torrejón et al. [282]'s 2010 survey of Kα emission finds EWs (particularly for HMXBs) are observed to be much higher, often a few hundred eV. This is potentially due to the origins of the Kα emission in HMXBs being the stellar wind - if not confined to one side of the binary system, the winds present a large solid angle through which X-ray reprocessing and, therefore, Kα emission may occur.

4.9 Caveats

Having presented simulations and expectations, it is necessary to discuss some of the limitations, caveats and assumptions that need to be kept in mind.

4.9.1 Resolving and locating the narrow line

This work depends on the X-ray spectrometer's ability to isolate the narrow component of the iron fluorescent emission. There is reason to be (cautiously) optimistic that this will be feasible with microcalorimeters, as a narrow-line component has been isolated in previous studies by *Chandra* HETG at the best spectral resolution currently available in the Fe K band ($\Delta E = 40$ eV). For comparison, some of the previous best studies with CCDs, using *XMM-Newton*, have found narrow features in the X-ray spectra of HMXBs, but with uncertainties in centroid energy of order 10 eV – corresponding to velocity errors $>200\,\mathrm{km\,s^{-1}}$ (and is consistent with estimates from `XSPEC` simulations - see Figure 4.12b) [110]. The gains with *XRISM* (and later *Athena*) are vast, such that the narrow line should not only be identified in a number of systems but also used to obtain velocity information concerning these binary systems.

It must be noted that, while the companion star is the most likely site for a narrow Kα component, other locations are known to be possibilities, e.g. stellar winds, inner accretion disc structure, and the impact bulge due to the accretion stream. If present, such components would make it harder to determine system masses. Using both velocity and flux variability information as a function of phase would allow them to be physically

located within the binary system, thereby allowing the detailed accretion geometry in and around the disc to be constrained in ways not hitherto possible (see also Section 5.2)

Whilst the aforementioned simulations treat the fluorescent emission as a simple Gaussian, for demonstration purposes, the actual line profile of the narrow component will likely be more complex. The high-energy fluorescence photons may have some probability of being Compton down-scattered to lower energies, resulting in a 'red shoulder' in the Kα line profile [297; 248]. This has been observed in some HMXBs with supergiant companions [282], and may be somewhat accounted for by reducing the EW of the Gaussian peak by 10% when performing the more detailed radial velocity simulations in Section 4.1. Models of the line's complex structure suggest that the central line energy should still remain constrained, and the peak flux will be 60–90% of the 'expected flux'. Attention to complexities in the line profile should be noted, both as a caveat to the accuracy of the predicted emission strengths and radial velocity measurements and as an opportunity to further understand the reprocessing material around the XRB.

4.9.2 Stellar metallicity

The Kα line's EW is dependent on the stellar metallicity, and spectra are usually fitted with solar-metallicity models. Given that the disc is accreted from a companion likely to have close to solar abundances, it is unsurprising that previous studies into XRB metallicities find iron abundances similar to, or slightly exceeding solar values (i.e. [Fe/H]$\approx$0.24 in neutron star binaries, and [Fe/H]$\approx$0.09 in black hole binaries (e.g. González Hernández et al. [112] and references therein), though metallicity can vary between different generations of stars. Additionally, there is evidence that the formation of the compact object via a supernova explosion can lead to significant amounts of processed material being captured by the companion star, thereby leading to higher metallicities [261]. It is, therefore, plausible that the companion star's atmosphere will have sufficient iron content to produce X-ray fluorescence. Nevertheless, this needs confirmation, and such studies will provide information about the donor's evolution.

4.9.3 Mass of the donor star

This work has focused on using the Kα line velocities to constrain $f(M_1)$. However, while HMXB donors present a much larger solid angle to the X-ray source (assumed to be a neutron star, as they dominate the HMXB population), the donors will typically have lower velocities ($\sim$ a few $10\,\mathrm{km\,s^{-1}}$), which may be comparable to their accompanying

errors, making meaningful radial velocities difficult to extract. Figure 4.13 demonstrates this effect, which is of course flux-dependent. A larger donor solid angle and resultant stronger Kα emission in such systems means that the velocity errors will be better constrained. Alternatively, on a longer timescale, *Athena* will have sufficient resolution and greater sensitivity, with errors decreasing from order $15\,\mathrm{km\,s^{-1}}$ to $\sim 5\,\mathrm{km\,s^{-1}}$ at $F < 10^{-9}\,\mathrm{ergs\,cm^{-2}\,s^{-1}}$.

Exposure times for these simulations ranged from 5 ks to 50 ks. For short-period XRBs, phase-binning will be required, and the periods are expected to be independently known.

4.9.4 Complex dynamics within the stellar wind

One of the biggest uncertainties associated with this methodology is the fact that the nature and impact of the stellar winds are still somewhat uncertain. There have been many studies of wind structure in XRBs, with strong effects (particularly large X-ray variability) indicating the presence of clumping [283]. This leads to deviations from the expected radial velocity curves, with the effects being most prominent near phase 0, i.e. inferior conjunction [116; 131; 177]. Previous studies of lower-energy lines (such as silicon and sulphur) have been used to study the stellar winds in Cyg X-1 [207], but earlier missions have lacked the high-energy resolution to extensively study the Kα line in the same way.

With sufficiently long observing times, the Doppler scatter due to clumpy winds will average out, and details of the complex wind structures will be of interest regardless. Torrejón et al. [282] did not in fact detect any substantial changes in the *peak line-energy* of their detected narrow line components that might have been expected due to winds, which provides encouraging support that any motion will be dominated by orbital mechanics. Instead, the maximum width (σ) of the unresolved narrow line components (5 eV) placed a constraint on a plausible wind velocity of $\nu = 800\,\mathrm{km\,s^{-1}}$. *Chandra*'s resolution meant that line centroid energies in that survey were constrained with errors of 6 eV, corresponding to $250\,\mathrm{km\,s^{-1}}$. One may therefore speculate that either the winds do not inflict random scatter in the peak energy of the Kα emission or that scatter of this type is of order $< 250\,\mathrm{km\,s^{-1}}$. This may still be comparable with orbital velocities, and so it will only be known for certain how much of an impact this will have once observations are carried out.

LMXBs generally have much weaker donor wind components, and so velocity measurements should be less susceptible to variations that are not associated with donor

orbital motions. Indeed, the success of Ponti et al. [233] in constraining the mass function through the radial velocities derived from absorption features associated with the compact object indicate that whilst more complex physics may be at play, this does not necessarily preclude X-ray mass function measurements. This further highlights the prerequisite of testing this technique on some well-characterized system (such as GRO J1655–40) in order to determine whether the stellar wind presents a significant and/or systematic hindrance.

4.9.5 Effects of ionisation

If there is any change in the ionisation state of the reflecting surface, the energy of the fluorescent emission will change. This would cause a shift in peak energy unrelated to orbital dynamics. Previous studies have used spectra of the fluorescent emission to determine the ionisation states of the reprocessing material (e.g. Giménez-García et al. [110] found that the peak energy of the Fe Kα fluorescent component was centred on 6.42 keV, and suggested that the reprocessing material must be in an ionisation state below Fe XVIII). Variations in the ionisation level and, consequently, peak energy could complicate radial velocity measurements.

If X-ray sources become transiently bright or dim, this could affect the ionisation of the stellar wind or companion star surface, resulting in variations in Kα line energy. Additionally, the impact of the accretion stream on the edge of the disc results in a "bulge" structure, and it has been suggested that this can cause ionisation instabilities, creating patchy clouds of colder gas among the hotter medium [264]. However, if these effects should be systematic and persist across the orbital cycle, this should not affect radial velocity curve measurements, since the main observable of interest is the Doppler variation with orbital phase.

While this remains to be tested, observations in *quiescence* may be more favourable to avoid the complications associated with ionisation effects, as at the expense of a lower source flux, systems will likely be subject to fewer changes in ionisation and continuum flux during quiescence. Simulations demonstrate that observations of Kα emissions even at low fluxes (10^{-11} - 10^{-12} ergs cm^{-2} s^{-1}) could be used to constrain velocities to ± 30 km s^{-1}. This will be challenging but would, obviously, be more effective with *Athena*, given its larger collecting area.

4.9.6 Instrumental systematics

In the absence of any observations at the time of writing, the above ought to be considered a proof-of-concept and, as such, largely ignores any instrument-specific biases (although it should be noted that microcalorimeters will be optimised for relatively faint sources). High count-rate observations may suffer from other systematic issues such as cross-talk [63], which would reduce the effective spectral resolution of some fraction of detected events at bright fluxes, thus adversely impacting radial velocity variation searches.

This is another reason to attempt to exploit fainter *quiescent* states for this work where possible. Ultimately, instruments on future facilities ought to be developed to robustly handle high count-rates. Kammoun et al. [160] propose that, when observing very bright sources, *Athena*'s X-IFU could make use of defocussing, where the telescope's point spread function (PSF) is spread over multiple pixels. In this way, spectra of bright sources could be successfully reconstructed, thereby mitigating some of the instrumental limitations.

On the subject of long-term investments in X-ray astronomy, at the time of writing, the future of *Athena* remains uncertain. Descoping of the project would, obviously, have a detrimental impact on mass function measurements. Mass measurements derived from the above method provide an additional science case supporting the retention of the full effective area of the microcalorimeter.

4.9.7 Orbital period

Finally, even in the best possible circumstances, exploiting these spectral data to extract radial velocity curves is a non-trivial task. Firstly, multiple observations are obviously required, and in most XRBs, the orbital period is likely to be already known (through other data, usually optical, IR or radio), making broad phase coverage possible. One advantage of X-ray observations is the possibility of co-adding multiple datasets into phase bins, allowing maximum sensitivity for searching for narrow spectral features.

Furthermore, the number and cadence of observations will also impact the ease with which a radial velocity curve can be extracted. When searching for periodicities in *photometric* light curves, for instance, the influence of red noise cannot be ignored [291]. Here, fitting is applied to *spectroscopic* data. Whilst the above simulations have relied upon being able to fit sinusoidal curves to the data, depending on the number and cadence of observations, the magnitude of statistical scatter in the data, and potential

radial velocity scatter due to multiple intrinsic line components, a more detailed Fourier period search will likely be required [253; 136].

These are important ultimate considerations. The goal here has been to investigate the viability of detecting X-ray radial velocity changes in the first place; fitting the ensemble measurements will be source-specific, which is beyond the scope of the present work.

4.10 Disc origin and inversion of the mass function

Whilst the focus of this investigation is on using the X-ray fluorescence from the companion star, there exists the potential for this method to be applied to reflection off disc emission instead (with some modifications). This would be relevant if the narrow line originates from the outer disc or from a disc wind anchored to the primary. In such cases, the mass function is effectively inverted, and it may be possible to measure the Doppler shift in the emission from the accretion disc in order to constrain the mass of the companion star instead. The inverted mass function is expressed as follows;

$$f(M_2) = \frac{M_2^3 \sin^3 i}{M_{Tot}^2} = \frac{P_{orb} K_1^3}{2\pi G} \tag{4.13}$$

The masses of companion stars are also often uncertain, as binary interactions can complicate stellar evolution. Such an inversion could then provide an interesting and independent validation of companion star parameters.

Conversely, an independent estimate of M_2 (for example, from its spectral type), could be used in tandem with the radial velocity curve from the outer disc of the compact object to constrain the mass of the compact object. In this case, M_1 is calculated:

$$0 = f(M_2) \times (M_1 + M_2)^2 - M_2^3 \sin^3 i \tag{4.14}$$

$$M_1 \leq \frac{\sqrt{M_2^3 \sin^3 i}}{f(M_2)} - M_2 \tag{4.15}$$

Both [233] and [317] use the Doppler motion of absorption features associated with the accretion disc to infer system parameters (i.e. companion star mass and black hole mass & system inclination respectively), making use of prior observations and well-defined system parameters (i.e. [317] used the known phase of the companion to fit velocity curves for the accretion disc). That this method has been validated with *Chandra* data demonstrates the vast potential of X-ray spectroscopy as a way to probe system characteristics.

4.11 Conclusions

Having demonstrated the theoretical validity of using X-ray spectroscopy to produce radial velocity curves for binary systems and discussed several of the main caveats to keep in mind, it is opportune that measurements of mass function be seriously attempted with current and upcoming X-ray missions.

The companion star in X-ray binary systems can present a large solid angle, particularly in systems where the mass ratio, q, exceeds 1. This leads to iron-line fluorescence with an expected equivalent width of the Kα emission $\sim$2–40 eV, for systems with $q > 0.1$ - although with significant variations with phase, which are dependent on both mass ratio and inclination (Figures 4.10 & 4.11).

Cutting-edge microcalorimeters, such as *XRISM*'s *Resolve*, will be able to detect the Kα iron line, and simulations indicate any deviation in centroid energy may be observed with sufficient accuracy to constrain velocities within $\sim$5–30 km s^{-1}. Given ample phase coverage, the radial velocity curves of the companion star can be well-measured, providing insight to the mass and nature of the compact object. Both LMXBs and HMXBs are viable targets, however, the latter are arguably more suited to this study due to having large stars and (usually) higher X-ray fluxes. This is in contradiction with optical and infrared studies, which favour LMXBs in states of low X-ray flux, meaning studies in the different wavebands are complementary.

This is subject to a number of caveats (including complexities within the stellar wind, low companion velocity, and the usual systematic constraints associated with radial velocity measurements). That being said, high-resolution observations of Kα emission in XRBs may also develop an understanding of the behaviour of the stellar winds in HMXBs.

Despite the above caveats, the potential gain in parameter space is huge, enabling new system constraints on previously inaccessible sources (that are either too faint, obscured, or otherwise difficult in the optical). The new era of high-resolution X-ray astronomy will be a step change in terms of improved precision constraints on binary system parameters. These advances should be exploited to address fundamental questions regarding the mass distribution of compact objects and related aspects of stellar evolution, both with the active *XRISM* mission and the upcoming *Athena*.

Chapter 5

Conclusions

The formation of compact objects is far from simple, governed by binary interactions, supernova mechanisms, and their initial parameters (which are often poorly constrained). Arguably, the two parameters most readily observed are mass and velocity, yet our understanding of both of these fundamentals remains subject to much uncertainty. In our dynamic universe, observations of the motion and kinematics of back holes are critical to understanding black hole formation, evolution, and death.

The origin and characteristics of natal kicks imparted to compact objects, including neutron stars and black holes, remains an active area of research, from both an observational and theoretical perspective. In the absence of a definitive understanding of natal kick drivers, this thesis finds the magnitudes of natal kicks for both neutron stars and black holes are best described by a Gamma distribution with a mean kick velocity of approximately $147\,\mathrm{km\,s^{-1}}$, which serves as a robust observationally motivated prescription for use in population synthesis studies. Given that the observational evidence does not decisively differentiate the distribution of natal kicks between neutron stars and black holes, it seems prudent to draw kicks from a common distribution, irrespective of the compact object in question.

Astrophysical studies have long hypothesized that the natal kicks received by neutron stars predominantly arise from asymmetries in both mass ejecta and neutrinos during supernova explosions, while black hole natal kicks are believed to be influenced by only the latter, resulting in comparatively lower velocities. However, this dichotomy is inconsistent with the observational data presented and analysed here. This new evidence suggests that some black holes exhibit natal kicks comparable to those of neutron stars, indicating that the separation of kick mechanisms may be overly reductive. This inconsistency points to a gap in our understanding of the underlying supernova processes.

One hypothesis posits that delayed supernova explosions, characterised by longer explosion timescales, could impart more substantial kicks [94; 255]. If this model holds true for black holes, it might explain the relatively larger kicks observed in some cases. Notably, such delayed explosions are hypothesized to occupy the mass gap between 3-5 $M_\odot$, though the reality of this mass gap remains debated.

Despite significant advances in hydrodynamic simulations and theoretical modelling, kinematic data from Galactic compact object populations continue to challenge theoretical expectations. High-precision observations, particularly those from astrometric surveys, underscore the necessity of integrating observations with simulations to reconcile discrepancies.

Future research ought to aim to establish models of natal kicks that not only accommodate the possibility of similar kicks for both neutron stars and black holes but remain consistent with other observational constraints. Importantly, analysing non-interacting compact object populations will help mitigate biases that arise from focusing predominantly on X-ray binaries. The case is the same for extending natal kick studies to gravitational wave sources, which will enhance our understanding of the natal kick distributions across different mass regimes.

X-ray binary systems present a unique opportunity for studying the mass and nature of compact objects through high-resolution spectroscopy. Chapter 4 calculated that the companion star in such systems, particularly when the mass ratio exceeds one, often exhibits iron-line fluorescence with an equivalent width of approximately 2–40 eV, although this is subject to variations due to inclination and orbital phase.

This work demonstrates that modern microcalorimeters, such as those on *XRISM's Resolve*, offer the precision required to detect slight shifts in the iron-line centroid energy, allowing for velocity constraints on the order of 5–10 $\mathrm{km\,s^{-1}}$, and the upcoming *Athena* mission will allow for even more stringent measurements. This advancement has profound implications for constructing radial velocity curves, particularly for high-mass X-ray binaries where the X-ray flux is brighter. Unlike optical studies, which predominantly focus on low-mass X-ray binaries, X-ray spectroscopy can thrive even when optical measurements are unfeasible due to faintness or obscuration.

Despite these promising techniques, several caveats must be considered. Systematic uncertainties associated with radial velocity measurements, complexities in stellar wind dynamics, and low companion velocities pose significant challenges. Moreover, the narrow line component from the donor remains elusive in many systems, complicating precise mass determinations. Nevertheless, the transition to high-resolution X-ray spectroscopy

marks a critical step forward in understanding the distribution and evolution of compact objects.

Beyond X-ray binaries, the European Space Agency's *Gaia* mission has revolutionized stellar and compact object astronomy through its unprecedented precision in astrometric measurements. Initially, *Gaia* Non-Single Solutions suggested the presence of massive dark companions in a number of systems. However, subsequent radial velocity measurements contradicted these data, and the analysis described in Chapter 3 indicates that these candidates are likely ordinary stellar binaries. This outcome provides invaluable insights into the complexities and limitations inherent in astrometric fitting. In particular, fitting astrometry to binary systems remains fraught with challenges. The *Gaia* pipeline's current methodology, while groundbreaking, is not without flaws. *Gaia* DR4, anticipated in 2026, is expected to provide individual epoch astrometry, allowing for more thorough modelling by researchers.

Regardless of the discrepancies between *Gaia* orbital observations and follow-up radial velocity campaigns, the potential of *Gaia* to discover compact objects remains immense. A more optimistic interpretation would be that the current null results do not reflect the absence of black holes but rather limitations in data interpretation. Future releases, with improved astrometric algorithms, may indeed reveal the population of black holes that theoretical predictions suggest. Individual epoch astrometry will allow researchers to conduct their own astrometric fitting, which could be informed by radial velocity studies. Additionally, the search algorithms & criteria developed for *Gaia* DR3 will be just as applicable for further data releases, and updated astrometric solutions for individual systems may lead to the identification of sources which do not currently present exotic characteristics.

As both X-ray observational capabilities and astrometric precision continue to develop, insights from *Gaia* and radial velocity studies from both space- and ground-based telescopes will likely yield a comprehensive understanding of binary dynamics, and, consequently, the nature of black holes.

While theoretical models provide a solid foundation, observations act as a necessary guide. We are working in an era in which the kinematics of compact objects can be constrained with extraordinary precision. In our energetic universe, these kinematics are interconnected to a variety of processes fundamental to black hole formation. The integration of astrometric data with spectroscopy will be crucial in unravelling the enigmatic processes governing compact object formation and evolution. The search for comprehensive models of both natal kicks and mass distributions remains challenging, but

opportunities for development are abundant. X-ray binaries remain rich with potential, and the work on extending our understanding of black holes to those which are not accreting has only just begun.

Appendix A

Estimating the velocity associated with mass loss (as in Nelemans et al. [214])

Consider the mass ejected from a compact object progenitor (e.g. a helium star) upon supernova. Conservation of momentum gives:

$$v_{\rm sys} = v_{\rm He} \frac{\Delta M}{M_{\rm BH} + m}$$

Where $M_{\rm BH}$ and m are the masses of the black hole and stellar companion respectively ΔM is the mass of the eject, and the relative velocity of the helium star, $v_{\rm HE}$, is given by:

$$v_{\rm He} = \frac{2\pi\, a_{\rm He}}{P_i}$$

where P_i is the initial orbital period - the system is assumed to be circular given the efficiency of tidal forces in circularising binary orbits [16]. The separation between the compact progenitor and the centre of mass $a_{\rm He} = a \frac{m}{M_{\rm He}+m}$. This can be determined from Kepler's Third Law:

$$\begin{aligned} a &= \left[\frac{P_i^2\, G\, (M_{\rm He} + m)}{4\,\pi^2} \right]^{1/3} \\ &= \left[\frac{G\, (M_{\rm He} + m)}{4\,\pi^2} \right]^{1/3} P_i^{2/3} \end{aligned}$$

Substituting this, and considering that the re-circularised orbital period, $P_r = P_i \left(\frac{M_{\rm He}+m}{M_{\rm BH}+m} \right)^2$ gives the relative velocity of the progenitor as follows:

$$
\begin{aligned}
v_{\rm He} &= \frac{2\pi\, a_{\rm He}}{P_i} \\
&= \frac{2\pi\, \left(a \frac{m}{M_{\rm He}+m}\right)}{P_i} \\
&= \frac{2\pi\, \left(\left(\frac{G}{4\,\pi^2}\right)^{1/3} P_r^{2/3}\, (M_{\rm BH}+m)^{4/3}\, (M_{\rm He}+m)^{-1}\, \frac{m}{M_{\rm He}+m}\right)}{P_i} \\
&= \frac{2\pi\, \left[\left(\frac{G}{4\,\pi^2}\right)^{1/3} P_r^{2/3}\, (M_{\rm BH}+m)^{4/3}\, (M_{\rm He}+m)^{-2}\, m\right]}{\left[P_r \left(\frac{M_{\rm BH}+m}{M_{\rm He}+m}\right)^2\right]} \\
&= 2\pi\, \left[\left(\frac{G}{4\,\pi^2}\right)^{1/3} P_r^{-1/3}\, (M_{\rm BH}+m)^{-2/3}\, m\right] \\
&= (2\pi\, G)^{1/3}\, P_r^{-1/3}\, (M_{\rm BH}+m)^{-2/3}\, m
\end{aligned}
$$

Returning to $v_{\rm sys} = v_{\rm sys} \frac{\Delta M}{M_{\rm BH}+m}$:

$$
\begin{aligned}
v_{\rm sys} &= v_{\rm He} \frac{\Delta M}{M_{\rm BH}+m} \\
&= (2\pi\, G)^{1/3}\, P_r^{-1/3}\, (M_{\rm BH}+m)^{-2/3}\, m \frac{\Delta M}{M_{\rm BH}+m} \\
&= (\mathrm{G}\, 2\pi)^{1/3}\, \Delta M\, m\, P_{\rm r}^{-1/3}\, (M_{\rm BH}+m)^{-5/3} \\
&\approx 213 \times \frac{m}{M_\odot} \frac{\Delta M}{M_\odot} \left(\frac{P_{\rm re-circ}}{\rm day}\right)^{-\frac{1}{3}} \left(\frac{M_{tot}}{M_\odot}\right)^{-\frac{5}{3}} {\rm km\,s^{-1}}
\end{aligned}
$$

Appendix B

Determining the resultant systemic velocity from a given natal kick

This derivation uses two frames of reference, shown in Figure B.1. I both frames, the x- and y-axes are defined by the binary orbital plane; the x-axis intersects the compact progenitor and the centre of mass of the binary, and the y-axis is parallel to the direction of the orbital motion in the case of a circular orbit. One frame, Figure B.1a, is centred on the system's centre of mass, the other, Figure B.1b, centred on the exploding star (the compact progenitor); the centre of each frame is considered at rest.

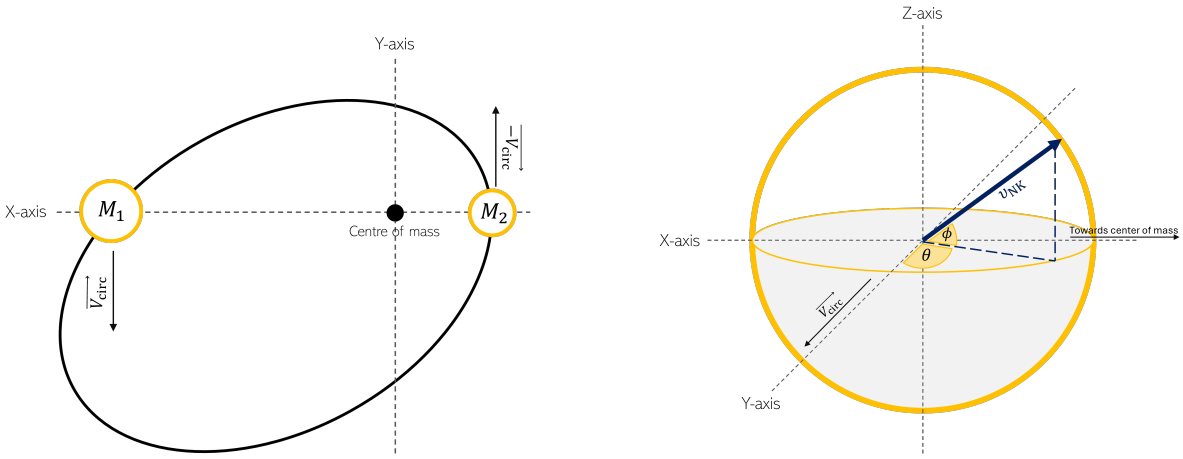

(a) Frame of reference centred on centre of mass of the binary.

(b) Frame of reference centred on exploding star (compact progenitor).

Figure B.1: Diagram showing the frame of references used in this derivation. In both cases, the x- and y- axes are defined by the binary orbital plane, with the z-axis aligned with the poles of the exploding star. The x-axis is directed between the exploding star and the centre of mass of the system, and the y-axis aligned with the direction of orbital motion in the case of a circular orbit. The right panel shows the angles (θ and ϕ) which define the natal kick, $\upsilon_{\rm NK}$.

Adopting the frame of reference centred on the centre of mass of the binary, the relative velocities, υ_r, of both stars are confined to the x-y plane. At the instant of the supernova, the velocities of the component stars (compact progenitor, M_1, and companion star, M_2) are:

$$\begin{pmatrix} -\upsilon_{rx}\frac{M_2}{M_1+M_2} \\ -\upsilon_{ry}\frac{M_2}{M_1+M_2} \\ 0 \end{pmatrix} \text{ and } \begin{pmatrix} \upsilon_{rx}\frac{M_1}{M_1+M_2} \\ \upsilon_{ry}\frac{M_1}{M_1+M_2} \\ 0 \end{pmatrix}$$

Directly following supernova (before orbital reconfiguration), the velocity of the companion star is the same, but the compact object has been perturbed by a natal kick, υ_k, and is now:

$$\begin{pmatrix} M_{\rm CO}\upsilon_{kx} - \upsilon_{rx}\frac{M_2}{M_1+M_2} \\ M_{\rm CO}\upsilon_{ky} - \upsilon_{ry}\frac{M_2}{M_1+M_2} \\ M_{\rm CO}\upsilon_{kz} \end{pmatrix}$$

Hence, systemic velocity is:

$$\begin{aligned} \upsilon_{\rm sys} &= \frac{M_{\rm CO}\upsilon_{\rm CO} + M_2 V_2}{M_{\rm CO}+M_2} \\ &= \frac{1}{M_{\rm CO}+M_2}\left[M_{\rm CO}\begin{pmatrix} \upsilon_{kx} - \upsilon_{rx}\frac{M_2}{M_1+M_2} \\ \upsilon_{ky} - \upsilon_{ry}\frac{M_2}{M_1+M_2} \\ \upsilon_{kz} \end{pmatrix} + M_2\begin{pmatrix} \upsilon_{rx}\frac{M_1}{M_1+M_2} \\ \upsilon_{ry}\frac{M_1}{M_1+M_2} \\ 0 \end{pmatrix}\right] \\ &= \frac{1}{M_{\rm CO}+M_2}\begin{pmatrix} M_{\rm CO}\upsilon_{kx} - M_{\rm CO}\upsilon_{rx}\frac{M_2}{M_1+M_2} + M_2\upsilon_{rx}\frac{M_1}{M_1+M_2} \\ M_{\rm CO}\upsilon_{ky} - M_{\rm CO}\upsilon_{ry}\frac{M_2}{M_1+M_2} + M_2\upsilon_{ry}\frac{M_1}{M_1+M_2} \\ M_{\rm CO}\upsilon_{kz} \end{pmatrix} \\ &= \frac{1}{M_{\rm CO}+M_2}\begin{pmatrix} M_{\rm CO}\upsilon_{kx} + \upsilon_{rx}\frac{M_2(M_1-M_{\rm CO})}{M_1+M_2} \\ M_{\rm CO}\upsilon_{ky} + \upsilon_{ry}\frac{M_2(M_1-M_{\rm CO})}{M_1+M_2} \\ M_{\rm CO}\upsilon_{kz} \end{pmatrix} \end{aligned}$$

The magnitude of the new systemic velocity may be calculated as:

$$
\begin{aligned}
v_{\rm sys}^2 =& \frac{1}{(M_{\rm CO}+M_2)^2}\begin{pmatrix}\left(M_{\rm CO}v_{kx}+v_{rx}\frac{M_2(M_1-M_{\rm CO})}{M_1+M_2}\right)^2\\ \left(M_{\rm CO}v_{ky}+v_{ry}\frac{M_2(M_1-M_{\rm CO})}{M_1+M_2}\right)^2\\ M_{\rm CO}^2v_{kz}^2\end{pmatrix}\\
v_{\rm sys}^2 =& \frac{1}{(M_{\rm CO}+M_2)^2}\begin{pmatrix}\left(M_{\rm CO}^2v_{kx}^2+v_{rx}^2\frac{M_2^2(M_1-M_{\rm CO})^2}{(M_1+M_2)^2}+2v_{kx}v_{xr}\frac{M_{\rm CO}M_2(M_1-M_{\rm CO})}{(M_1+M_2)}\right)\\ \left(M_{\rm CO}^2v_{ky}^2+v_{ry}^2\frac{M_2^2(M_1-M_{\rm CO})^2}{(M_1+M_2)^2}+2v_{ky}v_{ry}\frac{M_{\rm CO}M_2(M_1-M_{\rm CO})}{(M_1+M_2)}\right)\\ M_{\rm CO}^2v_{kz}^2\end{pmatrix}\\
v_{\rm sys}^2 =& \frac{1}{(M_{\rm CO}+M_2)^2}\left[(M_{\rm CO}v_k)^2+\left(\frac{M_2(M_1-M_{\rm CO})}{M_1+M_2}\right)^2\left(v_{rx}^2+v_{ry}^2\right)+\right.\\
&\left.2(v_{kx}v_{rx}+v_{ky}v_{ry})\left(\frac{M_{\rm CO}M_2(M_1-M_{\rm CO})}{M_1+M_2}\right)\right]\\
v_{\rm sys}^2 =& \left(\frac{v_kM_{\rm CO}}{M_{\rm CO}+M_2}\right)^2+\left(\frac{v_rM_2(M_1-M_{\rm CO})}{(M_{\rm CO}+M_2)(M_1+M_2)}\right)^2+\\
&2(v_{kx}v_{rx}+v_{ky}v_{ry})\frac{M_{\rm CO}M_2(M_1-M_{\rm CO})}{(M_1+M_2)(M_{\rm CO}+M_2)^2}\\
v_{\rm sys}^2 =& \left(\frac{v_kM_{\rm CO}}{M_{\rm CO}+M_2}\right)^2+\left(\frac{v_rM_2(M_1-M_{\rm CO})}{(M_{\rm CO}+M_2)(M_1+M_2)}\right)^2+\\
&2v_r(v_{kx}\alpha_S+v_{ky}\alpha_C)\frac{M_{\rm CO}M_2(M_1-M_{\rm CO})}{(M_1+M_2)(M_{\rm CO}+M_2)^2}
\end{aligned}
$$

where $v_{kx} = v_k\sin(\phi)\cos(\theta)$; $v_{ky} = v_k\cos(\phi)\cos(\theta)$; $\alpha_S = \sqrt{\frac{a^2(1-e^2)}{r(2a-r)}}$; and $\alpha_C = -\frac{e\sin(M)}{\sqrt{1-e^2\cos(M)^2}}$.

Given that the natal kick is defined in the frame centred on the exploding star, α_S and α_C are terms representing the decomposition of the orbital velocity to two vector components in the frame of reference centred on the exploding star (i.e. frame B.1b). $\alpha_S = \sin\Omega$ and $\alpha_C = \cos\Omega$ (where Ω indicates the direction of orbital motion, as shown in Figure B.2). This angle, Ω, is defined between x & y axes in the frame of the exploding star, and is given by:

$$\Omega = \tan^{-1}\left(\frac{b^2}{yae}\right) \tag{B.1}$$

where ae is the distance between the centre of the ellipse and the focal point(s); b is the semi-minor axis $\left(b = a\sqrt{1-e^2}\right)$; and y describes the position of the exploding star along its orbit ($y = b\sin\mathrm{E}$, with E defining the eccentric anomaly).

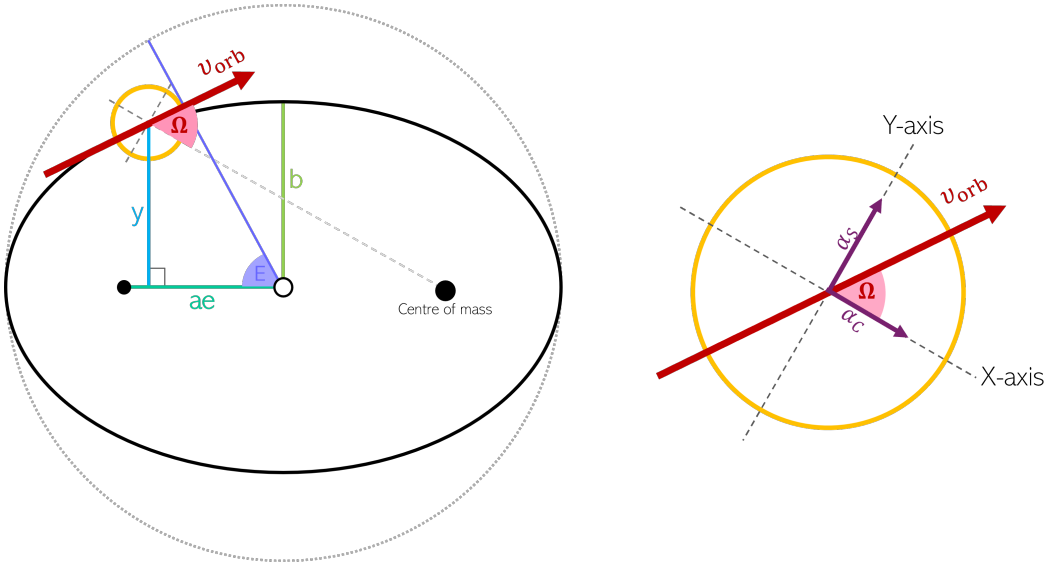

Figure B.2: Diagram demonstrating the decomposition of the orbital motion (υ_{orb}) to the frame of the exploding star. In this frame, the x-axis extends from the exploding star to the centre of mass of the system, and the y-axis indicates the direction of orbital motion if the orbit were circular. The orbital velocity vector is separated into two constituent vectors in the x- and y- axes, α_S and α_C, which can be calculated using the semi-major axis, the eccentricity, and the eccentric anomaly.

$$
\begin{aligned}
\tan(\Omega) &= \frac{b^2}{yae} \\
&= \frac{b^2}{ae\,(b\sin \mathrm{E})} \\
&= \frac{b}{ae\sin \mathrm{E}} \\
&= \frac{a\sqrt{1-e^2}}{ae\sin \mathrm{E}} \\
&= \sqrt{\frac{a^2\,(1-e^2)}{a^2e^2\sin^2 \mathrm{E}}} \\
&= \sqrt{\frac{(1-e^2)}{e^2\,(1-\cos^2 \mathrm{E})}} \\
&= \frac{\sqrt{1-e^2}}{e\sqrt{1-\cos^2 \mathrm{E}}}
\end{aligned}
$$

Making use of the following trigonometric identities: $\cos\left(\tan^{-1}(x)\right) = (1+x^2)^{-0.5}$ and $\sin\left(\tan^{-1}(x)\right) = x\,(1+x^2)^{-0.5}$, where $x = \frac{\sqrt{1-e^2}}{e\sqrt{1-\cos^2(E)}}$.

$$
\begin{aligned}
(1+x^2)^{-0.5} &= \left[1+\frac{1-e^2}{e^2(1-\cos^2(E))}\right]^{-0.5} \\
&= \left[\frac{e^2(1-\cos^2(E))}{e^2(1-\cos^2(E))}+\frac{1-e^2}{e^2(1-\cos^2(E))}\right]^{-0.5} \\
&= \left[\frac{e^2(1-\cos^2(E))+1-e^2}{e^2(1-\cos^2(E))}\right]^{-0.5} \\
&= \left[\frac{1-e^2\cos^2(E))}{e^2(1-\cos^2(E))}\right]^{-0.5} \\
&= \left[\frac{e^2(1-\cos^2(E))}{1-e^2\cos^2(E))}\right]^{0.5} \\
\alpha_C &= \frac{e\sin(E)}{\sqrt{1-e^2\cos^2(E))}}
\end{aligned}
$$

$$
\begin{aligned}
x(1+x^2)^{-0.5} &= \frac{\sqrt{1-e^2}}{e\sqrt{1-\cos^2(E)}} \times \frac{e\sin(E)}{\sqrt{1-e^2\cos^2(E))}} \\
&= \sqrt{\frac{1-e^2}{1-e^2\cos^2(E))}} \\
&= \sqrt{\frac{a^2(1-e^2)}{a^2(1-e^2\cos^2(E)))}} \\
&= \sqrt{\frac{a^2(1-e^2)}{2a^2-2a^2e\cos(E)-(a^2-2a^2e\cos(E)+a^2e^2\cos^2(E))}} \\
&= \sqrt{\frac{a^2(1-e^2)}{2a^2-2a^2e\cos(E)-(a-ae\cos(E))^2}} \\
&= \sqrt{\frac{a^2(1-e^2)}{2a(a-ae\cos(E))-(a-ae\cos(E))^2}} \\
\alpha_S &= \sqrt{\frac{a^2(1-e^2)}{2ar-r^2}}
\end{aligned}
$$

Appendix C

Converting the Thiele-Innes coefficients (A,B,F,G) into orbital elements (a_0, ω, Ω, i)

A number of candidate Gaia binaries are described with the Thiele Innes coefficients (see Section 3.2). The Thiele Innes coefficients A,B,F, and G are expressed with a_0 (semi-major axis of photocenter), ω (angle of the ascending node), Ω (argument of periastron), and i, the orbital inclination, by the following [23; 128]:

$$\begin{aligned}
A &= a_0 \left[\cos(\omega)\cos(\Omega) - \sin(\omega)\sin(\Omega)\cos(i)\right] \\
B &= a_0 \left[\cos(\omega)\sin(\Omega) + \sin(\omega)\cos(\Omega)\cos(i)\right] \\
F &= -a_0 \left[\sin(\omega)\cos(\Omega) + \cos(\omega)\sin(\Omega)\cos(i)\right] \\
G &= -a_0 \left[\sin(\omega)\sin(\Omega) - \cos(\omega)\cos(\Omega)\cos(i)\right]
\end{aligned}$$

For clarity, let a = $\frac{\mathrm{A}}{\mathrm{a_0}}$, b = $\frac{\mathrm{B}}{\mathrm{a_0}}$, etc. and make use of the shorthand $\cos(\omega) = c_\omega$, $\sin(\omega) = c_\omega$, and so on. Squaring all the equations gives:

$$\begin{aligned}
a^2 &= c_\omega^2 c_\Omega^2 + s_\omega^2 s_\Omega^2 c_i^2 - 2 s_\omega s_\Omega c_\omega c_\Omega c_i \\
b^2 &= c_\omega^2 s_\Omega^2 + s_\omega^2 c_\Omega^2 c_i^2 + 2 s_\omega s_\Omega c_\omega c_\Omega c_i \\
f^2 &= s_\omega^2 c_\Omega^2 + c_\omega^2 s_\Omega^2 c_i^2 + 2 s_\omega s_\Omega c_\omega c_\Omega c_i \\
g^2 &= s_\omega^2 s_\Omega^2 + c_\omega^2 c_\Omega^2 c_i^2 - 2 s_\omega s_\Omega c_\omega c_\Omega c_i
\end{aligned}$$

Summing these squares gives:

$$\begin{aligned}
a^2 + b^2 + f^2 + g^2 &= c_\omega^2 c_\Omega^2 [1 + c_i^2] + s_\omega^2 s_\Omega^2 [1 + c_i^2] + c_\omega^2 s_\Omega^2 [1 + c_i^2] + s_\omega^2 c_\Omega^2 [1 + c_i^2] \\
&= [1 + c_i^2] \left[c_\omega^2 c_\Omega^2 + s_\omega^2 s_\Omega^2 + c_\omega^2 s_\Omega^2 + s_\omega^2 c_\Omega^2\right] \\
&= [1 + c_i^2] \left[\left(c_\omega^2 + s_\omega^2\right)\left(c_\Omega^2 + s_\Omega^2\right)\right] \\
&= 1 + c_i^2
\end{aligned}$$

Then consider:

$$
\begin{aligned}
ag &= -\left(c_\omega c_\Omega - s_\omega s_\Omega c_i\right)\left(s_\omega s_\Omega - c_\omega c_\Omega c_i\right) \\
&= -c_\omega c_\Omega s_\omega s_\Omega + c_\omega^2 c_\Omega^2 c_i + s_\omega^2 s_\Omega^2 c_i - s_\omega s_\Omega c_\omega c_\Omega c_i^2 \\
&= c_i\left(c_\omega^2 c_\Omega^2 + s_\omega^2 s_\Omega^2\right) - [1 + c_i^2] c_\omega c_\Omega s_\omega s_\Omega \\
-bf &= \left(c_\omega s_\Omega + s_\omega c_\Omega c_i\right)\left(s_\omega c_\Omega + c_\omega s_\Omega c_i\right) \\
&= c_\omega c_\Omega s_\omega s_\Omega + c_\omega^2 s_\Omega^2 c_i + s_\omega^2 c_\Omega^2 c_i + s_\omega s_\Omega c_\omega c_\Omega c_i^2 \\
&= c_i\left(c_\omega^2 s_\Omega^2 + s_\omega^2 c_\Omega^2\right) + [1 + c_i^2] c_\omega c_\Omega s_\omega s_\Omega
\end{aligned}
$$

Summing the above gives:

$$
\begin{aligned}
ag - bf &= \left[c_i\left(c_\omega^2 c_\Omega^2 + s_\omega^2 s_\Omega^2\right) - [1 + c_i^2] c_\omega c_\Omega s_\omega s_\Omega\right] + \left[[1 + c_i^2] c_\omega c_\Omega s_\omega s_\Omega + c_i\left(c_\omega^2 s_\Omega^2 + s_\omega^2 c_\Omega^2\right)\right] \\
&= c_i\left[\left(c_\omega^2 c_\Omega^2 + s_\omega^2 s_\Omega^2\right) + \left(c_\omega^2 s_\Omega^2 + s_\omega^2 c_\Omega^2\right)\right] \\
&= c_i\left[\left(c_\omega^2 + s_\omega^2\right)\left(c_\Omega^2 + s_\Omega^2\right)\right] \\
&= 2c_i
\end{aligned}
$$

Defining $U = A^2 + B^2 + F^2 + G^2 = a_0^2\left(1 + \cos^2(i)\right)$ and $V = AG - BF = 2a_0^2\cos(i)$ leads to:

$$
\begin{aligned}
0 &= a_0^2\left(1 + V^2/a_0^4\right) - U \\
0 &= a_0^2 + V^2/a_0^2 - U \\
0 &= a_0^4 - U a_0^2 + V^2 \\
a_0^2 &= \frac{U \pm \sqrt{U^2 - 4V^2}}{2} \\
a_0^2 &= \frac{U \pm \sqrt{U^2 - 4V^2}}{2} \\
a_0 &= \left[\frac{U \pm \sqrt{U^2 - 4V^2}}{2}\right]^{0.5}
\end{aligned}
$$

Having found a_0, determining i from the above is trivial. For ω and Ω, one can make use of the trigonometric product identities, as follows:

$$\begin{aligned} b - f &= (c_\omega s_\Omega + s_\omega c_\Omega c_i) + (s_\omega c_\Omega + c_\omega s_\Omega c_i) \\ &= [1 + c_i]\,(c_\omega s_\Omega) + [1 + c_i]\,(s_\omega c_\Omega) \\ &= [1 + c_i]\,(c_\omega s_\Omega + s_\omega c_\Omega) \\ &= [1 + c_i] s_{(\omega+\Omega)} \end{aligned}$$

$$\begin{aligned} a + g &= (c_\omega c_\Omega - s_\omega s_\Omega c_i) - (s_\omega s_\Omega - c_\omega c_\Omega c_i) \\ &= [1 + c_i]\,(c_\omega c_\Omega) - [1 + c_i]\,(s_\omega s_\Omega) \\ &= [1 + c_i] c_{(\omega+\Omega)} \end{aligned}$$

$$\begin{aligned} b + f &= (c_\omega s_\Omega + s_\omega c_\Omega c_i) - (s_\omega c_\Omega + c_\omega s_\Omega c_i) \\ &= [1 - c_i]\,(c_\omega s_\Omega) - [1 - c_i]\,(s_\omega c_\Omega) \\ &= [1 - c_i]\,(c_\omega s_\Omega - s_\omega c_\Omega) \\ &= [1 - c_i] s_{(\omega-\Omega)} \end{aligned}$$

$$\begin{aligned} g - a &= -\,(s_\omega s_\Omega - c_\omega c_\Omega c_i) - (c_\omega c_\Omega - s_\omega s_\Omega c_i) \\ &= [c_i - 1]\,(c_\omega c_\Omega) + [c_i - 1]\,(s_\omega s_\Omega) \\ &= [c_i - 1]\,(c_\omega c_\Omega + s_\omega s_\Omega) \\ &= [1 - c_i] c_{(\omega-\Omega)} \end{aligned}$$

ω and Ω can be solved simultaneously:

$$\begin{aligned} \frac{b - f}{a + g} &= \frac{[1 + c_i] s_{\omega+\Omega}}{[1 + c_i] c_{\omega+\Omega}} \\ &= \tan(\omega + \Omega) \end{aligned}$$

$$\begin{aligned} \frac{b + f}{g - a} &= \frac{[1 - c_i] s_{\omega-\Omega}}{[1 - c_i] c_{\omega-\Omega}} \\ &= \tan(\omega - \Omega) \end{aligned}$$

$$\begin{aligned} \omega &= \frac{\arctan\left(\frac{B-F}{A+G}\right) + \arctan\left(\frac{B+F}{G-A}\right)}{2} \\ \Omega &= \frac{\arctan\left(\frac{B-F}{A+G}\right) - \arctan\left(\frac{B+F}{G-A}\right)}{2} \end{aligned}$$

All orbital elements may now be determined from the Thiele Innes coefficients as required.

Bibliography

[1] H. Andresen, E. Müller, H.-T. Janka, A. Summa, K. Gill, and M. Zanolin. Gravitational waves from 3d core-collapse supernova models: The impact of moderate progenitor rotation. *Monthly Notices of the Royal Astronomical Society*, 486(2): 2238–2253, Apr. 2019. ISSN 1365-2966. doi: 10.1093/mnras/stz990.

[2] K. A. Arnaud. XSPEC: The First Ten Years. In G. H. Jacoby and J. Barnes, editors, *Astronomical Data Analysis Software and Systems V*, volume 101 of *Astronomical Society of the Pacific Conference Series*, page 17, Jan. 1996.

[3] P. Arras and D. Lai. Can parity violation in neutrino transport lead to pulsar kicks? *The Astrophysical Journal*, 519(2):745–749, July 1999. ISSN 1538-4357. doi: 10.1086/307407.

[4] Athena Collaboration. The Hot and Energetic Universe: A White Paper presenting the science theme motivating the Athena+ mission. 2013.

[5] P. Atri, J. C. A. Miller-Jones, A. Bahramian, R. M. Plotkin, A. T. Deller, et al. A radio parallax to the black hole x-ray binary MAXI J1820+070. *Monthly Notices of the Royal Astronomical Society*, 493(1):L81–L86, jan 2020. doi: 10.1093/mnrasl/slaa010.

[6] P. D'Avanzo, T. Muñoz-Darias, J. Casares, I. G. Martínez-Pais, and S. Campana. A search for evidence of irradiation in Centaurus X-4 during quiescence. *Astronomy and Astrophysics*, 460(1):257–260, Dec. 2006. doi: 10.1051/0004-6361:20066010.

[7] A. Bahramian and N. Degenaar. *Low-Mass X-ray Binaries*, page 1–62. Springer Nature Singapore, 2023. ISBN 9789811645440. doi: 10.1007/978-981-16-4544-0_94-1.

[8] V. Baibhav and V. Kalogera. Revising the spin and kick connection in isolated binary black holes, 2024.

[9] C. A. L. Bailer-Jones, R. Andrae, B. Arcay, T. Astraatmadja, I. Bellas-Velidis, et al. The Gaia astrophysical parameters inference system (Apsis). Pre-launch description. *Astronomy and Astrophysics*, 559:A74, Nov. 2013. doi: 10.1051/0004-6361/201322344.

[10] C. D. Bailyn, R. K. Jain, P. Coppi, and J. A. Orosz. The Mass Distribution of Stellar Black Holes. *The Astrophysical Journal*, 499(1):367–374, May 1998. doi: 10.1086/305614.

[11] Z. Barkat, G. Rakavy, and N. Sack. Dynamics of Supernova Explosion Resulting from Pair Formation. *Physical Review Letters*, 18(10):379–381, Mar. 1967. doi: 10.1103/PhysRevLett.18.379.

[12] M. M. Basko. K-fluorescence lines in spectra of X-ray binaries. *The Astrophysical Journal*, 223:268–281, July 1978. doi: 10.1086/156260.

[13] M. M. Basko, R. A. Sunyaev, and L. G. Titarchuk. Reflection and reprocessing of X-ray source radiation by the atmosphere of the normal star in a binary system. *Astronomy and Astrophysics*, 31:249–263, Mar. 1974.

[14] G. Battaglia, A. Helmi, H. Morrison, P. Harding, E. W. Olszewski, et al. The radial velocity dispersion profile of the galactic halo: constraining the density profile of the dark halo of the milky way. *Monthly Notices of the Royal Astronomical Society*, 364(2):433–442, Dec. 2005. ISSN 1365-2966. doi: 10.1111/j.1365-2966.2005.09367.x.

[15] J. A. Bearden. X-ray wavelengths. *Rev. Mod. Phys.*, 39:78–124, Jan 1967. doi: 10.1103/RevModPhys.39.78.

[16] M. Beech. Tidal Circularization in Massive Binaries. *Astrophysics and Space Science*, 132(2):269–276, Apr. 1987. doi: 10.1007/BF00641759.

[17] J. D. Bekenstein. Gravitational-Radiation Recoil and Runaway Black Holes. *The Astrophysical Journal*, 183:657–664, July 1973. doi: 10.1086/152255.

[18] K. Belczynski, V. Kalogera, F. A. Rasio, R. E. Taam, A. Zezas, et al. Compact Object Modeling with the StarTrack Population Synthesis Code. *The Astrophysical Journal Supplement Series*, 174(1):223–260, Jan. 2008. doi: 10.1086/521026.

[19] K. Belczynski, V. Kalogera, F. A. Rasio, R. E. Taam, A. Zezas, et al. Compact Object Modeling with the StarTrack Population Synthesis Code. *The Astrophysical Journal Supplement Series*, 174(1):223–260, Jan. 2008. doi: 10.1086/521026.

[20] K. Belczynski, G. Wiktorowicz, C. L. Fryer, D. E. Holz, and V. Kalogera. Missing Black Holes Unveil the Supernova Explosion Mechanism. *The Astrophysical Journal*, 757(1):91, Sept. 2012. doi: 10.1088/0004-637X/757/1/91.

[21] K. Belczynski, S. Repetto, D. E. Holz, R. O'Shaughnessy, T. Bulik, et al. Compact Binary Merger Rates: Comparison with LIGO/Virgo Upper Limits. *The Astrophysical Journal*, 819(2):108, Mar. 2016. doi: 10.3847/0004-637X/819/2/108.

[22] K. Belczynski, J. Klencki, C. E. Fields, A. Olejak, E. Berti, et al. Evolutionary roads leading to low effective spins, high black hole masses, and O1/O2 rates for LIGO/Virgo binary black holes. *Astronomy and Astrophysics*, 636:A104, Apr. 2020. doi: 10.1051/0004-6361/201936528.

[23] L. Binnendijk. *Properties of double stars; a survey of parallaxes and orbits.* 1960.

[24] A. Blaauw. On the origin of the O- and B-type stars with high velocities (the "run-away" stars),and some related problems. *Bulletin of the Astronomical Institutes of the Netherlands*, 15:265, May 1961.

[25] L. Boccioli and L. Roberti. The physics of core-collapse supernovae: Explosion mechanism and explosive nucleosynthesis. *Universe*, 10(3):148, Mar. 2024. ISSN 2218-1997. doi: 10.3390/universe10030148.

[26] H. Boffin. Mass transfer by stellar wind. 06 2014. doi: 10.1007/978-3-662-44434-4_7.

[27] C. T. Bolton. Orbital elements and an analysis of models for HDE 226868 = Cygnus X-1. *The Astrophysical Journal*, 200:269–277, Sept. 1975. doi: 10.1086/153785.

[28] H. Bondi. On spherically symmetrical accretion. *Monthly Notices of the Royal Astronomical Society*, 112:195, Jan. 1952. doi: 10.1093/mnras/112.2.195.

[29] O. I. Borodina, A. F. Seleznev, G. Carraro, and V. M. Danilov. Unresolved Binaries and Galactic Clusters' Mass Estimates. *The Astrophysical Journal*, 874(2):127, Apr. 2019. doi: 10.3847/1538-4357/ab08e5.

[30] N. Brandt and P. Podsiadlowski. The effects of high-velocity supernova kicks on the orbital properties and sky distributions of neutron-star binaries. *Monthly Notices of the Royal Astronomical Society*, 274(2):461–484, 1995. doi: 10.1093/mnras/274.2.461.

[31] W. N. Brandt, P. Podsiadlowski, and S. Sigurdsson. On the high space velocity of X-ray Nova SCO 1994: implications for the formation of its black hole. *Monthly Notices of the Royal Astronomical Society*, 277(2):L35–L40, Nov. 1995. doi: 10.1093/mnras/277.1.L35.

[32] J. C. Bray and J. J. Eldridge. Neutron star kicks and their relationship to supernovae ejecta mass. *Monthly Notices of the Royal Astronomical Society*, 461(4):3747–3759, Oct. 2016. doi: 10.1093/mnras/stw1275.

[33] K. Breivik, S. Coughlin, M. Zevin, C. L. Rodriguez, K. Kremeer, et al. COSMIC Variance in Binary Population Synthesis. *The Astrophysical Journal*, 898(1):71, July 2020. doi: 10.3847/1538-4357/ab9d85.

[34] K. Breivik, S. Coughlin, M. Zevin, C. L. Rodriguez, K. Kremer, et al. Cosmic variance in binary population synthesis. *The Astrophysical Journal*, 898(1):71, 2020. doi: 10.3847/1538-4357/ab9d85.

[35] W. R. Brown, J. Anderson, O. Y. Gnedin, H. E. Bond, M. J. Geller, et al. A galactic origin for he 0437–5439, the hypervelocity star near the large magellanic cloud. *The Astrophysical Journal*, 719(1):L23–L27, July 2010. ISSN 2041-8213. doi: 10.1088/2041-8205/719/1/l23.

[36] D. A. H. Buckley, J. B. Hearnshaw, K. H. Nordsieck, and D. O'Donoghue. Science drivers and first generation instrumentation for the Southern African Large Telescope (SALT). In P. Guhathakurta, editor, *Discoveries and Research Prospects from 6- to 10-Meter-Class Telescopes II*, volume 4834 of *Society of Photo-Optical Instrumentation Engineers (SPIE) Conference Series*, pages 264–275, Feb. 2003. doi: 10.1117/12.457227.

[37] R. Buras, M. Rampp, H. T. Janka, and K. Kifonidis. Two-dimensional hydrodynamic core-collapse supernova simulations with spectral neutrino transport. I. Numerical method and results for a 15 M$\odot$ star. *Astronomy and Astrophysics*, 447 (3):1049–1092, Mar. 2006. doi: 10.1051/0004-6361:20053783.

[38] K. B. Burdge, K. El-Badry, E. Kara, C. Canizares, D. Chakrabarty, et al. The black hole low-mass X-ray binary V404 Cygni is part of a wide triple. *Nature*, 635 (8038):316–320, Nov. 2024. doi: 10.1038/s41586-024-08120-6.

[39] E. B. Burgh, K. H. Nordsieck, H. A. Kobulnicky, T. B. Williams, D. O'Donoghue, et al. Prime Focus Imaging Spectrograph for the Southern African Large Telescope:

optical design. In M. Iye and A. F. M. Moorwood, editors, *Instrument Design and Performance for Optical/Infrared Ground-based Telescopes*, volume 4841 of *Society of Photo-Optical Instrumentation Engineers (SPIE) Conference Series*, pages 1463–1471, Mar. 2003. doi: 10.1117/12.460312.

[40] A. Burrows and J. Hayes. Pulsar recoil and gravitational radiation due to asymmetrical stellar collapse and explosion. *Physical Review Letters*, 76(3):352–355, Jan. 1996. ISSN 1079-7114. doi: 10.1103/physrevlett.76.352.

[41] A. Burrows and D. Vartanyan. Core-collapse supernova explosion theory. *Nature*, 589(7840):29–39, Jan. 2021. doi: 10.1038/s41586-020-03059-w.

[42] A. Burrows, J. Hayes, and B. A. Fryxell. On the Nature of Core-Collapse Supernova Explosions. *The Astrophysical Journal*, 450:830, Sept. 1995. doi: 10.1086/176188.

[43] A. Burrows, E. Livne, L. Dessart, C. D. Ott, and J. Murphy. A new mechanism for core-collapse supernova explosions. *The Astrophysical Journal*, 640(2):878–890, Apr. 2006. ISSN 1538-4357. doi: 10.1086/500174.

[44] A. Burrows, D. Vartanyan, and T. Wang. Black-hole formation accompanied by the supernova explosion of a 40-$m_\odot$ progenitor star, 2023.

[45] A. Burrows, T. Wang, D. Vartanyan, and M. S. B. Coleman. A Theory for Neutron Star and Black Hole Kicks and Induced Spins. *The Astrophysical Journal*, 963(1): 63, Mar. 2024. doi: 10.3847/1538-4357/ad2353.

[46] A. Burrows, T. Wang, and D. Vartanyan. Channels of Stellar-mass Black Hole Formation. *The Astrophysical Journal*, 987(2):164, July 2025. doi: 10.3847/1538-4357/addd04.

[47] A. G. Butkevich and L. Lindegren. Rigorous treatment of barycentric stellar motion. Perspective and light-time effects in astrometric and radial velocity data. *Astronomy and Astrophysics*, 570:A62, Oct. 2014. doi: 10.1051/0004-6361/201424483.

[48] T. A. Callister, W. M. Farr, and M. Renzo. State of the Field: Binary Black Hole Natal Kicks and Prospects for Isolated Field Formation after GWTC-2. *The Astrophysical Journal*, 920(2):157, Oct. 2021. doi: 10.3847/1538-4357/ac1347.

[49] R. Canal, J. Isern, and J. Labay. The origin of neutron stars in binary systems. *Annual Review of Astron and Astrophys*, 28:183–214, Jan. 1990. doi: 10.1146/annurev.astro.28.1.183.

[50] C. Canizares, J. Davis, D. Dewey, K. Flanagan, E. Galton, et al. The chandra high energy transmission grating: Design, fabrication, ground calibration and five years in flight. *Publications of the Astronomical Society of the Pacific*, 117, 07 2005. doi: 10.1086/432898.

[51] A. G. Cantrell, C. D. Bailyn, J. A. Orosz, J. E. McClintock, R. A. Remillard, et al. The Inclination of the Soft X-Ray Transient A0620-00 and the Mass of its Black Hole. *The Astrophysical Journal*, 710(2):1127–1141, Feb. 2010. doi: 10.1088/0004-637X/710/2/1127.

[52] R. G. Carlberg, P. C. Dawson, T. Hsu, and D. A. Vandenberg. The age-velocity-dispersion relation in the solar neighborhood. *The Astrophysical Journal*, 294: 674–681, July 1985. doi: 10.1086/163337.

[53] J. Casares and P. G. Jonker. Mass Measurements of Stellar and Intermediate-Mass Black Holes. *Space Science Reviews*, 183(1-4):223–252, Sept. 2014. doi: 10.1007/s11214-013-0030-6.

[54] J. Casares, P. A. Charles, and T. Naylor. A 6.5-day periodicity in the recurrent nova V404 Cygni implying the presence of a black hole. *Nature*, 355(6361):614–617, Feb. 1992. doi: 10.1038/355614a0.

[55] J. Casares, D. Steeghs, R. I. Hynes, P. A. Charles, and K. O'Brien. Bowen Fluorescence from the Companion Star in X1822-371. *The Astrophysical Journal*, 590(2):1041–1048, June 2003. doi: 10.1086/375055.

[56] J. Casares, M. Ribó, I. Ribas, J. M. Paredes, F. Vilardell, et al. Erratum: On the binary nature of the γ-ray sources AGL J2241+4454 (=MWC 656) and HESS J0632+057 (=MWC 148). *Monthly Notices of the Royal Astronomical Society*, 426 (1):796–796, Oct. 2012. doi: 10.1111/j.1365-2966.2012.21055.x.

[57] S. Chandrasekhar. The Maximum Mass of Ideal White Dwarfs. *The Astrophysical Journal*, 74:81, July 1931. doi: 10.1086/143324.

[58] N. N. Chugai. Pulsar Space Velocities and Neutrino Chirality. *Soviet Astronomy Letters*, 10:87, Feb. 1984.

[59] J. S. W. Claeys, S. E. de Mink, O. R. Pols, J. J. Eldridge, and M. Baes. Binary progenitor models of type IIb supernovae. *Astronomy and Astrophysics*, 528:A131, Apr. 2011. doi: 10.1051/0004-6361/201015410.

[60] J. S. W. Claeys, O. R. Pols, R. G. Izzard, J. Vink, and F. W. M. Verbunt. Theoretical uncertainties of the Type Ia supernova rate. *Astronomy and Astrophysics*, 563:A83, Mar. 2014. doi: 10.1051/0004-6361/201322714.

[61] J. S. Clark, S. P. Goodwin, P. A. Crowther, L. Kaper, M. Fairbairn, et al. Physical parameters of the high-mass X-ray binary 4U1700-37. *Astronomy and Astrophysics*, 392:909–920, Sept. 2002. doi: 10.1051/0004-6361:20021184.

[62] J. Coakley. Reflectance and albedo, surface. *Encyclopedia of Atmospheric Sciences*, 12 2003. doi: 10.1016/B0-12-227090-8/00069-5.

[63] J. Colas, C. de La Taille, R. Lafaye, N. Massol, P. Pralavorio, et al. Crosstalk in the ATLAS Electromagnetic Calorimeter. *Inspire*, 10 1999.

[64] E. J. M. COLBERT and M. C. MILLER. Observational evidence for intermediate-mass black holes in ultra-luminous x-ray sources. In *The Tenth Marcel Grossmann Meeting*, page 530–549. World Scientific Publishing Company, Feb. 2006. doi: 10.1142/9789812704030_0032.

[65] M. S. B. Coleman and A. Burrows. Kicks and induced spins of neutron stars at birth. *Monthly Notices of the Royal Astronomical Society*, 517(3):3938–3961, Dec. 2022. doi: 10.1093/mnras/stac2573.

[66] J. M. Cordes and D. F. Chernoff. Neutron star population dynamics. ii. three-dimensional space velocities of young pulsars. *The Astrophysical Journal*, 505(1): 315–338, Sept. 1998. ISSN 1538-4357. doi: 10.1086/306138.

[67] C. C. Counselman, III. Radio astrometry. *Annual Review of Astron and Astrophys*, 14:197–214, Jan. 1976. doi: 10.1146/annurev.aa.14.090176.001213.

[68] H. T. Cromartie, E. Fonseca, S. M. Ransom, P. B. Demorest, Z. Arzoumanian, et al. Relativistic Shapiro delay measurements of an extremely massive millisecond pulsar. *Nature Astronomy*, 4:72–76, Jan. 2020. doi: 10.1038/s41550-019-0880-2.

[69] X.-Q. Cui, Y.-H. Zhao, Y.-Q. Chu, G.-P. Li, Q. Li, et al. The Large Sky Area Multi-Object Fiber Spectroscopic Telescope (LAMOST). *Research in Astronomy and Astrophysics*, 12(9):1197–1242, Sept. 2012. doi: 10.1088/1674-4527/12/9/003.

[70] C. Dashwood Brown, P. Gandhi, and Y. Zhao. On the natal kick of the black hole X-ray binary H 1705-250. *Monthly Notices of the Royal Astronomical Society*, 527 (1):L82–L87, Jan. 2024. doi: 10.1093/mnrasl/slad151.

[71] V. Dhawan, I. F. Mirabel, M. Ribó, and I. Rodrigues. Kinematics of Black Hole X-Ray Binary GRS 1915+105. *The Astrophysical Journal*, 668(1):430–434, Oct. 2007. doi: 10.1086/520111.

[72] P. Disberg, N. Gaspari, and A. J. Levan. Deceleration of kicked objects due to the Galactic potential. *Astronomy and Astrophysics*, 687:A272, July 2024. doi: 10.1051/0004-6361/202449996.

[73] O. F. Dorofeev, V. N. Rodionov, and I. M. Ternov. Anisotropic Neutrino Emission from Beta-Decays in a Strong Magnetic Field. *Soviet Astronomy Letters*, 11: 123–126, Apr. 1985.

[74] J. Droste. The field of a single centre in Einstein's theory of gravitation, and the motion of a particle in that field. *Koninklijke Nederlandse Akademie van Wetenschappen Proceedings Series B Physical Sciences*, 19:197–215, Jan. 1917.

[75] P. P. Eggleton. Aproximations to the radii of Roche lobes. *The Astrophysical Journal*, 268:368–369, May 1983. doi: 10.1086/160960.

[76] A. Einstein. Zur allgemeinen Relativitätstheorie. *Sitzungsberichte der Königlich Preussischen Akademie der Wissenschaften*, pages 778–786, Jan. 1915.

[77] K. El-Badry, C. Conroy, J. Fuller, R. Kiman, J. van Roestel, et al. Magnetic braking saturates: evidence from the orbital period distribution of low-mass detached eclipsing binaries from ZTF. *Monthly Notices of the Royal Astronomical Society*, 517(4):4916–4939, Dec. 2022. doi: 10.1093/mnras/stac2945.

[78] K. El-Badry, H.-W. Rix, E. Quataert, A. W. Howard, H. Isaacson, et al. A sun-like star orbiting a black hole. *Monthly Notices of the Royal Astronomical Society*, 518 (1):1057–1085, Nov. 2022.

[79] K. El-Badry, H.-W. Rix, Y. Cendes, A. C. Rodriguez, C. Conroy, et al. A red giant orbiting a black hole. *Monthly Notices of the Royal Astronomical Society*, 521(3): 4323–4348, May 2023. doi: 10.1093/mnras/stad799.

[80] ESA, editor. *The HIPPARCOS and TYCHO catalogues. Astrometric and photometric star catalogues derived from the ESA HIPPARCOS Space Astrometry Mission*, volume 1200 of *ESA Special Publication*, Jan. 1997.

[81] A. C. Fabian, M. J. Rees, L. Stella, and N. E. White. X-ray fluorescence from the inner disc in Cygnus X-1. *Monthly Notices of the Royal Astronomical Society*, 238: 729–736, May 1989. doi: 10.1093/mnras/238.3.729.

[82] M. Falanga, E. Bozzo, A. Lutovinov, J. M. Bonnet-Bidaud, Y. Fetisova, et al. Ephemeris, orbital decay, and masses of ten eclipsing high-mass X-ray binaries. *Astronomy and Astrophysics*, 577:A130, May 2015. doi: 10.1051/0004-6361/201425191.

[83] W. M. Farr, N. Sravan, A. Cantrell, L. Kreidberg, C. D. Bailyn, et al. The Mass Distribution of Stellar-mass Black Holes. *The Astrophysical Journal*, 741(2):103, Nov. 2011. doi: 10.1088/0004-637X/741/2/103.

[84] W. M. Farr, S. Stevenson, M. C. Miller, I. Mandel, B. Farr, et al. Distinguishing spin-aligned and isotropic black hole populations with gravitational waves. *Nature*, 548(7667):426–429, Aug. 2017. doi: 10.1038/nature23453.

[85] C. Ferrigno, E. Bozzo, and P. Romano. Xmm-newtonandswiftobservations of supergiant high mass x-ray binaries. *Astronomy &; Astrophysics*, 664:A99, Aug. 2022. ISSN 1432-0746. doi: 10.1051/0004-6361/202243294.

[86] F. Fortin, F. García, S. Chaty, E. Chassande-Mottin, and A. Simaz Bunzel. Constraints to neutron-star kicks in high-mass x-ray binaries with gaia edr3. *Astronomy & Astrophysics*, 665, 2022. doi: 10.1051/0004-6361/202140853.

[87] F. Fortin, F. García, A. Simaz Bunzel, and S. Chaty. A catalogue of high-mass X-ray binaries in the Galaxy: from the INTEGRAL to the Gaia era. *Astronomy and Astrophysics*, 671:A149, Mar. 2023. doi: 10.1051/0004-6361/202245236.

[88] F. Fortin, A. Kalsi, F. García, A. Simaz-Bunzel, and S. Chaty. A catalogue of low-mass X-ray binaries in the Galaxy: From the INTEGRAL to the Gaia era. *Astronomy and Astrophysics*, 684:A124, Apr. 2024. doi: 10.1051/0004-6361/202347908.

[89] G. Fragione and A. Loeb. Neutron star kicks and implications for their rotation at birth, 2023.

[90] T. Fragos, B. Willems, V. Kalogera, N. Ivanova, G. Rockefeller, et al. Understanding Compact Object Formation and Natal Kicks. II. The Case of XTE J1118 + 480. *The Astrophysical Journal*, 697(2):1057–1070, June 2009. doi: 10.1088/0004-637X/697/2/1057.

[91] T. Fragos, J. J. Andrews, E. Ramirez-Ruiz, G. Meynet, V. Kalogera, et al. The complete evolution of a neutron-star binary through a common envelope phase using 1d hydrodynamic simulations. *The Astrophysical Journal Letters*, 883(2):L45, Oct. 2019. ISSN 2041-8213. doi: 10.3847/2041-8213/ab40d1.

[92] J. Frank, A. King, and D. J. Raine. *Accretion Power in Astrophysics: Third Edition*. Cambridge University Press, 2002.

[93] C. L. Fryer. Mass Limits For Black Hole Formation. *The Astrophysical Journal*, 522(1):413–418, Sept. 1999. doi: 10.1086/307647.

[94] C. L. Fryer. Neutron Star Kicks from Asymmetric Collapse. *The Astrophysical Journal Letters*, 601(2):L175–L178, Feb. 2004. doi: 10.1086/382044.

[95] C. L. Fryer and V. Kalogera. Theoretical Black Hole Mass Distributions. *The Astrophysical Journal*, 554(1):548–560, June 2001. doi: 10.1086/321359.

[96] C. L. Fryer, K. Belczynski, G. Wiktorowicz, M. Dominik, V. Kalogera, et al. Compact remnant mass function: Dependence on the explosion mechanism and metallicity. *The Astrophysical Journal*, 749(1):91, Mar. 2012. ISSN 1538-4357. doi: 10.1088/0004-637x/749/1/91.

[97] Gaia Collaboration. The Gaia mission. *Astronomy and Astrophysics*, 595:A1, Nov. 2016. doi: 10.1051/0004-6361/201629272.

[98] Gaia Collaboration. Gaia Data Release 3. Summary of the content and survey properties. *Astronomy and Astrophysics*, 674:A1, June 2023. doi: 10.1051/0004-6361/202243940.

[99] Gaia Collaboration et al. Discovery of a dormant 33 solar-mass black hole in pre-release Gaia astrometry. *Astronomy and Astrophysics*, 686:L2, June 2024. doi: 10.1051/0004-6361/202449763.

[100] P. Gandhi, A. Rao, M. A. C. Johnson, J. A. Paice, and T. J. Maccarone. Gaia data release 2 distances and peculiar velocities for galactic black hole transients. *Monthly Notices of the Royal Astronomical Society*, 485(2):2642–2655, mar 2019. doi: 10.1093/\mnras/stz438.

[101] P. Gandhi, T. Kawamuro, M. Díaz Trigo, J. Paice, P. Boorman, et al. Accretion physics at high X-ray spectral resolution: New frontiers and game-changing science. *Nature Astronomy [in press]*, 2022.

[102] P. Gandhi, C. Dashwood Brown, Y. Zhao, K. El-Badry, T. J. Maccarone, et al. New Compact Object Binary Populations with Precision Astrometry (Roman White Paper). *arXiv e-prints*, art. arXiv:2306.16479, June 2023. doi: 10.48550/arXiv.2306.16479.

[103] A. K. Gautam, T. Do, A. M. Ghez, D. S. Chu, M. W. H. Jr., et al. An estimate of the binary star fraction among young stars at the galactic center: Possible evidence of a radial dependence, 2024.

[104] A. Generozov and H. B. Perets. A Triple Scenario for the Formation of Wide Black Hole Binaries Such as Gaia BH1. *The Astrophysical Journal*, 964(1):83, Mar. 2024. doi: 10.3847/1538-4357/ad2356.

[105] I. M. George and A. C. Fabian. X-ray reflection from cold matter in Active Galactic Nuclei and X-ray binaries. *Monthly Notices of the Royal Astronomical Society*, 249: 352, Mar. 1991. doi: 10.1093/mnras/249.2.352.

[106] D. Gerosa and C. J. Moore. Black hole kicks as new gravitational wave observables. *Physical Review Letters*, 117(1), June 2016. ISSN 1079-7114. doi: 10.1103/physrevlett.117.011101.

[107] R. Giacconi, H. Gursky, F. R. Paolini, and B. B. Rossi. Evidence for x Rays From Sources Outside the Solar System. *Physical Review Letters*, 9(11):439–443, Dec. 1962. doi: 10.1103/PhysRevLett.9.439.

[108] N. Giacobbo and M. Mapelli. Revising Natal Kick Prescriptions in Population Synthesis Simulations. *The Astrophysical Journal*, 891(2):141, Mar. 2020. doi: 10.3847/1538-4357/ab7335.

[109] M. Giesler, D. Clausen, and C. D. Ott. Low-mass X-ray binaries from black hole retaining globular clusters. *Monthly Notices of the Royal Astronomical Society*, 477 (2):1853–1879, June 2018. doi: 10.1093/mnras/sty659.

[110] A. Giménez-García, J. M. Torrejón, W. Eikmann, S. Martínez-Núñez, L. M. Oskinova, et al. An XMM-Newton view of FeKα in high-mass X-ray binaries. *Astronomy and Astrophysics*, 576:A108, Apr. 2015. doi: 10.1051/0004-6361/201425004.

[111] S. Gomez and J. E. Grindlay. Optical analysis and modeling of hd96670, a new black hole x-ray binary candidate. *The Astrophysical Journal*, 913(1):48, May 2021. ISSN 1538-4357.

[112] J. I. González Hernández, J. Casares, R. Rebolo, G. Israelian, A. V. Filippenko, et al. Chemical Abundances of the Secondary Star in the Black Hole X-Ray Binary V404 Cygni. *The Astrophysical Journal*, 738(1):95, Sept. 2011. doi: 10.1088/0004-637X/738/1/95.

[113] A. Gould. Self-lensing by Binaries. *The Astrophysical Journal*, 446:541, June 1995. doi: 10.1086/175812.

[114] G. Gräfener and W. R. Hamann. The nature of the Wolf-Rayet phenomenon: mass loss close to the Eddington limit. In *Revista Mexicana de Astronomia y Astrofisica Conference Series*, volume 33 of *Revista Mexicana de Astronomia y Astrofisica Conference Series*, pages 88–90, Aug. 2008.

[115] J. Green, P. Schechter, C. Baltay, R. Bean, D. Bennett, et al. Wide-field infrared survey telescope (wfirst) final report, 2012.

[116] V. Grinberg, M. A. Leutenegger, N. Hell, K. Pottschmidt, M. Böck, et al. Long term variability of Cygnus X-1. VII. Orbital variability of the focussed wind in Cyg X-1/HDE 226868 system. *Astronomy and Astrophysics*, 576:A117, Apr. 2015. doi: 10.1051/0004-6361/201425418.

[117] A. Gualandris, M. Colpi, S. Portegies Zwart, and A. Possenti. Has the Black Hole in XTE J1118+480 Experienced an Asymmetric Natal Kick? *The Astrophysical Journal*, 618(2):845–851, Jan. 2005. doi: 10.1086/426126.

[118] P. W. Guilbert. Numerical solution of time dependent Compton scattering problems by means of an integral equation. *Monthly Notices of the Royal Astronomical Society*, 197:451–460, Nov. 1981. doi: 10.1093/mnras/197.2.451.

[119] J. E. Gunn and J. P. Ostriker. On the Nature of Pulsars. III. Analysis of Observations. *The Astrophysical Journal*, 160:979, June 1970. doi: 10.1086/150487.

[120] F. Haberl, C. Maitra, S. Carpano, X. Dai, V. Doroshenko, et al. eROSITA calibration and performance verification phase: High-mass X-ray binaries in the Magellanic Clouds. *Astronomy and Astrophysics*, 661:A25, May 2022. doi: 10.1051/0004-6361/202141878.

[121] J.-L. Halbwachs, D. Pourbaix, F. Arenou, L. Galluccio, P. Guillout, et al. Gaia Data Release 3. Astrometric binary star processing. *Astronomy and Astrophysics*, 674:A9, June 2023. doi: 10.1051/0004-6361/202243969.

[122] W. Hamme. New limb-darkening coefficients for modeling binary star light curves. *The Astronomical Journal*, 106, 1993.

[123] F. Hanke, A. Marek, B. Müller, and H.-T. Janka. Is strong sasi activity the key to successful neutrino-driven supernova explosions? *The Astrophysical Journal*, 755 (2):138, Aug. 2012. ISSN 1538-4357. doi: 10.1088/0004-637x/755/2/138.

[124] M. Hanke, J. Wilms, M. A. Nowak, K. Pottschmidt, N. S. Schulz, et al. Chandra X-Ray Spectroscopy of the Focused Wind in the Cygnus X-1 System. I. The Nondip Spectrum in the Low/Hard State. *The Astrophysical Journal*, 690(1):330–346, Jan. 2009. doi: 10.1088/0004-637X/690/1/330.

[125] B. M. S. Hansen and E. S. Phinney. The pulsar kick velocity distribution. *Monthly Notices of the Royal Astronomical Society*, 291(3):569–577, Nov. 1997. ISSN 1365-2966. doi: 10.1093/mnras/291.3.569.

[126] E. R. Harrison and E. Tademaru. Acceleration of pulsars by asymmetric radiation. *The Astrophysical Journal*, 201:447–461, Oct. 1975. doi: 10.1086/153907.

[127] M. Heida, P. G. Jonker, M. A. P. Torres, and A. Chiavassa. The Mass Function of GX 339-4 from Spectroscopic Observations of Its Donor Star. *The Astrophysical Journal*, 846(2):132, Sept. 2017. doi: 10.3847/1538-4357/aa85df.

[128] W. D. Heintz. *Double stars*, volume 15. 1978.

[129] M. Herant, W. Benz, W. R. Hix, C. L. Fryer, and S. A. Colgate. Inside the Supernova: A Powerful Convective Engine. *The Astrophysical Journal*, 435:339, Nov. 1994. doi: 10.1086/174817.

[130] A. Hewish, S. J. Bell, J. D. H. Pilkington, P. F. Scott, and R. A. Collins. Observation of a Rapidly Pulsating Radio Source. *Nature*, 217(5130):709–713, Feb. 1968. doi: 10.1038/217709a0.

[131] M. Hirsch, N. Hell, V. Grinberg, R. Ballhausen, M. A. Nowak, et al. Chandra X-ray spectroscopy of the focused wind in the Cygnus X-1 system. III. Dipping in the low/hard state. *Astronomy and Astrophysics*, 626:A64, June 2019. doi: 10.1051/0004-6361/201935074.

[132] M. S. Hjellming and R. F. Webbink. Thresholds for Rapid Mass Transfer in Binary System. I. Polytropic Models. *The Astrophysical Journal*, 318:794, July 1987. doi: 10.1086/165412.

[133] G. Hobbs, D. R. Lorimer, A. G. Lyne, and M. Kramer. A statistical study of 233 pulsar proper motions. *Monthly Notices of the Royal Astronomical Society*, 360(3): 974–992, July 2005. doi: 10.1111/j.1365-2966.2005.09087.x.

[134] E. Hoeg, G. Bässgen, U. Bastian, D. Egret, C. Fabricius, V. Großmann, et al. The TYCHO Catalogue. *Astronomy and Astrophysics*, 323:L57–L60, July 1997.

[135] B. Holl, C. Fabricius, J. Portell, L. Lindegren, P. Panuzzo, et al. Gaia Data Release 3. Gaia scan-angle-dependent signals and spurious periods. *Astronomy and Astrophysics*, 674:A25, June 2023. doi: 10.1051/0004-6361/202245353.

[136] J. H. Horne and S. L. Baliunas. A Prescription for Period Analysis of Unevenly Sampled Time Series. *The Astrophysical Journal*, 302:757, Mar. 1986. doi: 10.1086/164037.

[137] J. R. Hurley, O. R. Pols, and C. A. Tout. Comprehensive analytic formulae for stellar evolution as a function of mass and metallicity. *Monthly Notices of the Royal Astronomical Society*, 315(3):543–569, July 2000. ISSN 1365-2966. doi: 10.1046/j.1365-8711.2000.03426.x.

[138] J. R. Hurley, C. A. Tout, and O. R. Pols. Evolution of binary stars and the effect of tides on binary populations. *Monthly Notices of the Royal Astronomical Society*, 329(4):897–928, Feb. 2002. doi: 10.1046/j.1365-8711.2002.05038.x.

[139] R. I. Hynes. Binsim: Visualising Interacting Binaries in 3D. Astrophysics Source Code Library, record ascl:1011.008, Nov. 2010.

[140] A. P. Igoshev, M. Chruslinska, A. Dorozsmai, and S. Toonen. Combined analysis of neutron star natal kicks using proper motions and parallax measurements for radio pulsars and be x-ray binaries. *Monthly Notices of the Royal Astronomical Society*, 508(3):3345–3364, Sept. 2021. ISSN 1365-2966. doi: 10.1093/mnras/stab2734.

[141] N. Ivanova and R. Taam. Magnetic braking revisited. *The Astrophysical Journal*, 599(1):516–521, Dec. 2003. ISSN 1538-4357. doi: 10.1086/379192.

[142] N. Ivanova and R. E. Taam. Thermal Timescale Mass Transfer and the Evolution of White Dwarf Binaries. *The Astrophysical Journal*, 601(2):1058–1066, Feb. 2004. doi: 10.1086/380561.

[143] H.-T. Janka. Natal kicks of stellar mass black holes by asymmetric mass ejection in fallback supernovae. *Monthly Notices of the Royal Astronomical Society*, 434(2): 1355–1361, Sept. 2013. doi: 10.1093/\mnras/stt1106.

[144] H.-T. Janka and D. Kresse. Interplay between neutrino kicks and hydrodynamic kicks of neutron stars and black holes. *Astrophysics and Space Science*, 369(8), Aug. 2024. ISSN 1572-946X. doi: 10.1007/s10509-024-04343-1.

[145] H. T. Janka and E. Mueller. Neutron star recoils from anisotropic supernovae. *Astronomy and Astrophysics*, 290:496–502, Oct. 1994.

[146] H.-T. Janka and E. Müller. The first second of a type ii supernova: Convection, accretion, and shock propagation. *The Astrophysical Journal*, 448(2), Aug. 1995. ISSN 0004-637X. doi: 10.1086/309604.

[147] S. Janssens, T. Shenar, N. Degenaar, J. Bodensteiner, H. Sana, et al. Mwc 656 is unlikely to contain a black hole. *Astronomy & Astrophysics*, 677:L9, Sept. 2023. ISSN 1432-0746. doi: 10.1051/0004-6361/202347318.

[148] JAXA *XRISM*. *XRISM* response background files for point-source simulations. URL `https://xrism.isas.jaxa.jp/research/proposer/obsplan/response/`. Accessed: 2023.

[149] T. Jayasinghe, K. Z. Stanek, T. A. Thompson, C. S. Kochanek, D. M. Rowan, et al. A unicorn in monoceros: the 3 $M_\odot$ dark companion to the bright, nearby red giant V723 Mon is a non-interacting, mass-gap black hole candidate. *Monthly Notices of the Royal Astronomical Society*, 504(2):2577–2602, June 2021. doi: 10.1093/mnras/stab907.

[150] L. Ji, N. S. Schulz, M. A. Nowak, and C. R. Canizares. Implications of X-ray Line Variations for 4U1822-371. *The Astrophysical Journal*, 729(2):102, Mar. 2011. doi: 10.1088/0004-637X/729/2/102.

[151] A. de Jong, J. van Paradijs, and T. Augusteijn. Reprocessing of X rays in low-mass X-ray binaries. *Astronomy and Astrophysics*, 314:484–490, Oct. 1996.

[152] P. G. Jonker and G. Nelemans. The distances to galactic low-mass x-ray binaries: Consequences for black hole luminosities and kicks. *Monthly Notices of the Royal Astronomical Society*, 354(2):355–366, 2004. doi: 10.1111/j.1365-2966.2004.08193.x.

[153] P. G. Jonker, M. A. P. Torres, R. I. Hynes, T. J. Maccarone, D. Steeghs, et al. The Galactic Bulge Survey: Completion of the X-Ray Survey Observations. *The Astrophysical Journal Supplement Series*, 210(2):18, Feb. 2014. doi: 10.1088/0067-0049/210/2/18.

[154] P. G. Jonker, K. Kaur, N. Stone, and M. A. P. Torres. The observed mass distribution of galactic black hole lmxbs is biased against massive black holes. *The Astrophysical Journal*, 921(2):131, Nov. 2021. ISSN 1538-4357. doi: 10.3847/1538-4357/ac2839.

[155] T. R. Kallman, P. Palmeri, M. A. Bautista, C. Mendoza, and J. H. Krolik. Photoionization Modeling and the K Lines of Iron. *The Astrophysical Journal Supplement Series*, 155(2):675–701, Dec. 2004. doi: 10.1086/424039.

[156] V. Kalogera. Orbital Characteristics of Binary Systems after Asymmetric Supernova Explosions. *The Astrophysical Journal*, 471:352, Nov. 1996. doi: 10.1086/177974.

[157] V. Kalogera. Formation of Low-Mass X-Ray Binaries. III. A New Formation Mechanism: Direct Supernova. *The Astrophysical Journal*, 493(1):368–374, Jan. 1998. doi: 10.1086/305086.

[158] V. Kalogera and G. Baym. The Maximum Mass of a Neutron Star. *The Astrophysical Journal Letters*, 470:L61, Oct. 1996. doi: 10.1086/310296.

[159] V. Kalogera and L. C. Fryer. Close double neutron star systems: evidence for supernova kicks. In J. D. Hadjidemetrioy and J. H. Seiradakis, editors, *Joint European and National Astronomical Meeting*, page 268, Jan. 1997.

[160] E. S. Kammoun, D. Barret, P. Peille, R. Willingale, T. Dauser, J. Wilms, M. Guainazzi, and J. M. Miller. The defocused observations of bright sources with Athena/X-IFU. *Astronomy and Astrophysics*, 664:A29, Aug. 2022. doi: 10.1051/0004-6361/202243606.

[161] C. Kimball, S. Imperato, V. Kalogera, K. A. Rocha, Z. Doctor, et al. A Black Hole Kicked at Birth: MAXI J1305-704. *The Astrophysical Journal Letters*, 952(2):L34, Aug. 2023. doi: 10.3847/2041-8213/ace526.

[162] A. R. King, U. Kolb, and L. Burderi. Black Hole Binaries and X-Ray Transients. *The Astrophysical Journal Letters*, 464:L127, June 1996. doi: 10.1086/310105.

[163] H. A. Kobulnicky and C. L. Fryer. A New Look at the Binary Characteristics of Massive Stars. *The Astrophysical Journal*, 670(1):747–765, Nov. 2007. doi: 10.1086/522073.

[164] C. S. Kochanek. Failed Supernovae Explain the Compact Remnant Mass Function. *The Astrophysical Journal*, 785(1):28, Apr. 2014. doi: 10.1088/0004-637X/785/1/28.

[165] C. S. Kochanek, J. F. Beacom, M. D. Kistler, J. L. Prieto, K. Z. Stanek, et al. A Survey About Nothing: Monitoring a Million Supergiants for Failed Supernovae. *The Astrophysical Journal*, 684(2):1336–1342, Sept. 2008. doi: 10.1086/590053.

[166] C. S. Kochanek, B. J. Shappee, K. Z. Stanek, T. W. S. Holoien, and T. A. o. Thompson. The All-Sky Automated Survey for Supernovae (ASAS-SN) Light Curve Server v1.0. *Publications of the ASP*, 129(980):104502, Oct. 2017. doi: 10.1088/1538-3873/aa80d9.

[167] F. Koliopanos. Intermediate mass black holes: A brief review, 2018.

[168] Z. Kopal. *Close binary systems*. New York: Wiley, 1959.

[169] N. Koshimoto, N. Kawanaka, and D. Tsuna. Influence of Black Hole Kick Velocity on Microlensing Distributions. *The Astrophysical Journal*, 973(1):5, Sept. 2024. doi: 10.3847/1538-4357/ad5feb.

[170] I. Kotko, S. Banerjee, and K. Belczynski. The enigmatic origin of two dormant bh binaries: Gaia bh1 and gaia bh2, 2024.

[171] Y. Kozai. Secular perturbations of asteroids with high inclination and eccentricity. *The Astronomical Journal*, 67:591–598, Nov. 1962. doi: 10.1086/108790.

[172] M. O. Krause and J. H. Oliver. Natural widths of atomic K and L levels, Kα X-ray lines and several KLL Auger lines. *Journal of Physical and Chemical Reference Data*, 8(2):329–338, Apr. 1979. doi: 10.1063/1.555595.

[173] L. Kreidberg, C. D. Bailyn, W. M. Farr, and V. Kalogera. Mass Measurements of Black Holes in X-Ray Transients: Is There a Mass Gap? *The Astrophysical Journal*, 757(1):36, Sept. 2012. doi: 10.1088/0004-637X/757/1/36.

[174] P. Kroupa. On the variation of the initial mass function. *Monthly Notices of the Royal Astronomical Society*, 322(2):231–246, Apr. 2001. doi: 10.1046/j.1365-8711.2001.04022.x.

[175] D. Lai. Neutron star kicks and supernova asymmetry. In P. Höflich, P. Kumar, and J. C. Wheeler, editors, *Cosmic explosions in three dimensions*, page 276, Jan. 2004. doi: 10.48550/arXiv.astro-ph/0312542.

[176] D. Lai and P. Goldreich. Growth of perturbations in gravitational collapse and accretion. *The Astrophysical Journal*, 535(1):402–411, May 2000. ISSN 1538-4357. doi: 10.1086/308821.

[177] E. V. Lai, B. De Marco, A. A. Zdziarski, T. M. Belloni, S. Mondal, P. Uttley, V. Grinberg, J. Wilms, and A. Różańska. The X-ray spectral-timing contribution of the stellar wind in the hard state of Cyg X-1. *Monthly Notices of the Royal Astronomical Society*, 512(2):2671–2685, May 2022. doi: 10.1093/mnras/stac688.

[178] D. A. Leahy and C. Igna. 35-day Cycle Lengths Turn-on Times for Hercules X-1 Studied with Rossi X-ray Timing Explorer Data. In *American Astronomical Society Meeting Abstracts #215*, volume 215 of *American Astronomical Society Meeting Abstracts*, page 360.03, Jan. 2010.

[179] M. L. Lidov. The evolution of orbits of artificial satellites of planets under the action of gravitational perturbations of external bodies. *Planetary and Space Science*, 9 (10):719–759, Oct. 1962. doi: 10.1016/0032-0633(62)90129-0.

[180] LIGO Scientific Collaboration. Advanced LIGO. *Classical and Quantum Gravity*, 32(7):074001, Apr. 2015. doi: 10.1088/0264-9381/32/7/074001.

[181] LIGO Scientific Collaboration. Laser Interferometer Space Antenna. 2017.

[182] LIGO Scientific Collaboration and Virgo Collaboration. TOPICAL REVIEW:Predictions for the rates of compact binary coalescences observable by ground-based gravitational-wave detectors. *Classical and Quantum Gravity*, 27(17): 173001, Sept. 2010. doi: 10.1088/0264-9381/27/17/173001.

[183] LIGO Scientific Collaboration and Virgo Collaboration. Observation of gravitational waves from a binary black hole merger. *Phys. Rev. Lett.*, 116:061102, Feb 2016. doi: 10.1103/PhysRevLett.116.061102.

[184] LIGO Scientific Collaboration and Virgo Collaboration. Gw190814: Gravitational waves from the coalescence of a 23 solar mass black hole with a 2.6 solar mass compact object. *The Astrophysical Journal Letters*, 896(2):L44, June 2020. ISSN 2041-8213. doi: 10.3847/2041-8213/ab960f.

[185] LIGO Scientific Collaboration and Virgo Collaboration. Gw190521: A binary black hole merger with a total mass of 150 . *Physical Review Letters*, 125(10), Sept. 2020. ISSN 1079-7114. doi: 10.1103/physrevlett.125.101102.

[186] LIGO Scientific Collaboration and Virgo Collaboration. Observation of gravitational waves from two neutron star–black hole coalescences. *The Astrophysical Journal Letters*, 915(1):L5, June 2021. ISSN 2041-8213. doi: 10.3847/2041-8213/ac082e.

[187] LIGO Scientific Collaboration and Virgo Collaboration. GWTC-3: Compact Binary Coalescences Observed by LIGO and Virgo during the Second Part of the Third Observing Run. *Physical Review X*, 13(4):041039, Oct. 2023. doi: 10.1103/PhysRevX.13.041039.

[188] L. Lindegren, F. Mignard, S. Söderhjelm, M. Badiali, H. H. Bernstein, et al. Double star data in the HIPPARCOS Catalogue. *Astronomy and Astrophysics*, 323:L53–L56, July 1997.

[189] A. G. Lyne and D. R. Lorimer. High birth velocities of radio pulsars. *Nature*, 369 (6476):127–129, May 1994. doi: 10.1038/369127a0.

[190] A. G. Lyne, B. Anderson, and M. J. Salter. The proper motions of 26 pulsars. *Monthly Notices of the Royal Astronomical Society*, 201(3):503–520, 1982. doi: 10.1093/mnras/201.3.503.

[191] R. K. D. MacDonald, C. D. Bailyn, M. Buxton, A. G. Cantrell, R. Chatterjee, et al. The Black Hole Binary V4641 Sagitarii: Activity in Quiescence and Improved Mass Determinations. *The Astrophysical Journal*, 784(1):2, Mar. 2014. doi: 10.1088/0004-637X/784/1/2.

[192] O. K. Madej, P. G. Jonker, M. Díaz Trigo, and I. Miškovičová. Variable Doppler shifts of the thermal wind absorption lines in low-mass X-ray binaries. *Monthly Notices of the Royal Astronomical Society*, 438(1):145–155, Feb. 2014. doi: 10.1093/mnras/stt2119.

[193] J. Magorrian, S. Tremaine, D. Richstone, R. Bender, G. Bower, et al. The Demography of Massive Dark Objects in Galaxy Centers. *The Astronomical Journal*, 115 (6):2285–2305, June 1998. doi: 10.1086/300353.

[194] A. Majczyna, J. Madej, P. C. Joss, and A. Różańska. Model atmospheres and X-ray spectra of bursting neutron stars. II. Iron rich comptonized spectra. *Astronomy and Astrophysics*, 430:643–654, Feb. 2005. doi: 10.1051/0004-6361:20034048.

[195] K. Makishima, Y. Maejima, K. Mitsuda, H. V. Bradt, R. A. Remillard, et al. Simultaneous X-Ray and Optical Observations of GX 339-4 in an X-Ray High State. *The Astrophysical Journal*, 308:635, Sept. 1986. doi: 10.1086/164534.

[196] R. N. Manchester. Millisecond pulsars, their evolution and applications. *Journal of Astrophysics and Astronomy*, 38(3), Sept. 2017. ISSN 0973-7758. doi: 10.1007/s12036-017-9469-2.

[197] I. Mandel. Estimates of black hole natal kick velocities from observations of low-mass x-ray binaries. *Monthly Notices of the Royal Astronomical Society*, 456(1): 578–581, 2015. doi: 10.1093/mnras/stv2733.

[198] M. Mapelli. *Formation Channels of Single and Binary Stellar-Mass Black Holes*, page 1–65. Springer Singapore, 2021. ISBN 9789811547027. doi: 10.1007/978-981-15-4702-7_16-1.

[199] P. Marchant and J. Bodensteiner. The evolution of massive binary stars, 2023.

[200] M. Marks, P. Kroupa, and S. Oh. An analytical description of the evolution of binary orbital-parameter distributions in N-body computations of star clusters. *Monthly Notices of the Royal Astronomical Society*, 417(3):1684–1701, Nov. 2011. doi: 10.1111/j.1365-2966.2011.19257.x.

[201] G. Matt, A. C. Fabian, and C. S. Reynolds. Geometrical and chemical dependence of k-shell x-ray features. *Monthly Notices of the Royal Astronomical Society*, 289 (1):175–184, 07 1997. ISSN 0035-8711. doi: 10.1093/mnras/289.1.175.

[202] J. E. McClintock, M. R. Garcia, N. Caldwell, E. E. Falco, P. M. Garnavich, et al. A Black Hole Greater Than 6 M_{solar} in the X-Ray Nova XTE J1118+480. *The Astrophysical Journal Letters*, 551(2):L147–L150, Apr. 2001. doi: 10.1086/320030.

[203] A. Merloni, G. Lamer, T. Liu, M. E. Ramos-Ceja, H. Brunner, et al. The SRG/eROSITA all-sky survey. First X-ray catalogues and data release of the western Galactic hemisphere. *Astronomy and Astrophysics*, 682:A34, Feb. 2024. doi: 10.1051/0004-6361/202347165.

[204] J. M. Miller, A. C. Fabian, R. Wijnands, R. A. Remillard, P. Wojdowski, et al. Resolving the Composite Fe Kα Emission Line in the Galactic Black Hole Cygnus X-1 with Chandra. *The Astrophysical Journal*, 578(1):348–356, Oct. 2002. doi: 10.1086/342466.

[205] J. C. A. Miller-Jones, A. Bahramian, J. A. Orosz, I. Mandel, L. Gou, et al. Cygnus x-1 contains a 21–solar mass black hole—implications for massive star winds. *Science*, 371(6533):1046–1049, Mar. 2021. ISSN 1095-9203. doi: 10.1126/science.abb3363.

[206] I. F. Mirabel, V. Dhawan, R. P. Mignani, I. Rodrigues, and F. Guglielmetti. A high-velocity black hole on a Galactic-halo orbit in the solar neighbourhood. *Nature*, 413(6852):139–141, Sept. 2001. doi: 10.1038/35093060.

[207] I. Miškovičová, N. Hell, M. Hanke, M. A. Nowak, K. Pottschmidt, et al. Chandra X-ray spectroscopy of focused wind in the Cygnus X-1 system. II. The non-dip spectrum in the low/hard state - modulations with orbital phase. *Astronomy and Astrophysics*, 590:A114, May 2016. doi: 10.1051/0004-6361/201322490.

[208] S. Mochnacki. Accurate integrations of the roche model. *The Astrophysical Journal Supplement Series*, 55:551–561, 07 1984. doi: 10.1086/190967.

[209] T. Muñoz-Darias, J. Casares, and I. G. Martínez-Pais. The "K-Correction" for Irradiated Emission Lines in LMXBs: Evidence for a Massive Neutron Star in X1822-371 (V691 CrA). *The Astrophysical Journal*, 635(1):502–507, Dec. 2005. doi: 10.1086/497420.

[210] B. Mueller, H.-T. Janka, A. Marek, F. Hanke, A. Wongwathanarat, and E. Mueller. Core-collapse supernovae: Explosion dynamics, neutrinos and gravitational waves, 2011.

[211] P. Nagarajan and K. El-Badry. Mixed Origins: Strong Natal Kicks for Some Black Holes and None for Others. *Publications of the ASP*, 137(3):034203, Mar. 2025. doi: 10.1088/1538-3873/adb6d6.

[212] P. Nagarajan, K. El-Badry, A. H. M. J. Triaud, T. A. Baycroft, D. Latham, et al. ESPRESSO Observations of Gaia BH1: High-precision Orbital Constraints and no Evidence for an Inner Binary. *Publications of the ASP*, 136(1):014202, Jan. 2024. doi: 10.1088/1538-3873/ad1ba7.

[213] NASA HEASARC. Nasa heasarc open data registry on aws. URL `https://registry.opendata.aws/nasa-heasarc/`. Accessed: 2023.

[214] G. Nelemans, T. M. Tauris, and E. P. Heuvel. Constraints on mass ejection in black hole formation derived from black hole x-ray binaries. *Black Holes in Binaries and Galactic Nuclei: Diagnostics, Demography and Formation*, page 312–313, 1999. doi: 10.1007/10720995_68.

[215] G. Nelemans, S. F. Portegies Zwart, F. Verbunt, and L. R. Yungelson. Population synthesis for double white dwarfs. II. Semi-detached systems: AM CVn stars. *Astronomy and Astrophysics*, 368:939–949, Mar. 2001. doi: 10.1051/0004-6361:20010049.

[216] K. Nomoto. Evolution of 8-10 solar mass stars toward electron capture supernovae. I - Formation of electron-degenerate O + NE + MG cores. *The Astrophysical Journal*, 277:791–805, Feb. 1984. doi: 10.1086/161749.

[217] J. Nordhaus, T. D. Brandt, A. Burrows, E. Livne, and C. D. Ott. Theoretical support for the hydrodynamic mechanism of pulsar kicks. *Physical Review D*, 82 (10):103016, Nov. 2010. doi: 10.1103/PhysRevD.82.103016.

[218] J. Nordhaus, A. Burrows, A. Almgren, and J. Bell. Dimension as a key to the neutrino mechanism of core-collapse supernova explosions. *The Astrophysical Journal*, 720(1):694–703, Aug. 2010. ISSN 1538-4357. doi: 10.1088/0004-637x/720/1/694.

[219] J. Nordhaus, T. D. Brandt, A. Burrows, and A. Almgren. The hydrodynamic origin of neutron star kicks: Neutron star kicks. *Monthly Notices of the Royal Astronomical Society*, 423(2):1805–1812, Apr. 2012. ISSN 0035-8711. doi: 10.1111/j.1365-2966.2012.21002.x.

[220] M. A. Nowak and J. Chiang. Implications of the X-Ray Variability for the Mass of MCG -6-30-15. *The Astrophysical Journal Letters*, 531(1):L13–L16, Mar. 2000. doi: 10.1086/312508.

[221] T. N. O'Doherty, A. Bahramian, J. C. A. Miller-Jones, A. J. Goodwin, I. Mandel, et al. An observationally derived kick distribution for neutron stars in binary systems. *Monthly Notices of the Royal Astronomical Society*, 521(2):2504–2524, May 2023. doi: 10.1093/mnras/stad680.

[222] A. T. Okazaki and I. Negueruela. A natural explanation for periodic x-ray outbursts in be/x-ray binaries. *Astronomy amp; Astrophysics*, 377(1):161–174, Oct. 2001. ISSN 1432-0746. doi: 10.1051/0004-6361:20011083.

[223] C. D. Ott, A. Burrows, L. Dessart, and E. Livne. A new mechanism for gravitational-wave emission in core-collapse supernovae. *Physical Review Letters*, 96(20), May 2006. ISSN 1079-7114. doi: 10.1103/physrevlett.96.201102.

[224] F. Özel, D. Psaltis, R. Narayan, and J. E. McClintock. The Black Hole Mass Distribution in the Galaxy. *The Astrophysical Journal*, 725(2):1918–1927, Dec. 2010. doi: 10.1088/0004-637X/725/2/1918.

[225] P. Palmeri, C. Mendoza, T. R. Kallman, M. A. Bautista, and M. Meléndez. Modeling of iron K lines: Radiative and Auger decay data for Fe II-Fe IX. *Astronomy and Astrophysics*, 410:359–364, Oct. 2003. doi: 10.1051/0004-6361:20031262.

[226] A. N. Parmar, J. L. Culhane, C. G. Rapley, C. J. Wolfson, L. W. Acton, et al. SMM observations of K-alpha radiation from fluorescence of photospheric iron by solar flare X-rays. *The Astrophysical Journal*, 279:866–874, Apr. 1984. doi: 10.1086/161957.

[227] E. Pfahl, S. Rappaport, and P. Podsiadlowski. A comprehensive study of neutron star retention in globular clusters. *The Astrophysical Journal*, 573(1):283–305, July 2002. doi: 10.1086/340494.

[228] E. Pfahl, S. Rappaport, and P. Podsiadlowski. The galactic population of low- and intermediate-mass x-ray binaries. *The Astrophysical Journal*, 597(2):1036–1048, Nov. 2003. ISSN 1538-4357. doi: 10.1086/378632.

[229] B. Pichon. The GAIA work package on Final Luminosity, Age and Mass Estimator (GWP : FLAME). In J. Bouvier, A. Chalabaev, and C. Charbonnel, editors, *SF2A-2007: Proceedings of the Annual meeting of the French Society of Astronomy and Astrophysics*, page 549, July 2007.

[230] P. Podsiadlowski, P. C. Joss, and J. J. L. Hsu. Presupernova Evolution in Massive Interacting Binaries. *The Astrophysical Journal*, 391:246, May 1992. doi: 10.1086/171341.

[231] P. Podsiadlowski, N. Langer, A. J. T. Poelarends, S. Rappaport, A. Heger, et al. The Effects of Binary Evolution on the Dynamics of Core Collapse and Neutron

Star Kicks. *The Astrophysical Journal*, 612(2):1044–1051, Sept. 2004. doi: 10.1086/421713.

[232] O. R. Pols, C. A. Tout, P. P. Eggleton, and Z. Han. Approximate input physics for stellar modelling. *Monthly Notices of the Royal Astronomical Society*, 274(3): 964–974, June 1995. doi: 10.1093/mnras/274.3.964.

[233] G. Ponti, S. Bianchi, T. Muñoz-Darias, and K. Nandra. Measuring masses in low mass X-ray binaries via X-ray spectroscopy: the case of MXB 1659-298. *Monthly Notices of the Royal Astronomical Society*, 481(1):L94–L99, Nov. 2018. doi: 10.1093/mnrasl/sly120.

[234] A. M. Price-Whelan, D. W. Hogg, D. Foreman-Mackey, and H.-W. Rix. The joker: A custom monte carlo sampler for binary-star and exoplanet radial velocity data. *The Astrophysical Journal*, 837(1):20, Feb. 2017. ISSN 1538-4357. doi: 10.3847/1538-4357/aa5e50.

[235] N. Rahman, H. T. Janka, G. Stockinger, and S. E. Woosley. Pulsational pair-instability supernovae: gravitational collapse, black hole formation, and beyond. *Monthly Notices of the Royal Astronomical Society*, 512(3):4503–4540, May 2022. doi: 10.1093/mnras/stac758.

[236] M. Rampp and H.-T. Janka. Spherically symmetric simulation with boltzmann neutrino transport of core collapse and postbounce evolution of a $15\,m_{\odot}$ star. *The Astrophysical Journal*, 539(1):L33–L36, Aug. 2000. ISSN 0004-637X. doi: 10.1086/312837.

[237] A. Rao, P. Gandhi, C. Knigge, J. A. Paice, N. W. C. Leigh, et al. Kinematic study of the association Cyg OB3 with Gaia DR2. *Monthly Notices of the Royal Astronomical Society*, 495(1):1491–1500, June 2020. doi: 10.1093/mnras/staa1217.

[238] M. J. Rees. Black Hole Models for Active Galactic Nuclei. *Annual Review of Astron and Astrophys*, 22:471–506, Jan. 1984. doi: 10.1146/annurev.aa.22.090184.002351.

[239] E. Regős and C. A. Tout. The effect of magnetic fields in common-envelope evolution on the formation of cataclysmic variables. *Monthly Notices of the Royal Astronomical Society*, 273(1):146–156, Mar. 1995. doi: 10.1093/mnras/273.1.146.

[240] M. J. Reid, K. M. Menten, X. W. Zheng, A. Brunthaler, L. Moscadelli, et al. Trigonometric Parallaxes of Massive Star-Forming Regions. VI. Galactic Structure,

Fundamental Parameters, and Noncircular Motions. *The Astrophysical Journal*, 700(1):137–148, July 2009. doi: 10.1088/0004-637X/700/1/137.

[241] R. C. Reis and J. M. Miller. On the Size and Location of the X-Ray Emitting Coronae around Black Holes. *The Astrophysical Journal Letters*, 769(1):L7, May 2013. doi: 10.1088/2041-8205/769/1/L7.

[242] R. A. Remillard and J. E. McClintock. X-Ray Properties of Black-Hole Binaries. *Annual Review of Astron and Astrophys*, 44(1):49–92, Sept. 2006. doi: 10.1146/annurev.astro.44.051905.092532.

[243] M. Renzo, E. Zapartas, S. E. de Mink, Y. Götberg, S. Justham, et al. Massive runaway and walkaway stars. A study of the kinematical imprints of the physical processes governing the evolution and explosion of their binary progenitors. *Astronomy and Astrophysics*, 624:A66, Apr. 2019. doi: 10.1051/0004-6361/201833297.

[244] S. Repetto and G. Nelemans. Constraining the formation of black holes in short-period black hole low-mass X-ray binaries. *Monthly Notices of the Royal Astronomical Society*, 453(3):3341–3355, Nov. 2015. doi: 10.1093/mnras/stv1753.

[245] S. Repetto, M. B. Davies, and S. Sigurdsson. Investigating stellar-mass black hole kicks. *Monthly Notices of the Royal Astronomical Society*, 425(4):2799–2809, 2012. doi: 10.1111/j.1365-2966.2012.21549.x.

[246] G. R. Ricker, J. N. Winn, R. Vanderspek, D. W. Latham, G. Á. Bakos, et al. Transiting Exoplanet Survey Satellite (TESS). *Journal of Astronomical Telescopes, Instruments, and Systems*, 1:014003, Jan. 2015. doi: 10.1117/1.JATIS.1.1.014003.

[247] A. Rostami-Shirazi, A. H. Zonoozi, H. Haghi, and M. Rabiee. Origin of the metal-rich versus metal-poor globular clusters dichotomies in the Milky Way: a sign of low black hole natal kicks. *Monthly Notices of the Royal Astronomical Society*, 535 (4):3489–3499, Dec. 2024. doi: 10.1093/mnras/stae2365.

[248] A. Różańska and J. Madej. Models of the iron Kα fluorescent line and the Compton Shoulder in irradiated accretion disc spectra. *Monthly Notices of the Royal Astronomical Society*, 386(4):1872–1880, June 2008. doi: 10.1111/j.1365-2966.2008.13173.x.

[249] K. C. Sahu, J. Anderson, S. Casertano, H. E. Bond, A. Udalski, et al. An Isolated Stellar-mass Black Hole Detected through Astrometric Microlensing. *The Astrophysical Journal*, 933(1):83, July 2022. doi: 10.3847/1538-4357/ac739e.

[250] G. Salvesen and S. Pokawanvit. Origin of spin–orbit misalignments: the microblazar v4641 sgr. *Monthly Notices of the Royal Astronomical Society*, 495(2):2179–2204, Apr. 2020. ISSN 1365-2966. doi: 10.1093/mnras/staa1094.

[251] H. Sana, S. E. de Mink, A. de Koter, N. Langer, C. J. Evans, et al. Binary Interaction Dominates the Evolution of Massive Stars. *Science*, 337(6093):444, July 2012. doi: 10.1126/science.1223344.

[252] D. M. Sanchez, M. A. P. Torres, J. Casares, T. Munoz-Darias, M. A. Padilla, and I. V. Yanes-Rizo. Dynamical confirmation for a black hole in the x-ray transient swift j1727.8-1613, 2024.

[253] J. D. Scargle. Studies in astronomical time series analysis. II. Statistical aspects of spectral analysis of unevenly spaced data. *The Astrophysical Journal*, 263:835–853, Dec. 1982. doi: 10.1086/160554.

[254] S. Schaffer. John Michell and Black Holes. *Journal for the History of Astronomy*, 10:42, Jan. 1979. doi: 10.1177/002182867901000104.

[255] L. Scheck, T. Plewa, H.-T. Janka, K. Kifonidis, and E. Müller. Pulsar recoil by large-scale anisotropies in supernova explosions. *Physical Review Letters*, 92(1), Jan. 2004. ISSN 1079-7114. doi: 10.1103/physrevlett.92.011103.

[256] L. Scheck, K. Kifonidis, H. T. Janka, and E. Müller. Multidimensional supernova simulations with approximative neutrino transport. I. Neutron star kicks and the anisotropy of neutrino-driven explosions in two spatial dimensions. *Astronomy and Astrophysics*, 457(3):963–986, Oct. 2006. doi: 10.1051/0004-6361:20064855.

[257] N. S. Schulz and W. N. Brandt. Variability of the X-Ray P Cygni Line Profiles from Circinus X-1 near Zero Phase. *The Astrophysical Journal*, 572(2):971–983, June 2002. doi: 10.1086/340369.

[258] K. Schwarzschild. On the Gravitational Field of a Mass Point According to Einstein's Theory. *Abh. Konigl. Preuss. Akad. Wissenschaften Jahre 1906,92, Berlin,1907*, 1916:189–196, Jan. 1916.

[259] C. K. Seyfert. Nuclear Emission in Spiral Nebulae. *The Astrophysical Journal*, 97: 28, Jan. 1943. doi: 10.1086/144488.

[260] T. Shahbaz, F. A. Ringwald, J. C. Bunn, T. Naylor, P. A. Charles, et al. The mass of the black hole in V404 Cygni. *Monthly Notices of the Royal Astronomical Society*, 271:L10–L14, Nov. 1994. doi: 10.1093/mnras/271.1.L10.

[261] T. Shahbaz, J. I. González-Hernández, R. P. Breton, M. R. Kennedy, D. M. Sánchez, et al. The peculiar chemical abundance of the transitional millisecond pulsar PSR J1023+0038 - Li enhancement. *Monthly Notices of the Royal Astronomical Society*, Mar. 2022. doi: 10.1093/mnras/stac492.

[262] S. L. Shapiro and S. A. Teukolsky. *Black holes, white dwarfs and neutron stars. The physics of compact objects*. 1983. doi: 10.1002/9783527617661.

[263] R. B. Shatsova. Peculiar Motions of O and B Stars. *Soviet Astronomy*, 11:313, Oct. 1967.

[264] M. Shidatsu, Y. Ueda, S. Nakahira, C. Done, K. Morihana, et al. The Accretion Disk and Ionized Absorber of the 9.7 hr Dipping Black Hole Binary MAXI J1305-704. *The Astrophysical Journal*, 779(1):26, Dec. 2013. doi: 10.1088/0004-637X/779/1/26.

[265] I. S. Shklovskii. Possible Causes of the Secular Increase in Pulsar Periods. *Soviet Astronomy*, 13:562, Feb. 1970.

[266] J. C. Siegel, I. Kiato, V. Kalogera, C. P. L. Berry, T. J. Maccarone, et al. Investigating the Lower Mass Gap with Low-mass X-Ray Binary Population Synthesis. *The Astrophysical Journal*, 954(2):212, Sept. 2023. doi: 10.3847/1538-4357/ace9d9.

[267] A. C. Sippel, J. R. Hurley, J. P. Madrid, and W. E. Harris. N-body models of globular clusters: metallicities, half-light radii and mass-to-light ratios. *Monthly Notices of the Royal Astronomical Society*, 427(1):167–179, Nov. 2012. doi: 10.1111/j.1365-2966.2012.21969.x.

[268] V. M. Slipher. The radial velocity of the Andromeda Nebula. *Lowell Observatory Bulletin*, 2(8):56–57, Jan. 1913.

[269] A. Socrates, O. Blaes, A. Hungerford, and C. L. Fryer. The Neutrino Bubble Instability: A Mechanism for Generating Pulsar Kicks. *The Astrophysical Journal*, 632(1):531–562, Oct. 2005. doi: 10.1086/431786.

[270] D. Steeghs and J. Casares. The Mass Donor of Scorpius X-1 Revealed. *The Astrophysical Journal*, 568(1):273–278, Mar. 2002. doi: 10.1086/339224.

[271] S. Stevenson. Biases in Estimates of Black Hole Kicks from the Spin Distribution of Binary Black Holes. *The Astrophysical Journal Letters*, 926(2):L32, Feb. 2022. doi: 10.3847/2041-8213/ac5252.

[272] J. Strader, L. Chomiuk, T. J. Maccarone, J. C. A. Miller-Jones, and A. C. Seth. Two stellar-mass black holes in the globular cluster M22. *Nature*, 490(7418):71–73, Oct. 2012. doi: 10.1038/nature11490.

[273] R. Sunyaev and E. Churazov. Equivalent width, shape and proper motion of the iron fluorescent line emission from molecular clouds as an indicator of the illuminating source X-ray flux history. *Monthly Notices of the Royal Astronomical Society*, 297(4):1279–1291, July 1998. doi: 10.1046/j.1365-8711.1998.01684.x.

[274] B. Sykes and B. Müller. Long-time 3d supernova simulations of non-rotating progenitors with magnetic fields, 2024.

[275] R. E. Taam and E. L. Sandquist. Common Envelope Evolution of Massive Binary Stars. *Annual Review of Astron and Astrophys*, 38:113–141, Jan. 2000. doi: 10.1146/annurev.astro.38.1.113.

[276] C. Tan. High-mass x-ray binary: Classification, formation, and evolution. *Journal of Physics: Conference Series*, 2012(1):012119, sep 2021. doi: 10.1088/1742-6596/2012/1/012119.

[277] T. M. Tauris, N. Langer, T. J. Moriya, P. Podsiadlowski, S. C. Yoon, et al. Ultra-stripped Type Ic Supernovae from Close Binary Evolution. *The Astrophysical Journal Letters*, 778(2):L23, Dec. 2013. doi: 10.1088/2041-8205/778/2/L23.

[278] X. S. Team. Xrism quick reference, 2022.

[279] T. A. Thompson, A. Burrows, and P. A. Pinto. Shock breakout in core-collapse supernovae and its neutrino signature. *The Astrophysical Journal*, 592(1):434–456, July 2003. ISSN 1538-4357. doi: 10.1086/375701.

[280] T. A. Thompson, C. S. Kochanek, K. Z. Stanek, C. Badenes, R. S. Post, et al. A noninteracting low-mass black hole-giant star binary system. *Science*, 366(6465): 637–640, Nov. 2019. doi: 10.1126/science.aau4005.

[281] J. E. Tohline. The Origin of Binary Stars. *Annual Review of Astron and Astrophys*, 40:349–385, Jan. 2002. doi: 10.1146/annurev.astro.40.060401.093810.

[282] J. M. Torrejón, N. S. Schulz, M. A. Nowak, and T. R. Kallman. A Chandra Survey of Fluorescence Fe Lines in X-ray Binaries at High Resolution. *The Astrophysical Journal*, 715(2):947–958, June 2010. doi: 10.1088/0004-637X/715/2/947.

[283] J. M. Torrejón, N. S. Schulz, M. A. Nowak, L. Oskinova, J. J. Rodes-Roca, et al. On the Radial Onset of Clumping in the Wind of the B0I Massive Star QV Nor. *The Astrophysical Journal*, 810(2):102, Sept. 2015. doi: 10.1088/0004-637X/810/2/102.

[284] M. Toscano, J. S. Sandhu, M. Bailes, R. N. Manchester, M. C. Britton, et al. Millisecond pulsar velocities. *Monthly Notices of the Royal Astronomical Society*, 307(4):925–933, Aug. 1999. ISSN 1365-2966. doi: 10.1046/j.1365-8711.1999.02685.x.

[285] C. A. Tout, S. J. Aarseth, O. R. Pols, and P. P. Eggleton. Rapid binary star evolution for N-body simulations and population synthesis. *Monthly Notices of the Royal Astronomical Society*, 291(4):732–748, Nov. 1997. doi: 10.1093/mnras/291.4.732.

[286] V. Trimble. Dynamics of the crab nebula. *The Crab Nebula*, page 12–21, 1971. doi: 10.1007/978-94-010-3087-8_2.

[287] J. A. Tyson. Large Synoptic Survey Telescope: Overview. In J. A. Tyson and S. Wolff, editors, *Survey and Other Telescope Technologies and Discoveries*, volume 4836 of *Society of Photo-Optical Instrumentation Engineers (SPIE) Conference Series*, pages 10–20, Dec. 2002. doi: 10.1117/12.456772.

[288] J. van Paradijs. On the Accretion Instability in Soft X-Ray Transients. *The Astrophysical Journal Letters*, 464:L139, June 1996. doi: 10.1086/310100.

[289] D. Vanbeveren and C. De Loore. The evolution of the mass gainer in massive close binaries. *Astronomy and Astrophysics*, 290:129–132, Oct. 1994.

[290] V. Varma, S. Biscoveanu, T. Islam, F. H. Shaik, C.-J. Haster, et al. Evidence of large recoil velocity from a black hole merger signal. *Physical Review Letters*, 128 (19), May 2022. ISSN 1079-7114. doi: 10.1103/physrevlett.128.191102.

[291] S. Vaughan. A Bayesian test for periodic signals in red noise. *Monthly Notices of the Royal Astronomical Society*, 402(1):307–320, Feb. 2010. doi: 10.1111/j.1365-2966.2009.15868.x.

[292] F. Verbunt, A. Igoshev, and E. Cator. The observed velocity distribution of young pulsars. *Astronomy and Astrophysics*, 608:A57, Dec. 2017. doi: 10.1051/0004-6361/201731518.

[293] J. S. Vink. The theory of stellar winds. *Astrophysics and Space Science*, 336(1): 163–167, Nov. 2011. doi: 10.1007/s10509-011-0636-7.

[294] J. S. Vink and A. de Koter. On the metallicity dependence of Wolf-Rayet winds. *Astronomy and Astrophysics*, 442(2):587–596, Nov. 2005. doi: 10.1051/0004-6361:20052862.

[295] J. S. Vink and G. N. Sabhahit. Exploring the Red Supergiant wind kink. A Universal mass-loss concept for massive stars. *Astronomy and Astrophysics*, 678: L3, Oct. 2023. doi: 10.1051/0004-6361/202347801.

[296] J. S. Vink, A. de Koter, and H. J. G. L. M. Lamers. Mass-loss predictions for O and B stars as a function of metallicity. *Astronomy and Astrophysics*, 369:574–588, Apr. 2001. doi: 10.1051/0004-6361:20010127.

[297] S. Watanabe, M. Sako, M. Ishida, Y. Ishisaki, S. M. Kahn, et al. Detection of a Fully Resolved Compton Shoulder of the Iron Kα Line in the Chandra X-Ray Spectrum of GX 301-2. *The Astrophysical Journal Letters*, 597(1):L37–L40, Nov. 2003. doi: 10.1086/379735.

[298] R. F. Webbink. Stellar evolution and binaries. In J. E. Pringle and R. A. Wade, editors, *Interacting Binary Stars*, page 39. 1985.

[299] B. L. Webster and P. Murdin. Cygnus X-1-a Spectroscopic Binary with a Heavy Companion ? *Nature*, 235(5332):37–38, Jan. 1972. doi: 10.1038/235037a0.

[300] S. Wellstein and N. Langer. Implications of massive close binaries for black hole formation and supernovae. *Astronomy and Astrophysics*, 350:148–162, Oct. 1999. doi: 10.48550/arXiv.astro-ph/9904256.

[301] N. E. White and K. O. Mason. The Structure of Low-Mass X-Ray Binaries. *Space Science Reviews*, 40(1-2):167–194, Feb. 1985. doi: 10.1007/BF00212883.

[302] G. Wiktorowicz, M. Middleton, N. Khan, A. Ingram, P. Gandhi, et al. Predicting the self-lensing population in optical surveys. *Monthly Notices of the Royal Astronomical Society*, 507(1):374–384, Oct. 2021. doi: 10.1093/mnras/stab2135.

[303] B. Willems, M. Henninger, T. Levin, N. Ivanova, V. Kalogera, et al. Understanding Compact Object Formation and Natal Kicks. I. Calculation Methods and the Case of GRO J1655-40. *The Astrophysical Journal*, 625(1):324–346, May 2005. doi: 10.1086/429557.

[304] E. T. R. Williams and A. N. Vyssotsky. Peculiar motions. *Publications of the Leander McCormick Observatory*, 10:48–56, Jan. 1948.

[305] J. R. Wilson. Supernovae and Post-Collapse Behavior. In J. M. Centrella, J. M. Leblanc, and R. L. Bowers, editors, *Numerical Astrophysics*, page 422, Jan. 1985.

[306] R. E. Wilson. Accuracy and Efficiency in the Binary Star Reflection Effect. *The Astrophysical Journal*, 356:613, June 1990. doi: 10.1086/168867.

[307] K. W. Wong and D. Gerosa. Machine-learning interpolation of population-synthesis simulations to interpret gravitational-wave observations: A case study. *Physical Review D*, 100(8), Oct. 2019. ISSN 2470-0029. doi: 10.1103/physrevd.100.083015.

[308] T.-W. Wong, F. Valsecchi, T. Fragos, and V. Kalogera. Understanding Compact Object Formation and Natal Kicks. III. The Case of Cygnus X-1. *The Astrophysical Journal*, 747(2):111, Mar. 2012. doi: 10.1088/0004-637X/747/2/111.

[309] A. Wongwathanarat, H. T. Janka, and E. Müller. Three-dimensional neutrino-driven supernovae: Neutron star kicks, spins, and asymmetric ejection of nucleosynthesis products. *Astronomy and Astrophysics*, 552:A126, Apr. 2013. doi: 10.1051/0004-6361/201220636.

[310] D. B. Wood. A reflection model for eclipsing binary stars. *Monthly Notices of the Royal Astronomical Society*, 164:53, Jan. 1973. doi: 10.1093/mnras/164.1.53.

[311] P. Wroblewski, T. Guver, and F. Ozel. Column densities towards three bursting low-mass x-ray binaries from high resolution x-ray spectroscopy, 2008.

[312] XRISM Collaboration. The XRISM first-light observation: Velocity structure and thermal properties of the supernova remnant N 132D. *Publications of the ASJ*, 76 (6):1186–1201, Dec. 2024. doi: 10.1093/pasj/psae080.

[313] XRISM Science Team. Concept of the X-ray Astronomy Recovery Mission. In J.-W. A. den Herder, S. Nikzad, and K. Nakazawa, editors, *Space Telescopes and Instrumentation 2018: Ultraviolet to Gamma Ray*, volume 10699 of *Society of*

Photo-Optical Instrumentation Engineers (SPIE) Conference Series, page 1069922, July 2018. doi: 10.1117/12.2309455.

[314] S. Yamada and K. Sato. Numerical Study of Rotating Core Collapse in Supernova Explosions. *The Astrophysical Journal*, 434:268, Oct. 1994. doi: 10.1086/174724.

[315] I. V. Yanes-Rizo, M. A. P. Torres, J. Casares, P. G. Jonker, J. Sánchez-Sierras, et al. Revisiting the fundamental parameters for the black hole x-ray transient swift j1753.5-0127, 2025.

[316] M. Yang, A. Z. Bonanos, B. Jiang, E. Zapartas, J. Gao, et al. Evolved massive stars at low-metallicity. V. Mass-loss rate of red supergiant stars in the Small Magellanic Cloud. *Astronomy and Astrophysics*, 676:A84, Aug. 2023. doi: 10.1051/0004-6361/202244770.

[317] S.-N. Zhang, J. Liao, and Y. Yao. Measuring the black hole masses in accreting X-ray binaries by detecting the Doppler orbital motion of their accretion disc wind absorption lines. *Monthly Notices of the Royal Astronomical Society*, 421(4): 3550–3556, Apr. 2012. doi: 10.1111/j.1365-2966.2012.20579.x.

[318] Y. Zhao, P. Gandhi, C. Dashwood Brown, C. Knigge, P. A. Charles, et al. Evidence for mass-dependent peculiar velocities in compact object binaries: towards better constraints on natal kicks. *Monthly Notices of the Royal Astronomical Society*, 525 (1):1498–1519, Oct. 2023. doi: 10.1093/mnras/stad2226.

[319] L.-L. Zheng, W.-M. Gu, T. Yi, J.-B. Fu, H.-J. Mu, et al. Searching for Black Hole Candidates by LAMOST and ASAS-SN. *The Astronomical Journal*, 158(5):179, Nov. 2019. doi: 10.3847/1538-3881/ab449f.

[320] C. Ziegler, N. M. Law, C. Baranec, T. Morton, R. Riddle, et al. Measuring the recoverability of close binaries in gaia dr2 with the robo-ao kepler survey. *The Astronomical Journal*, 156(6):259, nov 2018. doi: 10.3847/1538-3881/aad80a.

[321] M. Zorotovic, M. R. Schreiber, B. T. Gänsicke, and A. Nebot Gómez-Morán. Post-common-envelope binaries from SDSS. IX: Constraining the common-envelope efficiency. *Astronomy and Astrophysics*, 520:A86, Sept. 2010. doi: 10.1051/0004-6361/200913658.

[322] Zwicky Transient Facility Collaboration. Searching for Gravitational Self-Lensing Binaries with the Zwicky Transient Facility. In *AAS/High Energy Astrophysics*

Division, volume 20 of *AAS/High Energy Astrophysics Division*, page 116.116, Sept. 2023.